Etude à l'échelle nanométrique des interfaces de transformations austénite/ferrite dans Fe-Mn-C à différentes températures intercritiques

Olha Nakonechna

Normandie Université

THÈSE

Pour obtenir le diplôme de doctorat

Spécialité PHYSIQUE

Préparée au sein de l'Université de Rouen Normandie

Etude à l'échelle nanométrique des interfaces de transformations austénite/ferrite dans Fe-Mn-C à différentes températures intercritiques

Présentée et soutenue par
OLHA NAKONECHNA

Thèse soutenue le 21/06/2022 devant le jury composé de		
MME SOPHIE CAZOTTES	MAITRE DE CONFERENCES HDR, INSA LYON	Rapporteur du jury
M. JOAKIM ODQVIST	PROFESSEUR DES UNIVERSITES, Institut Royal de Technologie KTH	Rapporteur du jury
M. SEBASTIEN ALLAIN	PROFESSEUR DES UNIVERSITES, UNIVERSITE DE LORRAINE	Membre du jury
M. NICOLAS CHARBONNIER	INGENIEUR DE RECHERCHE RF,	Membre du jury
M. FREDERIC DANOIX	CHARGE DE RECHERCHE, Université de Rouen Normandie	Membre du jury
M. LIONEL GERMAIN	MAITRE DE CONFERENCES HDR, UNIVERSITE DE LORRAINE	Membre du jury
M. MOHAMED GOUNE	PROFESSEUR DES UNIVERSITES, UNIVERSITE BORDEAUX 1 SCIENCES ET TECHNO	Membre du jury
MME HELENA ZAPOLSKY	PROFESSEUR DES UNIVERSITES, Université de Rouen Normandie	Directeur de thèse

Thèse dirigée par HELENA ZAPOLSKY (GROUPE DE PHYSIQUE DES MATERIAUX),

UNIVERSITÉ DE ROUEN NORMANDIE

ED 591 PSIME

GPM Groupe de Physique des Matériaux

Normandie Université

THÈSE

Pour obtenir le diplôme de doctorat

Spécialité PHYSIQUE

Préparée au sein de l'Université de Rouen Normandie

Étude à l'échelle nanométrique des interfaces de transformation austénite/ferrite dans Fe-Mn-C à différentes températures intercritiques

Présentée et soutenue par
Olha NAKONECHNA

Thèse soutenue le 21/06/2022 devant le jury composé de		
Mme. Sophie CAZOTTES	Maître de conférences HDR – MATEIS, INSA Lyon	Rapporteur
M. Joakim ODQVIST	Professeur – KTH Royal Institute of Technology	Rapporteur
M. Sébastien ALLAIN	Professeur – IJL, Ecole des Mines de Nancy,Université de Lorraine	Examinateur
M. Mohamed GOUNÉ	Professeur – ICMCB, Université de Bordeaux	Examinateur
M. Didier HUIN	Ingénieur de Recherche – ArcelorMittal Global R&D Maizières	Invité
M. Nicolas CHARBONNIER	Ingénieur de Recherche – ArcelorMittal Global R&D Maizières	Invité
M. Lionel GERMAIN	Maître de Conférences HDR – LEM3, Université de Lorraine	Invité
Mme. Helena ZAPOLSKY	Professeur – GPM, Université de Rouen Normandie	Directeur de thèse
M. Frédéric DANOIX	Chargé de recherche – GPM, Université de Rouen Normandie	Co-encadrant de thèse

Thèse dirigée par Pr. Helena ZAPOLSKY et co-encadrée par Dr. Frédéric DANOIX
Groupe de Physique des Matériaux, UMR CNRS 6634
Université de Rouen Normandie

UNIVERSITÉ DE ROUEN NORMANDIE

ED PSIME

GPM Groupe de Physique des Matériaux

Acknowledgements

Acknowledgements will come after the defence.

Dedicated to my dear father Mykhailo

Як багато нашого пішло з тобою, як багато твого залишилося з нами …

Contents

Contents 1
List of figures 4
List of tables 11
Abbreviations 12
Introduction 13
Chapter 1 . Austenite-to-ferrite phase transformation: literature review 17
1.1 Steels for the automotive industry 17
1.1.1 Steels in automobile structure: advanced high-strength steels (AHSS) 17
1.1.2 Dual-Phase Steel (DP) 18
1.2 Microstructure-properties of modern steels: role of austenite to ferrite phase transformation 21
1.2.1 Fe-C phase diagram: austenite to ferrite phase transformation 21
1.2.2 Morphologies of proeutectoid ferrite: allotriomorphic ferrite 23
1.2.3 Orientation relationships (ORs) 25
1.2.4 Austenite-to-ferrite phase transformation: general remarks 26
1.3 Theoretical prediction of proeutectoid ferrite growth in the Fe-C binary system 27
1.4 Theoretical prediction of proeutectoid ferrite growth in a Fe-C-X ternary system 31
1.4.1 Local equilibrium in a ternary system 31
1.4.2 Local Equilibrium with Partitioning (LEP) or with Negligible Partitioning (LENP) 33
1.4.3 Paraequlibrium 35
1.4.4 Experimental observation 36
1.5 Solute Drag 38
1.6 Resume 43
Chapter 2 . Material processing and characterisation 45
2.1 Materials and heat treatment processing 45
2.2 Microstructure observation 47
2.3 Atom probe tomography (APT) 48
2.3.1 A basic principle of Local Electrode Atom Probe (LEAP) 48
2.3.2 Time-of-flight (TOF) mass spectrometry 52
2.3.3 APT mass and spatial resolutions 53
2.4 SEM-EBSD investigation 54
2.4.1 Scanning Electron Microscope (SEM) 54
2.4.2 Electron BackScatter Diffraction (EBSD) 55
2.4.3 Parent orientation maps reconstruction 57
2.5 Focused ion beam (FIB) sample preparation for APT 61

2.5.1 SEM-FIB dual-beam microscope 61
2.5.2 Conventional lift-out process 62
2.5.3 Site-specific lift-out for interface analysis 63
2.5.4 Modified site-specific lift-out for interface analysis 64
2.5.5 Annular milling 66
2.6 APT data acquisition and data processing 69
2.6.1 Experimental conditions of APT measurement 69
2.6.2 APT data reconstruction: parameter optimization 69
2.7 APT measurement of segregation 74
2.7.1 Gibbsian interfacial excess method 76
2.7.2 Methodology of Maugis and Hoummada 79
2.7.3 Influence of the Gibbs interface positioning accuracy 82
Chapter 3 . Experimental observation of the austenite/ferrite transformation interfaces 85
3.1 Austenite-to-ferrite phase transformation: material, transformation temperature, holding time 85
3.2 Kinetics of ferrite growth: dilatometry and microstructure observation 86
3.3 Experimental observation of γ/αtransformation interface by APT 89
3.4 Details of APT data representation 90
3.5 Austenite/ferrite interface at 625°C 92
3.5.1 Austenite/ferrite interface after 5s at 625°C 93
3.5.2 Austenite/ferrite interface after 15s at 625°C 97
3.5.3 Austenite/ferrite transformation interface after 30s at 625°C 104
3.5.4 Austenite/ferrite transformation interface after 3h at 625°C 108
3.6 Austenite/ferrite transformation interface after ageing at 680° 112
3.6.1 Austenite/ferrite transformation interface after ageing at 680° during 100s 112
3.6.2 Austenite/ferrite transformation interface after 600s at 680°C 117
3.6.3 Austenite/ferrite transformation interface after 3h at 680°C 128
3.6.4 Austenite/ferrite interfaces after 3 h at 720°C 137
3.7 Conclusions 139
Chapter 4 . Atomistic modeling of fcc-to-bcc phase transformation 141
4.1 Quasi-Particle approach: Atomic Fragment Theory (AFT) 141
4.1.1 Kinetic equation 143
4.2 Modeling of fcc-to-bcc phase transformation by QP approach: Simulation details 147
4.3 Modeling of fcc-to-bcc phase transformation by QP approach: Numerical results 150
4.3.1 Bcc growth kinetic during fcc-to-bcc transformation 150
4.3.2 Atomic structure of fcc/bcc interface 152
4.3.3 System with KS-V1 OR 155
4.4 Simulated diffraction patterns 159

4.5 Conclusions 160
Chapter 5 . Discussion 161
5.1 LENP vs. Solute Drag at 625°C and 680°C 161
5.1.1 DICTRA calculation at 625°C and 680°C 163
5.1.2 LENP spike thickness: estimation according to Coates 168
5.1.3 Comparison of APT data at 625°C and 680°C with theoretically expected under LENP condition 171
5.2 Model of D. HUIN, ArcelorMittal SA 173
5.2.1 Model overview 173
5.2.2 'Huin' model: simulation details 178
5.2.3 Constant interface velocities 180
5.2.4 Variable interface velocity 183
5.2.5 Comparison of APT data at 625°C and 680°C with the results of 'Huin' model 186
5.2.6 Homogeneous Mn distribution through the interface 191
5.3 LEP vs. Solute Drag at 720°C 192
5.4 Mobile interface of transformation. ORs influence 195
5.5 Conclusions 197
Conclusions and suggestions for further work 199
Conclusions based on experimental work 199
Prospective regarding the experimental work 202
Conclusions based on QP modelling 203
Prospective regarding the atomistic modelling using QP approach 203
Appendix A. Elastic constant calculation 205
A.1. Elastic constants of a cubic crystal 205
A.2. Calculation of elastic constant 205
Appendix B. The orientation transformation matrix 209
Appendix C. Numerical resolution of the diffusion equation 213
C.1. The adaptive mesh for the space discretization 213
C.2. Numerical resolution of the diffusion equation 214
REFERENCES 216

List of figures

Figure 1.1. Steel grades in automobile structure [2]. 17
Figure 1.2. Strength-ductility diagram for steels [3]. 18
Figure 1.3. Examples of a dual-phase steel's microstructures (bright regions – ferrite, dark – martensite) in Fe-0.17wt%C-2wt%Mn alloy obtained after 3hours of intercritical annealing at **(a)** 720°C, **(b)**680°C, **(c)** 625°C. 19
Figure 1.4. Temperature-time schedule of Dual-Phase steel production in the case for hot band products (a) and cold-rolled and hot-dip coated products (b) [32]. 20
Figure 1.5. Metastable Fe-Fe_3C phase diagram. The microstructures variation of alloy with the nominal composition c0 left to eutectic compositions during cooling is shown on the left (see points c, d, e, f) [36]. 22
Figure 1.6. Lattice structures with octahedral interstitial voids of **(a)** bcc and **(b)** fcc crystal [38]. 23
Figure 1.7. Schematic illustration of proeutectoid ferrite morphologies. 24
Figure 1.8. Bain distortion (fcc-bct-bcc transformation). The Fe and C atoms are in red and grey, respectively [38]. 25
Figure 1.9. Schematic Gibbs energy diagram **(a),** phase diagram **(b)**, and carbon composition profile **(c)** illustrating the local conditions at the α/γ migrating interface at T1. 28
Figure 1.10. The evolution of carbon concentration profile at the γ/α interface during the diffusion-controlled mode of phase transformation. 29
Figure 1.11. (a) Schematic representation of the full equilibrium conditions given by Eq.(1.8). **(b)** The isothermal section of a ternary system with possible tie-lines. 32
Figure 1.12. (a) Definition of interfacial composition using "Interface Composition Counters"; **(b)** Definition of the zero-partition line in a Fe-C-X diagram (when $D11/D22>>1$). 33
Figure 1.13. Schematic illustration of the phase boundaries, interfacial concentrations, and diffusion profiles under **(a)** LEP and **(b)** LENP conditions of a Fe-C-X alloy with bulk composition marked by red points. 34
Figure 1.14. Schematic illustration of the phase boundaries, interfacial concentrations, and diffusion profiles under PE conditions of a Fe-C-X alloy with bulk composition marked by red points. 36
Figure 1.15. (a) Equilibrium solute profile across a stationary grain boundary with wedge-shaped, attractive interaction energy; **(b)** examples of interaction energy profiles that have been used to represent the grain boundary [80]. 39
Figure 1.16. Solute profile through a grain boundary moving with velocity V, for which there is an attractive interaction with the solute. A wedge-shaped interaction G(x), a constant diffusivity D, and ideal (dilute) solution thermodynamics are assumed [83]. 40
Figure 1.17. (a) Chemical potential profile of substitution element across the transformation interface. Calculated X profiles inside the interface with **(b)** v=1 μm/s and **(c)** v=0.01 μm/s. 42
Figure 1.18. A schematic diagram to show the 'solute drag' force as a function of interface velocity [77]. 42
Figure 2.1. (a) Schematic history of the heat treatment process performed in a dilatometer and measured dilatometric curve **(b).** 46
Figure 2.2. Optical micrographs examples of observed microstructures (bright regions – ferrite, dark – martensite) in Fe-0.17wt%C-2wt%Mn alloy obtained after 3 hours of intercritical annealing at **(a)** 720°C, **(b)**680°C, **(c)** 625°C. 48
Figure 2.3. Schematic representation of the LEAP microscope [110]. 49
Figure 2.4. Schematic configuration of the curved reflectron configuration of LEAPT [110]. 51
Figure 2.5. Schematic graph showing different evaporation fields causing trajectory aberrations **(a)** from the low field and **(b)** high field evaporation precipitate with the density on the detector represented as a darker color for higher density [110]. 52

Figure 2.6. Different examples of the SEM micrographs with α'(γ)/α interfaces regions **(a)** 3h at 720°C, **(b)** 3h at 680°C, **(c)** 3h at 625°C. 55
Figure 2.7. Example of EBSD data observation (3h at 680°C).....56
Figure 2.8. The main steps of reconstruction: **(a)** domain detection, **(b)** fragments identification, **(c)** enlargement, **(d)** ambiguities management. 59
Figure 2.9. Illustration of the grain detection and transformation in a graph (the bold red lines represent not know during the reconstruction parent grain boundary) [137]. 59
Figure 2.10. Reconstruction of parent orientation map and measurement of the ORs ferrite/austenite: **(a)** measured EBSD map at room temperature, **(b)** manual separation of martensite/ferrite pashes, **(c)** reconstructed orientation map of austenite/ferrite phases (example of 3h at 680°C), **(d)** measured ORs of ferrite/austenite microstructure. 61
Figure 2.11. The main steps of the conventional lift-out procedure on a duplex stainless steel. **(A)** the deposition of a protective layer, **(B)** the milling material around the ROI, **(C)** the milling of a horizontal cut through the wall and welding of the micromanipulator tip, **(D)** sample mounting on a support tip, **(E)** cutting of the end of the wall, and **(F)** side view of the sample mounted on the support tip [112]. 63
Figure 2.12. Site-specific lift-out for interface analysis on austenitic steel: (**A)** SEM image of the milled wall perpendicular to previously selected interface; **(B)** specimen mounting parallel to a support tip; **(C)** specimen mounted on the support tip, ready for annular milling [112]. 63
Figure 2.13. The example of allotriomorph ferrite grain (5s at 625°C)with measured ORs at the interfaces. The set of schematical APT tips represent the desirable sample preparation configurations for APT investigation. 65
Figure 2.14. Modified site-specific lift-out for interface analysis: **(A)** SEM image of the ROI, **(B)** the deposition of a protective layer, **(C-D)** the milling material around the ROI, **(E)** the milling of a horizontal cut through the wall, **(F)** mounting of the welded on the micromanipulator sample on a support tip.....66
Figure 2.15. SEM images showing different steps of annular milling with (A) the initial sample mounted on the W support tip, (B) the obtained cylinder after the first milling step, (C) tip after the several steps of AM, close to the final shape and size, (D) schematic demonstration of a milling pattern. 67
Figure 2.16. (a) Schematic set-up in the SEM-FIB microscope chamber for TKD analysis**. (b)-(c)** annular milling controlled by the TKD analysis, the band contrast images, and the IPF Y color maps showing the interface position.....68
Figure 2.17. A typical mass spectrum of the analyzed Fe-C-Mn alloys with the position of Fe and Mn peaks. 70
Figure 2.18. 2D desorption map of **(a)** single events highlighting (011) pole and **(b)** multiple events highlighting (111) pole 71
Figure 2.19. Schematic view of the point-projection [115]. 72
Figure 2.20. Reconstructed APT subvolume at (011)-pole with $\xi = 1.6, \mathrm{kf}=4$: **(a)** the z-spatial distribution maps of Fe atoms revealing the interplanar distances, IVAS software; **(b)** measurement of the interplanar distances using GPM 3D software. 74
Figure 2.21. (a) The reconstructed 3D volume of Fe-2at% Mn-0.78 at% C model alloy containing an α' (γ)/α transformation interface reveals the segregation of C (red) and Mn atoms (gray); **(b)** concentration profile across interface represents the concentration of C and Mn atoms versus distance from the interface. 75
Figure 2.22. Schematic illustration of the expected "real" profile and experimentally measured (Measure 1, Measure2) [119]. 76
Figure 2.23. (a) Schematic illustration of the analyzed volume with the interface. **(b)** Hypothetical integral profile (line ABCD) represents the cumulative number of solute atoms versus the cumulative numbers of all atoms in the vicinity of the interface determined from an APT analysis [166]. 77
Figure 2.24. Schematic illustration of the interfacial excess calculation by Gibbs's method using a dividing surface: **(a)** symmetrical concentration profile; **(b), (c), (d)** concentration profiles with different compositions from both sides of the interface and dividing surface placed at the position of the peak and ±1nm from it, respectively. 79

Figure 2.25. (a) Schematic illustration of the expected "real" profile and experimentally measured (Measure 1, Measure2). **(b)** The excess concentration is calculated from the integral concentration profiles [119]. 80
Figure 2.26. An example of the reconstructed APT volumes of the Fe-2at%Mn-0.78at%C model alloy containing the α' (γ)/α transformation interface with the appropriate atomic fraction and integral fraction profiles, in % nm, through those interfaces. Analised volumes are the neighbor tips extracted from the same chunk....81
Figure 2.27. Example of the atomic fraction and integral fraction profiles with non-symmetric shape. 82
Figure 2.28. **(a)** Model concentration profiles of segregating atoms across the interface; **(b)** Interfacial excess calculated depending on the dividing surface position relative to the concentration profile's peak. 83
Figure 3.1. The isothermal section at **(a)** 625°C, **(b)** 680°C, **(c)** 720°C in the Fe-C-Mn phase diagrams. The nominal composition is given as a red point and located (a) below relatively to the zero-partitioning line, (b) slightly below, (c) slightly above. 85
Figure 3.2. Optical micrographs examples of observed microstructures in Fe-0.17wt%C-2wt%Mn alloy obtained after the intercritical annealing: **(a)** at 720°C during 3 h; **(b), (c)** and **(d)** at 680°C during 100 s, 600 s, and 3h respectively; **(e), (f), (d)** at 625°C during 10 s, 30 s, and 3 h respectively. The bright regions correspond to ferrite, while the dark contrast to martensite (former austenite). 88
Figure 3.3. Comparison of the ferrite growth kinetics measured combining image analysis and dilatometry at: 720°C (purple color), 680 °C (blue color), and 625 °C (orange). 88
Figure 3.4. Examples of the various interface morphologies within the same sample (isothermal holding at 720° during 3h). 90
Figure 3.5. The example of the image quality (IQ) map of the selected allotriomorph ferrite formed at the prior austenite grain boundary after isothermal holding at 625°C during 5s. This region is referred as **625_5s_ch1** for temperature, holding time, and extracted specimen (chunk). Colors on the two α'(γ)/α interfaces (named as1st and 2nd) represent the determined deviations from predefined ORs between ferrite and former austenite at 625 °C. It is expressed as the orientation difference with respect to KS orientation from 0 (red) to 24° (blue). The position of schematic APT tips approximately corresponds to the locations of APT specimens along the selected ferrite–austenite interface (only successful APT runs are shown). 91
Figure 3.6. IQ maps of the selected region with an allotriomorph ferrite formed at the prior austenite grain boundary after isothermal holding at 625°C during 5s. Colors at α' (γ)/α interfaces represent the orientation relation between ferrite and former austenite at 625°C, expressed as the orientation difference with respect to KS-OR. 93
Figure 3.7. 3D reconstructions and concentration profiles of C and Mn atoms across the 1st and 2nd interfaces of 625_5s_ch1: **(a)** tip1_1st; **(b)** tip2_1st; **(c)** tip3_1st; **(d)** tip4_1st; **(f)** tip6_1st, **(e)** tip4_2nd **(g)** tip6_2nd (see **Figure 3.6**). 95
Figure 3.8. (a) IQ map of the selected region with the allotriomorph ferrite formed after isothermal holding at 625°C during 5s (**625_5s_ch2)**. Colors represent the orientation difference with respect to KS-OR of the initial ferrite–austenite orientation relationships at 625 °C. 3D reconstructions and concentration profiles of C and Mn atoms across the **(b)** 1st and **(c)** 2nd interface of tip1. 97
Figure 3.9. IQ map of the selected region with the allotriomorph ferrite formed after isothermal holding at 625°C during 15s. This region is coded as **625_15s_ch4**. Colors at two α' (γ)/α interfaces (1st and 2nd) represent the orientation relation between ferrite and former austenite at 625°C. It is expressed as the orientation difference with respect to KS orientation from 0 (red) to 25° (blue)....98
Figure 3.10. 3D reconstructions and concentration profiles of C and Mn atoms across the α' (γ)/α interfaces depicted in **Figure 3.9** that has a code: **625_15s_ch4** (isothermal holding at 625°C during 15s). (**a),(c), (f)** – results correspond to tip4,tip5, tip10 of the 1st interface investigation and **(b), (d)** – tip4, tip6 of 2nd interface investigation. 100
Figure 3.11. (a) IQ map of the selected region with the allotriomorph ferrite formed after isothermal holding at 625°C during 15s (**625_15s_ch1)**. Colors represent the orientation difference with respect to

KS-OR of the initial ferrite–austenite orientation relationships at 625 °C. **(b)** 3D reconstructions and concentration profiles of C and Mn atoms across the 1st interface of tip5. 102
Figure 3.12. **(a)** IQ map of the selected region with the allotriomorph ferrite formed after isothermal holding at 625°C during 15 s (**625_15s_ch7)**. Colors represent the orientation difference with respect to KS-OR of the initial ferrite–austenite orientation relationships at 625 °C. **(b)** 3D reconstructions and concentration profiles of C and Mn atoms across the 2nd interface of tip3 and. **(c)** across the 2nd interface of tip5. 104
Figure 3.13. (a) IQ map of the selected region with the allotriomorph ferrite formed after isothermal holding at 625°C during 30 s (**625_30s_ch1)**. Colors represent the orientation difference with respect to KS-OR of the initial ferrite–austenite orientation relationships at 625 °C. **(b)** 3D reconstructions and concentration profiles of C and Mn atoms across the 2nd interface of tip3 and. **(c)** across the 1st interface of tip5. 106
Figure 3.14. (a) IQ map of the selected region with the allotriomorph ferrite formed after isothermal holding at 625°C during 30s (**625_30s_ch2)**. Colors represent the orientation difference with respect to KS-OR of the initial ferrite–austenite orientation relationships at 625 °C. **(c)** 3D reconstructions and concentration profiles of C and Mn atoms across the 2nd interface of tip2 and. **(c)** across the 1st interface of tip4. 107
Figure 3.15. (a) IQ map of the selected region with the allotriomorph ferrite formed at the prior austenite grain boundary after isothermal holding at 625°C for 3h (**625_3h_ch3)**. Colors represent the orientation difference with respect to KS-OR of the initial ferrite–austenite orientation relationships at 625 °C. **(a)** 3D reconstructions and concentration profiles of C and Mn atoms across the 2nd interface of tip2. 109
Figure 3.16. (a) IQ map of the selected region with the allotriomorph ferrite formed at the prior austenite grain boundary after isothermal holding at 625°C for 3h (**625_3h_ch5)**. Colors represent the orientation difference with respect to KS-OR of the initial ferrite–austenite orientation relationships at 625 °C. **(a)** 3D reconstructions and concentration profiles of C and Mn atoms across the 2nd interface of tip7. 110
Figure 3.17. (a) IQ map of the selected region with the allotriomorph ferrite formed at the prior austenite grain boundary after isothermal holding at 625°C for 3h (**625_3h_ch6)**. Colors represent the orientation difference with respect to KS-OR of the initial ferrite–austenite orientation relationships at 625 °C. **(a)** 3D reconstructions and concentration profiles of C and Mn atoms across the 1st interface of tip7. 111
Figure 3.18. IQ maps of the two selected regions with the allotriomorph ferrite films formed after isothermal holding at 680°C during 100 (**680_100s_ch1).** Colors at α' (γ)/α interfaces represent the orientation relation between ferrite and prior austenite at 680 °C. It is expressed as the orientation difference with respect to the KS orientation relationship. 112
Figure 3.19. 3D reconstructions and concentration profiles of C and Mn atoms across the 1st interface of (**a**)tip1, (**c**)tip3, (**d**)tip4, and across the 2nd interface of (**b**)tip1 of the **680_100s_ch1** (see **Figure 3.18**). 114
Figure 3.20. IQ maps of the two selected regions with the allotriomorph ferrite films formed after isothermal holding at 680°C during 100s (**680_100s_ch3).** Colors at α' (γ)/α interfaces represent the orientation relation between ferrite and prior austenite at 680 °C. It is expressed as the orientation difference with respect to the KS orientation relationship. 115
Figure 3.21. 3D reconstructions and concentration profiles of C and Mn atoms across the 1st interface of (**a**)tip3, (**b**)tip6 of the **680_100s_ch1** (see **Figure 3.20**). 116
Figure 3.22. IQ map of selected ROIs with the thin allotriomorph ferrite grains formed after isothermal holding at 680°C during 600s (**680_600s_ch8**). Colors at α'(γ)/α interfaces represent the orientation relation between ferrite and prior austenite at 680 °C. It is expressed as the orientation difference with respect to the KS orientation relationship. 118
Figure 3.23. 3D reconstructions and concentration profiles of C and Mn atoms across the 1st interface of 680_600s_ch8 of: **(a)** tip1_1st; **(b)** tip2_1st; **(c)** tip3_1st; **(d)** tip4_1st (see **Figure 3.22**). 120
Figure 3.24. IQ map of the selected allotriomorph ferrite grains formed after isothermal holding at 680°C during 600s (**680_600s_ch12**). Colors at α'(γ)/α interfaces represent the orientation relation between ferrite and prior austenite at 680 °C. It is expressed as the orientation difference with respect to the KS orientation relationship. 121

Figure 3.25. 3D reconstructions and concentration profiles of C and Mn atoms across the 2nd interface of 680_600s_ch12 of: **(a)** tip2_2nd; **(b)** tip3_2nd; **(c)** tip5_2nd; (see **Figure 3.24**). 123
Figure 3.26. (a) IQ map of selected ROIs with the thin allotriomorph ferrite grains formed after isothermal holding at 680°C during 600s (**680_600s_ch13**). Colors at α'(γ)/α interfaces represent the orientation relation between ferrite and prior austenite at 680 °C. It is expressed as the orientation difference with respect to the KS orientation relationship. 3D reconstructions and concentration profiles of C and Mn atoms across the 1st, **(b),** and 2nd (c) α/γ interfaces of tip3. 124
Figure 3.27. **(a)** IQ map of selected ROIs with the thin allotriomorph ferrite grains formed after isothermal holding at 680°C during 600s (**680_600s_ch15**). Colors at α'(γ)/α interfaces represent the orientation relation between ferrite and prior austenite at 680 °C. It is expressed as the orientation difference with respect to the KS orientation relationship. **(b)** 3D reconstructions and concentration profiles of C and Mn atoms across the 1st, of tip2. 125
Figure 3.28. (a) IQ map of selected ROIs with the thin allotriomorph ferrite grains formed after isothermal holding at 680°C during 600s (**680_600s_ch14**). Colors at α'(γ)/α interfaces represent the orientation relation between ferrite and prior austenite at 680 °C. It is expressed as the orientation difference with respect to the KS orientation relationship. **(b)** and **(c)** 3D reconstructions and concentration profiles of C and Mn atoms across the 1st, of tip3 and tip 4, respectively. 127
Figure 3.29. Image quality (IQ) map of the selected region with the allotriomorph ferrite formed at the prior austenite grain boundary after isothermal holding at 680°C during 600s. This region is coded as **680_3h_ch3**. Colors at two α' (γ)/α interfaces (1st and 2nd) represent the orientation difference with respect to KS-OR of the initial ferrite – austenite interfaces at 680 °C. 129
Figure 3.30. 3D reconstructions and concentration profiles of C and Mn atoms across the 1st, and 2nd α/γ interfaces of 680_3h_ch3, see **Figure 3.29**.....131
Figure 3.31. Image quality (IQ) map of the selected region with the allotriomorph ferrite formed at the prior austenite grain boundary after isothermal holding at 680°C during 600s. This region is coded as **680_3h_ch6.** Colors at two α' (γ)/α interfaces (1st and 2nd) represent the orientation difference with respect to KS-OR of the initial ferrite – austenite interfaces at 680 °C. 132
Figure 3.32. 3D reconstructions and concentration profiles of C and Mn atoms across the 1st, and 2nd α/γ interfaces of 680_3h_ch6, see **Figure 3.31**.....135
Figure 3.33. (a) Image quality (IQ) map of the selected region with the allotriomorph ferrite formed at the prior austenite grain boundary after isothermal holding at 680°C during 3h. This region is coded as **680_3h_ch4**. Colors at two α'(γ)/α interfaces (1st and 2nd) represent the orientation difference with respect to KS-OR of the initial ferrite – austenite interfaces at 680 °C. **(b)** and **(c)** 3D reconstructions and concentration profiles of C and Mn atoms across the 1st, and 2nd α/γ interfaces of tip 1, respectively. 136
Figure 3.34. (a) Image quality (IQ) map of the selected allotriomorph ferrite formed at the prior austenite grain boundary after isothermal holding at 720°C for 3h and 3D reconstructions with concentration profiles of C and Mn atoms across the α/γ interfaces: **(a-b) 720_3h_ch2**, **(c-d) 720_3h_ch3**, **(e-f) 720_3h_ch4**. Colors at two α'(γ)/α interfaces (1st and 2nd) represent the orientation difference with respect to KS-OR of the initial ferrite – austenite interfaces at 720 °C. 139
Figure 4.1. (a) Illustration of the ADF theory on a rigid Ising lattice, **(b)** illustration of AFT model with fraton approach [176]. 142
Figure 4.2 (a) The short-range potential in real space, **(b)** the short-range potential in reciprocal space. 144
Figure 4.3. Schematic representation of the distance a1 to the first neighbors in **(a)** bcc and **(b)** fcc lattices with the lattice parameter abccand afcc, respectively [38]. 145
Figure 4.4. The schematic illustration of the long-range potential for **(a)** bcc and **(b)** fcc structures in reciprocal space.....146
Figure 4.5. Initial configuration with Bain OR (t=0 simulation steps): **(a)** 3D view using CAN of OVITO software; **(b)**2D slice visualization of the 010γ plane using ParaView software (the 010γ plane is demonstrated as the common plane for fcc and bcc phases in the case of Bain OR). 149
Figure 4.6. Growth of the bcc phase in fcc matrix (system with KS-V1 OR). 151
Figure 4.7. Temporal evolution of the bcc phase fraction in the systems with different ORs. 151

Figure 4.8. The atomic density profile at t=30 000 in the 010γ plain for the system with **(a)** Bain and **(b)** Pitch ORs and 111γ plain for **(c)** KS-V1 and **(d)** NW-V1.The red and yellow arrows highlight the presence of structural defects at the fcc/bcc intricate.....154
Figure 4.9. Schematic representation of the shape change of a bcc lattice caused by the two-slip modes. Arrows indicate the slip direction [177].....154
Figure 4.10. Propagation of the fcc-to-bcc interface with respect to the KS-V1 OR, visualization in {111}γ plain at different simulation time steps (t=0, 5 000 and 10 000 simulation steps): **(a)**, **(b)**, **(c)** the 2D slices of CNA (green – fcc, blue – bcc, grey – unknown structure) and **(d)**, **(e)**, **(f)** elastic strain field redistribution map (using Voronoi analysis) are shown. 156
Figure 4.11. The fcc-to-bcc transformation with the KS-V1 OR at t=30 000 simulation steps in {111}γ plain. **(a)** 2D slice visualization using CNA of OVITO software (green – fcc, blue – bcc, grey – unknown structure). **(b)** The gradient color map of Voronoi analysis in the range from 150 to 150 atomic volume that corresponds to the regions of dilatation (blue color) and compression (red color), respectively. **(c)** The dislocation analysis in OVITO software: the Shockley dislocations with burger vector 1/6 (112) are detected at the interface. 158
Figure 4.12. (a) Simulated diffraction pattern in the {111}γ plane. Green spots correspond to the fcc structure and blue - bcc. **(b)** Simulated dark-field images. The example demonstrated for the system with KS-V1 OR at $t = 30\,000$. 159
Figure 5.1. The isothermal section at **(a)** 625° **(b)** 680° **(c**) 720°C in the Fe-C-Mn phase diagrams. The nominal composition is given as a red point, and the red tie-line is the operative tie-line. 162
Figure 5.2. The initial state of the DICTRA simulation system used for modeling austenite-to-ferrite phase transformation. There are two regions, Ferrite and Austenite, consisting of bcc and fcc phases, respectively. 163
Figure 5.3. The results of DICTRA calculation for the Fe-C-Mn model alloy with the nominal composition of 0.17 wt%C and 2.0 wt%Mn: **(a)** temporal evolution of the ferrite/austenite interface position, **(b)** predicted and measured ferrite growth kinetics, **(c-d)** and **(e-f)** Mn profiles predicted by DICTRA at 5s and 3h of transformation at 625°C and 680°C, respectively. 166
Figure 5.4. Schematic views of 1D geometries of interface propagation during ferrite growth at the austenite grain boundary considered in this study. 169
Figure 5.5. Average interface velocities estimated from the dilatometry data for transformation temperature **(a)** 625°C and **(b)** 680°C.....170
Figure 5.6. The evolution of spike thickness estimated from the relationship established by Coates for **(a)** 625°C and **(b)** 680°C of transformation temperature. 171
Figure 5.7. Comparison of theoretically calculated Mn excess with the Mn excess determined from APT data at **(a)** 625°C and **(b)** 680°C. 172
Figure 5.8. **(a)** Geometrical configuration of the 'Huin'model and **(b)** schematic representation of the initial profile of the substitutional element. 173
Figure 5.9. Chemical potential profile of the substitution element across the transformation interface: E0 – binding energy, ΔE – the half of the Mn chemical potential difference between austenite and ferrite. 175
Figure 5.10. The schematic illustration of the initial profile.....176
Figure 5.11. Evolution of the maximum Mn content within the interface as a function of binding energy E0 at **(a)** 625°C and **(b)** 680°C. 180
Figure 5.12. Mn profiles at T=625°C f simulated with constant velocities using 'Huin' model: Dif_1iter., $\mathbf{E0} = 7$ kJ/mol, **L2**=1 nm.....181
Figure 5.13. Mn profiles at T=680°C f simulated with constant velocities using 'Huin' model: Dif_1iter., $\mathbf{E0} = 7$ kJ/mol, **L2**=1 nm.....183
Figure 5.14. Temporal evolution of the interfacial zone propagation at T=680°C with variable velocity considering "1D" interface propagation simulated using 'Huin' model: Dif_1iter., $\mathbf{E0} = 7$ kJ/mol, **L2**=1 nm. 184
Figure 5.15. Mn profiles simulated at T=680°C with variable velocity considering "1D" interface propagation using 'Huin' model with different diffusion coefficients (Dif_liter and Dif_DICTRA),

binding energy values (7 and 14 kJ/mol) and thicknesses of the interfacial zone (1 nm, 3 nm and 5 nm). 185
Figure 5.16. Mn excess calculated from the results of simulations ('Huin' model considering the experimental velocity for 1D ferrite growth, and DICTRA) vs APT measured Mn excess at 680°C..187
Figure 5.17. (a) Mn profiles simulated at T=625°C with variable velocity considering "1D" interface propagation using 'Huin' model: Dif_1iter., $\mathbf{E0} = 7\ \mathrm{kJ/mol}$, **L2**=1 nm. **(b)** Mn excess calculated from the results of simulations ('Huin' model considering the velocity for 1D ferrite growth and DICTRA) vs APT measured Mn excess at 625°C.....188
Figure 5.18. Composition profiles of Mn across the 1st and 2nd α/γ interfaces of 680_3h_ch3, see more details in **Figure 3.29** and **Figure 3.30.**.....190
Figure 5.19. Investigation of austenite-to-ferrite at 720°C: **(a)** the isothermal section of Fe-C-Mn phase diagram; **(b)** predicted and measured ferrite growth kinetics; **(c)** average interface velocities estimated from the dilatometry data.....193
Figure 5.20. Mn composition profiles predicted by DICTRA calculation at 720°C.....194
Figure 5.21. Mn profiles with variable velocity considering "1D" interface propagation simulated at 720°C using 'Huin' model: Dif_1iter., $\mathbf{E0} = 7\ \mathrm{kJ/mol}$, **L2**=1 nm. **(a)** the evolition of Mn profile with time; **(b)** detailed views of Mn profiles at the interface.....194
Figure 0.1. Three types of deformations [176].....206
Figure 0.1 Schematic representation of nodes position for each subdomain. 214

List of tables

Table 1. The list of typical alloying elements used in commercial DP steels and their effect [3][32]. ...20
Table 2. Reported ferrite/austenite ORs in iron and steel. ORs are described by crystallographic plane and direction. N – is the number of variants deduced due to the crystal symmetry. The last column shows what is close-packed in the given model: the planes used (p), the given direction (d), both, or nothing [45]–[47]. ...26
Table 3. Probability P(A) of determining unambiguously the parent orientation as a function of the number of available variants Nv and OR. ...58
Table 4. Gibbsian interfacial excess calculated for the specimens shown in **Figure 2.26** ...84
Table 5. Intercritical temperatures and holding times investigated in this work. ...86
Table 6. The main parameters of observed profiles in the case of **625_5s_ch1** ...96
Table 7. The main parameters of observed profiles in the case of **625_15s_ch4** ...100
Table 8. The main parameters of observed profiles in the case of 625°C for holding time of 3h ...108
Table 9. The main parameters of observed profiles in the case of 680°C for holding time of 100s ...116
Table 10. The main characteristics of the analysed ferrite regions in the case of 680°C and holding time of 600s ...117
Table 11. The main results of the observed composition profiles measured for 600 s at 680°C ...128
Table 12. The main parameters of the observed composition profiles measured for the 3h of transformation at 680°C ...137
Table 13. The simulation parameters used in the simulation used in formulas ...147
Table 14. Elastic constants for the bcc and fcc lattice structures: calculated via simulations (used in this work) and experimentally measured ...148
Table 15. The ORs list and corresponding rotation matrices considered in this study ...148
Table 16. Tested mesh types with different numbers of points in the case of 625°C. ...164
Table 17. The peak width of the simulated Mn profile by DICTRA and calculated Mn excess at the interface for both 625°C and at 680°C TT. ...167
Table 18. Fitting parameters with the maximum velocity values ...169
Table 19. The values of the Mn diffusion coefficients used for calculation within this work ...179
Table 20. The 24 crystalographic variants of the KS ORs. Various Bain groups (BG) and misorientation angle (Θ) of variant V2 to V24 relative to V1 are given [210]. ...211
Table 21. The rotation matrices for the 24 variants of KS ORs [38] ...212
Table 22. The rotation matrices for the 12 variants of NW ORs ...212

Abbreviations

ADF – Atomic Density Function
AFT – Atomic Fragment Theory
AHSS - Advanced High-Strength Steel
APT – Atom Probe Tomography
bcc – body-cybic central
BH – Bake Hardenable
CNA – Common Neighboring Analysis
CP – complex phase
DLD – delay line detectors
DP – dual-phase steels
EBSD – Electron Backscatter Diffraction
ECs – Elastic constants
EU – Europe Union
fcc – face-cybic central
FEM – Field Electron Emission Microscope
FIB – Focus Ion Beam
FIM – Field Ion Microscope
FOV – field of view
FT – Fourier Transformation
HSLA – high-strength low alloy steels
HSS – high-strength steel
LE – Local Equilibrium
LENP – Local Equilibrium with Negligible Partition
LEP – Local Equilibrium with Partitioning
MC – Monte Carlo
MCP – microchannel plate
MD – Molecular Dynamic
MRP – mass resolving power
MS – martensitic steels
ORs – Orientation Relationships
PE – Para-Equilibrium
PFC – Phase Field Crystal
QP – Quasi-Particle
ROI – region of interest
RT – room temperature
SD – Solute Drag
SEM – Scanning Electron Microscope
TKD – Transmission Kikuchi Diffraction
TOF – time-of-flight
TRIP – transformation-induced plasticity
TT – transfromation temperature

α – ferrite
γ – austenite

Introduction

The versatile spectrum of mechanical properties combined with relatively low cost makes steel the dominant structural material for various applications, particularly for the automotive industry. Low-cost mild steel with a simple ferritic microstructure was one of the most commonly used. However, over the last few decades, the automobile market requirements have changed significantly regarding the weight to mechanical properties ratio. Consequently, mild steels do not satisfy those new requirements due to a limited spectrum of mechanical properties [1]–[4]. Simultaneously, the world oil crisis of the 70's can be seen as the beginning of a steel development revolution. The necessity for fuel consumption reduction led to a significant decreasing vehicles' weight – without compromising safety, which required the development of new steel grades [2]. Besides, global warming and climate change caused by the increase in greenhouse gases becomes a major scientific and political issue of the 21st century. The transport sector produces one of the highest percentages of carbon dioxide emissions. Therefore, new norms and standards for CO_2 emissions by vehicles were introduced in accordance with the Paris Climate Agreement of 2015 and the new EU climate policy [3][5][6].

One of the most efficient ways to reduce fuel consumption and thus gas emissions is decreasing automobile weight. The estimations show that every 10% weight reduction reduces by 6-8% and 5% fuel consumption and gas emissions, respectively [3][7]. The best way to achieve an automobile weight reduction is to replace the heavy and massive parts with strong, lightweight materials without compromising safety, functionality and comfort. Numerous modern materials, such as nonferrous light aluminium and magnesium alloys, polymers, and fibre composites, have a high strength-to-weight ratio and can be potentially used. However, these lightweight materials are associated with their high cost and longtime, expensive manufacturing cycle [3][8]. Recyclability is an increasingly important criterion for construction materials. Compared to other materials, steel is the most recycled material and has a high recycling efficiency level. In addition, there is competitive pressure on the market and customer demands for higher quality, safety, and better design but lower price [9]. Considering all existing requirements and anticipating new challenges, steels remain the preferable material for the automotive industry. The automobile sector's new demands have become a driving force for steel

suppliers to develop a new light and strong modern steel class called “Advanced High Strength Steels” (AHSS).

The large variety of microstructures and properties of modern steel is the result of thermo-mechanical treatments. As a result of these treatments, different mixtures of phases can be obtained. Thus, solid-solid phase transformations during the steel production line play a critical role in tailoring the final steel microstructure, and thus mechanical properties. In particular, austenite-to-ferrite phase transformation has great importance since it occurs during the production of most modern steels. A better understanding of its mechanism can help to improve the models used to predict the final steel microstructures [10]. Due to its importance, austenite to ferrite phase transformation has been extensively studied in the last century.

The austenite-to-ferrite transformation in steels is a complex physical process that involves at least two main phenomena: crystal structural change, from face-centered cubic (fcc) to body-centered cubic (bcc) lattice, and diffusional redistribution alloying elements. In the case of the binary Fe-C system, due to the difference in carbon solubilities in ferrite and austenite, the α-ferrite phase growth is accompanied by a long-range carbon redistribution. It is usually assumed that this transformation is only governed by carbon diffusion, the so-called diffusional-controlled model. This assumption has been proved experimentally for binary systems[11][12][13]. However, the most modern steels are multicomponent systems containing both interstitial and substitutional alloying elements. Thus, the situation is more complicated in multi-component systems where additional alloying elements change dramatically the thermodynamic conditions at the fcc/bcc interface, and significantly influence the kinetics of ferrite growth. In the case of Fe-C-X ternary alloys, the particular difficulty is that the diffusion of interstitial elements (C, N) is often many orders of magnitude larger than the one of most substitutional solutes (such as Mn, Cr, Mn, Mo). As a result, austenite-to-ferrite phase transformation occurs with either partitioning or negligible partitioning of the substitutional element across the transformation interface [10][14].

Many different models have been developed to account for the interfacial partitioning of substitutional elements during the austenite-to-ferrite transformation in Fe-C-X alloys. Two thermodynamic approaches, Local Equilibrium (with partitioning – LEP and without partitioning of alloying elements – LENP) and ParaEquilibrium (PE), have been widely used models recently. LEP kinetics is expected to be slow since it is controlled by the diffusion of substitutional elements. Under this condition, a long-range diffusion profile of substitutional atoms into austenite is expected. LENP refers to the non-partitioning of the substitutional elements. However, to satisfy local thermodynamic equilibrium conditions, a spike of the

substitutional solute must appear at the transformation interface. PE mode assumes that substitutional elements are completely immobile during the transformation. This condition is expected to be approached at high interface velocities and low transformation temperatures [15][16][17]. However, these assumptions represent thermodynamic limits and can be reached only in some special cases. Therefore, the deviations from LE and PE are often observed and are related to the interaction of the solute atoms with the moving transformation interface through a phenomenon known as Solute Drag (SD). Such interaction leads to the solute segregation at the interface that consumes part of the phase transformation driving force and thus retards the motion of the austenite/ferrite transformation interface. Solute Drag models have been widely used by many authors to describe the segregation of solutes at moving interfaces [18][19][20][21][22]. It was shown that this approach describes reasonably well the kinetics of ferrite growth in steels.

The interaction of alloying elements with a moving transformation interface is a complex problem that depends on many factors, such as crystallography and coherency of atomic structure at the interface, as well as the shape of the interface. All these factors are strongly coupled and influence the kinetic (trans-interface diffusivity) and thermodynamic (binding energy) parameters used in the SD approach. Therefore, it is expected that nanoscale investigation of the transformation interface can bring some light to the influence of segregation on ferrite growth kinetics. However, previously, the experimental investigation of a particular interface has received relatively little attention. One of the reasons was the limited capabilities of experimental techniques or very complex experimental procedures. Most experimental observations were focused on the measurement of the ferrite volume fraction evolution. For example, in the case of widely used decarburization experiments, it is possible to follow only the planar transformation interface migration. However, these conditions are somehow simplified compared to the conditions of ferrite growth during industrial steel production. In particular, the transformation interface with a simple planar geometry is not typical for industrial steel microstructures. In addition, decarburization experiments do not provide the chemical composition at the interface.

The recent development of advanced techniques for material characterization significantly expanded the capabilities of experimental investigation of transformation interface at the atomic scale. There are several techniques, such as Auger Spectroscopy (AES), wavelength dispersive X-ray spectroscopy (WDS), secondary ion mass spectroscopy nano-analysis (NanoSIMS), transmissions electron microscopy (TEM), and atom probe tomography (APT), that can be used for the measurement solute segregation at the interface. AES, WDS, and NanoSIMS are not the most appropriate methods to quantify interfacial segregation. These

experimental technics have limited spatial resolution compared to the width of the interface, which is the order of a few nanometers. In contrast, TEM and APT are two of the most appropriate techniques to measure interfacial segregation at the atomic scale. However, APT has a particular advantage due to its unique capability to provide both a precise quantitative measurement of the chemistry at the interface, and provide three-dimensional (3D) reconstructions of the microstructure at the near atomic scale.

The APT is opening unique capabilities for nano-scale investigation of transformation interface that may advance the development of the models for more accurate prediction of ferrite growth kinetics and thus better controlling the mechanical properties of modern steels. Therefore, this work is focused on investigating the solute concentration profiles through the transformation interface in Fe-C-Mn ternary model alloy of dual-phase steel. The goal is to identify the operative regime (SD vs. LEP/LENP or PE) of ferrite growth during the austenite-to-ferrite phase transformation. In order to understand the influence of the atomic structure of the moving austenite/ferrite transformation interface on the phase transformation kinetics, atomistic modeling based on the recently developed Quasi-Particle (QP) was also performed in addition to the APT experiments.

This manuscript is divided into five chapters. The first chapter provides a brief overview of the importance of the austenite-to-ferrite phase transformation for the development of modern steel. A description of the most widely used models for the prediction of ferrite growth is also given. The role of the transformation interface and its interaction with solutes are highlighted. The second chapter is dedicated to the description of the experimental technics used in this study. Namely, it describes the basics of the APT work principle, gives details of site-specific sample preparation in the particular case of interphase interface, and provides information regarding data treatments. The results of the APT investigation of the transformation interface are presented in the third chapter. The fourth chapter provides a brief overview of the QP approach and its application for modeling fcc/bcc phase transformation in pure iron. The comparison of the experimentally measured and theoretically predicted Mn profiles are given and discussed in chapter five. Finally, a general conclusion and suggestions for further work are presented at the end of this document.

Chapter 1

Austenite-to-ferrite phase transformation: literature review

1.1 Steels for the automotive industry

1.1.1 Steels in automobile structure: advanced high-strength steels (AHSS)

The large variety of microstructures and properties made steel the dominant material in the automotive industry. Currently, approximately 30 steel grades are used in automobile structures (the mains are represented in **Figure 1.1**.) and can be separated into several classes [3][4]:

- traditional mild steel that has low strength but relatively good formability;
- conventional high strength steels (HSS): carbon-manganese, bake hardenable (BH), high-strength low alloy steels (HSLA), that have a tensile strength of 210-550MPa and yield strength of 270-700MPa, and higher strength and lower ductility in comparison with traditional steels;
- advanced HSS: dual-phase (DP), complex phase (CP), transformation-induced plasticity (TRIP), martensitic steels (MS) that have an excellent combination of extremely high tensile strength and high formability.

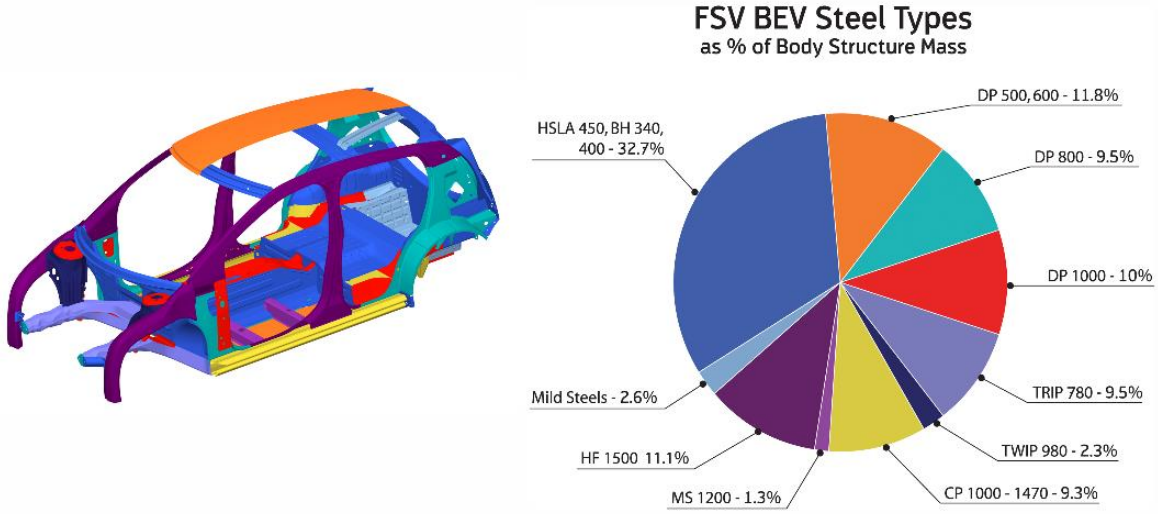

Figure 1.1. *Steel grades in automobile structure* [2].

The comparison of mechanical properties for different steel grades can be represented as the 'banana-shaped' steel strength-ductility diagram in **Figure 1.2**. This diagram demonstrates the limited mechanical advantages of the first two classes of steel. The new class of AHSS seems to be one of the most promising materials for the automotive industry in the nearest future.

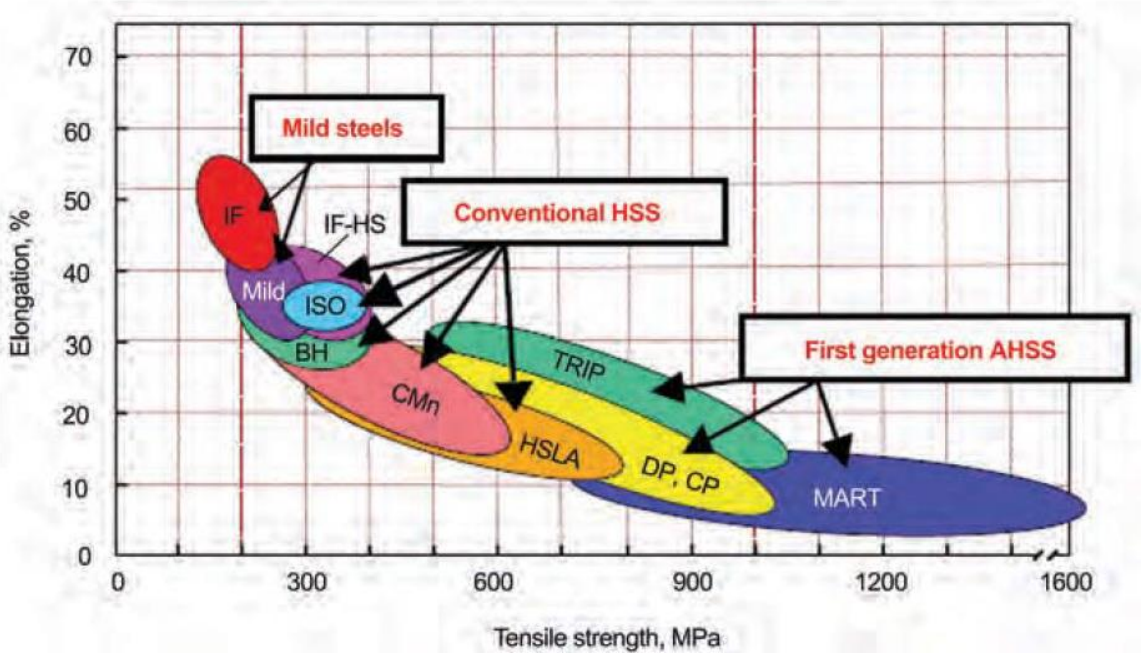

Figure 1.2. *Strength-ductility diagram for steels* [3].

AHSS are characterized by a multiphase microstructure produced by controlling heat treatments and solid-phase transformations during steel processing. Such a complex microstructure provides a wide range of mechanical properties. The AHSS make up 40-60% of the weight of a modern vehicle, which reduces the vehicle weight by 25-39% as compared to conventional steels [3][6][23].

Nowadays, the automotive industry has new demands for steels: high tensile strength (to establish fatigue and crash resistance), high elongation (to ensure formability), high deformation hardening (to provide a high energy absorption), and low alloy content (to assure weldability without significant influence on the production cost) [2][3][8]. In practice, different types of AHSS can be used to achieve this goal, but Dual-Phase (DP) steels are the most promising regarding the cost-efficiency of the manufacturing process [24].

1.1.2 Dual-Phase Steel (DP)

Dual-Phase steels were the first family of AHSS developed in the mid-70s mainly to meet the automotive industry's requirements [25][26]. The goal was not only to reduce the

automobile's weight but also to improve safety and crash performance. DP steels are low-alloy steels with a duplex microstructure of soft, ductile ferrite phase and significantly harder martensite phase. The examples of DP steel microstructures are shown in **Figure 1.3**.

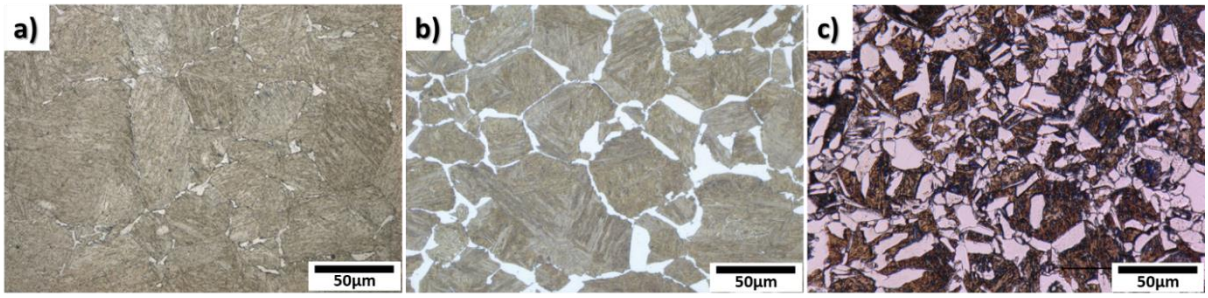

Figure 1.3. *Examples of a dual-phase steel's microstructures (bright regions – ferrite, dark – martensite) in Fe-0.17wt%C-2wt%Mn alloy obtained after 3hours of intercritical annealing at* **(a)** *720°C,* **(b)***680°C,* **(c)** *625°C.*

Such a microstructure provides an excellent combination of strength and ductility of DP steels. Their position in a strength-ductility diagram is shown in **Figure 1.2**. Currently, the tensile strength of DP has extended from the initial 500-700MPa to 1000-1200MPa with total elongation in the range of 12-34%. These mechanical properties are controlled by the volume fractions of the hard martensite and soft ferrite phases [27]. High tensile strength establishes good fatigue and crash resistance, and high tensile elongation ensures excellent formability and good energy absorption capability [28].

Dual-Phase steels were the first type of steels that involved specific phase transformations in the manufacturing process [1][2][4][29][30]. There are various processing routes for commercial dual-phase steel production. The DP microstructures are produced by controlled cooling from the austenite phase in the case of hot band products (see **Figure 1.4** (a)), or by the intercritical annealing from the two (α+γ) phase regions followed by rapid cooling to room temperatures in the case of continuously annealed cold-rolled and hot-dip coated products (see **Figure 1.4** (b)). Cooling rate, annealing temperature and time are therefore important parameters of the DP steel microstructures development. In particular, by changing the temperature T_1 and the time t_1 of intercritical annealing, a large variety of DP mechanical properties can be obtained [31].

Another critical factor in DP steel processing is, of course, the chemical composition, which can significantly affect the kinetics of the phase transformations that take place during DP steel manufacturing and the final mechanical properties of steel. Therefore, the chemical composition must be carefully selected according to the production capabilities (melting, rolling,

and cooling facilities). The spectrum of typical alloying elements used in commercial DP steels and their effect are given in **Table 1** [3][32].

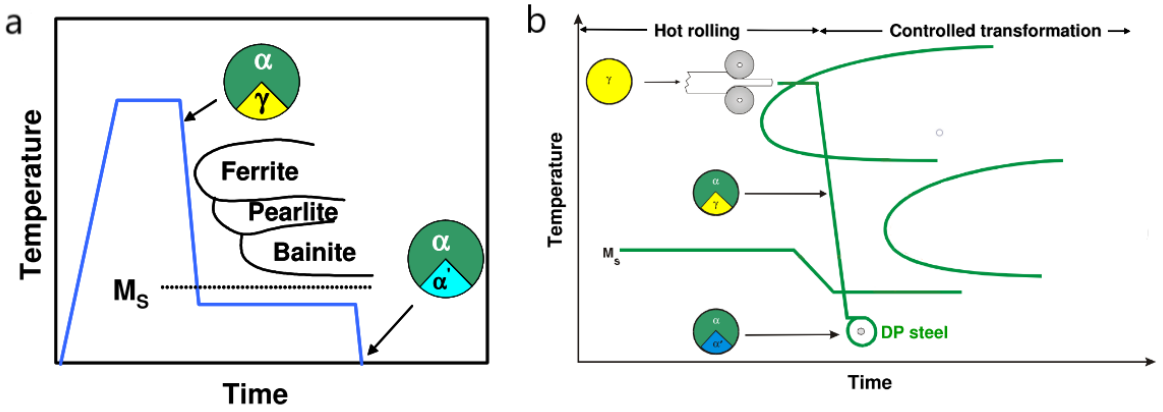

Figure 1.4. *Temperature-time schedule of Dual-Phase steel production in the case for hot band products (a) and cold-rolled and hot-dip coated products (b)* [32].

Table 1. *The list of typical alloying elements used in commercial DP steels and their effect* [3][32].

Alloying element	Effect and reason for adding
C, *0.06-15wt%*	Austenite stabilizer Strengthens martensite Determines the phase distribution
Mn, *1.5-3.0wt%*	Austenite stabilizer Solid-solution strengthener of ferrite Retards perlite and bainite formation Allows martensite formation during cooling from intercritical T
Si	Promotes ferrite formation
Cr, Mo, *up to 0.4wt%*	Austenite stabilizer Retard perlite and bainite formation
V, up to *0.06wt%*	Austenite stabilizer Precipitation strengthener Refines microstructure
Nb, up to *0.04wt%*	Austenite stabilizer Reduces M_s temperature Refines microstructure and promotes ferrite transformation from nonrecrystallized austenite
P or Al	Reduce or replace Si (which may cause the problem during hot rolling and coating)

1.2 Microstructure-properties of modern steels: role of austenite to ferrite phase transformation

1.2.1 Fe-C phase diagram: austenite to ferrite phase transformation

It is well known that the mechanical properties of materials depend on their microstructure. Typically in steels, the microstructure depends on the three major factors: chemical compositions of present alloying elements, thermal treatment parameters, and work hardening [1][29]. However, a wider and more attractive spectrum of mechanical properties of modern steels, such as AHSS, has been received as a result of controlled solid-state transformations during the production process. Such phase transformations are possible due to the existence of allotropic forms of pure iron (α-, γ-, δ-iron). The investigation of the phase transformation mechanisms is crucial for a more profound understanding of tailoring the final steel microstructure at the end of metallurgical processes [33][34].

Most modern steels contain several alloying elements, whose presence basically modifies the position of phase boundaries on the phase diagram, which serve as a guide for understanding phase transformations in steels. Nevertheless, the most complex steels' microstructure can be understood by the basic features of the Fe-C system, as in their simplest form, steels are alloys of iron (Fe) and carbon (C). **Figure 1.5** displays the phase diagram of the Fe-C system, where the “steel” region corresponds to the carbon content less than 2.1wtC% (with more than 2.1wtC% - cast iron) [35].

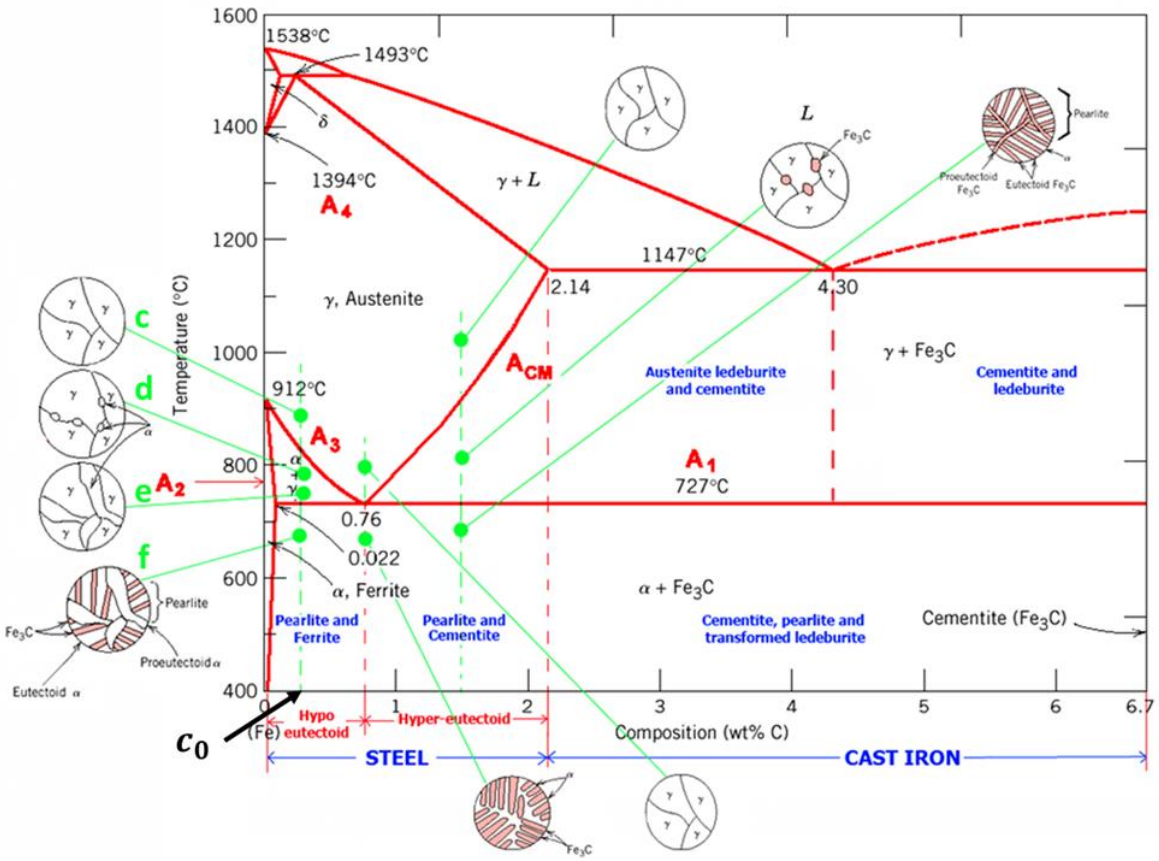

Figure 1.5. *Metastable Fe-Fe₃C phase diagram. The microstructures variation of alloy with the nominal composition c0 left to eutectic compositions during cooling is shown on the left (see points c, d, e, f)* [36].

The α- and γ- allotropes of iron determine the principal phases of steel. In pure iron, the γ-iron, with a face-centered cubic (fcc) crystal lattice, exists at temperatures belove 1394°C and up to 912°C. Its lattice parameter is about $a^{fcc} = 0.360\,nm$ at 1000 °C. The α-iron is stable below 912°C (A_3 point) and has a body-centered cubic (bcc) lattice structure with the lattice parameter at room temperature of about $a^{bcc} = 0.286\,nm$. Carbon atoms dissolve in both α- and γ-irons and form a soft, ductile ferrite phase and a high-temperature austenite phase, respectively [35].

The austenite-to-ferrite phase transformation is a key reaction during steel processing as it is involved in most modern steel production lines. In addition, as it is a first-order phase transformation that occurs during steel processing, it can provide a lot of essential information for other closely related phase transformations [10][14].

Austenite to ferrite phase transformation occurs below the γ/(γ+α) transition temperature (A_3). Ferrite formed in hypo eutectoid steels (carbon content less than eutectic composition, <0.76wt%C) and at a temperature higher than eutectoid temperature (in the Fe-C system, the eutectoid temperature is T_0 =727°C, A_1) is termed proeutectoid ferrite. The points c, d, f, e in **Figure 1.5** (on the left) represents the variation of the microstructures of a Fe-C alloy with the

nominal carbon content c_0 during cooling under conditions that ensure thermodynamic equilibrium conditions at any time.

At the begging, the structure is fully austenitic (point c, **Figure 1.5**). Slow rate continuous cooling down to a region of coexistence of both phases, slightly below (γ/γ+α) boundary, leads to the nucleation of α-phase at γ grain boundaries (point d). The α-phase continues to grow (point f) until the eutectoid temperature $T_0 = 727°C$ (A_1) is reached. In this temperature domain, the composition of both phases changes during the cooling and can be determined from the phase diagram.

The carbon solubility is significantly different in the austenite and ferrite phases. The maximum solubility of carbon in austenite is about 2.14 wt% at 1148°C. It is approximately 100 times greater than carbon solubility in ferrite, which is about 0.022 wt% at 727°C [35]. Such a limited solubility of carbon in the ferrite can be explained by the difference in the size of the fcc and bcc octahedral interstitial sites ($r_{oct}^{fcc} = 0.052\ nm$ and $r_{oct}^{bcc} = 0.019\ nm$) that carbon atoms preferentially occupied due to its small atomic radius (the radius of a carbon atom $r_C = 0.077\ nm$) compared to the iron one ($r_{Fe} = 0.14\ nm$), see **Figure 1.16**.

Different morphologies of proeutectoid ferrite, depending on many factors (such as the chemical compositions, transformation temperature, cooling rate, nucleation sites, and prior austenite microstructure) can be observed [1][35][37].

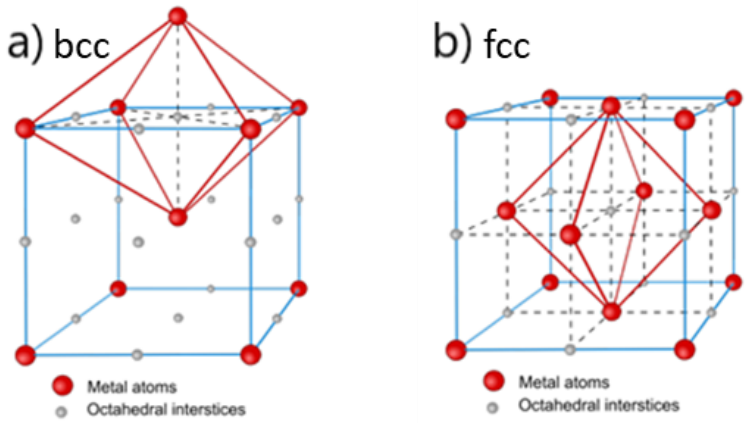

Figure 1.6. *Lattice structures with octahedral interstitial voids of* **(a)** *bcc and* **(b)** *fcc crystal* [38].

1.2.2 Morphologies of proeutectoid ferrite: allotriomorphic ferrite

Based on the classification system proposed by Dube, which later was extended by Aaronson, the morphologies of ferrite formed from austenite can be separated into a few main types: *grain boundary allotriomorphic, intragranular idiomorphic, Widmanstätten* (*primary or*

secondary) side-plates or needles [1][37][39]. These morphologies are shown schematically in **Figure 1.7**.

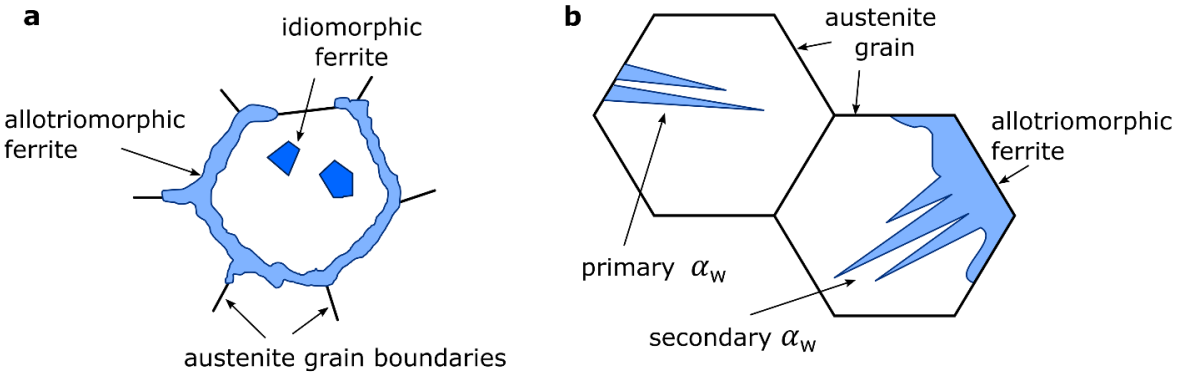

Figure 1.7. *Schematic illustration of proeutectoid ferrite morphologies.*

Grain boundary allotriomorphic ferrite (see **Figure 1.7** (a)) is the first morphology of ferrite that appears during the continuous slow rate cooling of austenite slightly below (γ/γ+α) boundary. The allotriomorphic ferrite preferentially nucleates at the prior austenite grain boundaries. Its growth occurs both along the boundary and into the γ grains. However, as the diffusion along the boundary is more rapid than the grain matrix's growth, the growth of grain boundary allotriomorphic ferrite can be treated as a one-dimensional planar growth in normal to the boundary plane. Such planar α growth is the perfect starting point for investigating the influence of the transformation interface on the austenite-ferrite phase. Therefore, the investigation of grain boundary allotriomorphic ferrite has a particular interest in this work [1][15].

The ferrite nucleus, during the growth, is in contact with at least two austenitic grains. Therefore at least two α/γ interfaces are created during the growth of allotriomorphic ferrite. The interface can be considered as a crystallographic defect, and the tendency of the system to minimize free energy leads to the creation of at least one coherent (or semicoherent) interface. Therefore, a growing ferrite crystal generally has a well-defined crystal orientation with one of the grains and a more random one with the other. In the case, if the prior austenite microstructure is crystallographically textured, ferrite formation with a good-fit orientation relationship with all the austenite grain is possible [40][41].

Since the allotriomorph ferrite has reproducible orientation relationships with one of the austenite grains, before considering theoretical approaches for the treatment of ferrite growth kinetics, the concept of orientation-relations (ORs) in steels will be briefly presented in the following paragraphs.

1.2.3 Orientation relationships (ORs)

Austenite to ferrite phase transformation involves the crystal structure rearrangement from parent fcc to the product bcc lattice structure. Among the numerous ways to convert fcc structure into bcc, Bain was one of the first (in 1924) who proposed a transformation path describing the rearrangement of atoms in Fe-C from the fcc to bcc crystal by applying deformation in two steps (see **Figure 1.8**). The first one involves an intermediate body-centered tetragonal (bct) unit cell in the fcc crystal by choosing the $^1/_2\,[110]_\gamma$, $^1/_2\,[\bar{1}10]_\gamma$, $^1/_2\,[001]_\gamma$ directions as a new reference frame. Then the second step contains a homogeneous tetragonal lattice deformation. To obtain the bcc lattice with appropriate lattice parameters (as bct has a ratio $^c/_a = \sqrt{2}$), the second step of the Bain path involves compression of the z-axis by about 21% and the expansion of x, y-axes by about 12% [42][43].

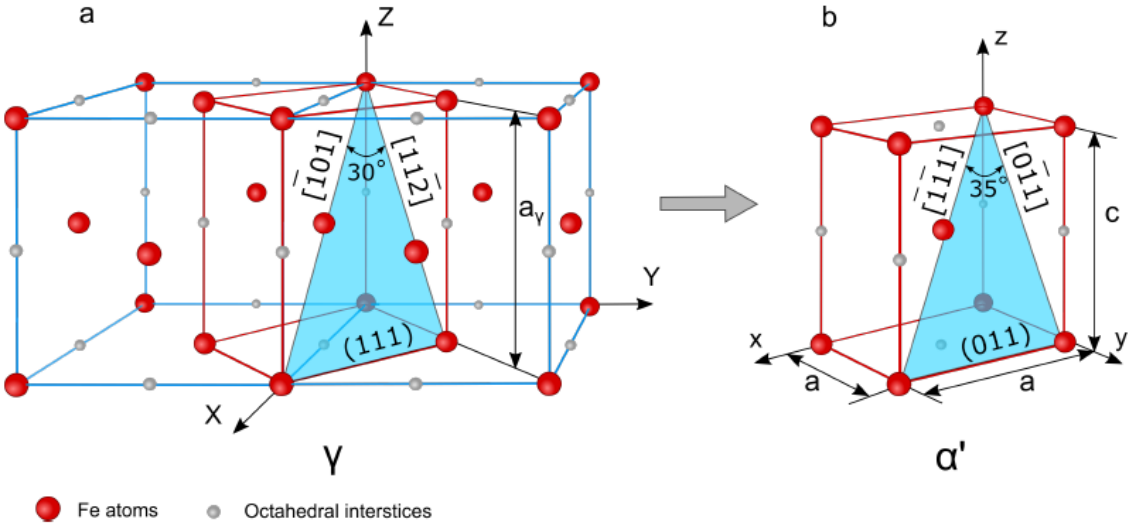

Figure 1.8. *Bain distortion (fcc-bct-bcc transformation). The Fe and C atoms are in red and grey, respectively* [38].

The Bain deformation is energetically the most favorable way for structural change from fcc to bcc lattice because it requires the minimum deformation. However, the Bain strain on its own can not completely explain the fcc/bcc phase transformation because it does not satisfy the condition of the invariant plane [44].

In general, the elastic strain energy is not significant for the diffusion-dominated formation of ferrite. Still, the crystallography of the parent and product phases does affect the formation and morphology of ferrite. The tendency of the system to minimize interfacial energy caused by the misfit between fcc and bcc structures leads to the adoption of a specific orientation relationship (OR) between the austenite and ferrite [39][42]. The list of the reported ferrite/austenite ORs in iron and steel is given in **Table 2.** This table describes the orientation

relationships by giving the corresponding common crystallographic plane and direction in the two phases.

Table 2. *Reported ferrite/austenite ORs in iron and steel. ORs are described by crystallographic plane and direction. N – is the number of variants deduced due to the crystal symmetry. The last column shows what is close-packed in the given model: the planes used (p), the given direction (d), both, or nothing* [45]–[47].

Name of OR	Plane	Direction	N variants	
Bain (B)	$\{010\}_\gamma \parallel \{010\}_\alpha$	$\langle 001\rangle_\gamma \parallel \langle 101\rangle_\alpha$	3	-
Kurdjumov-Sachs (KS)	$\{111\}_\gamma \parallel \{110\}_\alpha$	$\langle 1\bar{1}0\rangle_\gamma \parallel \langle 1\bar{1}1\rangle_\alpha$	24	p,d
Nishiyama-Wassermann (NW)	$\{111\}_\gamma \parallel \{110\}_\alpha$	$\langle 0\bar{1}1\rangle_\gamma \parallel \langle 001\rangle_\alpha$	12	p
Pitsch (P)	$\{001\}_\gamma \parallel \{\bar{1}01\}_\alpha$	$\langle 110\rangle_\gamma \parallel \langle 111\rangle_\alpha$	12	d
Greninger-Troiano (GT)	$\{111\}_\gamma \sim 1° to \{110\}_\alpha$	$\langle \bar{1}2\bar{1}\rangle_\gamma \sim 1° to \langle 1\bar{1}0\rangle_\alpha$	24	~p,d

In the case of iron and steels, KS and NW (or an OR close to these two) are among the most frequently cited and experimentally observed ORs. Both of these relationships have the close-packet planes of each phase in contact $\{111\}_\gamma$ and $\{110\}_\alpha$, but NW has a 5.26° misorientation about the plane normal. These ORs are based on the Bain model and both characterized by a shear of 19.5° on the $\{111_\gamma\}$ plane and followed distortion of 10.5° on the $\langle 112_\alpha\rangle$ direction. It can explain the existence of the conjugate habit planes. Due to the crystal symmetry, a specific number of equivalent combinations, so-called variants of ORs, can be deduced. For example, there are 24 different variants of KS-ORs. The majority of the α/γ interfaces are observed to be KS or near to KS ORs [48][49].

1.2.4 Austenite-to-ferrite phase transformation: general remarks

The formation of ferrite from austenite in steels is a complex physical process that involves at least two main phenomena: the crystal structural rearrangement and the redistribution of the alloying element caused by the diffusion processes. Initially, most of the studies were concentrated only on the diffusional processes as it was assumed to control the transformation rate. In these models, the intrinsic properties of the transformation interface were not considered. Therefore, the processes connected with crystal rearrangement at the interface and interfacial friction caused by the interface migration were assumed to be negligible. However, it was shown later that several important phenomena related to the transformation interfaces could significantly affect austenite/ferrite transformations' kinetics. One of the main phenomena is the

interaction of migrating interface with the alloying elements, which may lead to solute segregation at the interface and retard its motion. In addition, the transformation rate may also depend on ORs and the coherency of atomic structure within the interface [10][14].

Since the importance of the transformation interface in ferrite growth has been underestimated, there are still many unresolved issues regarding these questions. It is suspected that detailed information about the moving transformation interface, especially its interaction with alloying atoms, can be a key point in a more profound understanding of the phase transformation. Therefore, this work's experimental and modeling parts were focused on the atomic-scale investigation of the γ/α transformation interfaces and solute behavior within these interfaces. Before discussing the obtained data within this work, the overview of the main concepts of the most widely used models for the prediction of ferrite formation kinetics will be presented.

1.3 Theoretical prediction of proeutectoid ferrite growth in the Fe-C binary system

The simplest case for γ/α phase transformation kinetics is a one-dimensional growth of ferrite in a binary Fe-C system. In this case, a thin layer of ferrite, growing at austenite grain with a planar movement of the α/γ transformation interface, is considered. In the theoretical analysis of the proeutectoid ferrite growth, the most common assumption is that α-phase growth is treated as purely diffusional-controlled phase transformation, and the dissipation of the transformation free-energy at interfacial related to structural rearmament and interface migration is neglected. The theory of solute diffusion through the interface can then be applied for the interface velocity definition. The concept of the diffusion-controlled model for the analysis of the isothermal ferrite growth was first presented by Zener [11], [50], [51]. In the binary Fe-C system at constant temperature and pressure, the equilibrium condition at the interface between α and γ is defined as:

$$\begin{cases} \mu_C^{\alpha} = \mu_C^{\gamma} \\ \mu_{Fe}^{\alpha} = \mu_{Fe}^{\gamma} \end{cases} \quad (1.1)$$

where μ_C^{α}, μ_{Fe}^{α} and $\mu_C^{\gamma}, \mu_{Fe}^{\gamma}$ are the chemical potentials of C and Fe in ferrite and austenite, respectively.

For isothermal phase transformation in a binary alloy, the interfacial concentration of carbon can be evaluated using a tie-line directly from the phase diagram. A tie-line is a line connecting the composition of two phases in equilibrium at a certain temperature obtained by

drawing a common tangent to the α and γ phases' free energy curves, as illustrated in **Figure 1.9**. At a given temperature T1 for a system with the c_C^0 bulk carbon content, c_C^α and c_C^α are equilibrium composition of the ferrite and austenite, respectively [51].

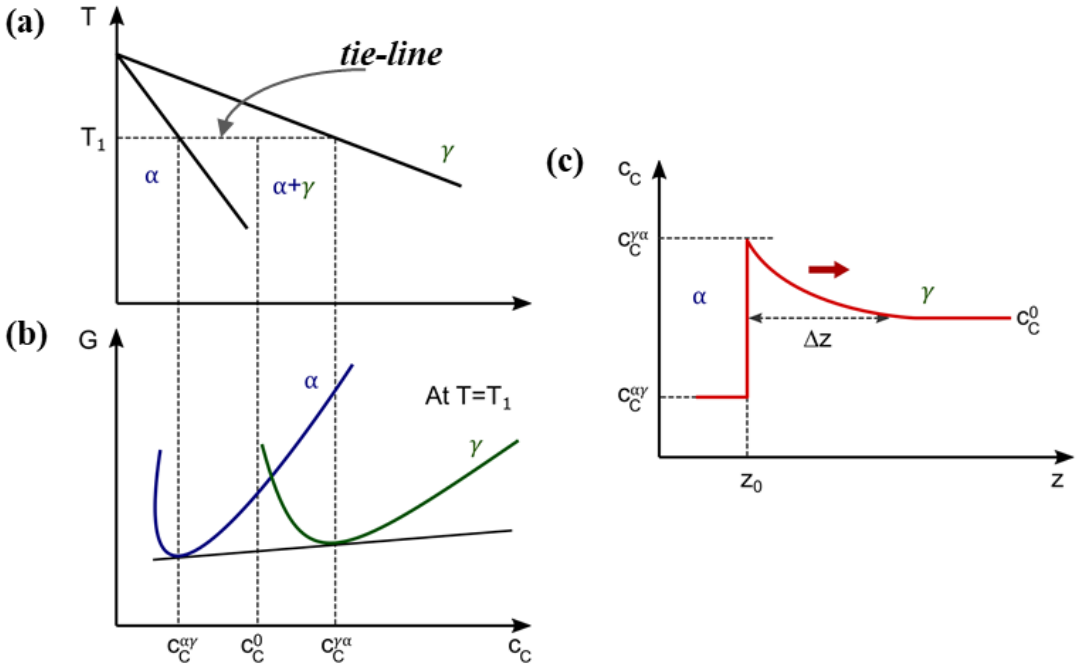

Figure 1.9. *Schematic Gibbs energy diagram* **(a),** *phase diagram* **(b)**, *and carbon composition profile* **(c)** *illustrating the local conditions at the α/γ migrating interface at T1.*

A significant difference in carbon solubility between α- and γ-iron leads to carbon partitioning during austenite to ferrite phase transformation. The rejected carbon atoms from growing ferrite diffuse to austenite ahead interface, building up the concentration profile into austenite with a maximum carbon concentration c_C^γ at the α/γ interface. The diffusional-controlled model predicts the concentration profile of carbon in austenite near the α/γ interface. According to Zener, in order to simplify the theoretical description, the concentration gradient in the matrix is assumed to be constant until the austenite C composition is reached (c_C^0). The carbon concentration profile evolution according to Zener model is shown in **Figure 1.10** (a schematic view). The carbon content in the ferrite phase is smaller than the bulk content c_C^0 and concentration of carbon in the austenite far away from the interface is c_C^0. Z is the interface's position, and ΔZ is the distance traversed by the interface during time t into the austenite. **Figure 1.10** (b) represents the concentration profile at time t.

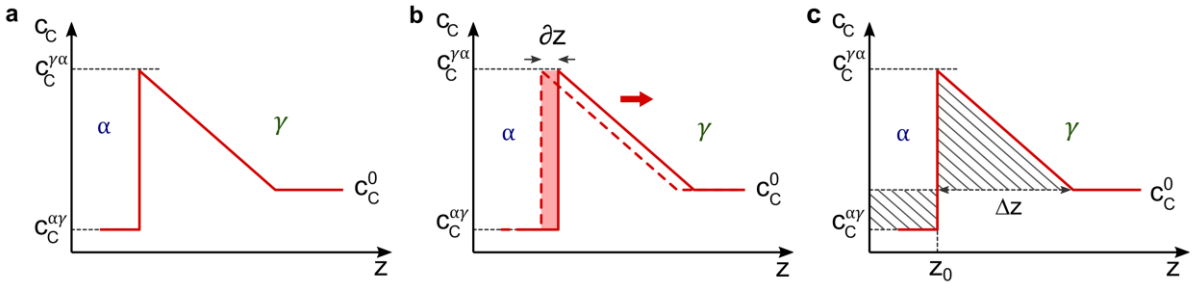

Figure 1.10. *The evolution of carbon concentration profile at the γ/α interface during the diffusion-controlled mode of phase transformation.*

The interface velocity determines the rate of the carbon partitioning. The velocity of the interface is controlled by the carbon fluxes caused by the diffusion of carbon that takes place in austenite. The diffusion flux of solute can be calculated by applying Fick's first law. As a result, the rate of the solute partitioning must be equal to the diffusion flux solute from the interface:

$$\left(c_C^{\gamma\alpha} - c_C^{\alpha\gamma}\right)\frac{\partial Z}{dt} = -D_C^{\gamma}\frac{c_C^0}{\partial Z} \tag{1.2}$$

Due to the assumption of a constant gradient, the diffusion flux can be rewritten as follows:

$$-D_C^{\gamma}\frac{c_C^0}{\partial Z} \cong D_C^{\gamma}\frac{c_C^0 - c_C^{\gamma\alpha}}{\Delta Z} \tag{1.3}$$

And eq. (1.2) can be written as:

$$\left(c_C^{\gamma\alpha} - c_C^{\alpha\gamma}\right)\frac{\partial Z}{dt} \cong D_C^{\gamma}\frac{c_C^0 - c_C^{\gamma\alpha}}{\Delta Z} \tag{1.4}$$

but with unknown ΔZ. Using the masse balance of carbon atoms between γ and α phases ΔZ can be find from:

$$\left(c_C^{\gamma\alpha} - c_C^{\alpha\gamma}\right)Z = \frac{1}{2}\left(c_C^0 - c_C^{\gamma\alpha}\right)\Delta Z \tag{1.5}$$

Combination of Eq. (1.4) and (1.5) gives:

$$\frac{\partial Z}{dt} = \frac{D_C^{\gamma}\left(c_C^0 - c_C^{\gamma\alpha}\right)^2}{2Z\left(c_C^{\gamma\alpha} - c_C^{\alpha\gamma}\right)\left(c_C^0 - c_C^{\gamma\alpha}\right)} \tag{1.6}$$

It follows that:

$$Z \sim \sqrt{D_C^{\gamma} t} \tag{1.7}$$

According to Eq. (1.7), a ferrite's thickness follows to a parabolic law. Consequently, the ferrite growth increases the amount of carbon enrichment in the austenite. As a result, the carbon has to diffuse over a longer distance, slowing down the growth rate [15][17].

An extensive number of experimental and numerical analyses of the proeutectoid ferrite formation in a binary Fe-C system were reported in the literature, assuming the thermodynamic equilibrium condition at the γ/α interface [13], [52]–[55]. The experimental data of ferrite growth are usually represented as the evolution of the thickening or the lengthening of a typical ferrite grain (most of the times measured metallographically) at different temperatures.

Zurob, Hutchinson et al. [18] documented a comprehensive set of experimental data on ferrite growth kinetics under decarburization conditions. It was shown that experimental data are in good agreement with results predicted by the diffusion-controlled model. However, the earlier obtained experimental data by Bradley [13] (using the isothermal experiments with Fe-0.11Cwt%, Fe-0.23Cwt%, Fe-0.42Cwt% alloys, at 710°C, 710°C, 710°C) show a good agreement with the theoretically predicted kinetics by Crusius [12] in Fe-0.42Cwt% alloy, whereas lower rates kinetics in comparison with predicted one was observed in the Fe-0.23Cwt%. The difference becomes even more significant in the case of Fe-0.11Cwt%. Such difference was assumed to be connected with the free energy dissipation by the interfacial friction and the various effects caused by the interface structure [51].

The interfacial processes in the diffusion control model are assumed to be neglected. As a consequence, the rate of ferrite growth is limited only by the volume diffusion velocity of carbon. Therefore, contrary to the diffusion control model, the interface controlled model has been developed [56]. This model assumes an infinitely fast diffusion of carbon in austenite. In this case, ferrite growth is governed by the rate of fcc to bcc crystal rearrangement. However, even in a binary Fe-C system, none of these approaches can accurately describe the austenite to ferrite phase transformation kinetics. Therefore, the model, which would include both diffusional and interfacial processes, is required.

Consequently, a model that includes both carbon diffusion and interfacial mobility in Fe-C steels has been developed in [39][57]–[60]. This model is called the mixed-mode model. In this model, the interfacial compositions of the austenite and ferrite phases are affected by the finite interface mobility, leading to decreasing interface velocity. In general, this model provides satisfactory results for proeutectoid ferrite growth kinetics in binary systems, demonstrating that interface structure and crystal rearrangement play an important role. The transformation interface's role becomes even more significant in multi-component systems. It was shown that in this case, Solute Drag effects take place [61].

1.4 Theoretical prediction of proeutectoid ferrite growth in a Fe-C-X ternary system

Most of the steels of practical importance, in addition to the interstitial C, contain one or even several substitutional alloying elements (X=Mn, Si, Cr, Mo, Nb, Co, etc.). The presence of such additional elements can dramatically change the thermodynamic condition at the γ/α transformation interface. In particular, one of the difficulties comes from the fact that the substitutional solute diffusivity is typically many orders of magnitude smaller than the interstitial one. Besides, the expected interaction of the substitutional solute with a moving interface and interstitial C atoms can significantly complicate the situation since the redistribution of alloying elements across the transformation interface can significantly modify the kinetics of austenite-to-ferrite phase transformation. Therefore many different models have been developed to account for the interfacial partitioning during the austenite-to-ferrite transformation in Fe-C-X alloys. Two purely thermodynamic approaches, Local Equilibrium (Local Equilibrium with Partitioning (LEP) or with Non-Partitioning (LENP)) and ParaEquilibrium (PE) have been one of the most used. The main concepts of these treatments are presented in the following session.

1.4.1 Local equilibrium in a ternary system

[10][14][39][15][17]

To introduce the main points of the LE and PE models, let us consider the ternary Fe-C-X system. As a starting point, it is possible to assume that in a ternary system, the rate of austenite-to-ferrite transformation is controlled by the diffusion processes and that the phases at the interface are in local equilibrium with each other. Therefore, the first approach to ternary system treatment is based on an extension of the Zener solution of the binary system. Then the thermodynamic equilibrium for a ternary Fe-C-X system requires to fulfill the condition (1.8) for each component:

$$\begin{cases} \mu_C^\alpha = \mu_C^\gamma \\ \mu_X^\alpha = \mu_X^\gamma \\ \mu_{Fe}^\alpha = \mu_{Fe}^\gamma \end{cases} \qquad (1.8)$$

In the case of the ternary system, the rule of a common tangent construction is transported into a rule of tangent plane construction, as illustrated in **Figure 1.11** (a). The isothermal section of a ternary system with possible tie-lines is schematically represented in **Figure 1.11** (b). Unlike the Fe-C system, there is an infinite number of tie-linens, and a specific, so-called operative tie-

line has to be defined. The operative tie-line definition will be briefly discussed a bit later in this paragraph.

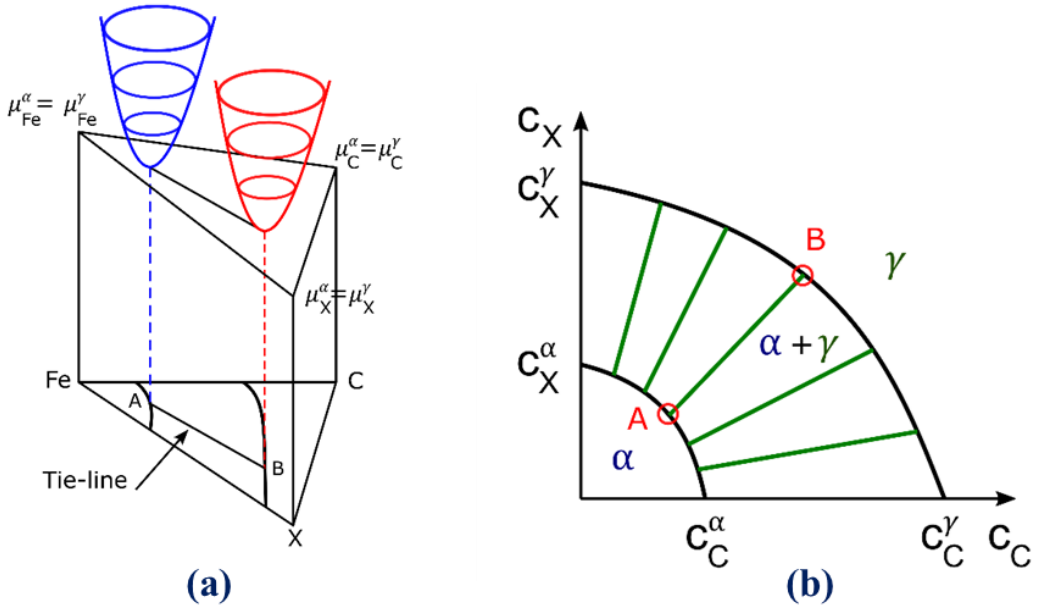

Figure 1.11. (a) *Schematic representation of the full equilibrium conditions given by Eq.(1.8).* **(b)** *The isothermal section of a ternary system with possible tie-lines.*

Similar to the binary system, to solve the ternary system's ferrite growth problem, both the mass balance equation and Fick's law have to be considered. The diffusional fluxes through the interface of both interstitial C and substitutional X, are:

$$J_C = -D_{11}\nabla c_c - D_{12}\nabla c_X$$
$$J_X = -D_{22}\nabla c_X - D_{21}\nabla c_C \qquad (1.9)$$

where $D_{11}, D_{22}, D_{12}, D_{21}$ are the inter-diffusion coefficients. It was observed that coefficients D_{12} and D_{21} are an order of magnitude smaller than the main coefficients D_{11}, D_{22} meaning that the diffusional interactions between C and X are relatively small [15]. Therefore, D_{12} and D_{21}, are usually negligible, then two mass balance equations at a moving interface with a velocity v in the direction normal to the interface plane can be written as:

$$\left(c_C^{\gamma\alpha} - c_C^{\alpha\gamma}\right)v = -D_{11}\nabla c_c$$
$$\left(c_X^{\gamma\alpha} - c_X^{\alpha\gamma}\right)v = -D_{22}\nabla c_X \qquad (1.10)$$

where $c_C^{\gamma\alpha}, c_C^{\alpha\gamma}, c_X^{\gamma\alpha}, c_X^{\alpha\gamma}$ are the interface concentrations determined by the operative tie-line, which satisfies the local equilibrium condition. It should be noted that the operative tie-line has to satisfy both LE conditions at the moving interface and mass balance. The interface concentrations must be chosen in the way that the two mass balance equations give the same

velocity despite the significant difference in the diffusivities of interstitial and substitutional species.

The calculation of interfacial compositions for a given nominal composition is generally very difficult for multi-component systems since it is necessary to define the operative tie-line that may require many numerical approaches. An easier and more practical method is to solve the inverse problem and to calculate the nominal compositions corresponding to a given tie-line. **Figure 1.12** shows a graphical representation of this method. The dotted line (red and blue, see **Figure 1.12** (a)) represents a specific curve, so-called "Interface Composition Counters" (ICC). Interfacial compositions for a given bulk composition that lying on an ICC are defined by a tie-line that connects the ends of this ICC. The ratio of the interdiffusion coefficients (D_{11}/D_{22}) of the solute elements influence on the derivation of ICC. Typically, the diffusion coefficient of interstitial species is approximately six orders of magnitude larger than the diffusion coefficient of substitutional one (D_{11}/D_{22})~10^6. In this case, the shape of ICC approximates to a shape of a quasi-right angle triangle. The line connected right-angled edges of all possible ICC can divide the α+γ phase field of the ternary diagram into two regions and has been termed "zero partitioning line" (see **Figure 1.12** (b)). These two regions represent the two extreme transformation modes for ferrite growth: Local Equilibrium with Partitioning (LEP) and Local Equilibrium with Negligible Partitioning (LENP).

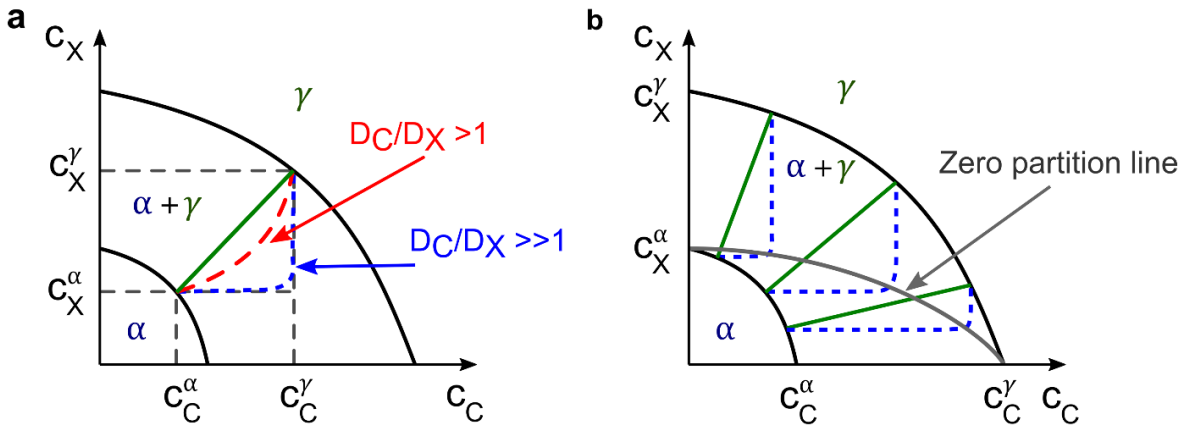

Figure 1.12. (a) *Definition of interfacial composition using "Interface Composition Counters";* ***(b)*** *Definition of the zero-partition line in a Fe-C-X diagram (when* D_{11}/D_{22}*>>1).*

1.4.2 Local Equilibrium with Partitioning (LEP) or with Negligible Partitioning (LENP)

Depending on thermal and chemical conditions, the rate of the α/γ phase transformation is determined either by the diffusion of substitutional or interstitial components and is

accompanied by the partitioning of the X component between the austenite and product ferrite phase. As a result, depending on whether an alloy's nominal concentration lies above or below of the zero-partitioning line, two different transformation modes for the ferrite growth under local equilibrium conditions can be distinguished (see **Figure 1.13**): Local Equilibrium with Partitioning (LEP) or Local Equilibrium with Negligible Partitioning (LENP).

Local Equilibrium with Partitioning (LEP) mode of growth is active in low supersaturated alloys (low undercooling). In this case, the ferrite formation is accompanied by the redistribution of both C and X alloying elements. However, there is a large difference in C and X solutes' diffusivities. To compensate this difference, the system has to choose the operative tie-line that provides interfacial carbon concentration in austenite close to the carbon bulk concentration. The expected concentration profiles of both alloying elements through α/γ interference are illustrated in **Figure 1.13** (a).

As shown in **Figure 1.13** (a), the carbon concentration profile is almost flat. It means that the carbon concentration gradient is very small, almost negligible. In this case, the diffusion flux of carbon slowdowns to a rate consistent with the diffusion of substitution element. The shape of the substitutional element concentration profile is completely different from the interstitial carbon one. The X concentration gradient extends far from the interface in the austenite matrix. The X concentration is lower in the austenite phase than in a bulk composition on the ferrite side. Consequently, the transformation process is accompanied by the partitioning of substitution solute. Partitioning refers to the bulk allowing elements redistribution on a distance larger than the interfacial region. The kinetic of ferrite growth under LEP is expected to be slow since it is mainly controlled by the substitution element's long-range diffusion.

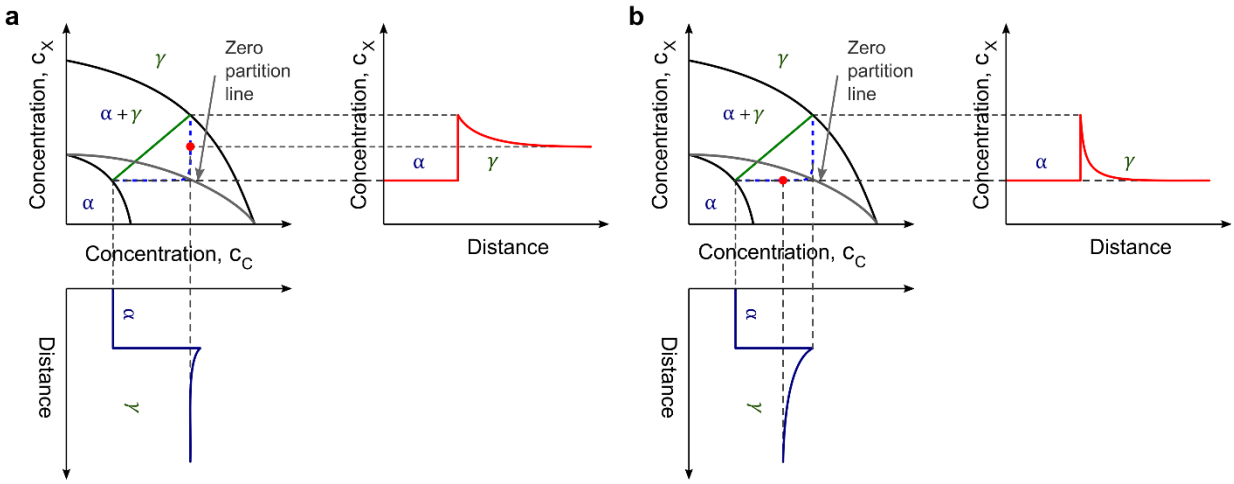

Figure 1.13. *Schematic illustration of the phase boundaries, interfacial concentrations, and diffusion profiles under* **(a)** *LEP and* **(b)** *LENP conditions of a Fe-C-X alloy with bulk composition marked by red points.*

Local Equilibrium with Negligible Partitioning (LENP) operates in the composition domain below zero partitioning line at high supersaturated alloys. In this regime, ferrite formation occurs without bulk redistribution of substitution elements. The kinetics is in this regime is much faster than in the LEP regime since mainly controlled by the diffusion of the interstitial C atoms.

The concentration profiles under LENP conditions are illustrated in **Figure 1.13** (b). Contrary to the LEP model, the gradient of carbon concentration on the austenite side is larger and represents the long-range diffusion of carbon into the γ phase. The X concentration is homogeneous and both phases. To maintain LE condition at the interface, short-range diffusion of X solute occurs in the vicinity of the interface, and a narrow "spike" of substitution element is expected to build-up ahead of the moving interface on the austenite side. The "spike" width can then be used as the parameter for the validation of the LE assumption. Its width Δs can be estimated as $\Delta s \sim \frac{2D_X^\gamma}{v}$ (D_X^γ is the diffusion coefficient of X in austenite, and v is the interface velocity). However, the physical meaning of such "spike" is questionable since its width is the order of inter-atomic distance [16].

1.4.3 Paraequlibrium

The 'spike' width of the LENP approach decreases with the increase of growth rate, and at a very high rate of phase transformation, its value becomes below a lattice spacing. To overcome this difficulty, a third alternative phase transformation mode, known as ParaEquilibrium (PE), has been proposed. As PE conditions are expected to be approached at high interface velocities. In this model, the substitutional atoms are assumed to be immobile with respect to the transformation interface. Therefore, under PE conditions, ferrite formation occurs without partitioning of substitutional solute across the interface. However, the interstitial C atoms with a much higher diffusions rate can redistribute during the phase transformation. Therefore, the local equilibrium at the interface can be maintained only with respect to C atoms. Mathematically, it can be defined as the equal of C chemical potential at the interface, and only the weighted average of Fe and C atoms chemical potentials is across the α/γ interface:

$$\begin{cases} \mu_C^\alpha = \mu_C^\gamma \\ \mathrm{X}_X\left(\mu_X^\gamma - \mu_X^\alpha\right) + \mathrm{X}_{Fe}\left(\mu_{Fe}^\gamma - \mu_{Fe}^\alpha\right) = 0 \end{cases} \qquad (1.11)$$

where X_i is the mole fraction of component i in the alloy. The operative tie-line under PE conditions is parallel to the interstitial element axis, see **Figure 1.14**.

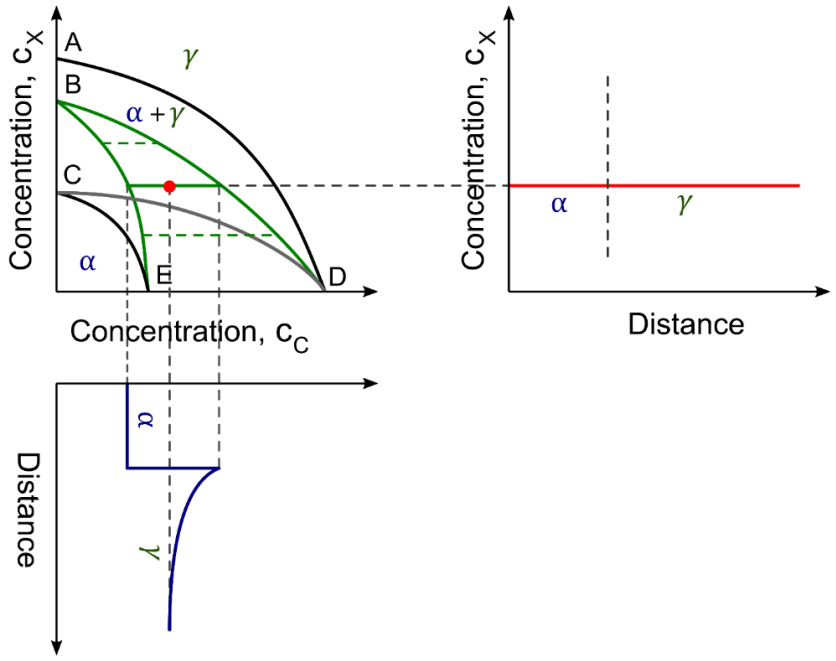

Figure 1.14. *Schematic illustration of the phase boundaries, interfacial concentrations, and diffusion profiles under PE conditions of a Fe-C-X alloy with bulk composition marked by red points.*

1.4.4 Experimental observation

The Local Equilibrium (with partitioning – LEP, or with Negligible Partitioning – LENP) and ParaEquilibrium models as possible mechanisms for the austenite-to-ferrite phase transformation have been discussed intensively in the literature. Consequently, the experimental measurements of the ferrite growth rate have been widely reported and compared with different modes of growth. Initially, the experimental phase transformation kinetics investigations were mainly performed at the macroscopic level and were based on the optical microscope measurement of the thickening and lengthening of allotriomorph ferrite.

Aaronson et al. [62], one of the first who made an impressive review of experimental data of α growth for various alloy compositions. However, some of the data obtained for the steels with several alloying elements, were hard for the theoretical interpretation. Nevertheless, the parabolic law for ferrite thickness growth was confirmed that indicated the diffusion-controlled interface's motion.

Further, to improve the experimental investigation of ferrite growth, Purdy et al. [52] developed a new experimental protocol using the decarbonization technic. Preliminary experimental results for the binary Fe-C system (Fe-0.567wt% C at 792°C) gave an excellent agreement with the theoretical predictions based on the LE model. It was proved that the interface movement is controlled by the carbon diffusion for the studied alloys. Latter, this experimental approach was applied by Purdy et al. [63] for the investigation of ternary Fe-C-Mn

alloys (with a C range of 0.21-0.34wt% and Mn 1.52-3.16wt%, the transformation temperatures were between 725-760°C). The expected Mn partitioning was observed in the LEP region and no Mn partitioning in the LENP zones. These accurate and important results were among the first reported experimental data that confirmed the LE model predictions. However, the calculated Mn 'spike' width was found to be too small to be physically possible. It indicates that PE mechanism for phase transformation is more probable instead of LENP.

The experimental observations of Aaronson et al. and Purdy et al. were only the beginning of the experimental study of austenite-to-ferrite phase transformation. Over the last few decades, substantial experimental work has been done in order to confirm or refute the validation of LENP or PE growth modes. Excellent reviews of such experimental data were presented in [15][17][19].

The experimental observations often demonstrate good agreement between measured and predicted by LENP or PE kinetics [63][64]–[67][68][69]. Simultaneously, numerous experimental observations with slightly different results were reported. Hence, several experimental data [69]–[73] indicated faster growth kinetics than was predicted and expected by LENP mode but slower than PE. In some cases, [18][68]–[70][72]–[74][67][68] observed kinetics is slower compare to both LENP and PE predictions. The experimentally determined 'zero partition line' was found to be located above the computed one for LENP but significantly below the PE [77].

In addition, a recently developed and actively applied cyclic phase transformation approach provides indirect evidence of the alloying element spike existence and leads to the preferential LE model than PE. Nevertheless, LE prediction is not fitting the experimental data, as experimentally observed kinetics is much faster [78]–[80].

Another experimental observation demonstrated that the PE condition's preferential exist at earlier stages of the transformation process (at high interface velocity) and further followed by a transition to the LENP condition at later stages [81][82]. These observations lead to discussions about the possible existence of the so-called transition models (transitions between LENP and PE mode during transformation).

The observed discrepancies between the experimentally measured ferrite growth rates during austenite-to-ferrite phase transformation and theoretically predicted by LENP and PE models indicate that some phenomena related to the interface were not taken into account in these models. It should be noted that LENP and PE approaches are–purely thermodynamic models, assuming full equilibrium at the transformation interface and neglecting the free energy dissipation by interface migration, crystal rearrangement, or trans-interface diffusion. Therefore,

new models for the treatment of this problem are required. Many different approaches have been developed in order to obtain a more accurate model for ferrite growth prediction. Solute Drug Model is one of the most widely discussed recently and, from the recent experimental results, seems to be one of the most suitable to describe the austenite-to-ferrite phase transformation.

1.5 Solute Drag

[10][70][83][84]

Initially, the Solute Drug (SD) effect was introduced to explain the reduction of recrystallization rate in high purity metals due to solute interaction with mowing grain boundary. The quantitative treatment of this effect was first developed by Lucke and Detert [85]. Then this theory was developed by Cahn [86], followed by Lucke and Stuwe [87]. Their treatment was based on a description of the binding force between the solute atoms and the migrating grain boundary. It is known as the "force-based approach".

Cahn considered the interaction energy between solute atoms and the boundary E(x) and a diffusion coefficient D(x), as functions of the distance x from an arbitrarily chosen center plane of the boundary. The force with which an individual impurity atom is attracted to the center of the boundary can be expressed as dE/dx. The total drag force P exerted by all the impurity atoms on the boundary can be obtained by integrating over the width of grain boundary [88]:

$$P = -N_v \int_{+\delta}^{-\delta} \frac{(C_M - C_M^0)}{V_m} \frac{dE}{dx} \qquad (1.12)$$

where N_v is the number of solute atoms, V_m is the molar volume, C_M and C_M^0 are the concentration of the solute M at boundary and far away from the grain boundary, respectively. For a stationary boundary with the symmetric equilibrium solute concentration profile the total force sums is zero. For a moving boundary, the solute distribution will be changed, and there will be a net force. To find P for a moving boundary, it is necessary to evaluate the variation of solute concentration across the boundary [89].

The solute concentration profiles for the different velocities of a migrating boundary can be obtained by solving the diffusion equation (Fick's law). In general, this equation is very complex, and its solution requires knowledge of the interaction energy $E(x)$ and solute diffusivity $D(x)$across the boundary.

Let us consider some limited cases. For the case of a very high velocity of the solute diffusion, the concentration profiles through boundary are expected to be close to the uniform

bulk alloy composition C_M^0. In the opposite case, for a very slow velocity, the profile will be close to the equilibrium solute profile for a stationary boundary (**Figure 1.15** (a)):

$$C(x) = C_0 \exp\left[-\frac{E(x)}{kt}\right] \qquad (1.13)$$

where, C_0 is the bulk alloy content, k – Boltzmann's constant and T is the temperature.

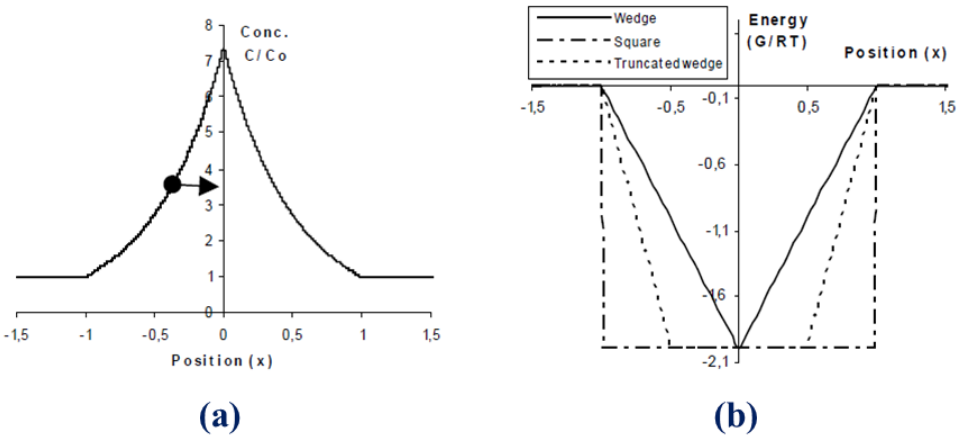

Figure 1.15. (a) *Equilibrium solute profile across a stationary grain boundary with wedge-shaped, attractive interaction energy;* **(b)** *examples of interaction energy profiles that have been used to represent the grain boundary [80].*

For intermediate velocity, to demonstrate the physics of the proposed treatment and present the resulting concentration profiles graphically, Cahn chose a simple wedge-shaped well for interaction energy $E(x)$ (see **Figure 1.15** (b)) and a constant diffusivity D(x). The resulting solute profiles are illustrated in **Figure 1.16**.

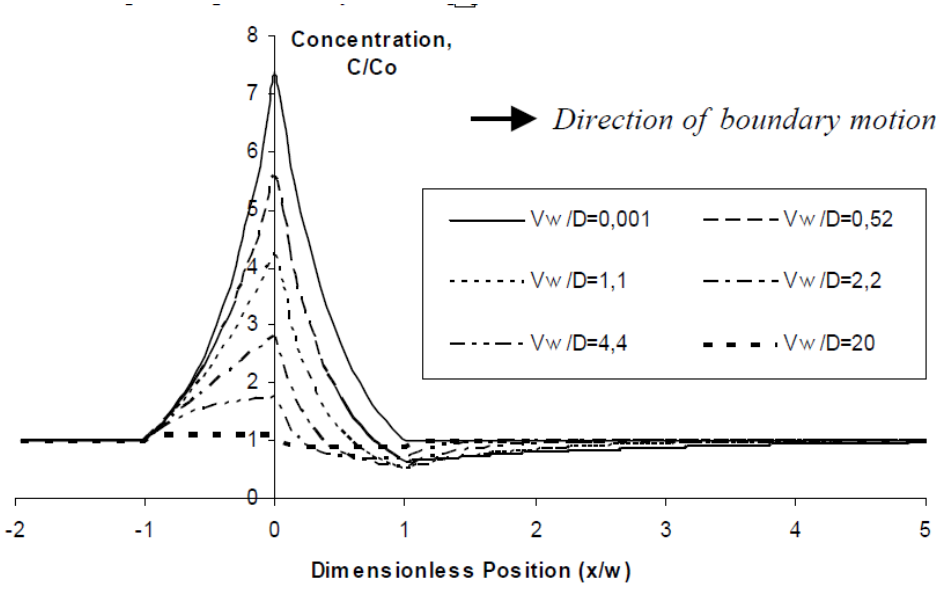

Figure 1.16. *Solute profile through a grain boundary moving with velocity V, for which there is an attractive interaction with the solute. A wedge-shaped interaction G(x), a constant diffusivity D, and ideal (dilute) solution thermodynamics are assumed* [83].

The concentration profiles at the moving boundary are not symmetric compere to the stationary boundary (**Figure 1.15** (a)). The perturbation of the solute concentration ahead of the interface caused by its motion is observed. From Eq. (1.12) follows that the drag pressure arises only from the regions where the gradient in the interaction energy is non-zero (only over the potential well) width. The drag effect increases with increasing of solute content and decreasing the temperature.

An alternative approach to the treatment of the solute drag problem was proposed by Hillert [90]. It is based on the dissipation of Gibbs energy and is known as the 'dissipation approach". Hillert considered that the retarding effect of the solute atoms at the mowing boundary corresponds to some work done by the boundary to overcome the solute drag. This work can be expressed as dissipation of Gibs free energy due to the diffusion of solute atoms across the migrating interface. Considered the total chemical potential, Hillert derived the following expression for the dissipation of Gibbs energy (ΔG^{diss}):

$$\Delta G^{diss} = \int_{-\infty}^{+\infty} (C - C_0) \frac{d\mu}{dx} dx \qquad (1.14)$$

where, μ is the chemical potential. There is no force acting on the solute atoms for a stationary grain boundary with the equilibrium concentration profile since no gradients in chemical potential exist at equilibrium.

In his work, Hillert used both the square and the truncated wedge to mimic the function $E(x)$ (**Figure 1.15**(b)). The evolution of the solute composition profiles at the boundary is similar for both cases. Hillert and al. [91] demonstrated that both"Force" and "Dissipation" approaches give the same results for the grain boundary if $E(x)$ and $D(x)$ were chosen the same. Hillert was the first who applied the SD theory to the phase transformation interface. He extended his approach to the moving interface with the initial assumption of constant properties of the interface over its width. Later, Hillert and Sudman [90] proposed an improvement by considering the continuous change of properties through the interface.

Purdy and Brechet [92] were the first who extended Cahn's solute drug theory to a moving transformation interface. They applied it to the growth of proeutectoid ferrite from austenite in the ternary Fe-C-X system. The aim of this work was to investigate the unpartitioned growth of ferrite phase and develop a kinetics model valid in the domain between the thermodynamic limits defined by LENP and PE conditions.

The transformation interface was considered as a particular phase with a certain thickness. The substitutional solute can diffuse inside the interface with the different (own) diffusion coefficient. An asymmetric wedge-shaped well was used for the interaction potential of solute X with the α/γ interface (**Figure 1.17** (a)). A gap $2\Delta E$ is a difference of chemical potential in PE condition at interface, a potential well $E_0$is the binding energy, which characterizes the ability of X to segregate at the interface, 2δ is the interface thickness. The substitutional solute profile $C(x)$, for an interface moving with a quasi-steaded velocity v must fulfill the following diffusion equation:

$$\frac{\partial}{\partial x}\left[D_x \frac{\partial C}{\partial x} + \frac{D_x C}{RT}\frac{\partial E}{\partial x} + vC\right] = 0 \qquad (1.15)$$

where D_x is the diffusion coefficient of solute X inside the interface (assumed to be constant), x the spatial coordinate relatively to the moving interface, and v - the interface velocity. **Figure 1.17** (b) illustrates a computed solute profile inside the transformation interface for a solute X (for example, Mn) that partitions to the parent austenite phase.

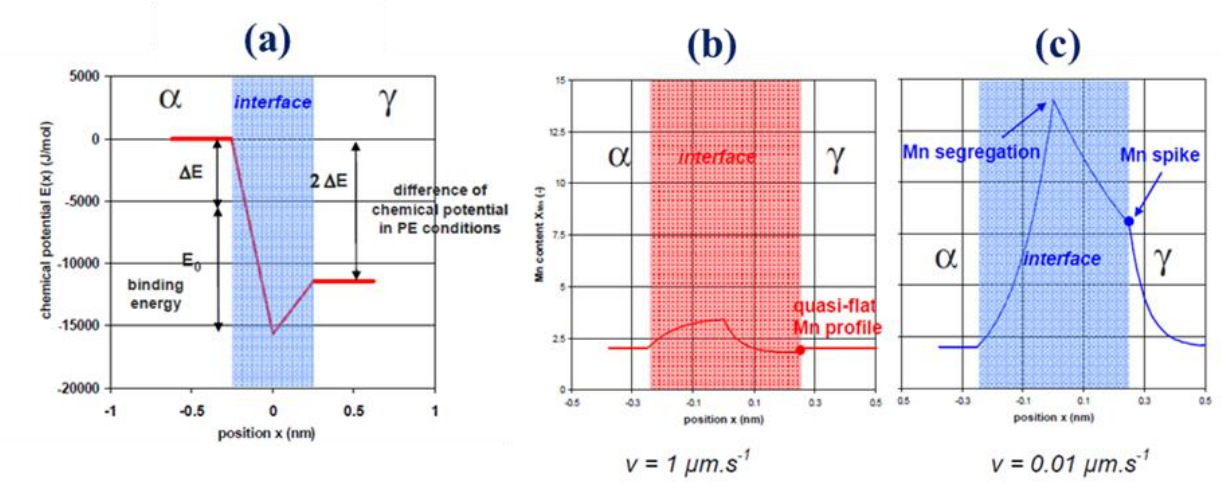

Figure 1.17. (a) *Chemical potential profile of substitution element across the transformation interface. Calculated X profiles inside the interface with* **(b)** *v=1 μm/s and* **(c)** *v=0.01 μm/s.*

At high velocity, the predicted solute profile is quasi flat. Substitutional elements have no time to segregate inside the interface, which corresponds to the Paraequilibrium condition. For a very slow interface velocity, the significant segregation of X at the interface are present. Besides, enrichment of X is observed in austenite at the contact with interface. This enrichment is comparable with the spike level in the LENP condition.

The analysis of Purdy-Brechet is shown schematically in **Figure 1.18** [77]. The solute-drag force is represented as s function of interface velocity and compared with the local chemical driving force.

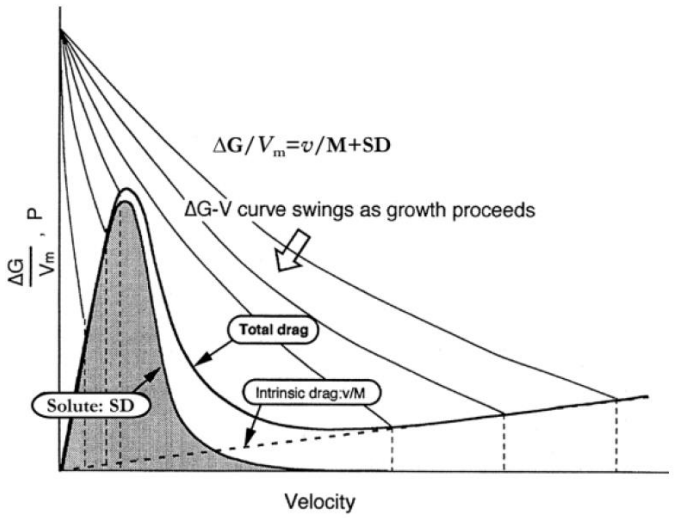

Figure 1.18. *A schematic diagram to show the 'solute drag' force as a function of interface velocity* [77].

Enomoto [93]–[95] develop further the PB model, including the energy of interaction between substitutional and interstitial solutes in the vicinity of the interface. Later, Odqvist et al.

[91][96] demonstrated by numerical calculation that the two approaches of Cahn nad Helliret give the same results if the solute drug is compared with the driving force acting over the interface.

1.6 Resume

In this chapter, the importance of the AHSS developments is discussed considering the automotive industry, but improving the steel mechanical properties is essential for the modern industry in general. Austenite-to-ferrite phase transformation is one of the key reactions of steel processing that play a crucial role in tailoring the final steel microstructure and, thus, their mechanical properties. It occurs in the production line of most modern AHSS steels, such as DP steels that are widely used in automobile body structure and investigated in this work.

Due to the technological and scientific importance, the austenite-to-ferrite phase transformation has been intensively studied during the last centuries. Therefore, many different models have been developed in order to describe ferrite phase formation from the high-temperature parent austenite phase. The overview of models for the prediction of ferrite growth in binary Fe-C and ternary Fe-C-X systems is given in this chapter. There are two purely thermodynamic treatments Local Euquilibrimum (with partitioning – LEP and without partitioning of alloying elements – LENP) and ParaEuquilibrimum, that were the most widely used. However, these models are only the thermodynamic limits that may or may not be reached. It has long been understood that the interaction between the alloying elements and the migrating transformation interface in steels through the phenomenon known as Solute Drag.

Solute Drag based models have recently attracted a lot of attention since they appear to provide a more accurate description of ferrite growth in steels. However, the Solute Drag approach has small weaknesses since the choice of the thermodynamic properties of the interface and kinetics parameter often had to be made without any real guidance. Therefore, further development of Solute Drag models requires the experimental measurement of the solute segregation at the transformation interface.

Thanks to the intensive development of advanced measurement technics, the experimental investigation of the interfacial interfaces recently started to receive more and more attention because of its great impact on steel production. However, there is still significant luck of date that could cast some light on the role of the transformation interface during the phase transformation. Therefore, one of the main purposes of this work is to report the experimental results of alloying element (Mn) redistribution in the close vicinity to $\alpha/\gamma(\alpha')$ interface. The unequaled advanced measurement capabilities of the Atom Probe Tomography is one of the most

promising directions of the experimental work to reach this aim. However, advanced technics (such as in-situ STEM or in-situ EBSD) for the in-situ tracking of the interface movement during the phase transformation and investigation of its atomic structure were unavailable within this project. Therefore, numerical simulation at the atomic scale has been used for this purpose.

Chapter 2

Material processing and characterisation

The experimental studies of this work were focused on investigating the segregation and partitioning of alloying elements at the transformation interface during austenite-to-ferrite phase transformation. APT has shown to be a powerful technique to study solute segregation in steels and has a particular interest due to its unique capability to provide both the precise measurement of the chemistry of the interface and three-dimensional (3D) visualization of the microstructure at the near atomic scale. Nevertheless, the APT investigation of site-specific regions, such as an interface, requires a particular procedure for sample preparation and great care for the data processing and interpretation of the results. Therefore, this chapter is dedicated to the description of the precise experimental procedure used in this work.

The chemistry of the investigated model alloy and the heat treatment procedure details are first presented in this chapter. An overview of the working principle and application of APT technique, as the main tool in this study, is given. The protocol of the site-specific sample preparation using SEM-FIB dual-beam is described in detail. The SEM-EBSD application to the crystallographic interface identification requires a special post-treatment of the measured EBSD data that is also presented in this chapter.

2.1 Materials and heat treatment processing

In addition to interstitial carbon, manganese is one of the most important and widely used substitutional elements for dual-phase steels. Therefore ternary Fe-0.17wt%C-2wt%Mn (Fe-0,787at%C-2at%Mn) model alloy has been studied in this work, as a simplified version of commercial DP steels. The alloy was produced by ArcelorMittal Company (Maizières-lès-Metz, France). This ternary system was prepared by vacuum induction melting. The ingot was hot-rolled down to 15mm. The samples were re-austenitized at 1300 °C for 24h under Ar atmosphere in order to remove any Mn microsegregation. Then 2.5 mm of material is removed from each side (to remove possible decarburized part). Finally, the 10 mm thick plate (the length of the dilatometer samples) was ready for the final heat treatment procedure.

As mentioned in Chapter 1, the dual microstructure of DP steels can be achieved by various processing routes, where the intercritical annealing treatments are one of the simplest.

Such heat treatments were conducted in a dilatometer DIL805A (ArcelorMittal research center, Maizières-lès-Metz, France), which was also used to measure the dilation of the sample (initial dimension: 4 mm in diameter and 10 mm length). Two S-type thermocouples (positioned at the center and at the edge of the cylindrical sample) were spot-welded to the temperature measurement sample.

The heat treatment process in the dilatometer involved three main steps. The first step is the austenitization at elevated temperatures (>1000°C) to obtain a fully austenitic microstructure. The next step is cooling down to a selected intercritical temperature in the two-phase (α+γ) region (between A_{C1} and A_{C3} critical temperatures) and then isothermally holding for defined times at the intercritical temperature to produce the ferrite-austenite microstructure. The last step is direct cooling from intercritical to room temperature, which leads to the transformation of retained austenite to martensite. It is important to keep a fast cooling rate to avoid bainite formation and make sure that all austenite transforms to martensite [32][29][1]. The heat treatment process with the transformation temperature of 625°C is shown as the example in Figure 2.1 (a). The austenitization temperature and time have been chosen 1100°C and 60s, respectively. The heating and cooling rates were 10°C/s and 90 °C/s respectively; quenching time for room temperature was equal to 0.1s. The measured dilatometric curve is shown in **Figure 2.1** (b) and shows the change of sample length with the temperature.

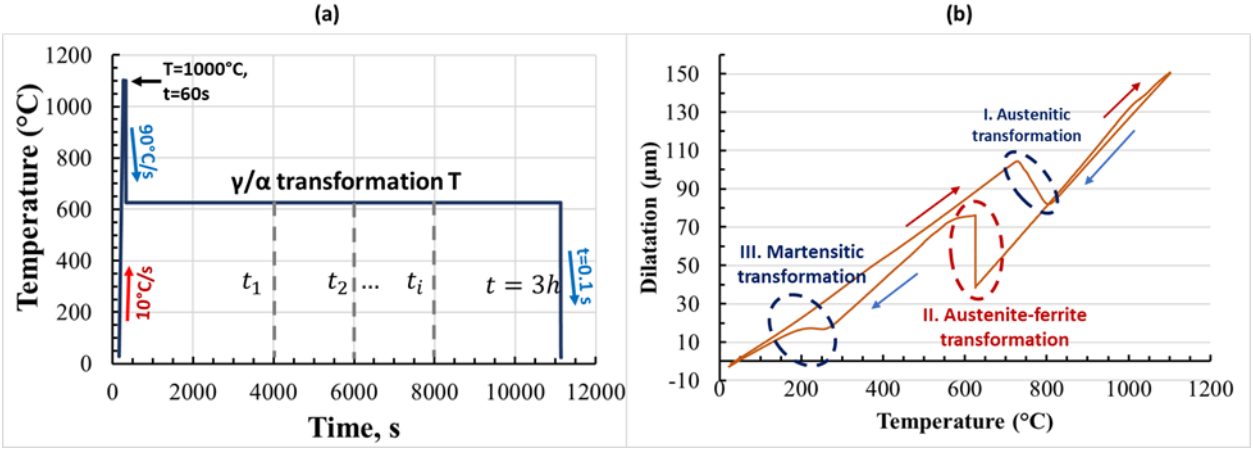

Figure 2.1. (a) *Schematic history of the heat treatment process performed in a dilatometer and measured dilatometric curve* **(b).**

The change in sample length in the temperature domain of austenite-to-ferrite phase transformation (*II. Austenite-ferrite transformation* in **Figure 2.1** (b)) is connected to the evolution of the ferrite fraction. Therefore, the dilatometric curves can be easily used to estimate the austenite-to-ferrite phase transformation kinetic. The ferrite phase fraction evolution, f_α can be calculated as:

$$f_\alpha = \frac{l(t) - l(0)}{l(t_{fin.}) - l(0)} \qquad (2.1)$$

where $l(t)$ is the sample length at time t of the transformation, $l(0)$ – the length just before the phase transformation, and $l(t_{fin.})$ – the length just after complete transformation. Usually, the global kinetic of the ferrite formation obtained from dilatometry data is normalized to the final ferrite fraction as measured from optical micrographs of the microstructure observation at the end of the heat treatment.

It is worth mentioning that after the initial metallographic characterization of the heat-treated samples, two problems were observed in some cases. The first problem is severe decarburization, quite often observed in the sample with a long holding time. This problem was successfully prevented by plating a Ni layer on the sample surface. The second problem is the heterogeneity of the ferrite phase distribution along the sample: a so-called 'banded' microstructure appears in different regions of the sample, depending on the holding time and the temperature [97][98]. It was assumed that this heterogeneity is related to the microsegregation of alloying elements (in this case Mn) during the solidification process in steels, which often leads to a banded microstructure, with the bands lying parallel to the deformation flow [99][100]. Energy-dispersive X-ray spectroscopy (EDS) and electron microprobe analysis (EMPA) (Microprobe SX100, ArcelorMittal research center, Maizières-lès-Metz) were used for verification of the hypothesis. Further investigation and data analysis after dilatometry heat treatment was conducted in GPM laboratory.

2.2 Microstructure observation

A standard metallographic procedure was employed to observe the microstructure and evaluate the ferrite fraction using optical microscopy [101]. The samples were polished using SiC papers from 380 grade down to 4000, followed by diamond paste polishing from 6μm to 0.25μm. The polished samples were etched with 3% Nital for a few seconds. Optical microscopy observation of etched samples clearly reveals both phases, ferrite appearing in bright contrast, martensite (former austenite) in the dark, see **Figure 2.2**.

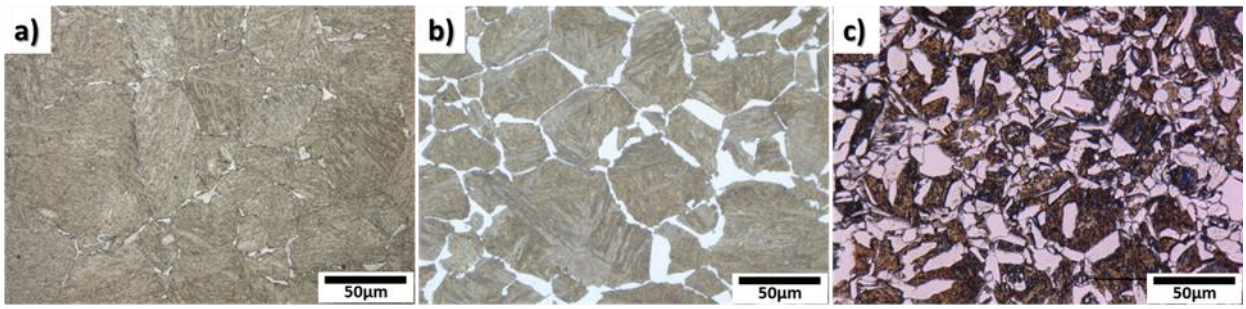

Figure 2.2. *Optical micrographs examples of observed microstructures (bright regions – ferrite, dark – martensite) in Fe-0.17wt%C-2wt%Mn alloy obtained after 3 hours of intercritical annealing at* **(a)** *720°C,* **(b)***680°C,* **(c)** *625°C.*

The kinetics of ferrite growth was estimated and compared using both methods, dilatometry (by analyzing the received dilatometry curve) [102][103] and image analysis (using image processing software ImageJ) [104].

The ferrite/martensite (prior austenite) interfaces (α/γ(α')) are region-of-interest (ROI) in this study because one of the main purposes of this work is to report the experimental investigation of Mn redistribution through α/γ(α') interfaces at the nanoscale. Atom probe tomography is one of the most promising techniques for this kind of investigation. It can provide both three-dimensional (3D) imaging and accurate chemical characterization of the investigated material with a near-atomic spatial resolution but requires specific sample preparation. More details are provided in the following sections.

2.3 Atom probe tomography (APT)

2.3.1 A basic principle of Local Electrode Atom Probe (LEAP)

The APT technique's history begins from the Field Electron Emission Microscope (FEM) developed by the team of E. Müller in the 1930's and comes to the Local Electrode Atom Probe (LEAP) that Kelly introduced commercially in 2003. A nice historical overview of APT technic development can be found elsewhere [105][106][107][108][109]. LEAP is the latest generation of atom probe instruments, and by far the most widest used nowadays. As LEAP was also used in this work, its basic principle is shortly presented below.

In general, the APT principle is based on the field ionization and field evaporation physical processes – the tendency of surface atoms to ionize and desorb from material in the presence of a strong electric field, allowing disassembling the specimen atom by atom. Thus, APT is a destructive technique that, instead of using photons or electrons interactions with the sample for imaging like many other microanalytical tools, actually uses the atoms of the sample itself. The schematic representation of LEAP is shown in **Figure 2.3**. A sharped needle-shaped

specimen is placed in the analysis chamber under ultra-hight vacuum ($\sim 10^{-10}\, mbar$) at cryogenic temperature (in the range of 20-80K) and pointed towards a funnel-shaped local electrode. A high voltage of a few kilovolts is applied to the specimen. In the presence of a high electric field generated by the high voltage at the specimen surface, surface atoms tend to ionize, and when the electric field is high enough, this leads to the break of atomic bonds. The required electric field for the atom ionization of most elements is in the range $\sim 10\, {}^{V}/_{nm}$. Such a high value of electric field is challenging to reach by applying a very high DC voltage to the sample. It is necessary to use the contribution from the sample geometry. Therefore, APT has unique requirements for a sample geometry that has to be prepared in the shape of a sharp needle with an apex curvature radius of ~ 50nm.

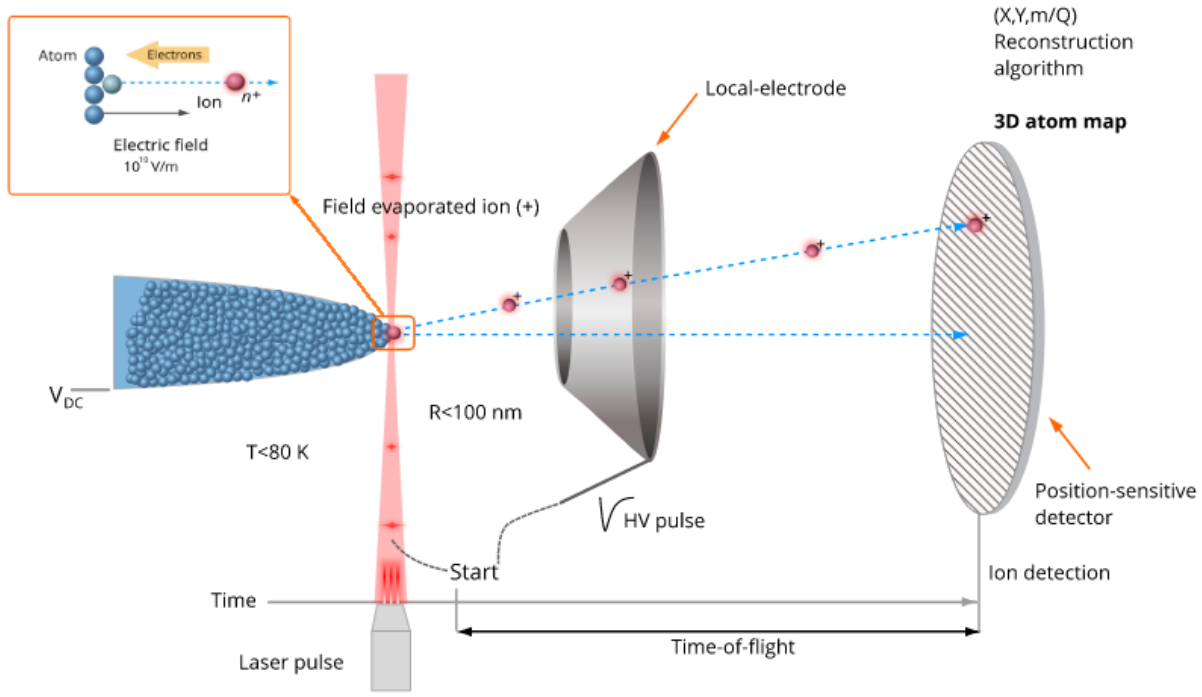

Figure 2.3. *Schematic representation of the LEAP microscope* [110].

Applying a positive DC voltage, V, to a sharp tip specimen induces at the sample surface a high electric field, F, that can be described by the following equation:

$$F = \frac{V}{k_f\, R} \qquad (2.2)$$

were R is the radius of the tip curvature and k_f is a field factor, which is used as a correction parameter for the accounting of the electrostatic environment, and compensating the deviation of the tip shape from a pure sphere. The electric field is essentially proportional to the applied voltage but inversely proportional to the tip radius.

Combining the tip sharpness and the applied high voltage, the electric field with a value just below the value necessary to initiate the field evaporation ($\sim 10\,{}^{V}/_{nm}$) has to be induced right at the tip surface. Then using additional controlled voltage pulses (for electrically conductive materials) makes it possible to reach a sufficient electrostatic field to evaporate the atom from the surface. The ideal case is to extract one atom at the one pulse, avoiding multi-hit events (more than one atom detected on the same pulse). The extracted atoms accelerated by the electric field fly away from the specimen surface through a small aperture in the local electrode towards the position-sensitive time-of-flight detector that measures the time and the impact position of each ion on the detector.

The local electrode (LE) is a key component of the LEAP instrument, which is reflected by its name. It has a funnel-shaped form with a 40 ±10 μm diameter aperture at the apex. The needle-shaped specimen is aligned to the LE aperture center and typically placed at a distance of around the aperture diameter. The position of the LE in such close proximity to the sample surface will cause a significant enhancement of the electric field at the tip, and will decrease the voltage needed to achieve a given value of the local electric field at the specimen surface, the evaporation field [109]. As the voltage is lower, it is possible to use voltage pulse generators with a pulse repetition rate of up to 200kHz, leading to a faster acquisition rate. Such a higher data rate capability of the LEAP requires to use faster delay line detector (DLD) for positioning the ion impacts [106][111].

The delay line detectors (DLD) are now universally used in the most recent generation of commercial atom probes. DLD detectors consist of one (or two) microchannel plate(s) (MCP) and two independent perpendicular delay lines (the first one is used to measure x position and the second one – y). MCP is a thin disk consisting of a two-dimensional close-packed array of glass microchannels of a honeycomb structure. The internal surfaces of these tubes have high secondary-electron yield coatings. When the ion enters into one of those channels, the ion impact is converted to a secondary electron cascade. The exit electron cloud is focused on two delay lines, and (x, y) coordinates of the impact on the detector are measured. MCP basically serves as the signal amplification of the ion impact. However, it is required that ions enter the channel to be detected. Otherwise, it will not be detected. Therefore the APT detection efficiency is strongly affected by the open area of the MCP [112]. The open area of used MCP is about 60%.

In general, compared to the first 3DAP, the presence of a LE improves the APT data collection providing a higher acquisitions rate with a high mass resolution over the larger field of view (FOV). There are two configurations of the modern LEAP. The LEAP system with the straight-flight-path (see **Figure 2.3**) type provides a high detection efficiency but a lower mass

resolution and limited FOV. Systems with a reflectron configuration (see **Figure 2.4**) show an improved mass resolution and a large FOV, but slightly decreasing the detection efficiency because of 90% transparency meshes placed at the entrance and exit of the reflectron. These meshes, necessary to optimize the electrostatic configuration, reduce the final detection efficiency down to about 40% [105][109].

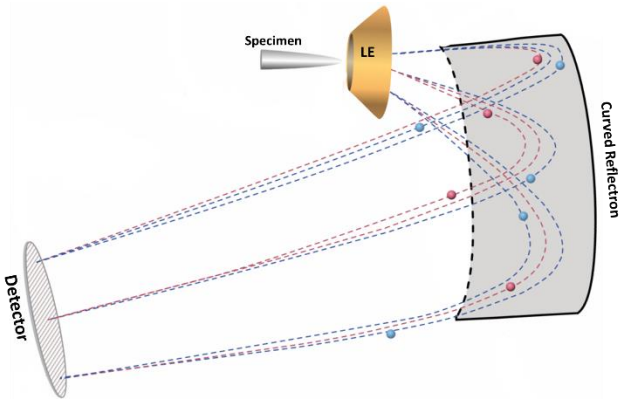

Figure 2.4. *Schematic configuration of the curved reflectron configuration of LEAPT* [110].

The experimental conditions for APT acquisition have to be chosen in order to provide the systematic evaporation of all the elements avoiding preferential evaporation in between individual evaporation plulses. Depending on their crystallography and/or chemistry, microsctructural features, such as precipitates, interfaces…. can present different local evaporation fields (directly related to the binding energy of its constituent atoms). The presence of low or high evaporation field (compared to the one of the matrix) regions generates an effect called local magnification [113]. It is related to the variations in the local curvature of the tip surface (see equation (2.2)) that cause the ion trajectory aberrations [114]. As a consequence, different densities of the hits on the detector are observed. The ions trajectory aberrations and related detector densities in the case of low and high field evaporation regions are schematically illustrated in **Figure 2.5**. Such non-uniform field evaporation distribution in the sample can lead to significant degrading of the spatial resolution and overestimating (or underestimation) of the atomic density of such regions after the APT reconstruction. The trajectory overlaps may affect the local composition measurements close to the different field regions.

The grain boundaries or heterophase interfaces (as investigated in this work) are examples of microstructure features with potentially different local field evaporation, as compared to the matrix. The grain boundary structure is different from the one of the matrix, and typically it is a region with a lower evaporation field because atomic bonds are usually weaker

than in the matrix. However, the presence of the solute segregation at the interface can significantly modify the field evaporation.

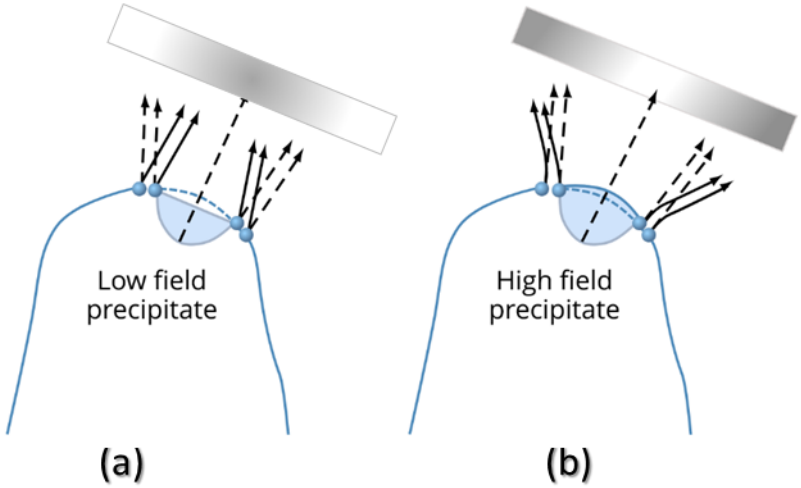

Figure 2.5. *Schematic graph showing different evaporation fields causing trajectory aberrations* **(a)** *from the low field and* **(b)** *high field evaporation precipitate with the density on the detector represented as a darker color for higher density* [110].

2.3.2 Time-of-flight (TOF) mass spectrometry

Time-of-flight (TOF) mass spectrometry is used for chemical identification. The TOF of each ion is the measured time between the applied pulse and the timing signal detected on the MCP. The 'detection window' is a given duration during which timing signals can be recorded. It limits the amplitude of masses that can be collected. The measured TOF is used to determine the mass-to-charge ratio of each detected ion that can be estimated from energy conservation low, assuming that the potential energy of the escaping ion is instantly fully converted into kinetic energy and thus that the evaporated ion acquires all its velocity instantly:

$$neV = \frac{1}{2}mv^2 \qquad (2.3)$$

where n is the ion charge, e the elementary charge of the electron, V the total applied voltage, m is the ion mass, and v is the ion velocity. The ion evaporated from the surface is assumed to have constant velocity during the flight. Then a mass-to-charge ratio can be written as:

$$\frac{m}{n} = \frac{2eVt_f^2}{L_f^2} \qquad (2.4)$$

where $v = \frac{L_f}{t_f}$, L_f is the flight distance, t_f is the measured time-of-flight. The value $\frac{m}{n}$, historically is given in atomic mass unit (a.m.u) per Coulomb (or more simply a.m.u) or more recently (and questionably) in Dalton [115][111]. A histogram of detected ions' mass-to-charge ratios is

usually represented as a mass spectrum with peaks that correspond to the various isotopes of the present species. The ions number within each peak represents information about the elemental composition of the material. Therefore the careful peak identification and definition of its mass ranges (ranging) are necessary for the accurate measurement of the material chemistry [115][105].

2.3.3 APT mass and spatial resolutions

The goal of any measurement is to provide the results with optimum quality. The APT data quality metrics basically include mass resolving power (MRP), background level, and multi-hit performance. MRP is generally defined as $m/\Delta m$ ratio, where Δm is the full-width at half-maximum of the peak, but sometimes at 10% or even 1% of the maximum is also used. A high MRP (a narrow peak) corresponds to a better mass resolution. Multi-hit events correspond to the situation when two or more ions hit the detector "simultaneously" at close proximity. In this case, only one ion is recognized by the detection system instead of the several incoming because the simultaneity of the impacts implies that they have the same mass over charge ratio. This will result in a selective loss of selected ions. In general, the most abundant are the most affected by this phenomenon. A high percentage of multi-hit events will therefore affect the compositional accuracy [115][105][112]. In order to limit this effect, relatively low detection rates are used (<1% atom/pulse).

The near atomic-scale spatial resolution is one of the advantages of the APT technique. However, the spatial resolution in APT is rather different in the analysis direction (in-depth, z tip axis) and laterally (x, y). The resolution in depth is shown to be high enough to resolve atomic planes (at the optimum condition, it is expected better than 0.06nm, and on average, it is around 0.1-0.3nm), whereas the lateral resolution is more limited (around 0.3-0.5nm). Many factors can affect spatial resolution. Variations of the specimen geometry, trajectory aberrations, and local magnification caused by the specimen's chemical variations lead to spatial resolution degradation. The reconstruction algorithm used for the atom positioning may also limit the APT spatial resolution. Among other factors, experimental conditions include the temperature, pulse fraction, detection rate, and electric field [116][117][118].

The unique capabilities of the APT technique (accurate measurement of the chemical composition and 3D visualization of the microstructure at the atomic scale) make it well-suited for the nanoscale interface investigation [21][119] and have been successfully used in this work. However, the APT tips require a particular sample preparation procedure, especially for the investigation of the site-specific region, such as a transformation interface. Moreover, selecting

the specific α/γ transformation interface of interest (in this study) requires additional crystallographical analysis. Therefore the detailed sample preparation procedure is presented in the following sections.

2.4 SEM-EBSD investigation

2.4.1 Scanning Electron Microscope (SEM)

Scanning Electron Microscope produces an image of solid objects by scanning the surface with an electron beam of high energy (from 5 to 20kV). The primary electrons (PEs) from the SEM electron source gun are bombarding the sample surface and interacting with it. Depending on the electron accelerating voltage, electron incident beam current, spot size, and electron density of the investigated material, various types of signals, such as auger electrons (AEs), secondary electrons (SEs), backscattered electrons (BSEs), characteristic X-rays can be emitted from the different depths of the sample [120][121][122].

The examples of SEM images of the investigated material are shown in **Figure 2.6**. These micrographs were generated using the SEs. Since SEs have low energy (<50eV), only SEs generated from the extreme sample surface (a few nanometers) can be detected. Thus, thin ferrite grains that are under interest in this work can be relatively easily distinguished from martensite (prior austenite) on SEM micrographs due to the different surface topography. However, there is no crystallographic information. Taking into account that orientation relationships (ORs) at the transformation α/α'(γ) interfaces may potentially affect their propagation, there is a necessity of Electron Backscatter Diffraction (EBSD) technique application for crystallographic analysis.

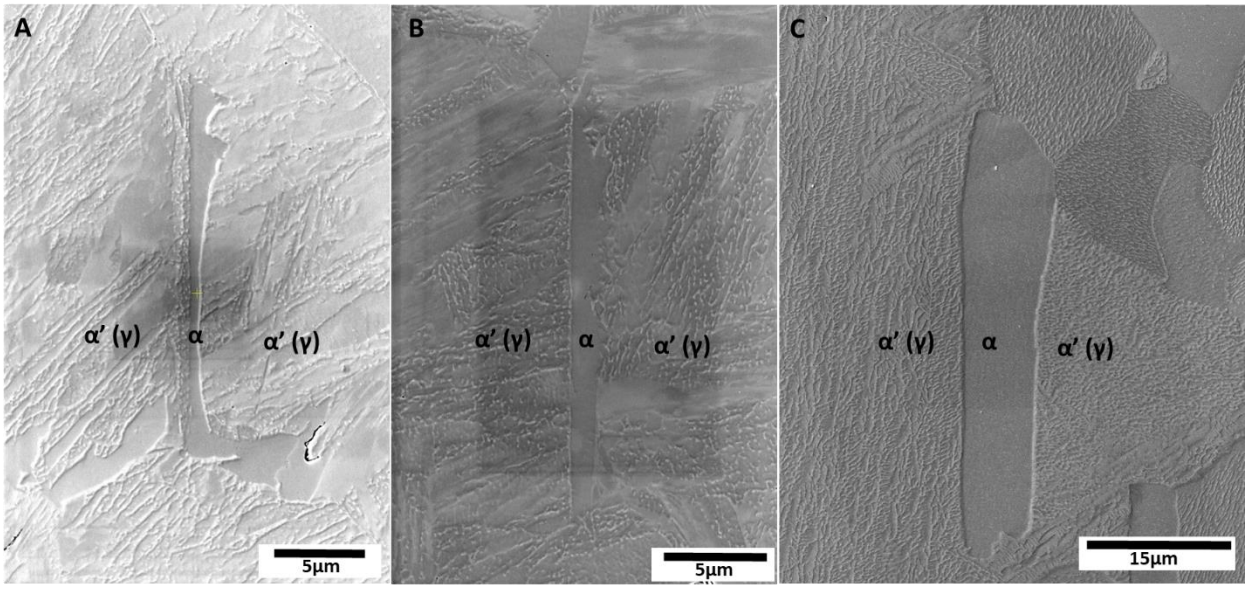

Figure 2.6. *Different examples of the SEM micrographs with α'(γ)/α interfaces regions* ***(a)*** *3h at 720°C,* ***(b)*** *3h at 680°C,* ***(c)*** *3h at 625°C.*

2.4.2 Electron BackScatter Diffraction (EBSD)

Electron BackScatter Diffraction (EBSD) is a powerful technique that provides crystallographic information of the specimen [123][124]. The physical principle of EBSD is based on the electron diffraction by the atomic planes in crystalline materials in conditions that would satisfy Bragg's law [125]. The scattered electrons are projected on the phosphor screen and form a pair of almost parallel lines with a width proportional to the Bragg angle of electron diffraction on the related lattice plane. Such pairs of lines are called Kikuchi bands. The center of Kikuchi bands corresponds to the diffracting planes and their intersection to the zone axes. Therefore, using Hough transformation [124], it is possible to identify the Kikuchi bands in the Miller indices. EBSD can provide information about a specimen's crystal orientation, crystallographic phase distribution, texture, defect densities, grain morphology, grain size, and grain boundary character [124] [126][127].

To obtain EBSD patterns of crystalline materials, a sample with a flat and carefully polished surface is placed in the SEM chamber and oriented at 70° tilt toward the EBSD camera. The SEM chamber configuration and the ability of the EBSD camera acquisition define the possible mapping area. The spatial resolution of the EBSD map is related to the resolution of the SEM, and for the more recent instrument, it can be expected better than 50 nm. The nominal angular resolution limit is ~0.5 [128].

The sample preparation is critical to obtain high-quality EBSD patterns. Therefore, samples after optical microscope observation (after Nital etching) were repolished with diamond

suspension (0.25 µm particle size) and with a silica suspension for final polishing (OP-S NonDry, 0.25 µm). Most EBSD mappings within this work were performed using the JEOL JSM-7900F SEM equipped with an EDAX EBSD camera. The data were collected using the TEAM software. Generally, EBSD scans were performed at 20kV, at a working distance of ~20mm, using the 4×4 binning. The example of the obtained EBSD data is shown in **Figure 2.7**, where the thin layer of allotriomorph ferrite is observed. The crystal orientation map is usually represented via the inverse pole figure color key (IPF-map) with respect to one of the macroscopic directions (X, Y, Z). The map of interest IPF Z with color-coding is presented in **Figure 2.7** (a).

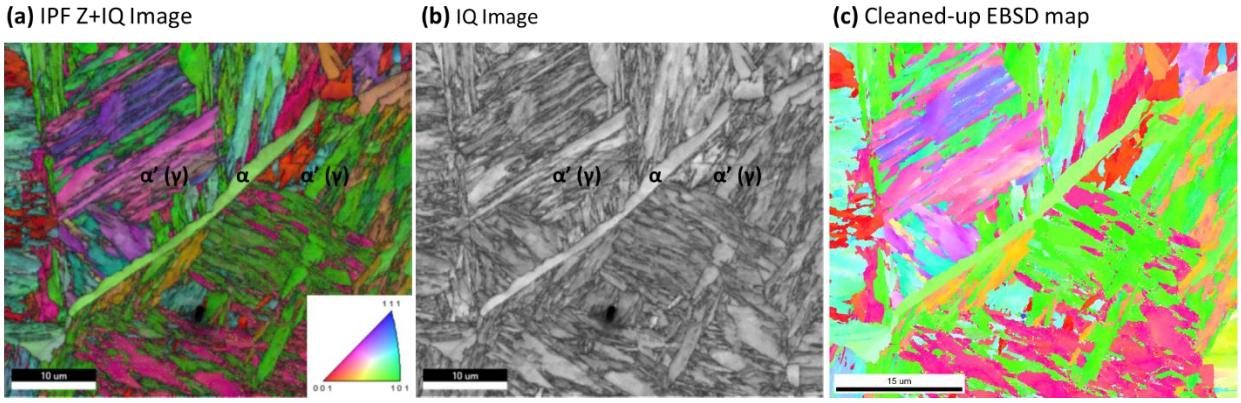

Figure 2.7. *Example of EBSD data observation (3h at 680°C).*

The final microstructure of the investigated steel consists of a mixture of ferrite and martensite (during quenching to the room temperature prior austenite is transformed to martensite). Therefore, it is necessary to differentiate these phases and localize the α'(γ)/α interface. Unfortunately, based only on the EBSD patterns, it is almost impossible to discriminate body-centered tetragonal (bct) martensite from body-centered cubic (bcc) ferrite in low carbon steels. However, diffraction patterns of martensite are generally observed to have lower quality than ferrite patterns, as they are highly disturbed by numerous dislocations, lath and block boundaries [129]. Thus, the image quality (IQ) map constructed based on the average overall intensity of the diffraction patterns provides a better visualization of martensite/ferrite microstructure [130], see **Figure 2.7** (b). The IQ image is very similar to the optical microscope's image with the brighter region being ferrite and the darker martensite.

Due to the surface blemishes, voids, cracks, an EBSD map with 100% indexing is rarely achieved, or some areas have a false indexed solution in an EBSD scan. Typically, there are often points that have not been successfully indexed along grain boundaries. This is usually due to the superposition of diffraction patterns from the crystallites on both sides. Therefore, some

data cleaning almost always needs to be performed to access the relevant information from the measured EBSD dataset [131]. The EBSD data cleaning processes were performed by OIM Analysis software (EDAX) using the Nearest Neighbour Algorithm [132][133], the result shown in **Figure 2.7** (c).

Finally, to obtain deviations from a predefined ORs (KS in this study) between the original γ/α (instead of the observed α'(γ)/α interface), it is possible to reconstruct the parent orientation map from the child EBSD map measured at the room temperature. Such processing was performed by using Merengue 2 software developed at the LEM3 [134].

2.4.3 Parent orientation maps reconstruction

A basic principle of the reconstruction method

One of the important characteristics of the γ/α transformation interface is the orientation relationship between the formed ferrite and prior austenite, as it is expected that OR may affect the interface mobility and thus solute segregation at the interface. Thus retrieving the ORs of the ferrite and parent austenite for the investigated interface may be important. The parent microstructure (α+γ) can potentially be directly measured at a high temperature. However, direct high-temperature orientation map measurement has a limitation: the measurement speed limits the observable phase transformation kinetics [135]. Alternatively, crystallographic reconstruction can be used when the product phase nucleates and grows inside the parent phase according to specific known orientation relationships (ORs).

The OR is usually expressed by the parallelism of the crystal planes and crystal directions of the parent and product phases. For example, the Kurdjumov-Sachs orientation relationship (KS-OR) is among the most frequently reported ORs at α/γ interfaces and can be used as an example. The KS-OR is expressed as follows:

$$KS-OR:\ \begin{matrix}(111)_\gamma\ //\ (110)_\alpha \\ [1\bar{1}0]_\gamma\ //\ [1\bar{1}1]_\alpha\end{matrix} \qquad (2.5)$$

It is possible to note that crystal directions ($[\bar{1}01]_\gamma$ and $[\bar{1}\bar{1}1]_\alpha$) are inside the crystal planes ($(111)_\gamma$ and $(110)_\alpha$) for both parent and product phases. The scalar product of the direction vector and normal to the plane is zero. Then, the third axis of the reference frames can be determined from the correspondent vector product for each phase. Consequently, by knowing the specific reference frames of fcc-parent crystal and bcc-child crystal, it is possible to define the way the two crystals merge at the interface. Considering the symmetry between the parent and product phases, all possible variants of the product phase inherited from the same parent

grain can be computed, and inversely. In the case of KS-OR, there are 24 possible α-variants for each γ-parent grain [38][42]. For calculation purposes, it is convenient to express the OR as a rotation. The orientation of all variants inherited from an austenite parent grain can be computed as follows [136]:

$$[g_\alpha(r_i)] \cong [g_\gamma(r_i)][P_j(r_i)][\Delta g(r_i)][C_k(r_i)] \qquad (2.6)$$

where, $g_\alpha(r_i)$ is the orientation of a variant, $g_\gamma(r_i)$ is the orientation of the parent, $P_j(r_i)$ is the j^{th} symmetry element of the parent phase, $\Delta g(r_i)$ is the orientation relationship, $C_k(r_i)$ is the k^{th} symmetry element of the child phase.

It is logical to consider that the crystallographic variants inherited from the same parent grain are close to each other on the 'child' map and will be in good correlation within the OR with the parent grain. Therefore, the crystallographic reconstruction principle is based on the determination and collection sets of neighboring domains whose orientations are related to a unique parent. It is important to note that it is impossible to find the real parent orientation from the set of the potential ones with only one variant. Thus a minimal number of variants is required to determine the parent orientation without ambiguity, see **Table 3**.

Table 3. *Probability P(A) of determining unambiguously the parent orientation as a function of the number of available variants Nv and OR.*

N_v		1	2	3	4	5	6	>6
$P(A), \%$	Kurdjumov-Sachs (KS)	0	69.6	93.5	99.2	99.9	99.997	100
	Nishiyama-Wasserman (NW)	0	72.2	98.2	100	100	100	100

Merengue 2 software has been developed to automatically reconstruct a parent microtexture from an EBSD map measured on the transformation product. P. Blaineau developed the first Merengue during his PhD thesis. Today L. Germain is continuing the developments [137]–[139].

Main steps of the reconstruction

The main steps of the reconstruction are illustrated in **Figure 2.8**. The first step of the reconstruction is to identify the orientation of all crystallographic domains on the child orientation map measured at room temperature (**Figure 2.8** (a)). The crystallographic domains are defined as a set of adjacent pixels misoriented less than a critical angle ϑ. The value of this angle ϑ is defined by the user (usually in a range from 2° to 4°). The domain identification is based on the same 'grain detection' algorithm used in commercial EBSD software.

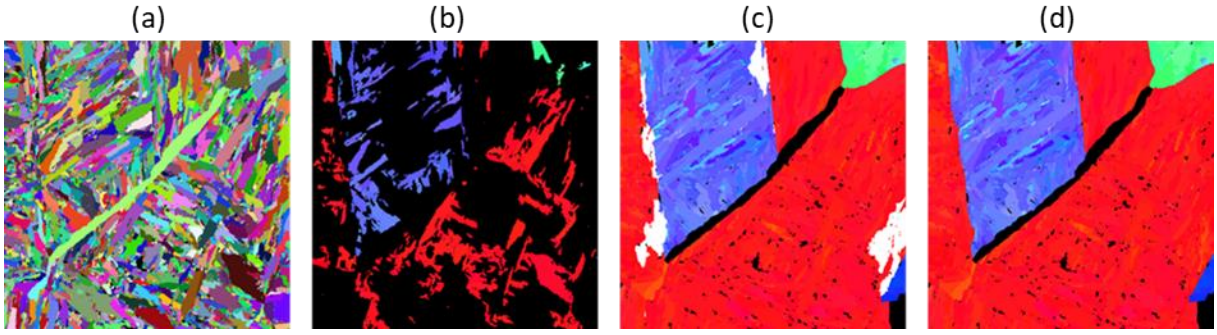

Figure 2.8. *The main steps of reconstruction:* **(a)** *domain detection,* **(b)** *fragments identification,* **(c)** *enlargement,* **(d)** *ambiguities management.*

The presence of low angle misorientation can be a challenging part of domain identification. If the misorientation between two domains is beyond the angular resolution of the EBSD map (the typical angular resolution of the EBSD is ~1°), instead of two separate domains – one domain with the average orientation will be considered. The algorithm called ALGrId (stands for "Anti-Leak" GRain IDentification") can be used for the detection of the low angle boundary. The detailed description of the method and its validation are described in [140]. The result of grain detection is represented by a graph that links the neighboring domains (**Figure 2.9**. In such representation, the nodes contain information about each related domain (orientation, size, identification number), and links contain misorientation and length of the interface between neighbors.

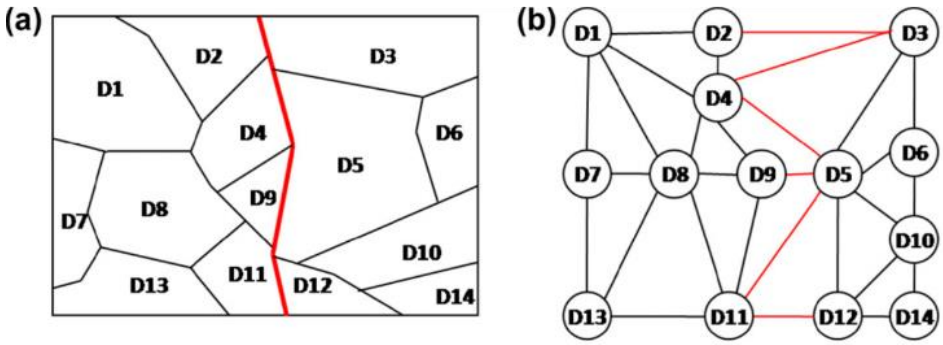

Figure 2.9. *Illustration of the grain detection and transformation in a graph (the bold red lines represent not know during the reconstruction parent grain boundary)* [137].

The next step (**Figure 2.8** (b)) consists in identifying domains for which a parent orientation can be reliably found. Each domain has 24 potential parents which are ranked from the highest to the lowest probable according to a score. This score is defined as:

$$score = \sum_{neighbors} w(\theta) \qquad (2.7)$$

where θ is the misorientation between the considered parent and the closest potential parent of a considered neighbor. $w(\theta)$ is a weighting function defined as:

$$w(\theta) = \max\left(1 - \frac{\theta}{2 \times \omega_1}, 0\right) \quad (2.8)$$

where ω_1 is a tolerance angle (usually 3°). The *score* is high when many neighboring domains share a parent with the considered parent within a small tolerance. Finally, a fragment is kept if the difference of *score* among the two highest scores of the potential parents is above a certain threshold (usually 1.2). The resulting fragments serve now as starting points for the next step.

However, if a child domain is not within the tolerance angle ω_0 with any neighboring parent orientation, it will remain not assigned. Thus, an additional step (fragment enlargement, **Figure 2.8** (c)) is applied. The identified parents can be enlarged to the neighboring not assigned domain with a tolerance angle ω_1. Starting from every identified parents, all unassigned neighbor are considered recursively until all unassigned domain has been considered. In this process, some domains may be assigned to different parents and are then considered ambiguous (in white in **Figure 2.8** (c)). Those ambiguities are frequent and are the result of a variant selection mechanism at γ/γ grains boundaries [141]. This mechanism is so that when a variant can nucleate in KS OR with both grains, it will with a high probability. These special γ/γ boundaries are often called double-KS boundaries.

A dedicated step (**Figure 2.8**. (d)) has been introduced to solve ambiguities. Since ambiguities are frequent at γ twin boundaries, this step takes advantage that the twin boundary plane trace can be determined by the crystallography alone [137].

The example of the austenite/ferrite orientation map reconstruction from the experimentally measured EBSD map at room temperature of martensite/ferrite microstructure obtained in this work is presented in **Figure 2.10**. As a result, the ORs were measured from the two sides of a thin allotriomorph ferrite grain: one interface has the ORs close to KS-OR (red colors), and the second has a significant deviation from KS-OR (from green ~18° to ~31° of deviation).

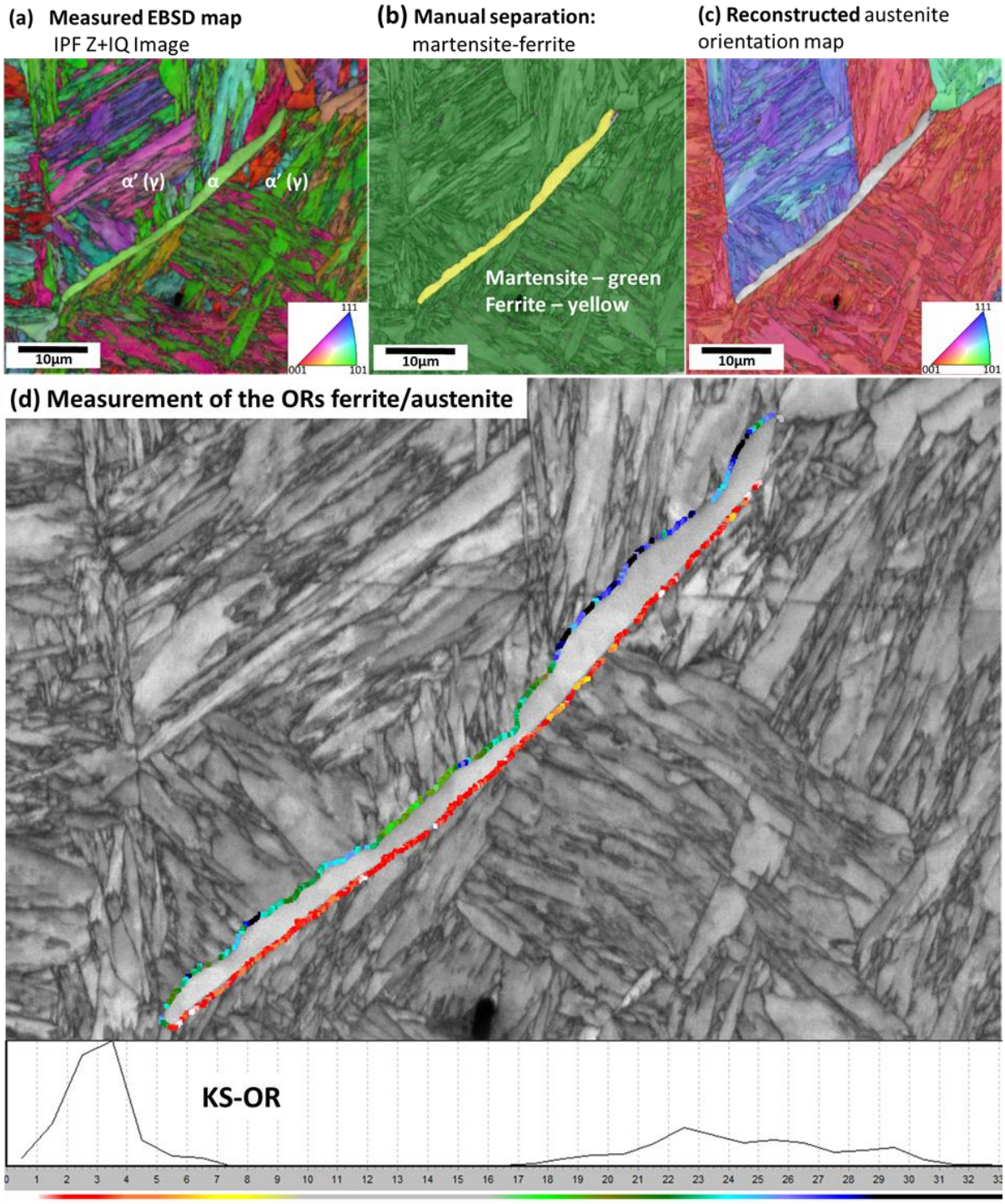

Figure 2.10. *Reconstruction of parent orientation map and measurement of the ORs ferrite/austenite:* ***(a)*** *measured EBSD map at room temperature,* ***(b)*** *manual separation of martensite/ferrite pashes,* ***(c)*** *reconstructed orientation map of austenite/ferrite phases (example of 3h at 680°C),* ***(d)*** *measured ORs of ferrite/austenite microstructure.*

2.5 Focused ion beam (FIB) sample preparation for APT

2.5.1 SEM-FIB dual-beam microscope

After the SEM/EBSD investigation and crystallographic characterisation of the transformation interface, the following step in the experimental sequence is to prepare the APT

specimen. A needle-sharp APT tip has to contain the transformation interface within approximately one hundred nanometers of the specimen apex. The SEM-FIB dual-beam instrument is the only technique available currently for such site-specific specimen preparation of APT tips [142][143][144].

The FIB instrument itself is a sputtering technique that uses a beam of highly energetic ions (up to 30 keV). Still, it can be used as an observation technique when operated at a low current [145][146]. SEM-FIB system is usually equipped with micromanipulators and precursor-based gas injection systems (GIS) used for nanometric local deposition of material or local welding. The additional presence of the detectors such as EBSD, energy-dispersive spectra (EDS), or wavelength-dispersive spectra (WDS) in the configuration of the dual-beam SEM-FIB creates a multifunctional advanced analytical platform for imaging, milling, deposition, micromanipulation, and specimen micro-fabrication, especially for the site-specific analysis. However, the FIB high-energy ion beam can lead to significant material structure damage during the milling process due to the ions implantation into the specimen's bulk [147][148]. Such damages depend on accelerating voltage, beam current, incident beam angle, and the specificities of the investigated material. Therefore, the experimental parameters during FIB manipulation have to be carefully selected [149].

2.5.2 Conventional lift-out process

Various methods using SEM-FIB for the APT sample preparation exist, and the lift-out process is one of the well-known and widely used [105][115][150][151]. This method is especially appropriate when the region of the interest (ROI) is near the surface. The different steps of the conventional lift-out method, also used for thin foils for transmission electron microscopy incvestigations, are shown in **Figure 2.11**. First, a thin protective layer (approx. 1 to 2µm thick) is usually deposited on the ROI to minimize the sample surface damage during ion imaging and milling. In addition, it can help to mark the ROI. Then a chunk of material under the deposited layer is milled by FIB and retracted from the specimen using the micromanipulator and welded on the support tip. Then, the annular milling procedure is used to give a tip shape to the mounted sample. This procedure will be described in more detail later. There are various “recipes” with the lift-out process parameters (mainly accelerating voltage and beam current at the different steps) that depend on the investigated material and the purpose of the analysis. Such “recipes” can serve as a reference point, but most of the time, the lift-out process parameters have to be individually adapted for each sample.

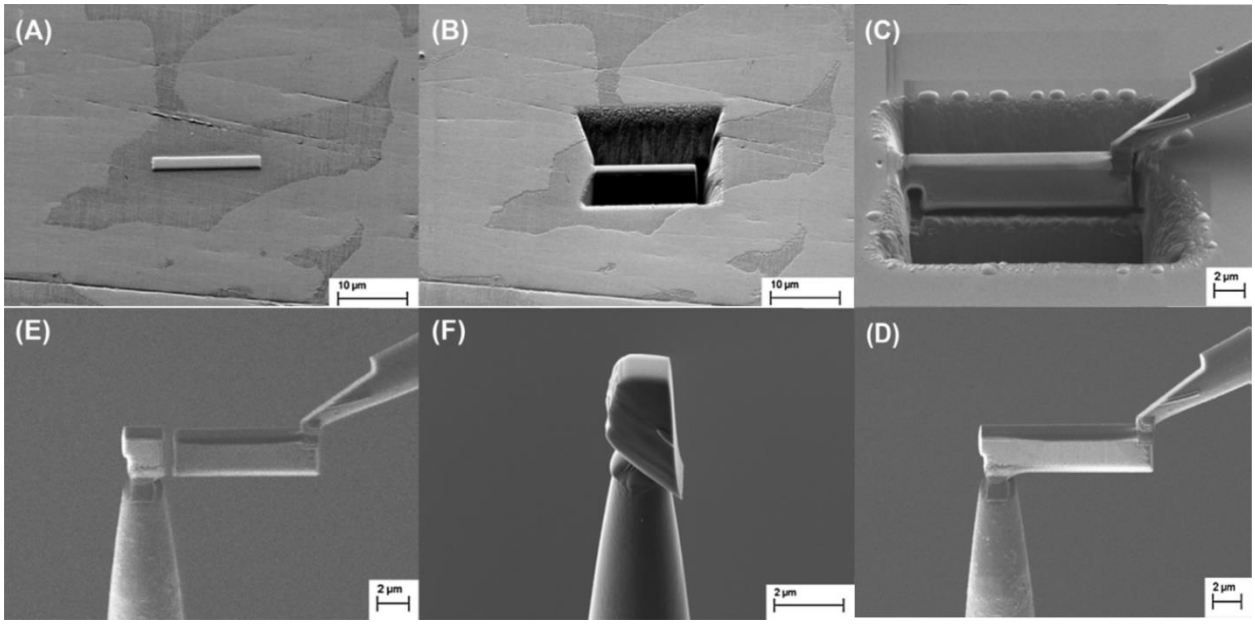

Figure 2.11. *The main steps of the conventional lift-out procedure on a duplex stainless steel.* ***(A)*** *the deposition of a protective layer,* ***(B)*** *the milling material around the ROI,* ***(C)*** *the milling of a horizontal cut through the wall and welding of the micromanipulator tip,* ***(D)*** *sample mounting on a support tip,* ***(E)*** *cutting of the end of the wall, and* ***(F)*** *side view of the sample mounted on the support tip* [112].

2.5.3 Site-specific lift-out for interface analysis

[152][153][154][155]

In the case of site-specific specimen preparation for APT measurement of grain boundaries or heterophase interfaces, the configuration of the lift-out process has to be modified so that investigated interface would have an optimal orientation relative to the direction of the analysis. It is important since the spatial resolution of APT is better along the direction of the analysis (i.e. tip axis) than the perpendicular direction. Therefore to obtain the most accurate concentration profile across the interface, it is preferable to have the interface oriented perpendicular to the analysis direction, which can not be achieved with the conventional lift-out. **Figure 2.12** is illustrating the alternative method that has been developed in this work for such a purpose.

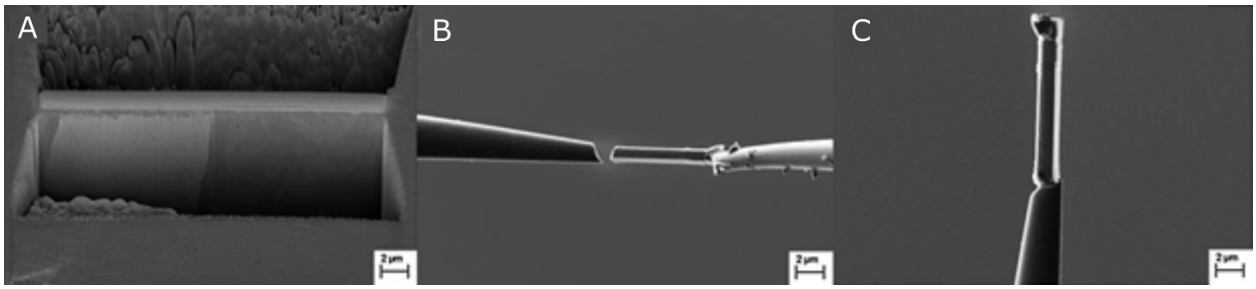

Figure 2.12. *Site-specific lift-out for interface analysis on austenitic steel:* ***(A)*** *SEM image of the milled wall perpendicular to previously selected interface;* ***(B)*** *specimen mounting parallel to a support tip;* ***(C)*** *specimen mounted on the support tip, ready for annular milling* [112].

The example of interface orientation presented in **Figure 2.12** (a) is closely perpendicular to the tip axis. However, since the interface localization is initially made on the 2D surface, it is difficult to predict its direction in the material's bulk (or depth). Even if there is some concern about the interface orientation prediction within the bulk, the method presented above is more suitable for the interface analysis than the conventional lift-out.

2.5.4 Modified site-specific lift-out for interface analysis

Nevertheless, within this work, we went further in the adaptation of the standard lift-out process for interface analysis. It was mainly caused by the aim of measuring the concentration profiles across the (moving) α'(γ)/α transformation interface in the case of allotriomorph in dual-phase steel. However, from typical examples of the micrographs with a thin layer of alotriomorph ferrite (see **Figure 2.6** and **Figure 2.10**), two α'(γ)/α interfaces can be identified. It is rather challenging to determine the moving one. It is natural to assume that one of the observed interfaces would be a mobile transformation interface, and the other will correspond to the prior austenite grain boundary, which was the place for the nucleation of the ferrite grain. However, it is not excluded that both interfaces can be mobile and that ferrite grows in both directions. Therefore it was necessary to measure the concentration across both interfaces, and on both sides of a pro-eutectoid ferrite layer. Besides, from the examples in **Figure 2.6** and **Figure 2.10**, the observed interfaces have various geometries even within the same sample. Often, the shape and thickness of the interface significantly varies along the same ferrite grain. Hence, another question arises: is there any difference in segregation amount (and thus in interfacial composition profile) all along the same interface? If so, can it be linked to the interface geometry and its crystallographic nature? These questions encouraged the modification of the lift-out process to be able to prepare a set of APT specimens along the same ferrite grain, as it is schematically shown in **Figure 2.13**. The modified lift-out process is based on the conventional lift-out but with additional modifications described below.

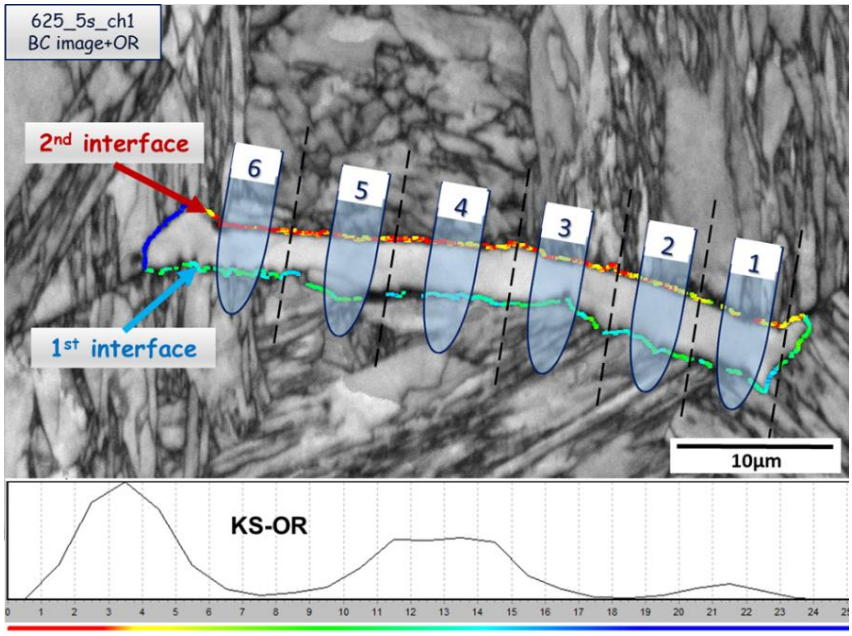

Figure 2.13. *The example of allotriomorph ferrite grain (5s at 625°C)with measured ORs at the interfaces. The set of schematical APT tips represent the desirable sample preparation configurations for APT investigation.*

A PFIB-Helios Xe plasma FIB has been used for the lift-out. An allotriomorphic ferrite previously selected by SEM-EBSD is placed at the cross-beam position (at 52° and 4mm working distance) **Figure 2.14** (a). The protection Pt layer is deposited on the ROI, **Figure 2.14** (b). hen, the important step is to mill the material around the ROI in order to leave a wall perpendicular to the interfaces and verify the interface progression down into the material, see **Figure 2.14** (c). As mentioned above, finding a nearly perpendicular interface to the APT analysis direction (tip axis) could be very challenging and time-consuming. However, since a significant deviation of the interface orientation down into the material from the desired position leads to the measurement of less accurate concentration profile, sometimes it is better to find a more suitable ROI for further investigation.

The chunk with the selected ROI is cut and retracted according to the standard lift-out **Figure 2.14** (d)-(e). However, the size of the ROI (in 2D) could vary from one ferrite grain to another in the range of 3 to 20µm in width and 20 to 70 µm in length. Such dimensions required the adaptation of FIB milling parameters for each individual case. The next step is the sample mounting on the support tips. The W pre-tips prepared by micro-loop electropolishing [112] using a 10%NaOH were used as supporting tips. In order to prepare the APT specimens set according to **Figure 2.13**, the supporting tips are placed at the sides of the chunk, as shown in **Figure 2.14** (f), which is the main adaptation of the proposed method. In such a configuration, the sample welding to the supporting tip was challenging since there is a shadowing effect for the FIB beam. Therefore, the initial welding was performed first by electron beam, and after

changing the configuration according to the standard lift-out process (**Figure 2.11**), it was supplemented by FIB deposition.

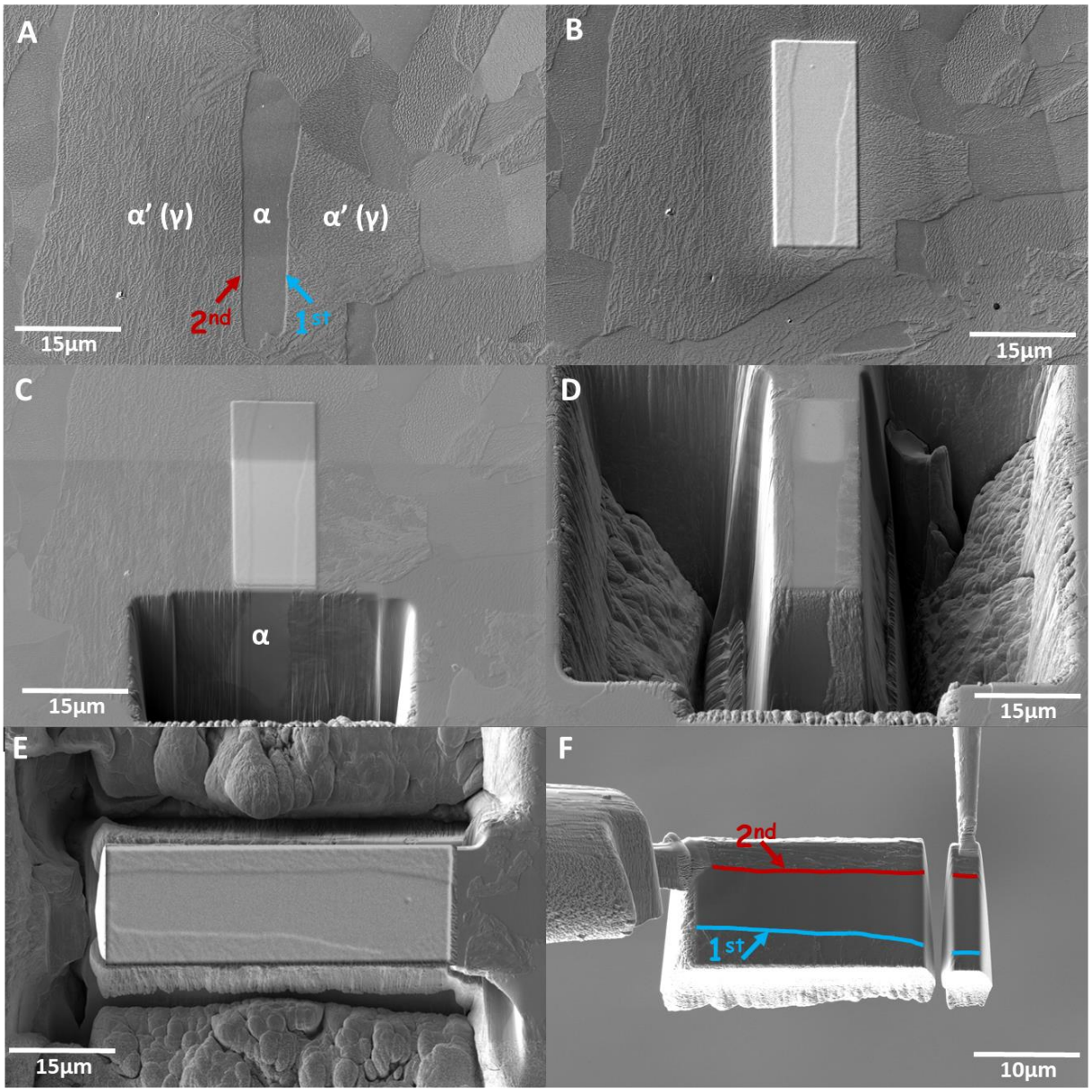

Figure 2.14. *Modified site-specific lift-out for interface analysis:* **(A)** *SEM image of the ROI,* **(B)** *the deposition of a protective layer,* **(C-D)** *the milling material around the ROI,* **(E)** *the milling of a horizontal cut through the wall,* **(F)** *mounting of the welded on the micromanipulator sample on a support tip.*

2.5.5 Annular milling

The final step of APT sample preparation by SEM-FIB is converting a lift-outed sample on the supported pre-tip into a sharp needle with the dimensions required for APT through a series of annular milling steps (see **Figure 2.15**). However, an important point to keep in mind is that the interface must be located ~75-50 nm from the tip apex, which is impossible to achieve with the standard annular milling procedure. Therefore, the application of Transmission Kikuchi

Diffraction (TKD) is required. TKD is the transmission version of EBSD that applies the conventional EBSD hardware to a thin electron-transparent sample and provides a spacial resolution (~10 nm) better than EBSD (~50 nm). The TKD work principle can be found in references [156]. The annular milling steps and TKD examinations were conducted on a Zeiss NVision 40 microscope (with Ga^+ ion source) equipped with an EBSD Oxford instruments camera. The schematical configuration for the experimental set-up in the SEM chamber for TKD is shown in **Figure 2.16** (a).

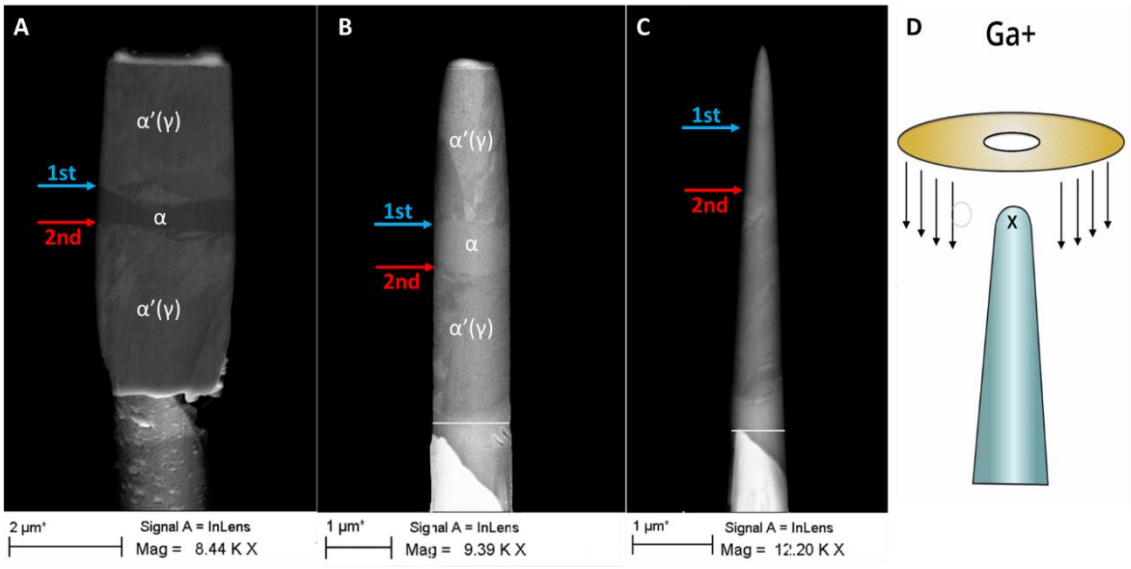

Figure 2.15. *SEM images showing different steps of annular milling with (A) the initial sample mounted on the W support tip, (B) the obtained cylinder after the first milling step, (C) tip after the several steps of AM, close to the final shape and size, (D) schematic demonstration of a milling pattern.*

In **Figure 2.15** (A)-(B), it is possible to recognize the interface's location due to the contrast on the SEM image. However, there is not enough contrast to place an interface precisely ~75-50 nm from the tip apex at the final steps of annular milling (see **Figure 2.15** (C)). Therefore, several final steps of FIB annular milling with consequent TKD mapping are required. Usually, TKD is used after the tip diameter reaches ~ 400 nm and up to the stage of a final APT tip. In addition, TKD can bring additional crystallographic information in close vicinity to the interface.

Figure 2.16 (b-e) shows the TKD IPF Y color map for several annular milling steps. In **Figure 2.16** (b), both 1st (blue arrow) and 2nd (red arrow) interfaces (interfaces noted according to the configuration in **Figure 2.14**) can be observed. In **Figure 2.16** (b), the 1st interface is ~1µm from the tip apex, and after several annular milling steps, it is located approximately at ~75nm from the tip apex. As the second interface is located ~1µm from the first one, this volume is too big to analyse both interfaces in APT at one. Therefore, two individual APT experiments are necessary. The first APT acquisition must be stopped after the first interface is analyzed and,

more importantly, before the specimen rupture (flash). The APT analysis of the interface can be observed live during the acquisition by checking the evolution of the composition profile, and thus the analysis can be stopped after the interface is fully analysed. Then, it is necessary to repeat the annular milling procedure controlled by TKD for positioning the second interface at the new tip apex. Of course, there is always a risk of tip fracture during the first APT analysis. Therefore not all of the interfaces "couples" have been successfully analysed.

After FIB specimen preparation, even after low voltage cleaning, the significant gallium and carbon contamination of the specimen can be observed at the beginning of APT acquisitions. Therefore, to limit at least the carbon contamination resulting from TKD analysis, it is better to limit the number of steps controlled by TKD. Besides, surface oxides are also present initially, which is not representative of the material composition itself. This is one of the reasons for not positioning the interface exactly at the tip apex, and leave some material to protect the interface of interest.

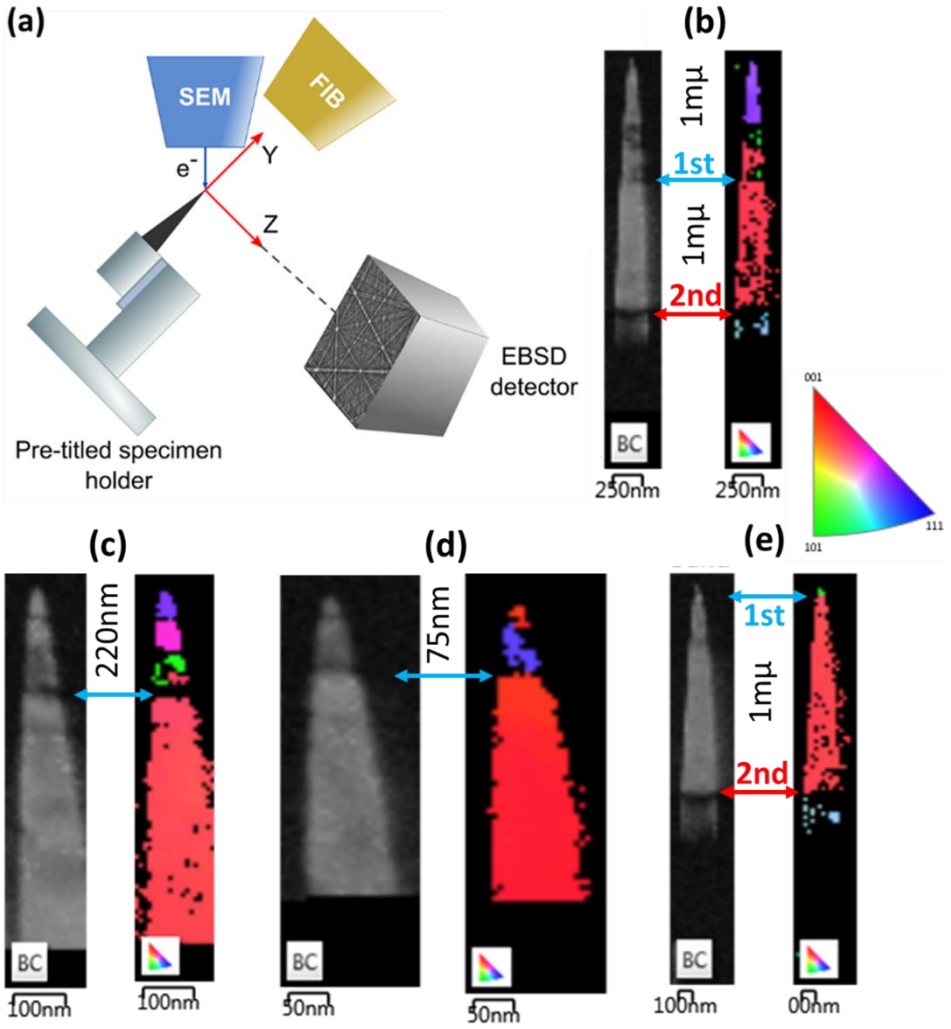

Figure 2.16. (a) *Schematic set-up in the SEM-FIB microscope chamber for TKD analysis.* **(b)-(c)** *annular milling controlled by the TKD analysis, the band contrast images, and the IPF Y color maps showing the interface position.*

In the case of FIB specimens preparation, even after low voltage cleaning, the mass spectrum early at the beginning of APT acquisitions can contain gallium and carbon (because of TKD). Besides, surface oxides and water condensation are also present initially, which is not representable for the material composition itself. Therefore it is better do not to take into account the early part at the beginning of APT acquisitions.

2.6 APT data acquisition and data processing

2.6.1 Experimental conditions of APT measurement

CAMECA LEAP 4000 HR with an energy compensated system (reflectron) has been used for data acquisitions in voltage mode. Within this work, the following parameters were used:

- base temperature (K): 50;
- initial specimen voltage (V): 500V, as the lowest available.
- pulse repetition rate (kHz): 200;
- pulse fraction (%): 20;
- detection rate (%): 0.15, with auto-detection rate control.

2.6.2 APT data reconstruction: parameter optimization

The APT is mostly used for the chemical investigation of very fine microstructural features, such as precipitates, atom clustering, segregation at defects, etc. Its accurate 3D visualization and chemical composition analysis requires careful data mining to achieve ultimate performance. The initial step of APT data analysis is the reconstruction process of the raw acquired data (which basically consists of x, y coordinates of the ions impact position on the 2D detector, the time of flight (TOF), the applied voltage, the sequence of ion evaporation) into a 3D set of spatial coordinates (x, y, z) and mass-to-charge (m/)n ratio for each atom [157].

The reconstruction can be performed via several semi-automated steps using the IVAS 3.8.2 version software [158]. First, it is necessary to select the voltage range (from voltage history) and region of interest (from the detector event histogram) that will be included in the reconstruction. Then an important step is a voltage and a flight path ("bowl") TOF correction that usually requires several iterations. During the APT experiment, the radius of the tip increases, and to maintain the evaporation rate, the applied voltage has to increase as well, which affected ions' kinetics over the acquisition time. Thus, to compensate for the voltage dependence from the TOF, voltage correction is used. "Bowl" correction refers to the tip shape that would be required to compensate for the difference in the flight path length from the tip surface to

different impact locations on the detector. After the satisfactorily TOF correction (mass resolving power, MRP, stops improving), the mass-to-charge conversion and mass spectrum calibration are performed using a linearization method [105]. Several known peaks, preferentially far from each other, are identified and placed at their exact atomic mass unit position. The rest of the mass spectrum is shifted automatically by the software using linear interpolation. The example of a mass-spectrum obtained of the material analysed in this study is shown in **Figure 2.17**. The peak identification complexity depends on the number of elemental species in the investigated material, and the number of related isotopes of each element. A particular challenge for peak identification is peak overlapping caused by different reasons. One of the most common is related to the same or nearly same mass-to-charge ratio of two or more isotopes of different elements (also known as isobars). In the case of peak overlapping, peak decomposition can be performed based on the natural abundance of the various isotopes. Careful peak identification is necessary for accurate chemical composition measurement. In our case of model ternary Fe-Mn-C alloy, no isobars are present.

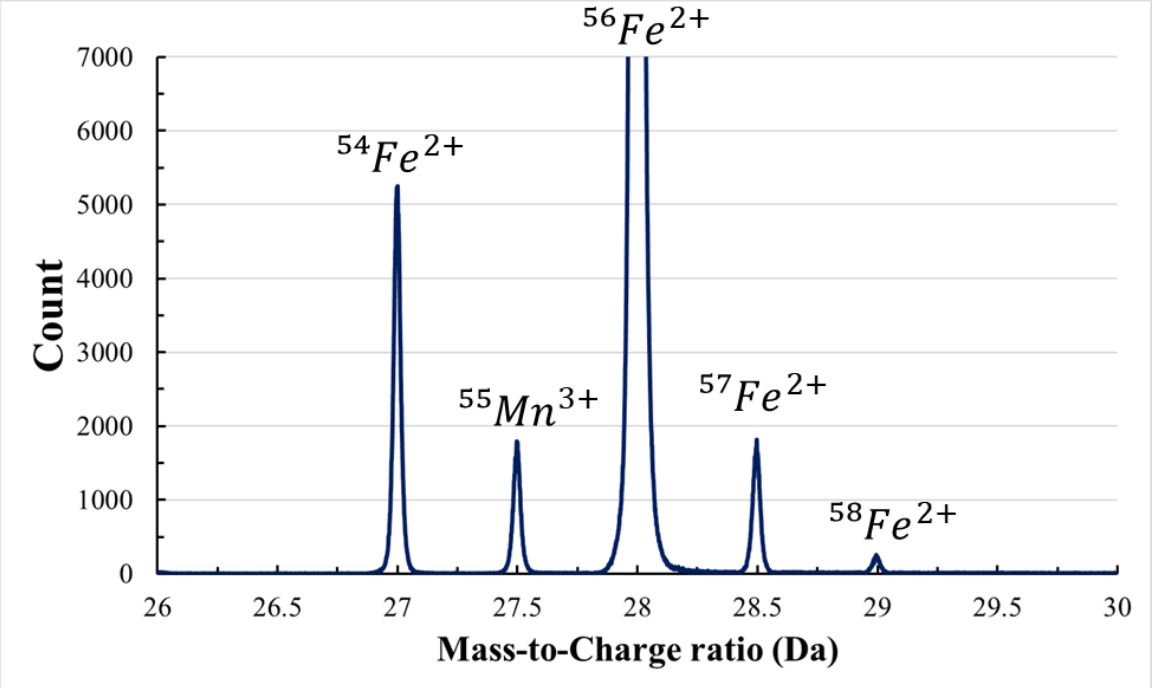

Figure 2.17. *A typical mass spectrum of the analyzed Fe-C-Mn alloys with the position of Fe and Mn peaks.*

The reliable 3D ions positioning in the specimen requires the accurate calculation of the ion flight path from the surface to its hit position (x and y) on the detector. Initially, the trajectory of emitted ion will be progressively compressed and becomes linear approximately after a few times the radius of the apex curvature. Therefore, accurate flight path calculation is extremely complex since it requires knowledge of the exact electric-field distribution from the specimen

surface's vicinity. One way to calibrate the reconstruction is to use the APT desorption maps that partly reflect the crystallographic nature of the tip. The APT desorption map is the 2D cumulative histogram of impact density of on detector. The different evaporation behavior at certain poles (trace of low index crystallographic directions) leads to low or high-density of impacts on the detector, **Figure 2.18**. Moreover, the single or multiple events maps may highlight different information that can be used for pole identification, especially in the case when several poles are observed. The pole identification provides indirect crystallographic information and thus helps to describe the average ion trajectory based on a point-projection model [159][160].

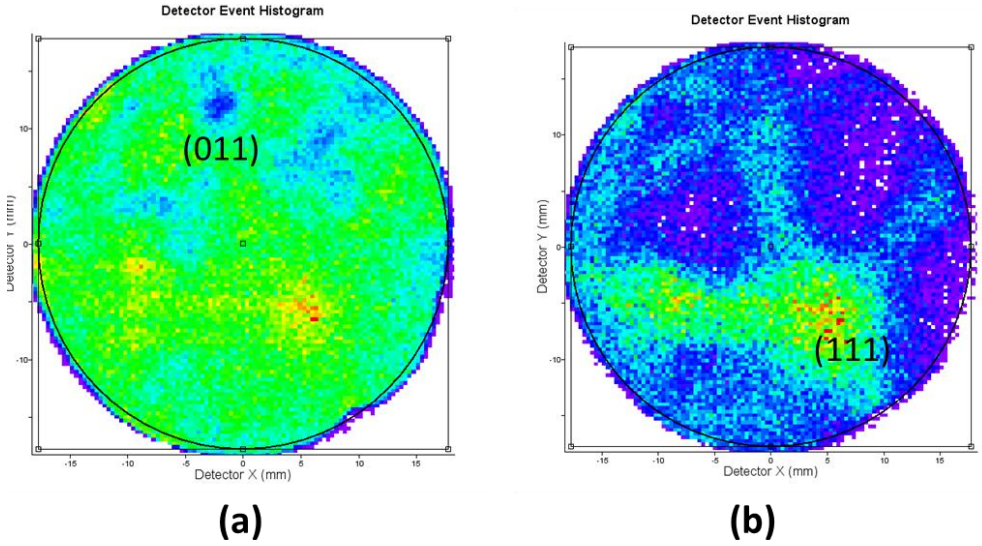

Figure 2.18. *2D desorption map of* **(a)** *single events highlighting (011) pole and* ***(b)*** *multiple events highlighting (111) pole*

A point-projection model, one of the most commonly used models for the description of ion trajectories, is schematically shown in **Figure 2.19**. This model assumes a linear ion trajectory for ions with a unique origin P, suited behind the spherical cap's center, O.

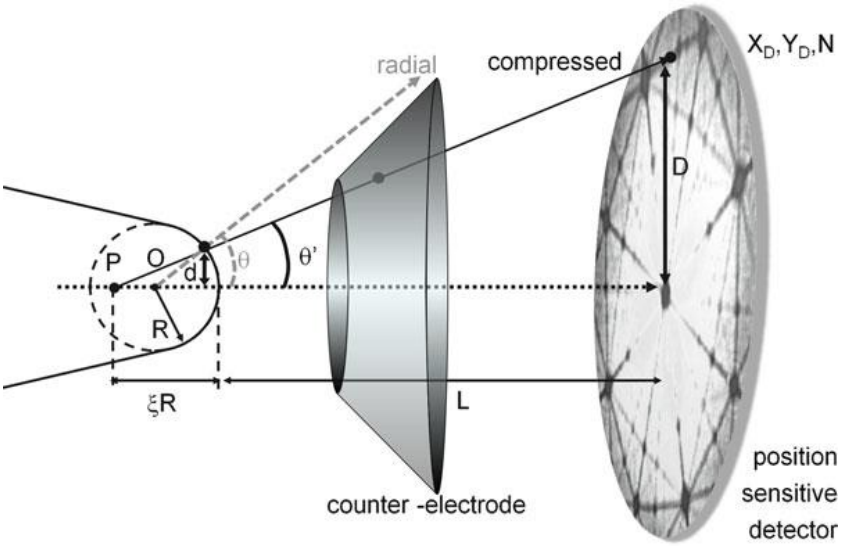

Figure 2.19. *Schematic view of the point-projection* [115].

As L is much greater than the specimen curvature radius R, the projection magnification, M_{proj}, can be expressed as:

$$M_{proj} \approx \frac{L}{\xi R} \tag{2.9}$$

where, ξ – *the image compression factor* (ICF) reflects the compressions of the field lines due to the conical shape of the specimen. Combing the expression for the distance between the point P and tip surface: $\xi R = (m+1)\,R$, were, mR – the distance OP, with the expression of the link between θ and θ': $\theta = \theta' + \arcsin(m\,sin\theta')$ (see **Figure 2.19**), for small angles, ξ, can be defined as the ratio of the theoretical angel, $\theta_{theoretical}$, between two observed poles to the experimentally measured, θ_{exp}, on the projecyed image:

$$\xi \approx \frac{\theta}{\theta'} \approx \frac{\theta_{theoretical}}{\theta_{exp}} \tag{2.10}$$

The theoretical angel, $\theta_{theoretical}$, between the two poles in the bcc structure can be calculated from:

$$\cos\theta_{theoretical} = \frac{h_1h_2 + k_1k_2 + l_1l_2}{\sqrt{(h_1^2 + k_1^2 + l_1^2)\,(h_2^2 + k_2^2 + l_2^2)}} \tag{2.11}$$

where (hkl) are the Miller indexes. The experimentally observed angle between two poles can be calculated as:

$$\theta_{exp} \approx \frac{D}{L} \tag{2.12}$$

where *D* is the distance between these two poles, calculated using the (x, y) coordinates of the 2D detector image, and *L* is the distance between the specimen and the detector. The distance *L* for the LEAP 4000 HR is about 49.4 mm.

The specimen curvature radius *R* is determined directly from the relation between applied voltage *V* to the specimen and electric field *F* generated at the tip apex:

$$K = \frac{V}{k_f R} \tag{2.13}$$

where k_f is *the field reduction factor* or *field factor* (again related to the tip geometry).

The field factor, k_f, is another important reconstruction parameter that depends on the electrostatic environment and specimen geometry, such as shank angle and radius. While the ICF factor is calculated using Eq. (2.10), the field factor is experimentally adjusted to adapt the lattice planes spacing in the reconstructed volume to the one of a known crystallographical direction. In the case of bcc structure, which is the structure of the material investigated in this work, pole <011> has a particular interest in adjusting field factor since the interatomic distance is the largest for bcc-Fe structure in this direction. Then, the spatial distribution map (SDM) map in IVAS software can be used to verify the atomic periodicities in the <110> direction (**Figure 2.20** (a)). SDM is a map of the average neighbor positions around each detected atom in the chosen dataset [161][162]. In our case, we are interested in the dataset that corresponds to the region of the pole. Also, interatomic distance can be measured in GPM 3D software (**Figure 2.20** (b)). After testing several values of field factors, it is relatively easy to fit the observed interplanar spacing with the theoretical value of bcc <011> $d_{011}^{bcc-Fe} = 0.204nm$ that is illustrated in **Figure 2.20**. Such an approach has been used for the reconstruction parameters optimization for each specimen when the necessitated crystallographic directions was known.

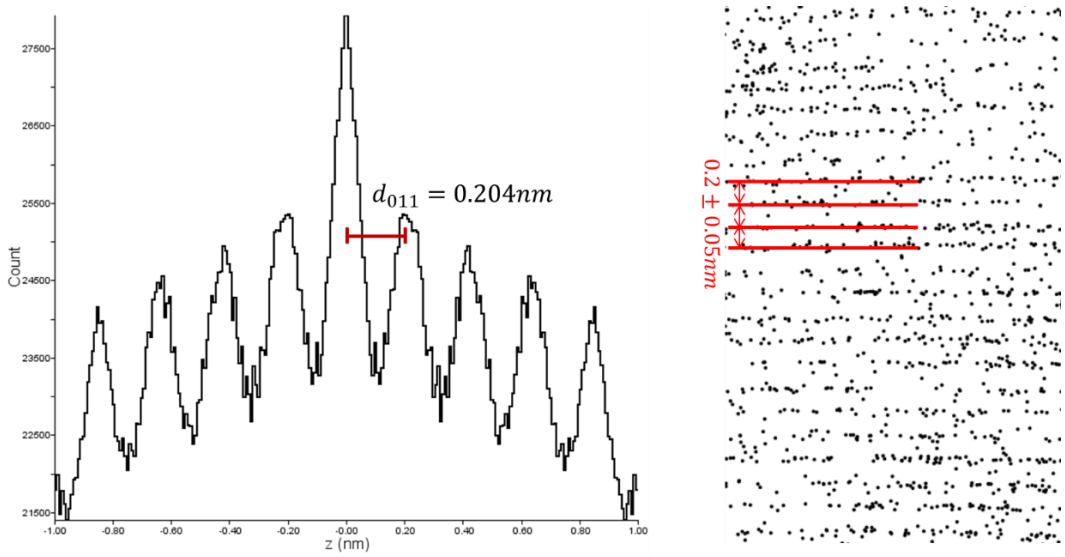

Figure 2.20. *Reconstructed APT subvolume at (011)-pole with* $\xi = 1.6, k_f = 4$ *:* ***(a)*** *the z-spatial distribution maps of Fe atoms revealing the interplanar distances, IVAS software;* ***(b)*** *measurement of the interplanar distances using GPM 3D software.*

2.7 APT measurement of segregation

The APT was used to quantify the segregation of solute atoms at the transformation austenite/ferrite interface in Fe-2at%Mn-0.78at%C model alloy. For example, **Figure 2.21** (a) shows the reconstructed volume after an APT experiment containing an α'(γ)/α transformation interface. The interface can be easily ocated by the segregation of C (shown in red) and Mn (shown in grey) atoms. The composition profiles calculated from these data are shown in **Figure 2.21** (b). Plotting such a profile requires defining a region of interest (ROI) that contains the interface. In this work, a 3D cylindrical ROI is used within the reconstructed volume in IVAS software [163]. The dimension of the ROI depends on the size of the analyzed volume and can vary from one sample to another. Then, such a cylinder is divided in subvolumes with a fixed width over which composition is calculated. The thickness of the subvolumes along the analysis axis in this work is chosen equal to 0.25 nm (close to the bcc lattice parameter – 0.286 nm). To achieve the best resolution, the orientation of the interface must be positioned perpendicular to the z-axis of the sampling cylinder (indicated by the blue arrow), as shown in **Figure 2.21** (a). This position is user-dependent, and therefore, it requires accuracy since it can be an additional source of measurement error. Finally, the composition profile as shown in **Figure 2.21** (b) can be generated. Such a procedure for extracting the composition profiles was applied for each APT volume containing an α'(γ)/α transformation interface considered in this work.

It is essential to note that within this work, the main attention was drawn to study the segregation of Mn atoms. Even if the C atoms segregation is clearly observed on the APT data, its level of segregation is not representative of the austenite/ferrite phase transformation process. It is because of the ability of carbon atoms to diffuse even at room temperature. Therefore, its segregation can reflect the diffusion of carbon after the interface is formed, either in austenite or martensite states. Currently, there is no way to know the contribution of the C redistribution right after the interface was frozen by the quench. Therefore thereafter, only segregation of Mn atoms will be discussed.

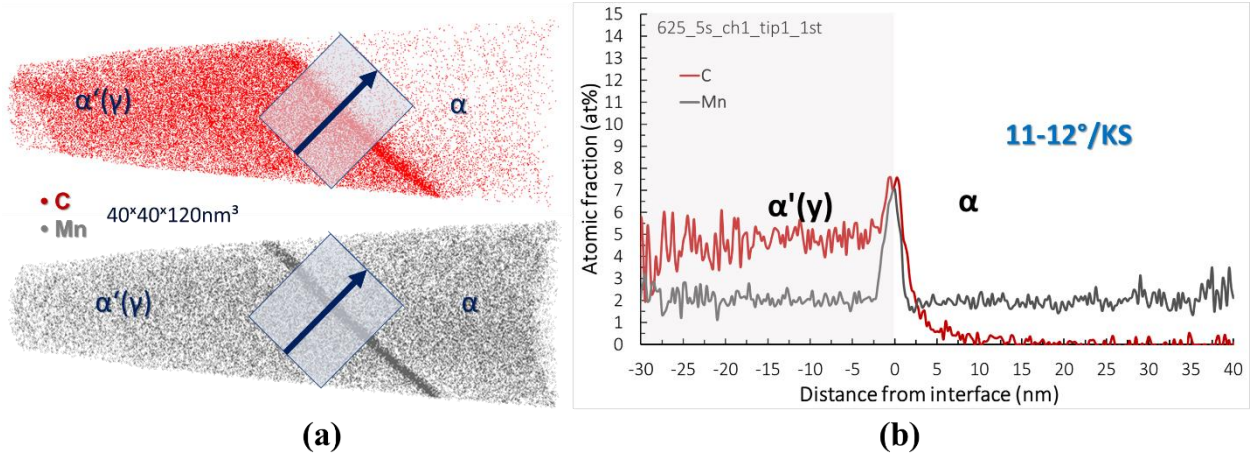

Figure 2.21. (a) *The reconstructed 3D volume of Fe-2at% Mn-0.78 at% C model alloy containing an α' (γ)/α transformation interface reveals the segregation of C (red) and Mn atoms (gray);* **(b)** *concentration profile across interface represents the concentration of C and Mn atoms versus distance from the interface.*

The next question is "how to quantify the amount of Mn segregation at the interface?". Initially, the peak value of the concentration profile has been chosen as an experimental measurement of interfacial segregation. However, the raw concentration profile obtained by APT provides inaccurate results because of several issues. Foremost, the peak value and width of segregation are strongly dependent on the spatial resolution of the used characterization technique. In APT measurement, this value can be underestimated due to the local magnification effect that may occur if the segregation elements have an evaporation field different from the matrix one and if the interface is not perpendicular to the tip axis [164][114]. This effect is minimized if the interface plane is perpendicular to the analysis direction. However, experimentally, it is rather tricky and time-consuming to find interfaces with their normal parallel to the analysis axis (or perform such alignment). The additional challenge is to take into account the shape of the investigated interface, which may not be strictly planar at the nanoscale. **Figure 2.22** displays a schematic representation of the consequences of these artefacts on an ideal profile ('real'), and the resulting experimental outcomes. Measure1 and Measure 2

correspond to the same quantity of segregating atoms but are measured with different experimental misorientations by APT[119]. These issues are also common with other experimental techniques.

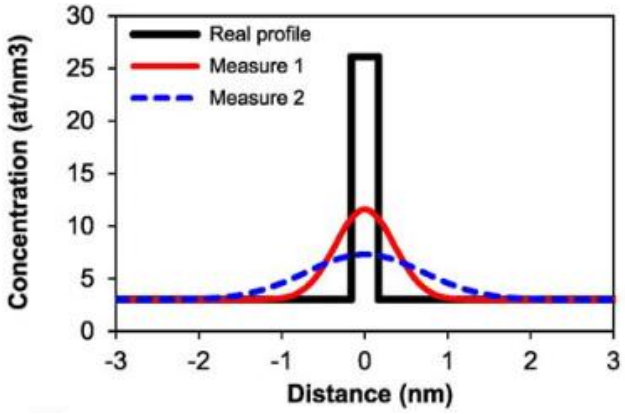

Figure 2.22. *Schematic illustration of the expected "real" profile and experimentally measured (Measure 1, Measure2)* [119].

Due to the drawbacks of the experimental procedure, the measured profiles (blue and red) are spread out along the observation axis as compared to the expected rectangular profile (black). However, the total amount of solute atoms segregated in the vicinity of the interface are the same. Therefore, to overcome this spatial convolution and to standardize the quantitativity of the analyses of interfacial segregation (independent of the experimental conditions), it is preferred to use the Gibbsian interfacial excess method.

2.7.1 Gibbsian interfacial excess method

Gibbs was a pioneer in developing the thermodynamic model of the interface. He introduced the concept of interfacial excess of solutes relative to a geometric surface dividing the coexisting phases [165]. This surface is known as the Gibbs dividing surface. The Gibbsian interfacial excess of solute, Γ_i, is the number of solute i, segregated at this interface per unit area. It is a thermodynamic property that can be related to the variation of interfacial free energy as:

$$\Gamma_i = -\left(\frac{\partial \gamma}{\partial \mu_i}\right)_{T,P\ \mu_{j\neq 1}} \qquad (2.14)$$

where γ is the interface energy, μ_i is the chemical potential of solute i at constant T and P. The Gibbsian excess equals the excess number of atoms associated with the interface, N_i^{excees}, divided by the interfacial area, A:

$$\Gamma_i = \frac{N_i^{excees}}{A} \qquad (2.15)$$

The APT technique used in this work delivers a discrete count of the atoms in the analyzed volume. Consequently, Γ_i can be extracted directly from APT reconstructed data using a similar procedure as the one first introduced by Seidman and Krakauer [166] (see **Figure 2.23**). The authors demonstrated Gibbsian interfacial excess can be determined from a so called integral profile, schematically shown in **Figure 2.23** (b). This graph represents the cumulative number of atoms of a given species versus the cumulative numbers of all atoms in the vicinity of the interface. If there is no segregation at the interface, the cumulative number of atoms of solute element i will increase proportionally to the cumulative number of all atoms. The slope of such a linear dependence will represent the average atomic fraction of specie i in the analyzed volume. In that sence, this plot is the mathematical integral of the composition profile.

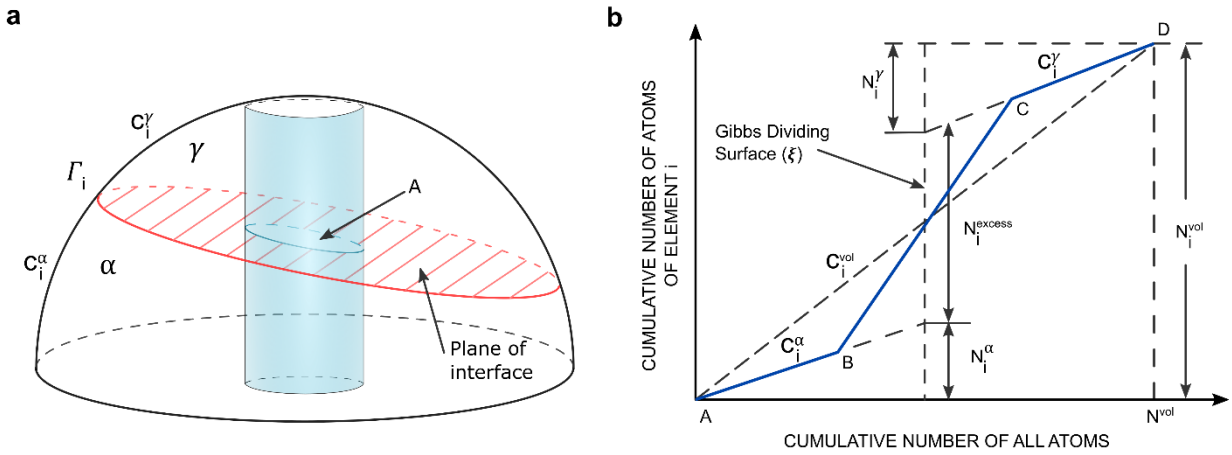

Figure 2.23. (a) *Schematic illustration of the analyzed volume with the interface.* **(b)** *Hypothetical integral profile (line ABCD) represents the cumulative number of solute atoms versus the cumulative numbers of all atoms in the vicinity of the interface determined from an APT analysis* [166].

If there is interfacial segregation of element i, the slope of this curve will change as shown in **Figure 2.23**(b). The linear segments AB and CD in **Figure 2.23** (b) correspond to the phases on both sides of the interface, α and γ phases in this work, respectively, and BC to the interface region. The slope of each linear segment corresponds to the average atomic fraction of specie i of a particular part of the analyzed sample. In this case, the Gibbsian excess can be calculated as:

$$\Gamma_i = \frac{N_i^{excees}}{A\eta} = \left(\frac{1}{A\eta}\right)\left(N_i^{vol} - N_i^{\alpha} - N_i^{\gamma}\right) = \left(\frac{1}{A\eta}\right) N^{vol}\left[C_i^{vol} - C_i^{\alpha}\xi - C_i^{\gamma}(1-\xi)\right] \quad (2.16)$$

where η – is the detection efficiency of the used characterization technique, and A is the interfacial area over which Γ_i is determined. In the case of the LEAP 4000 HR, the detector

efficiency η is equal to 0.36 and the area $A = 2\pi r^2$ (r is the radius of the cylindrical ROI shown in **Figure 2.21**(a)). The quantities: N_i^{α} and N_i^{γ} are the number of i atoms in the α and γ phases; N_i^{vol} is the total number of i atoms in the cylindrical ROI containing the interface; C_i^{α}, C_i^{γ} and C_i^{vol} are the atomic fractions of solute i in the bulk of the two phases, and in the total volume with the interface, respectively; N^{vol} – the total number of all atoms in the considered volume; finally, ξ is the position of the Gibbs dividing surface.

However, in this method, the Gibbs dividing surface position is a free parameter. Generally speaking, the position of this surface should coincide strictly with the plane which separates the two phases. Since one of the main assumptions of Gibbs' method is that the two phases exist up to this dividing surface, it is evident that the Γ_i value depends on its position, which can be easily seen from Eq.(2.16).

When the atomic fractions of solute atoms in both phases are identical, the position of the dividing interface does not influence the value of N_i^{excees} . In this case, the slope of AB segment is identical to the one of CD one (see **Figure 2.23** (b)). It is not the case for the non-symmetric composition profile with different compositions on both sides of interface. This situation is demonstrated in **Figure 2.24**. Then the interfacial excess can be defined as the area under the peak minus the reference areas (grey areas) determined by the bulk composition of the considered phases in the absence of interfacial segregation. **Figure 2.24** (a) illustrates the schematic composition profile of the homophase system (in terms of solute content) with interfacial segregation. In this case, the red area is independent of the position of Gibbs dividing surface, represented by the dashed line. In the case of different compositions on both sides of the interface, interfacial excess can be determined as a sum of the blue and green areas; see **Figure 2.24** (b). The resulting excess value will therefore depend on the choice of the dividing surface

position, see **Figure 2.24** (c-d). This effect will be amplified with increasing composition differences between both phases.

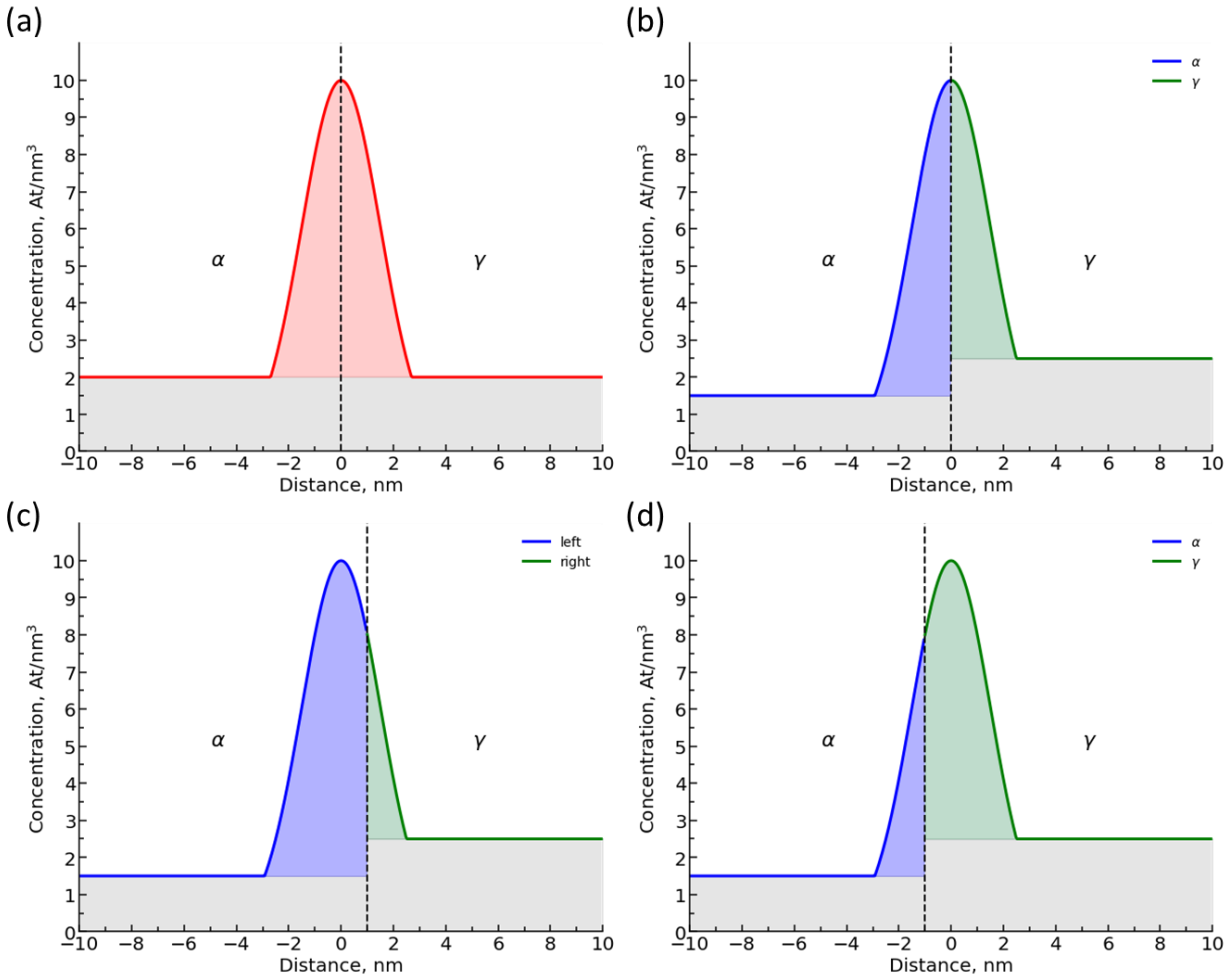

Figure 2.24. *Schematic illustration of the interfacial excess calculation by Gibbs's method using a dividing surface:* ***(a)*** *symmetrical concentration profile;* ***(b), (c), (d)*** *concentration profiles with different compositions from both sides of the interface and dividing surface placed at the position of the peak and ±1nm from it, respectively.*

Gibbs tried to solve this problem by calculating the relative interfacial excess concerning one or two reference elements. Such a solution does not require the dividing surface positions, but it does not provide the absolute excess value.

2.7.2 Methodology of Maugis and Hoummada

To avoid the precise determination of the dividing surface position, another approach was suggested by Maugis and Hoummada [119], [167]. The authors proposed to calculate the excess interfacial concentration, C_i^{ex}, of solute i using following expression:

$$C_i^{ex} = \int_{-L/2}^{+L/2} (C(z) - C^{\infty}) dz \qquad (2.17)$$

where C^{∞} is the bulk composition of solute atoms and C(z) is the composition profile calculated in inhomogeneous region between $-L/2$ and $+L/2$ The value of C_i^{ex} is determined as the asymptotic value in **Figure 2.25**, and it is equivalent to the Γ_i.

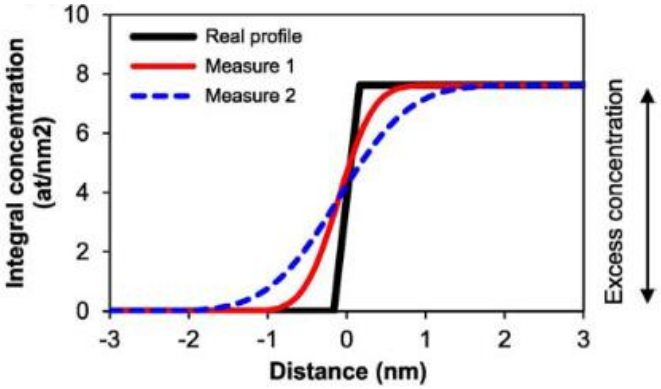

Figure 2.25. (a) *Schematic illustration of the expected "real" profile and experimentally measured (Measure 1, Measure2).* **(b)** *The excess concentration is calculated from the integral concentration profiles* [119].

In the case of APT measurement, instead of the composition profile $C(z)$ which is in atoms per unit volume, the profile of an atomic fraction $X(z)$ in at% is usually plotted. Thus, the excess fraction X_i^{ex} can be calculated by providing the atomic volume, V_{at}, which assumed to be uniform along the profile:

$$X_i^{ex} = \int_{-L/2}^{+L/2} (X(z) - X^{\infty}) dz = V_{at}\Gamma_i \qquad (2.18)$$

It should be noted that the method proposed by Maugis and Hummada is an extension of the concept of "integral profile" used in Seidman approach [119]. It has several advantages. In particular, as schematically shown in **Figure 2.25**, it is independent of the Gibbs dividing interface. Nevertheless, this method is only valid for a homophase boundary, when the bulk compositions are the same on both sides of the interface. As our work is devoted to the investigation of the transformation interface during the austenite to ferrite phase transformation. The atomic volume V_{at} along the profile are not uniform in the ferrite and austenite phases, even if its influence can be negligible. More important, depending on the thermal history treatment, the bulk compositions of solute elements in ferrite and austenite phases are expected to be different due to the difference in the chemical potential between those phases. Consequently, the

choice of a single C^{∞} value is not adapted in this case, as illustrated by examples shown in **Figure 2.26**.

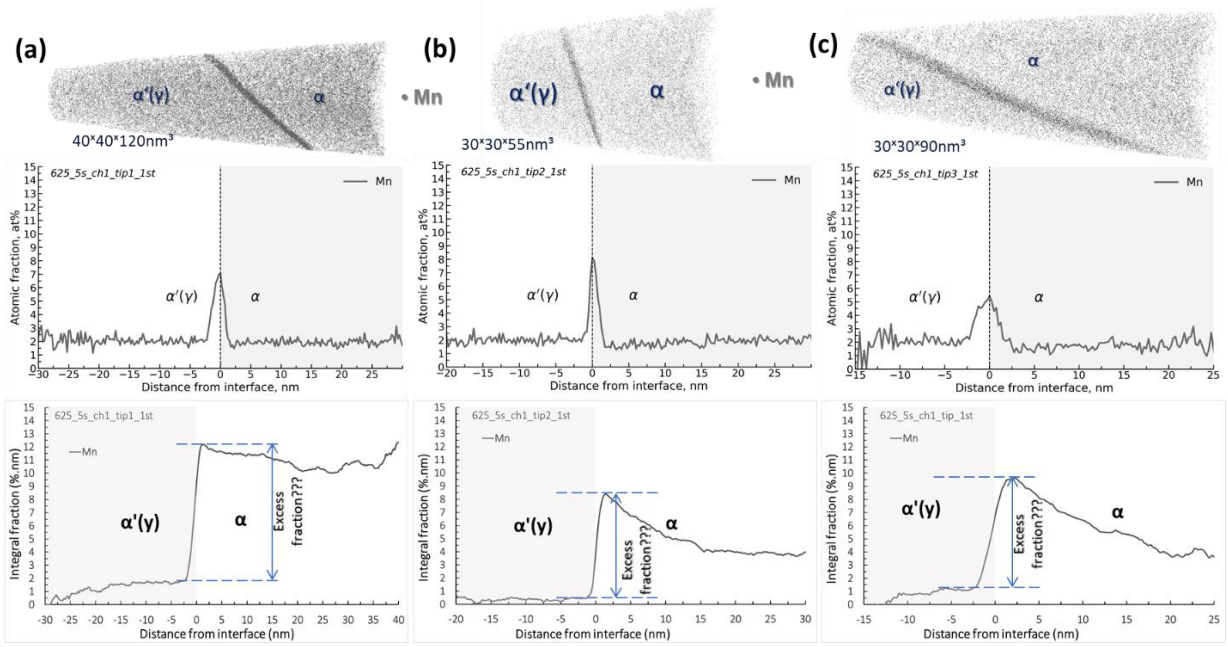

Figure 2.26. *An example of the reconstructed APT volumes of the Fe-2at%Mn-0.78at%C model alloy containing the α' (γ)/α transformation interface with the appropriate atomic fraction and integral fraction profiles, in % nm, through those interfaces. Analised volumes are the neighbor tips extracted from the same chunk.*

The integral fraction profiles, in % nm, evidence the consequences of bulk fractions on both sides far from the interface are not equal to the expected bulk atomic fraction in 2at% of Mn (integral fraction profiles are calculated according to Eq.(2.18). Usually, X^{∞} is slightly higher for the austenite and lower for the ferrite phase, $X_{\gamma}^{\infty} > X_{\alpha}^{\infty}$. It can be suggested to define the excess fraction value, as schematically shown in **Figure 2.26**. However, it is hard to justify that choice. Besides, it requires a user to choose the two points between which that value will be established. That choice is often not evident, especially in more complicated cases of non-symmetric profiles, as demonstrated in **Figure 2.27**.

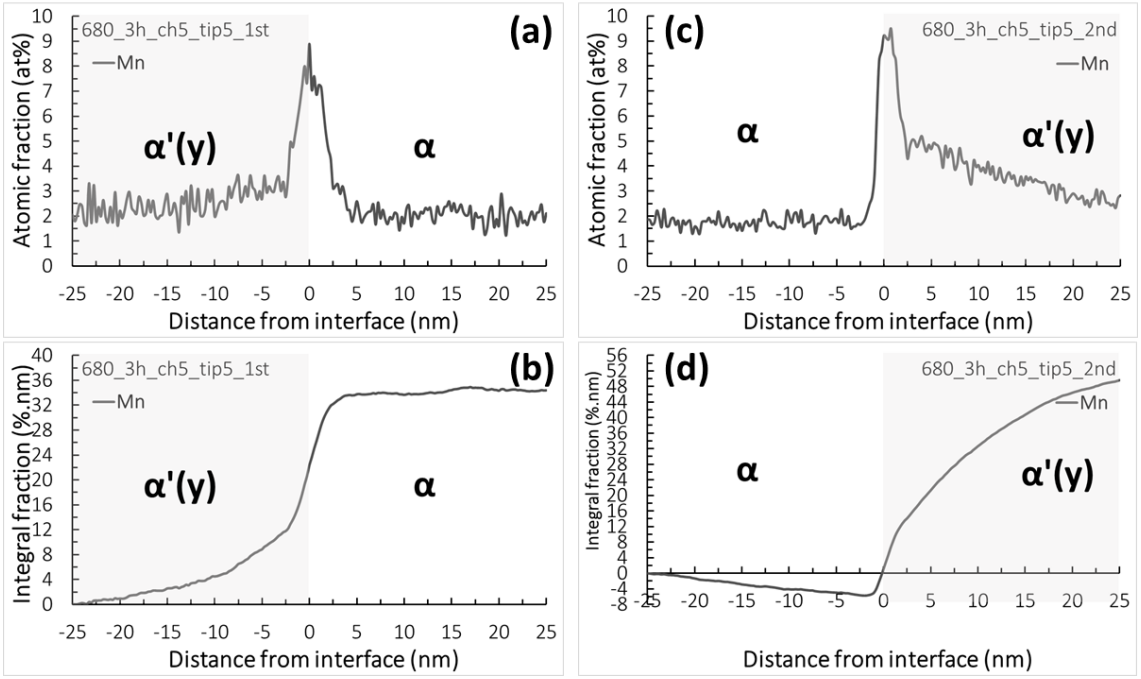

Figure 2.27. *Example of the atomic fraction and integral fraction profiles with non-symmetric shape.*

Another suggestion can be to take a different X^{∞} for austenite and ferrite phases ($X_{\gamma}^{\infty}, X_{\alpha}^{\infty}$). It will provide acquiring a similar integral fraction profile as illustrated in **Figure 2.25,** but leads to a similar problem as with Gibbs dividing surface – to which extend the γ and α phases exist, or which value of X^{∞} has to be taken for interface region, and again the definition of the interface region?

2.7.3 Influence of the Gibbs interface positioning accuracy

Despite the necessity to solve the problem of the excess interfacial determination for other properties at the interface (such as interfacial free energy, surface stress, and strain), there are still many open questions in the case of the hetero system [168]–[172]. As the unambiguously and unbiased solution has not been found yet to calculate the Gibbs excess, the influence of the mis positioning of the Gibbs dividing surface is investigated.

In this work, the calculation of Gibbs excess is based on the method described by Seidman and Krakauer [166] with the dividing surface concept. This method requires assumptions regarding the position of the dividing surface. The authors proposed to place a dividing surface at the center of the region with an interface. However, it is unclear how to define the region's limits containing an interface or the center of the interface. The first hypothesis is to set the Gibbs dividing surface (ξ) at the position of the peak of the composition profile. Still, it is not evident that the peak position corresponds to the point up to which two phases exist, especially when the segregation peak is non-symmetric. However, experimental segregation

peaks are usually less than a few nanometer large [173]. Therefore, it is crucial to estimate the variations of the Gibbs access value when the dividing surface is miss-positioned within these few nanometers.

These estimations were performed for model profiles, with compositions of the α- and γ-phases close to those experimentally observed within this work. Those profiles are shown in **Figure 2.28** (a). Interfacial excesses were calculated for different positions of the dividing surface relative to the peak position. First, the excess value was calculated assuming that the dividing surface is placed exactly at the peak of the composition profile (it corresponds to the $x = 0$ on the x-axis). Then the position of the dividing surface was moved within a few nm to the left ($x = -1;\ -2;\ -3\ nm$) and then to the right ($x = 1;\ 2; 3\ nm$) from the peak positions. The results of the excess values calculation with the variation of the dividing surface positions are represented as a graph in **Figure 2.28** (b). As expected, for the blue profile (where $C_{Mn}^{\alpha} = C_{Mn}^{\alpha}$), interfacial excess is a constant value (blue line, **Figure 2.28** (b)). Increasing the composition difference on both sides of the interface increases the effect of dividing surface position on the excess value. However, to some extent, the influence of the dividing surface position is not very significant. For example, in the case of green profile ($C_{Mn}^{\alpha} = 1.8\ and\ C_{Mn}^{\alpha} = 2.2$), the excess value with the dividing surface position at the maximum of the peak ($x = 0$) of the concentration profile differs only by ±1,66% from the excess value with the dividing surface placed for ($x = \pm 1nm$) from the peak of the concentration profile, and ±3.32%, ±4.98% if the dividing surface placed for ($x = \pm 2nm$) and ($x = \pm 3nm$ from the peak respectively. This difference is even smaller in the case of the red profile ($C_{Mn}^{\alpha} = 1.9\ and\ C_{Mn}^{\alpha} = 2.1$) but of course more significant for the purple one ($C_{Mn}^{\alpha} = 1.5\ and\ C_{Mn}^{\alpha} = 2.5$).

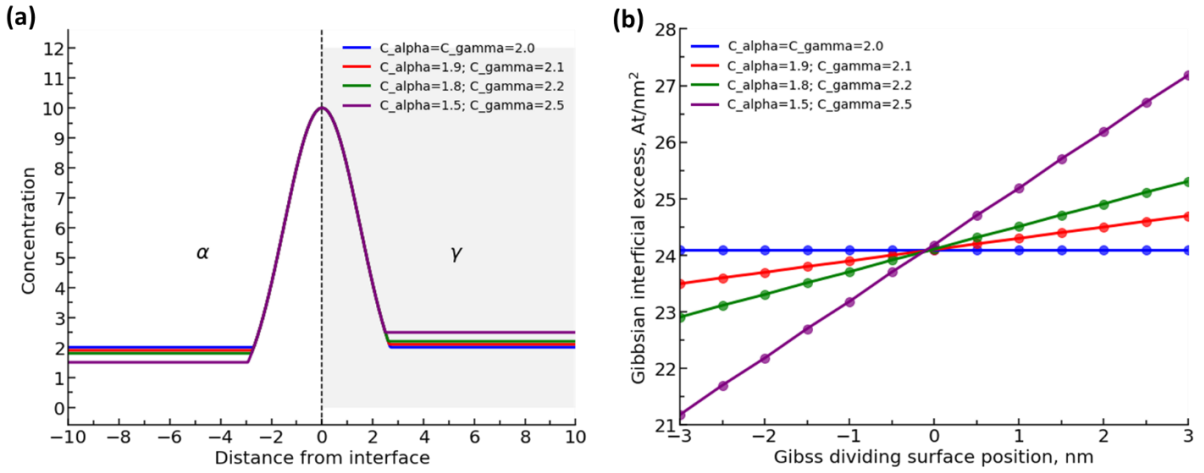

Figure 2.28. **(a)** *Model concentration profiles of segregating atoms across the interface;* **(b)** *Interfacial excess calculated depending on the dividing surface position relative to the concentration profile's peak.*

These calculations demonstrate that depending on the character of the composition profile, the Gibbs dividing surface position within a few nanometers can have a relatively limited effect on the excess value and is commensurated with measurement error. Therefore, further calculations of Gibbsian interfacial excess in this work are performed with the dividing surface placed at the peak of the composition profile. The excess values are represented with a deviation that corresponds to the dividing surface's displacement for ±1nm from the peak.

As an example, the results of Γ_{Mn} for the specimens are shown in **Figure 2.26** are presented in **Table 4**. This table contains information about the atomic fraction from both sides of the interface and the excess value of Mn atoms at the interface. These experimental results confirm that this method can be applied for most of the composition profiles obtained in this work.

Table 4. *Gibbsian interfacial excess calculated for the specimens shown in* ***Figure 2.26***

Tip#	X^{α}_{Mn}, *at%*	X^{γ}_{Mn}, *at%*	Γ_{Mn} ***(±1nm) atom/nm²***
625_5s_ch1_tip1_1st	2.02	1.94	**10.38±0.08**
625_5s_ch1_tip2_1st	2.00	1.77	**7.51±0.23**
625_5s_ch1_tip3_1st	2.07	1.67	**8.64±0.41**

Chapter 3

Experimental observation of the austenite/ferrite transformation interfaces

This chapter is dedicated to the investigation of the transformation interface by atom probe tomography (APT). To cover a large range of transformation mechanisms, various ferrite/austenite (ferrite/martensite at room temperature) interfaces for three transformation temperatures (720°C, 680°C, and 625°C) and different holding times have been studied. The measured composition profiles across the interfaces and their analysis are presented.

3.1 Austenite-to-ferrite phase transformation: material, transformation temperature, holding time

The results of the austenite/ferrite transformation interface investigation presented in this chapter were obtained for Fe-C-Mn ternary model alloy with a nominal composition of 0.17 wt%C and 2.0 wt%Mn (0.787 at%C and 2.0 at%Mn). In order to investigate the potential solute drag effect close to PE and LENP domains, three transformation temperatures for intercritical annealing treatments have been chosen: 720°C, 680°C, and 625°C. The isothermal section at those temperatures in the Fe-C-Mn phase diagrams is presented in **Figure 3.1** with a nominal composition shown as a red point (dash line is a zero-partitioning line). According to **Figure 3.1**, the experimental investigations were conducted in the temperature domain where, for the selected nominal composition, there may be competition between several regimes for austenite/ferrite transformation: (a) LENP or PE, (b) LENP/LEP or PE, (c) LEP or PE, and of course potentially Solute Drag.

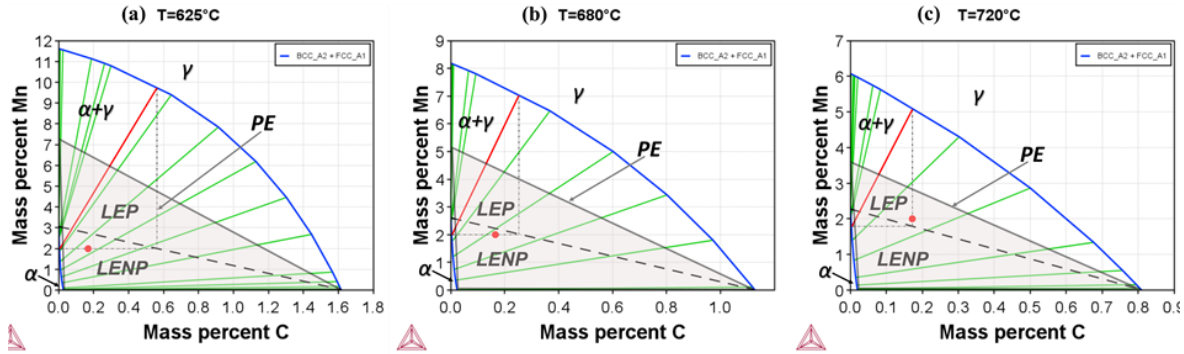

Figure 3.1. *The isothermal section at* ***(a)*** *625°C,* ***(b)*** *680°C,* ***(c)*** *720°C in the Fe-C-Mn phase diagrams. The nominal composition is given as a red point and located (a) below relatively to the zero-partitioning line, (b) slightly below, (c) slightly above.*

Depending on which regimes are operated during the phase transformation, different composition profiles are expected across the transformation interface. Under LEP conditions, the transformation kinetics is expected to be slow since it is controlled mainly by the diffusion of substitutional Mn atoms. A long-range diffusion profile of Mn atoms into austenite is expected under this condition. In the LENP mode, the partition of Mn is limited just at the interface in order to respect the local thermodynamic equilibrium conditions. This assumption leads to the existence of a "spike" of Mn at the interface. The growth kinetic in this regime is much faster than in LEP, as it is controled by C diffusion. PE mode assumes that substitutional Mn is completely immobile during the transformation. Therefore only carbon diffusion controls the phase transformation, and thus it is expected to be very fast. The solute drag (SD) effect reflects the tendency of solute atoms to segregate at the moving interface. It is assumed that the segregation of atoms consumes part of the phase transformation driving force, and thus will retard the motion of the austenite/ferrite transformation interface. If SD mechanism drives ferrite growth, the amount of accumulated Mn atoms at the interface is expected to evolve rapidly.

The kinetics are rather different for three transformation temperatures therefore, different holding times have been chosen for each temperature and presented in **Table 5**. The equilibrium state is considered to be achieved after 3 hours of treatment as no evolution of ferrite volume fraction was not observed after this time. As heat treatments were performed in the dilatometer, the first step of the experimental study consisted of dilatometry data curves processing and microstructure observation by optical microscope.

Table 5. *Intercritical temperatures and holding times investigated in this work.*

Transfromation temperature, T(°C) (intercritical temperature)	720	680	625
Holding time at intercretical temprature	3h	25s; 50s;100s; 600s; 3h	2s; 5s; 10s; 15s; 30s, 10min; 3h

3.2 Kinetics of ferrite growth: dilatometry and microstructure observation

The dilatometric curves were used to estimate the austenite-to-ferrite phase transformation kinetic (see 2.1). The global kinetics of ferrite growth derived from the dilatometry data was adjusted to fit the ferrite fraction at the end of the holding time according to the optical inspection of the microstructure. Therefore, the combination of both image analysis and dilatometry has been used to estimate the kinetics of ferrite growth for the transformation temperature.

The optical micrographs of the investigated samples at the different aged times for three investigated transformation temperatures (720°C, 680°C, and 625°C) are shown in **Figure 3.2**.

Here, only examples of the optical micrographs for the few holding times that help better demonstrate the ferrite growth kinetic depending on the chosen intercritical temperature are given. The formation and growth of a thin layer of ferrite at the austenite grain boundaries are observed in the presented optical micrographs, especially for the short holding times. It is clear that α nucleated predominantly at the prior austenite grain boundaries and grew into the austenite grains with an allotriomorph morphology. Using the image processing tools (ImageJ software), the ferrite fractions were estimated from the area fractions of the brighter phase. Averaged values are specified next to each example shown in **Figure 3.2**.

In the case of transformation at 720°C, the kinetics of ferrite growth is very slow. According to image analysis, after 3 h (10800 s) of heat treatment, the ferrite fraction reaches about ~2.2% compared to ~25% and ~33% at 680°C and 625°C, respectively. Due to the difficulties in locating ferrite for shorter holding times, investigations of the transformation interfaces will only be conducted for 3 hours holding at 720°C. In the case of 680°C and 625°C, the phase transformation is significantly faster. Therefore, it was decided to perform intermediate heat treatments with selected shorter holding times for these two transformation temperatures (see **Table 5**). It allowed measuring the ferrite growth kinetic by the image analysis. The graphs in **Figure 3.3** summarise the results of ferrite growth kinetics measured by combining both image analysis and dilatometry. Dilatometry data normalized to the ferrite phase fraction obtained from image analysis after a holding time of 3h.

The observed volume fraction evolution allows estimating the average velocity of the interface migration during the phase transformation at the investigated temperature. The result of interface velocity calculation from the dilatometry data will be presented in the next chapter when used as one of the input parameters for the theoretical prediction of Mn composition profiles across the transformation interfaces. The next experimental results will now focus on the investigation of the austenite/ferrite transformation interface by atom probe tomography (APT).

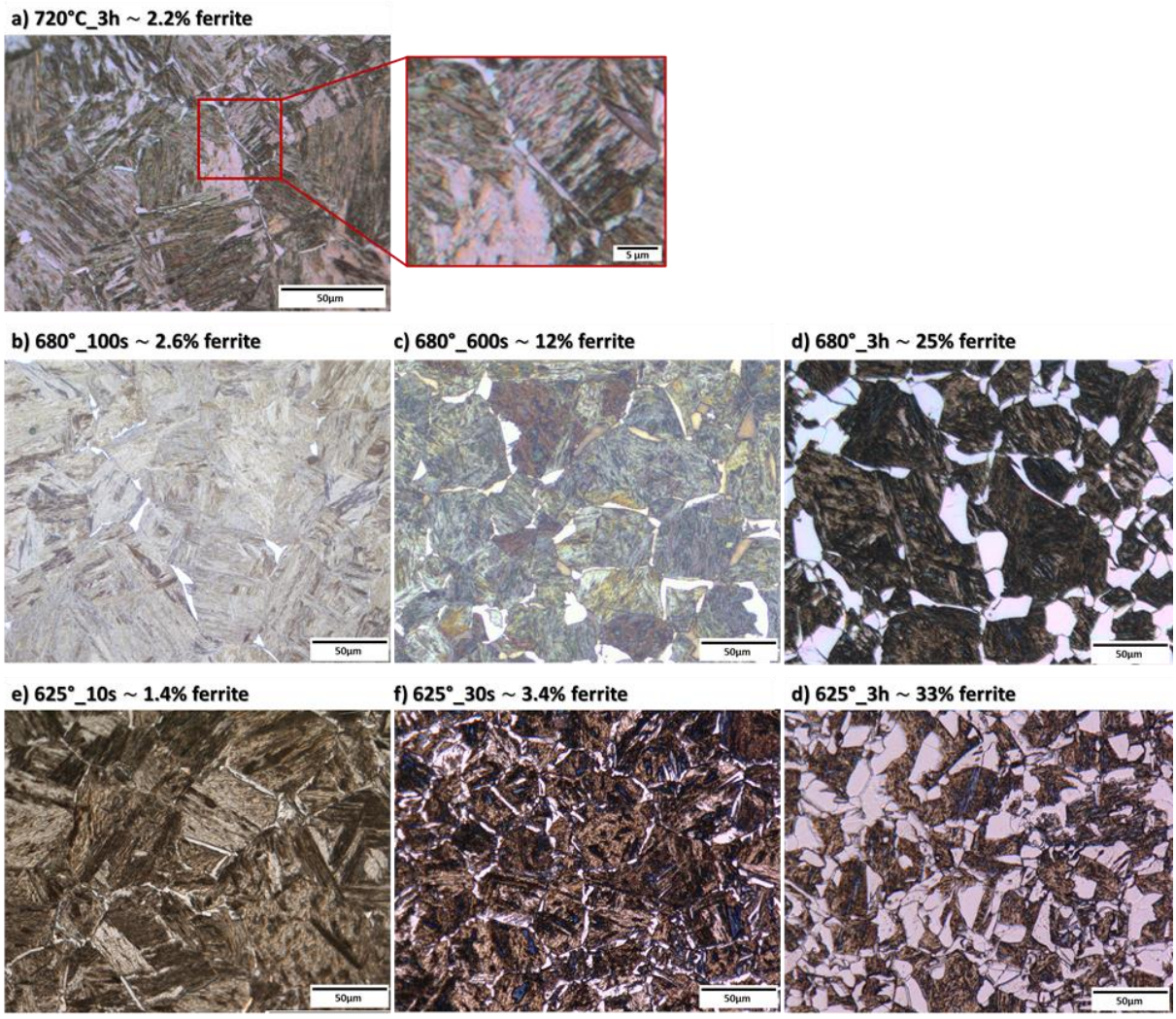

Figure 3.2. *Optical micrographs examples of observed microstructures in Fe-0.17wt%C-2wt%Mn alloy obtained after the intercritical annealing:* ***(a)*** *at 720°C during 3 h;* ***(b), (c)*** *and* ***(d)*** *at 680°C during 100 s, 600 s, and 3h respectively;* ***(e), (f), (d)*** *at 625°C during 10 s, 30 s, and 3 h respectively. The bright regions correspond to ferrite, while the dark contrast to martensite (former austenite).*

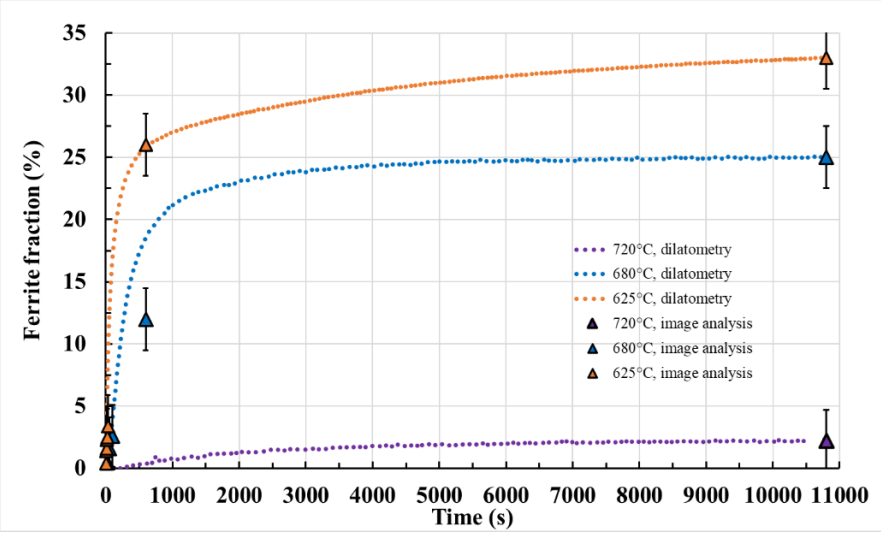

Figure 3.3. *Comparison of the ferrite growth kinetics measured combining image analysis and dilatometry at: 720°C (purple color), 680 °C (blue color), and 625 °C (orange).*

3.3 Experimental observation of γ/αtransformation interface by APT

Selected ferrite/austenite interfaces (ferrite/martensite at RT) have been chosen for further chemical analysis at the atomic scale by atom probe tomography (APT). As previously explained, the evolution of the solute profiles at the transformation interface with time for the different transformation temperatures is the main point of interest. First of all, the very short and the longest times are interesting since the profiles at the earliest stage of transformation and at the end can be compared. In addition, the analysis at the intermediate stages of transformation can help to see the evolution of solute profiles. However, there is an issue with very short holding times, especially at higher transformation temperatures, when the kinetics of ferrite formation is very slow. Indeed, due to the low amount of ferrite fraction, it can be challenging to localized and analyse the transformation interfaces. Another issue is related to very fast kinetics at lower transformation temperatures since the ferrite grain size can be too large for the modified lift-out process applied in this study (more details in (2.5.4)). Besides, APT investigation of the transformation interface requires a time-consuming site-specific specimen preparation procedure. Therefore, taking into account the previous remarks, only several holding times from **Table 5** for each transformation temperature were selected for APT analysis:

- *720°C – 3h (only one available);*
- *680°C – 100s, 600s, and 3h;*
- *625°C – 5s, 15s, 30s, and 3h.*

Following the experimental procedure described in Chapter 2, the samples were first investigated by electron back-scattered diffraction (EBSD). Subsequent post EBSD data treatment using Megengue2 software provided the initial ferrite/austenite interfaces location and orientation relationships. Then, the region of interest was extracted and prepared by Focused Ion Beam (FIB) for APT analysis in order to access to the composition profiles across the interfaces.

At this point, it is worth adding a few words about selecting the region of interest for the APT analysis. One of the important interface characteristics considered in this work is the orientation relationship between the formed ferrite and parent austenite at the investigated interface. Also, attention was paid to the width of ferrite grain, which could vary significantly within the same sample. Of course, partly, it can be the result of a 2D view (2D sectioning of a plate may increase its apparent width), but to a greater extent, it can reflect the different nucleation times of different grains, which is becoming more noticeable for a longer transformation time (the oldest ferrite grain will be larger). We will be facing the problem of the actual growing time for each considered grain over and over within this work, especially for the longer holding times. Nor can it be ruled out that due to various local variations in structure or

chemical composition (i.e. banding), the mode of ferrite growth can vary in the different parts of the sample, even for the same holding condition.

The initial idea was to analyze by APT the interfaces with different misorientations along the ferrite grain of various widths (as we do not know the nucleation time) for each selected transformation temperature and holding times. However, after the primary EBSD investigations, ferrite grains with significantly different morphologies (the shapes of the α' (γ)/α interfaces) were observed to form for the same transformation condition. Examples of formed ferrite grains after isothermal holding at 720° for 3h are shown in **Figure 3.4**. In general, the straight, smoothly curved, and wave-like morphology of the interface can be distinguished.

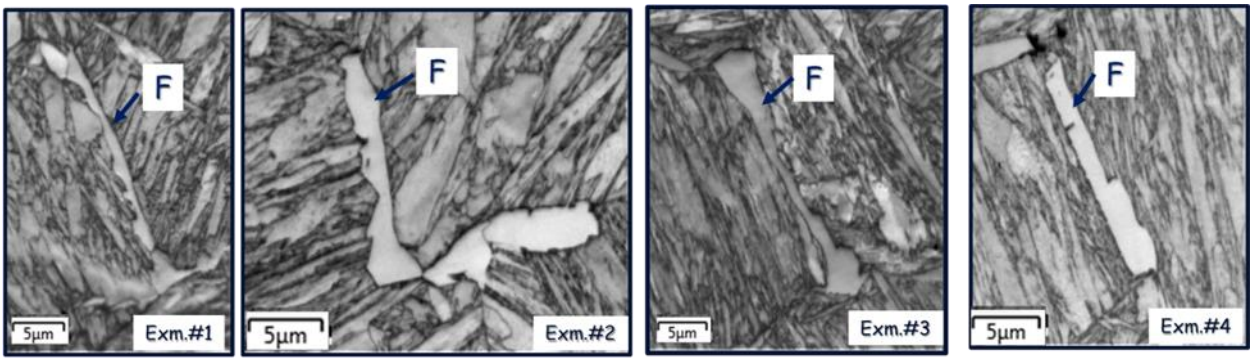

Figure 3.4. *Examples of the various interface morphologies within the same sample (isothermal holding at 720° during 3h).*

Taking into account the various interface morphology, it is hard and time-consuming to investigate all observed configurations. Nevertheless, an attempt to analyze several different configurations for each chosen condition has been made. A large number of the APT results obtained for different conditions are presented in the following paragraphs. Therefore first, some guidelines and remarks are provided first to better understand some notations.

3.4 Details of APT data representation

In this section, only the image quality (IQ) maps (rather than electron micrograph) obtained from EBSD measurement are used to illustrate the configuration of the selected regions of investigated allotriomorph ferrite. The example is illustrated in **Figure 3.5**. The IQ map is always presented with the determined deviations from predefined ORs at the initial interfaces between the ferrite and parent austenite at the considered transformation interface. These deviations are expressed as the orientation difference with respect to the KS orientation relationships and coded with a color gradient.

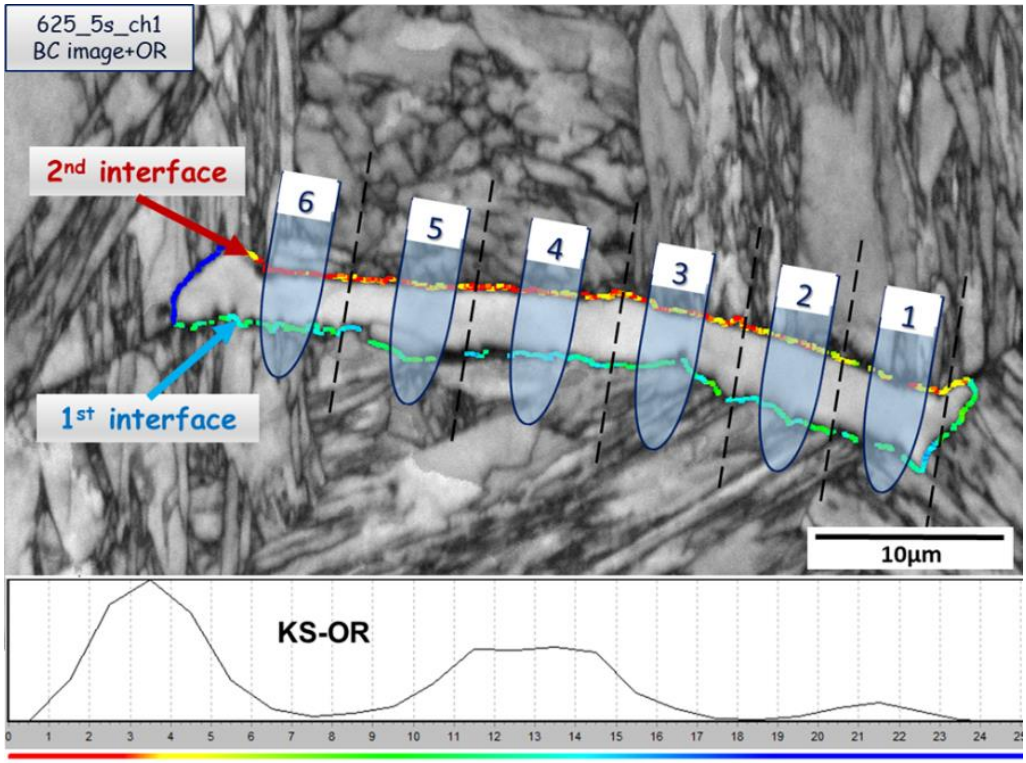

Figure 3.5. *The example of the image quality (IQ) map of the selected allotriomorph ferrite formed at the prior austenite grain boundary after isothermal holding at 625°C during 5s. This region is referred as* ***625_5s_ch1*** *for temperature, holding time, and extracted specimen (chunk). Colors on the two α'(γ)/α interfaces (named as1st and 2nd) represent the determined deviations from predefined ORs between ferrite and former austenite at 625 °C. It is expressed as the orientation difference with respect to KS orientation from 0 (red) to 24° (blue). The position of schematic APT tips approximately corresponds to the locations of APT specimens along the selected ferrite–austenite interface (only successful APT runs are shown).*

Since we do not know if only one or both interfaces from two sides of ferrite are transformation interfaces, the goal is to analyze both by APT to get as much information related to composition profiles as possible. Therefore lift-outs were performed in such a way that APT tips contain both interfaces. The position of the schematic APT tips in **Figure 3.5** approximately corresponds to the locations of APT specimens along the selected ferrite grain. The interfaces on each side of the investigated ferrite grain are named as the 1st interface and 2nd interface, only related to the order of APT analyses, which is defined by the lift-out. It means that a chunk of materials containing two interfaces was extracted from the bulk and mounted on the pre-tips in the way that the first APT run will be performed with the 1st interface located at the apex of the APT specimen. Then after analysing the 1st interfaces by APT data acquisitions, the run is stopped, and the APT tip is reshaped to locate the 2nd interface at the tip apex for the second APT run (see more details 2.5.5). However, the APT analysis of interfaces is challenging and tricky since the specimen can fracture at any stage of the APT acquisition, so not all APT runs were successful. The tips only of the successful APT measurements instead of all prepared will be illustrated schematically in IQ maps in the following paragraphs.

Usually, several ferrite grains were extracted and investigated for each chosen heat treatment condition. Each examined ROI refers to the lift-out of a chunk. Therefore, the code was assigned to each extracted chunk for the data organization and condition notation. As an example, the chunk in **Figure 3.5** has a code: ***625_5s_ch1***, which means that it is related to the sample isothermally held at 625°C during 5s, and ***ch1*** – chunk1, is just the number of the selected and extracted regions. The code: ***625_5s_ch1_tip1_1st*** is related to the APT analysis of the 1st interface of tip1 of chunk1.

The results of the APT analyses are presented by the appropriate reconstructed APT volume represented as three-dimensional (3D) atom maps of the C and Mn and by one-dimensional composition profiles normal to the interfaces generated from the collected APT data. In this work, we will focus mainly on the interpretation of Mn segregation since the origin of C segregation is questionable due to its high diffusivity even at room temperature. Therefore, it is impossible to compare the C composition profiles measured at room temperature (RT) with the theoretically predicted at austenite/ferrite transformation temperature (i.e. close to 600 – 700°C). Nevertheless, all experimentally measured C concentration profiles within these studies have some common features. One of such features is the low carbon content solubility in ferrite. Therefore, the C composition changes from carbon-rich martensite (prior austenite) to carbon-poor ferrite is one of the main criteria for the α'(γ)/α interface identification. In some cases, as will be discussed later, the C composition profiles can bring some additional information in the framework of discussion. Hence, the 3D reconstruction and composition profile for C atoms are shown for each result, but the quantitative evaluation of segregation is performed only for Mn atoms.

3.5 Austenite/ferrite interface at 625°C

The first group of results presented is related to the austenite/ferrite transformation interface investigation by APT at the transformation temperature of 625°C. The alloy considered in this study (Fe-0.17wt%C-2.0wt%Mn) is located below the zero partition line on the isothermal section of the Fe-C-Mn phase diagram at this temperature (see **Figure 3.1** (a)). Therefore the competition between LENP and PE or possibly SD modes for ferrite growth is expected. Considering the kinetics of ferrite growth at this temperature (see **Figure 3.3**), isothermal holdings at 625°C during 5s, 15s, 30s, and 3h have been chosen for the analysis by APT.

3.5.1 Austenite/ferrite interface after 5s at 625°C

IQ map of the region with a thin allotriomorph ferrite formed after isothermal holding at 625°C during 5s with the measured misorientation from predefined KS-ORs is shown in **Figure 3.6**. The ORs at the interface noted as the 1st are within the misorientation of 10-15° with respect to KS-OR, and the 2nd one has a near KS-OR. The 2nd interface has a smoothly curved morphology, while the 1st one has a more wave-like shape. The length and width of the examined ferrite in 2D are 40 µm and around 3 µm, respectively. The results of APT measurements (3D reconstruction of the analyzed volumes for the C and Mn atoms with the corresponding concentration profiles) for the 1st interface of tips 1-4, 6 are shown in **Figure 3.7**.

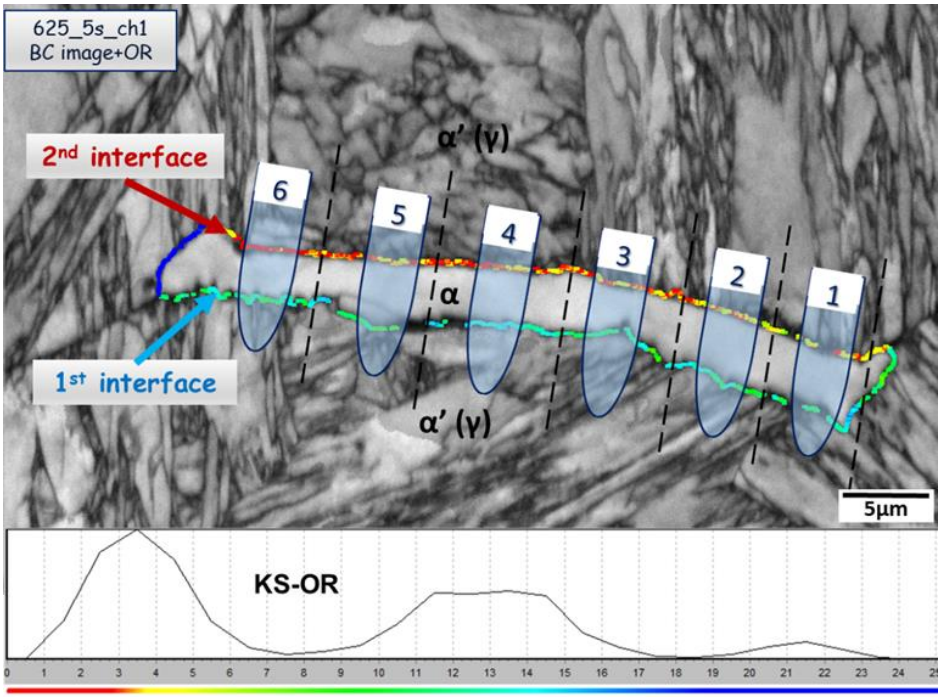

Figure 3.6. *IQ maps of the selected region with an allotriomorph ferrite formed at the prior austenite grain boundary after isothermal holding at 625°C during 5s. Colors at α' (γ)/α interfaces represent the orientation relation between ferrite and former austenite at 625°C, expressed as the orientation difference with respect to KS-OR.*

(a) ***625_5s_ch1_tip1_1st***

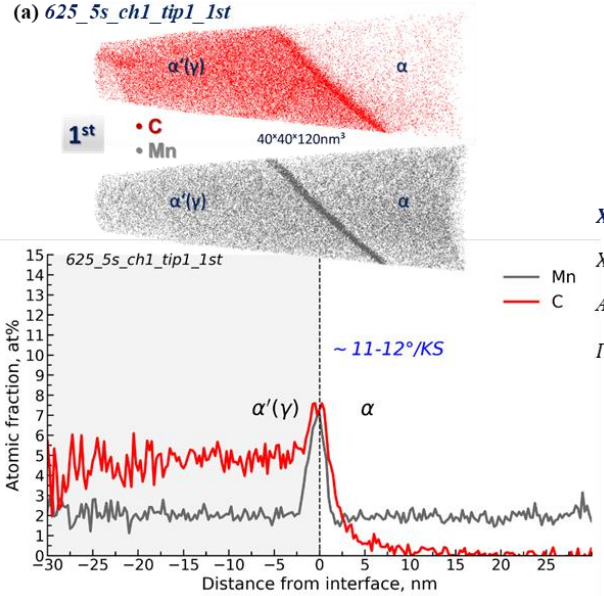

X_{Mn}^{max}=7.1 at%;

X_{Mn}^{γ}=2.0 at%; X_{Mn}^{α}=1.9 at%;

Approximate width ~ 4 nm

$\Gamma_{Mn}(\pm 1nm) = 10.4 \pm 0.1 \frac{atom}{nm^2}$.

(b) ***625_5s_ch1_tip2_1st***

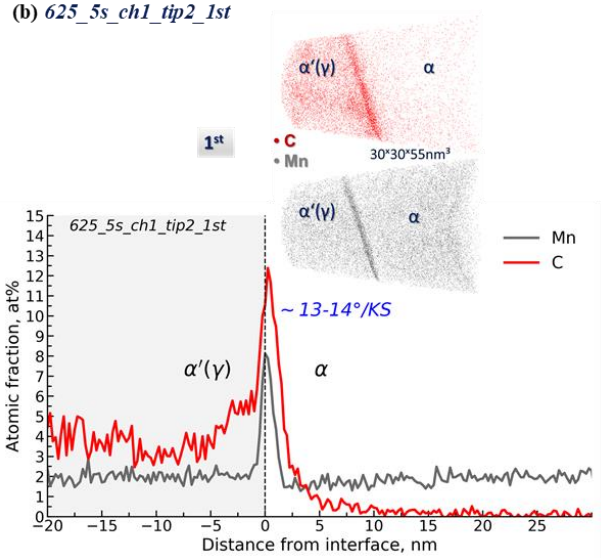

X_{Mn}^{max}=8.1 at%;

X_{Mn}^{γ}=2.0 at%; X_{Mn}^{α}=1.8 at%;

Approximate width ~ 3 nm

$\Gamma_{Mn}(\pm 1nm) = 7.5 \pm 0.2 \frac{atom}{nm^2}$.

(c) ***625_5s_ch1_tip3_1st***

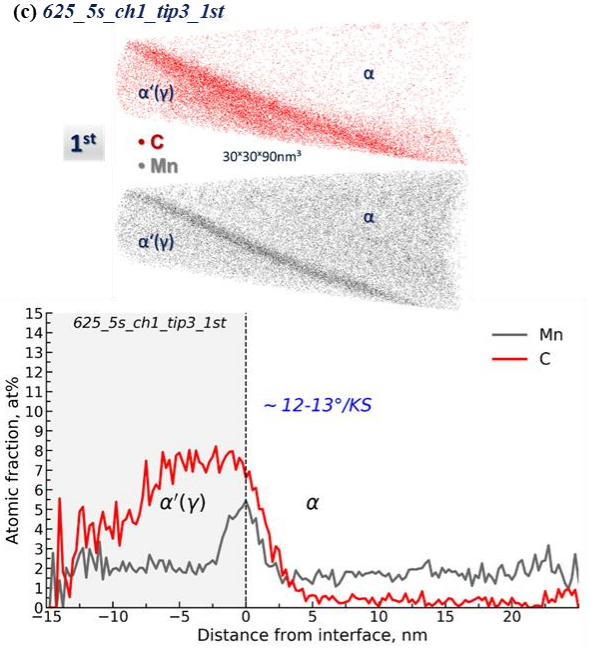

X_{Mn}^{max}=5.4 at%;

X_{Mn}^{γ}=2.1 at%; X_{Mn}^{α}=1.7 at%;

Approximate width ~ 5 nm

$\Gamma_{Mn}(\pm 1nm) = 8.6 \pm 0.4 \frac{atom}{nm^2}$.

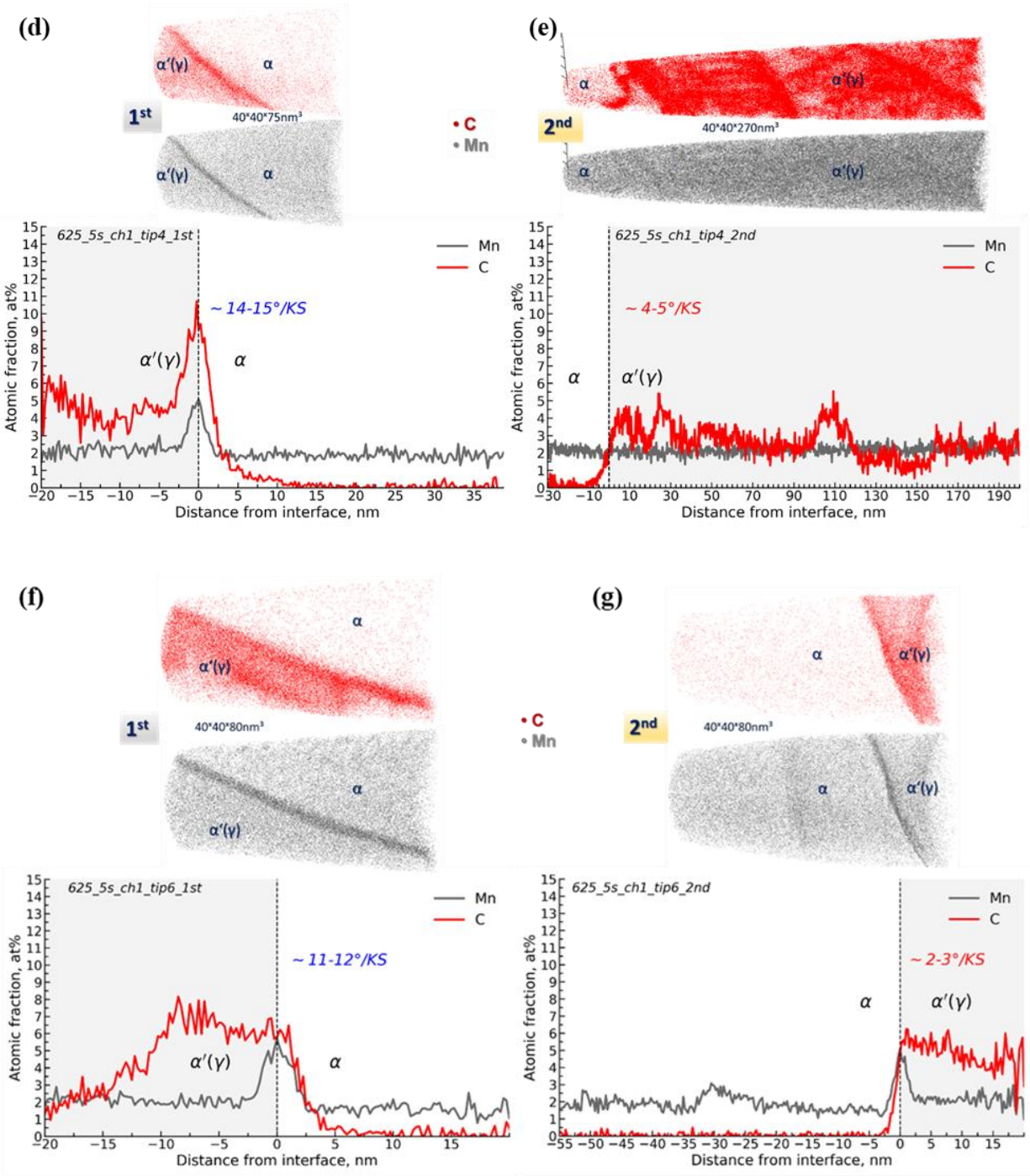

Figure 3.7. *3D reconstructions and concentration profiles of C and Mn atoms across the 1st and 2nd interfaces of 625_5s_ch1:* ***(a)*** *tip1_1st;* ***(b)*** *tip2_1st;* ***(c)*** *tip3_1st;* ***(d)*** *tip4_1st;* ***(f)*** *tip6_1st,* ***(e)*** *tip4_2nd* ***(g)*** *tip6_2nd (see* **Figure 3.6***).*

The APT data show similar behavior of Mn atoms for all measured composition profiles across the 1st interface (**Figure 3.7** (a-d, f)) with the segregation of both elements at the interface. The Mn peaks obtained for tip1 and tip2 (**Figure 3.7** (a) and (b)) are higher with rather sharp shapes, compared to **Figure 3.7** (c) and (f). Such dissimilarity can be related to the different spatial resolutions during the measurements caused by the different orientations of the interface with respect to the APT analysis axis. These measurements are a nice example of the discussed

problem in (2.7) connected to the fact that the peak concentration can not be chosen as an experimental measurement of interfacial segregation. Therefore, it is necessary to calculate the excess solute at the interface (Γ_{Mn}, see details in 2.7.1-2.7.3). **Table 6** summarizes the main parameters of observed profiles. The observed peaks represent the Mn accumulation at the interface during its propagation. In addition, the lower Mn content in the ferrite side and higher in martensite (prior austenite) may be noticed. However, the situation is not trivial for the interpretation in **Figure 3.7** (e) and (g) of two results obtained for the 2nd interface and will be considered in the discussion part.

Table 6. *The main parameters of observed profiles in the case of* ***625_5s_ch1***

Condition	tip#	KS-OR	X^{α}_{Mn}, $at\%$	X^{γ}_{Mn}, $at\%$	Approximate width, nm	Max, at%	Γ_{Mn} $(\pm 1nm)$, $atom/nm^2$
T=625°C t=5s	Chunk1						
	tip1_1st	11-12	1.9	2.0	4	7.1	**10.4±0.1**
	tip2_1st	13-14	1.8	2.0	3	8.1	**7.5±0.2**
	tip3_1st	12-13	1.7	2.1	5	5.4	**8.6±0.4**
	tip4_1st	14-15	1.9	2.2	4	5.1	**7.2±0.4**
	tip6_1st	11-12	1.6	2.1	5	5.7	**8.8±0.4**
	tip4_2nd	4-5	2.1	2.1	No Mn segregation on 2nd interface		
	tip6_2nd	2-3	1.5	2.1	5	5.1	**6.7±0.6**

Another investigated ferrite grain for the same sample (5s at 625°C) is shown in **Figure 3.8**. The ORs at both interfaces have the orientation difference with respect to KS in the range of 1-9°. The ferrite grain length and width are around 21 µm and 2.2 µm, respectively. In this case, the APT analysis was successful only for tip1 (see the result in **Figure 3.8** (b-c)), and Mn segregation was not observed either at the 1st or 2nd interfaces.

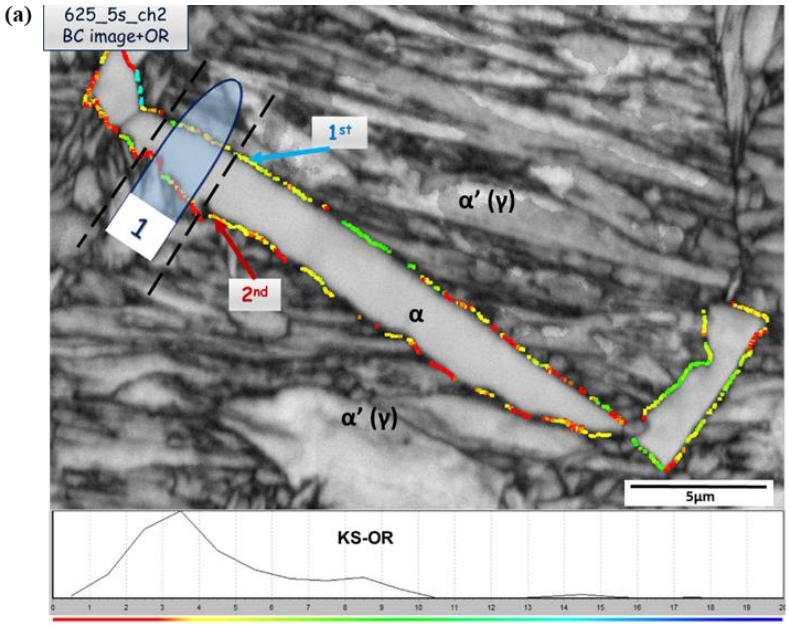

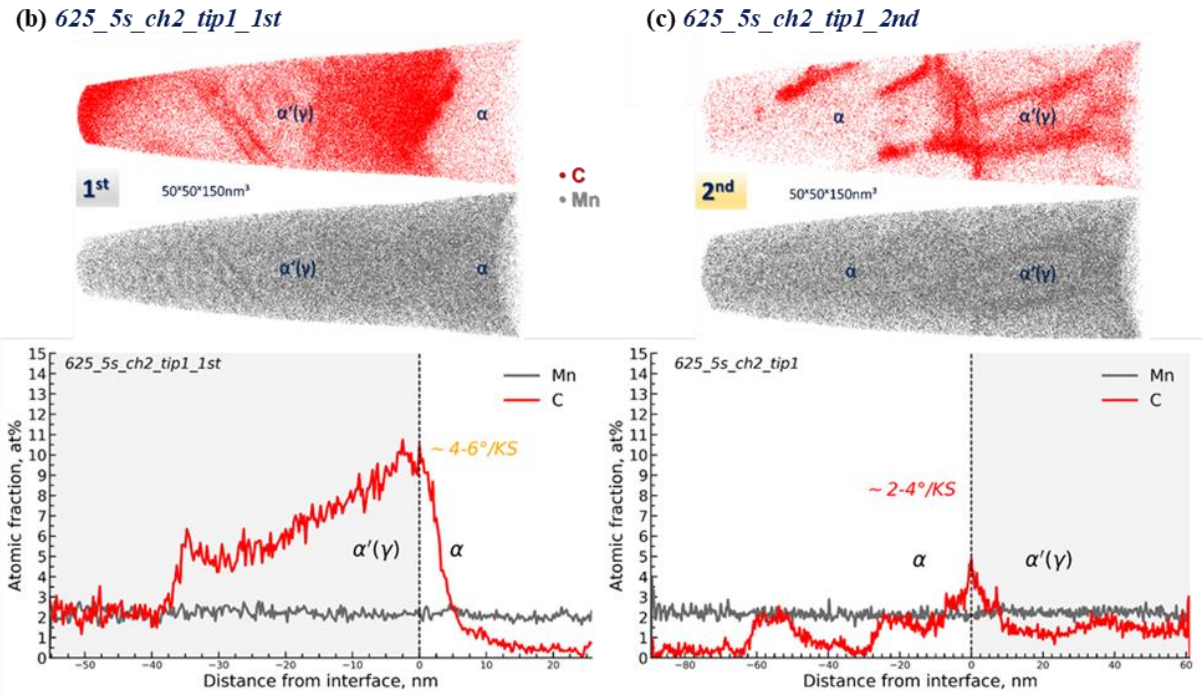

Figure 3.8. (a) *IQ map of the selected region with the allotriomorph ferrite formed after isothermal holding at 625°C during 5s (**625_5s_ch2**). Colors represent the orientation difference with respect to KS-OR of the initial ferrite–austenite orientation relationships at 625 °C. 3D reconstructions and concentration profiles of C and Mn atoms across the* **(b)** *1st and* **(c)** *2nd interface of tip1.*

3.5.2 Austenite/ferrite interface after 15s at 625°C

In the case of isothermal holding during 15s at 625°C, the APT studies of austenite/ferrite interfaces are presented for several investigated regions with thin ferrite grains. The IQ map with the measured ORs of one of such selected regions is given in **Figure 3.9**. Regarding the orientation of the shown interfaces, the 2nd has a near KS orientation relationship, while the first has a large misorientation (in the range of 19-25°) with respect to KS-OR. The interfaces from both sides of the analyzed part of the ferrite grain (the position of the schematically illustrated APT tips from tip4 to tip10) have relatively straight morphology. The ferrite width varies smoothly from 2.4 µm (left) to 3.8 µm (right). 3D reconstructions of the analyzed volumes for C and Mn with the corresponding composition profiles for the 1st interface of tips 4, 5, 10, and for the 2nd interface of tips 4, 10 are shown in **Figure 3.10**, and the main values related to the measured profiles are given in **Table 7**.

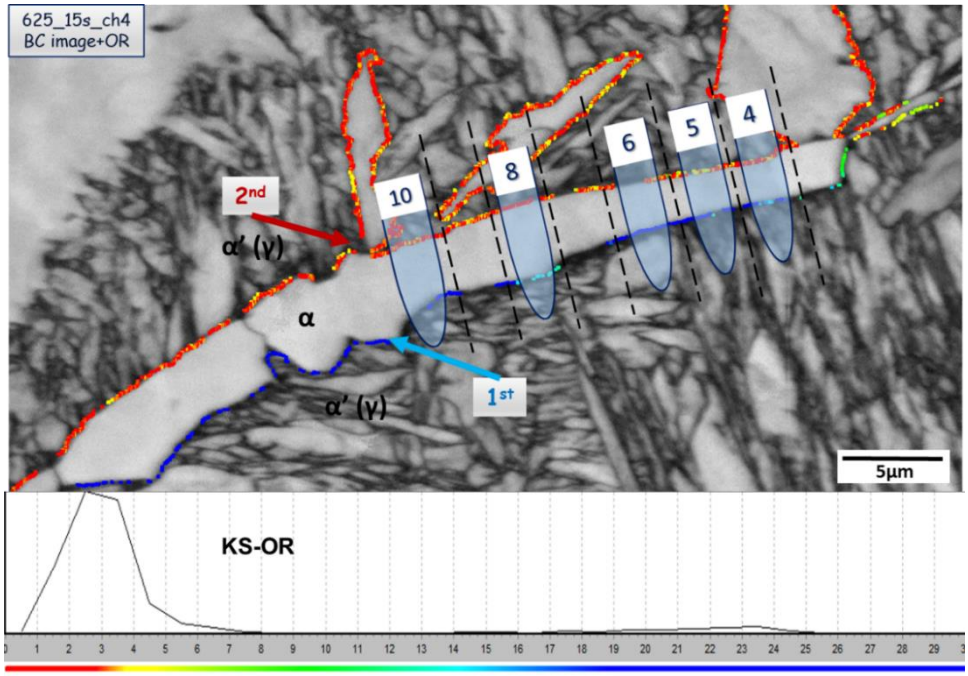

Figure 3.9. *IQ map of the selected region with the allotriomorph ferrite formed after isothermal holding at 625°C during 15s. This region is coded as* ***625_15s_ch4****. Colors at two α' (γ)/α interfaces (1st and 2nd) represent the orientation relation between ferrite and former austenite at 625°C. It is expressed as the orientation difference with respect to KS orientation from 0 (red) to 25° (blue).*

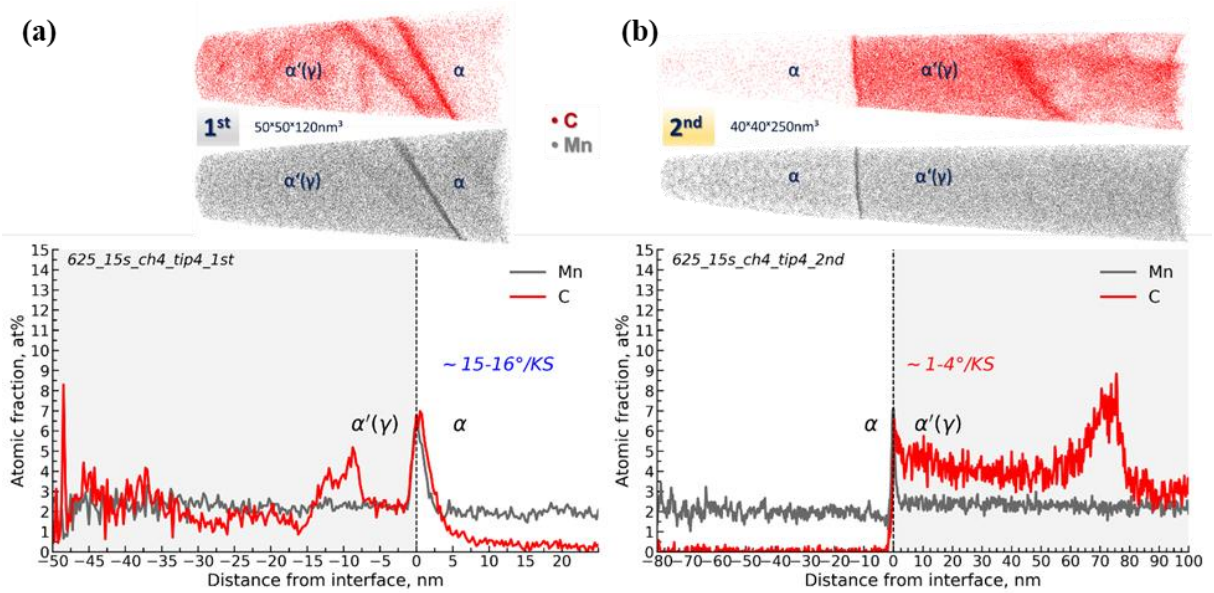

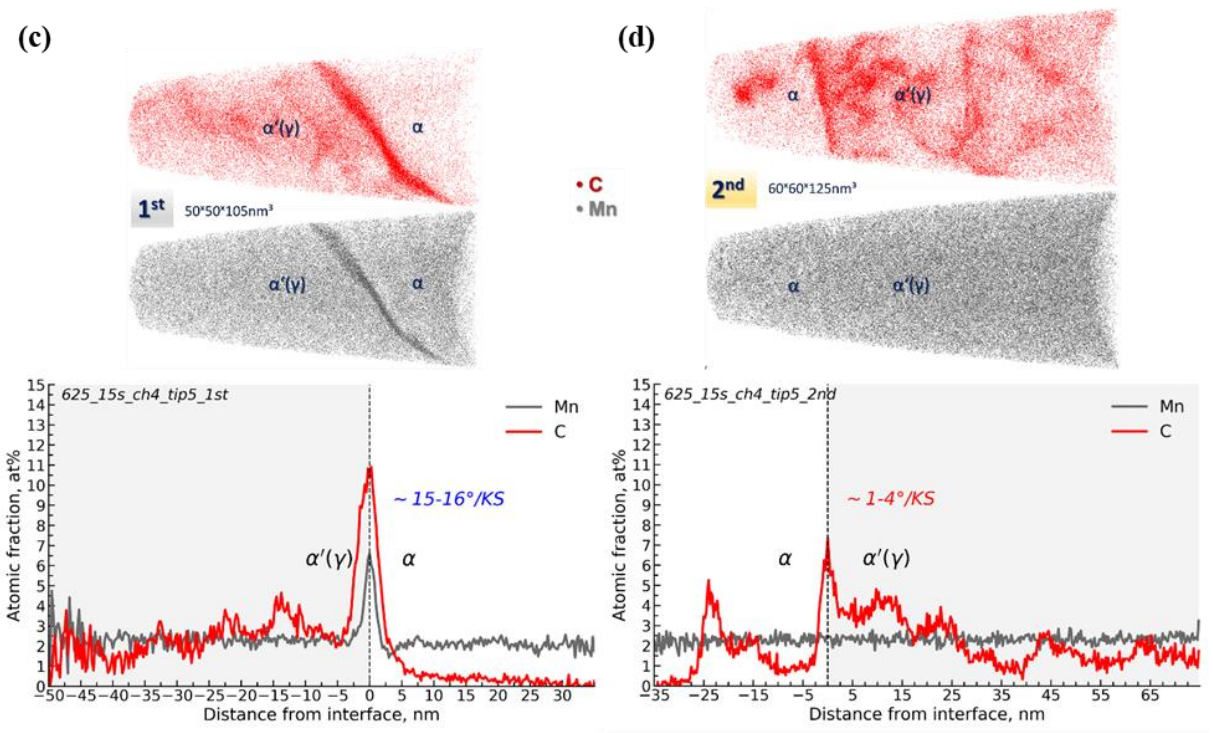
(c)
α'(γ)
α
1st
50*50*105nm³
α'(γ)
α
625_15s_ch4_tip5_1st
Mn
C
~ 15-16°/KS
α'(γ)
α
Atomic fraction, at%
Distance from interface, nm
(d)
• C
• Mn
α
α'(γ)
2nd
60*60*125nm³
α
α'(γ)
625_15s_ch4_tip5_2nd
Mn
C
~ 1-4°/KS
α
α'(γ)
Atomic fraction, at%
Distance from interface, nm

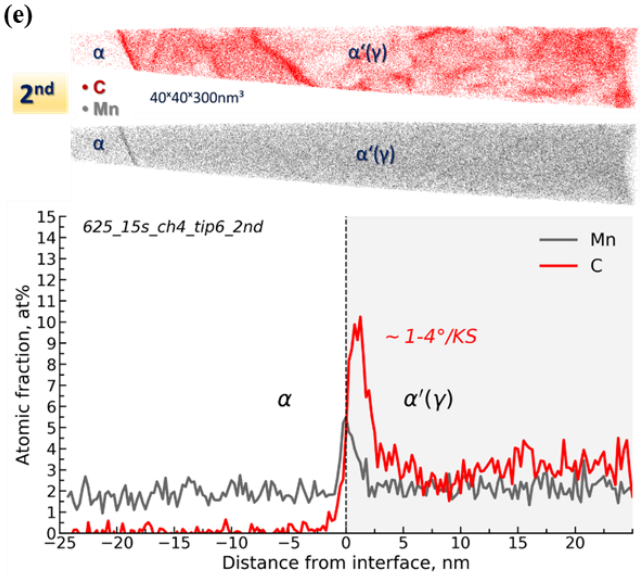
(e)
α
α'(γ)
2nd
• C
• Mn
40*40*300nm³
α
α'(γ)
625_15s_ch4_tip6_2nd
Mn
C
~ 1-4°/KS
α
α'(γ)
Atomic fraction, at%
Distance from interface, nm

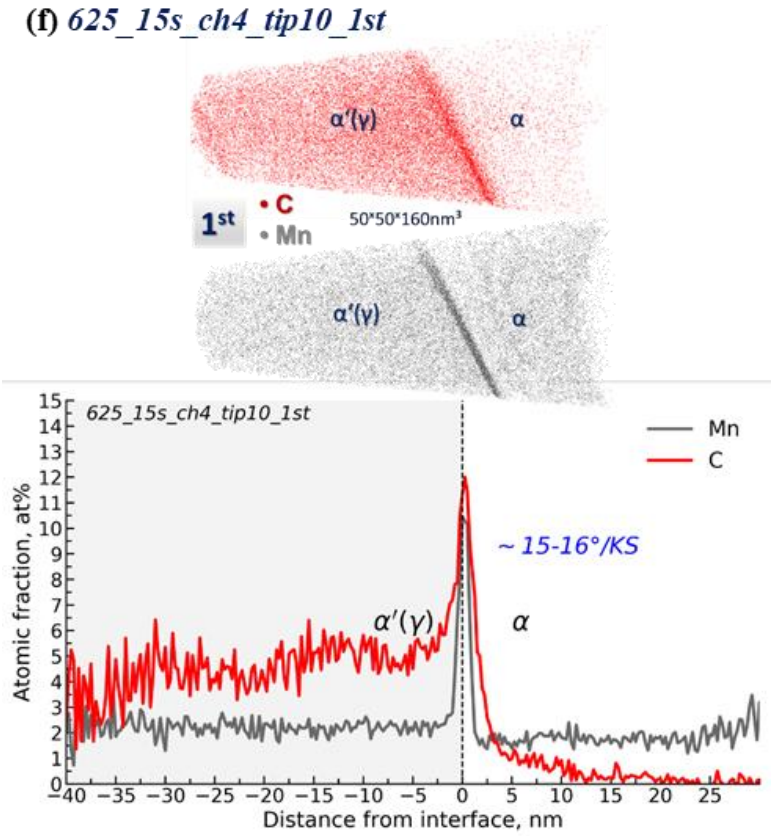

Figure 3.10. *3D reconstructions and concentration profiles of C and Mn atoms across the α' (γ)/α interfaces depicted in* **Figure 3.9** *that has a code:* ***625_15s_ch4*** *(isothermal holding at 625°C during 15s).* ***(a),(c), (f)*** *– results correspond to tip4,tip5, tip10 of the 1st interface investigation and* ***(b), (d)*** *– tip4, tip6 of 2nd interface investigation.*

Table 7. *The main parameters of observed profiles in the case of* ***625_15s_ch4***

Condition	tip#	KS-OR	X^{α}_{Mn}, at%	X^{γ}_{Mn}, at%	Approximate width, nm	Max, at%	Γ_{Mn} (±1nm), atom/nm²
T=625°C t=5s	Chunk1						
	tip1_1st	11-12	1.9	2.0	4	7.1	**10.4±0.1**
	tip2_1st	13-14	1.8	2.0	3	8.1	**7.5±0.2**
	tip3_1st	12-13	1.7	2.1	5	5.4	**8.6±0.4**
	tip4_1st	14-15	1.9	2.2	4	5.1	**7.2±0.4**
	tip6_1st	11-12	1.6	2.1	5	5.7	**8.8±0.4**
	tip4_2nd	4-5	2.1	2.1	No Mn segregation on 2nd interface		
	tip6_2nd	2-3	1.5	2.1	5	5.1	**6.7±0.6**

3D reconstructions and composition profiles show both C and Mn segregation at interfaces in each presented result in **Figure 3.10** except for **Figure 3.10** (d). The composition profiles with the observed peaks of Mn exhibited relatively similar features on both sides of ferrite grain, but with a slightly higher amount of Mn accumulation at the 1st α/γ interface compared to the 2nd (see the maximum value and solute excess of Mn in **Table 7**). The average Mn composition in martensite (prior austenite) is obviously higher than in the ferrite, and all the

measured composition profiles have a similar peak width in the range of 3-5 nm. Of course, it is necessary to keep in mind that the width of the peaks depends on the interface orientation. The particular case without Mn segregation at the interface (**Figure 3.10** (d)) will be discussed later (together with the previously observed similar situation in **Figure 3.7** (e)).

The observed results in **Figure 3.10** with the Mn segregation for the 15s are very close to the results shown in **Figure 3.7** for the 5s. There is no evident evolution of the Mn profile between 5 s and 15 s of holding in these two cases. However, there is no direct evidence that this specific ferrite grain started growing time in **Figure 3.9** corresponds to the 15s of holding time. As there is no information about the nucleation time for each individual grain, the only information is that its actual 'age' (growing time) is between 0 and 15s.

The presented ferrite grain in **Figure 3.11** (a) has very similar features as the previous considered one. Both α'(γ)/α interfaces have relatively straight morphologies with the near KS-ORs at the 2nd interface and 20-25° misorientation at the 1st interface. However, for the same transformation time (15s), the width of ferrite, in this case, is about 1.5 µm (compared to the 3.8-2.4 µm of *625_15s_ch4* regions). Of course, it can be argued that is the dimension as seen in 2D (and therefore potentially biased by the preparation). Nevertheless, the composition profile across the 1st interface of tip5 (see **Figure 3.11** (b)) exhibits very similar features to the composition profiles across the 1st interface of chunk 4 (see **Figure 3.10**), with almost the same amount of the accumulated Mn atoms (X_{Mn}^{max}=7.0 at%; $\Gamma_{Mn} \sim 8.6\,\mathrm{atom}/nm^2$).

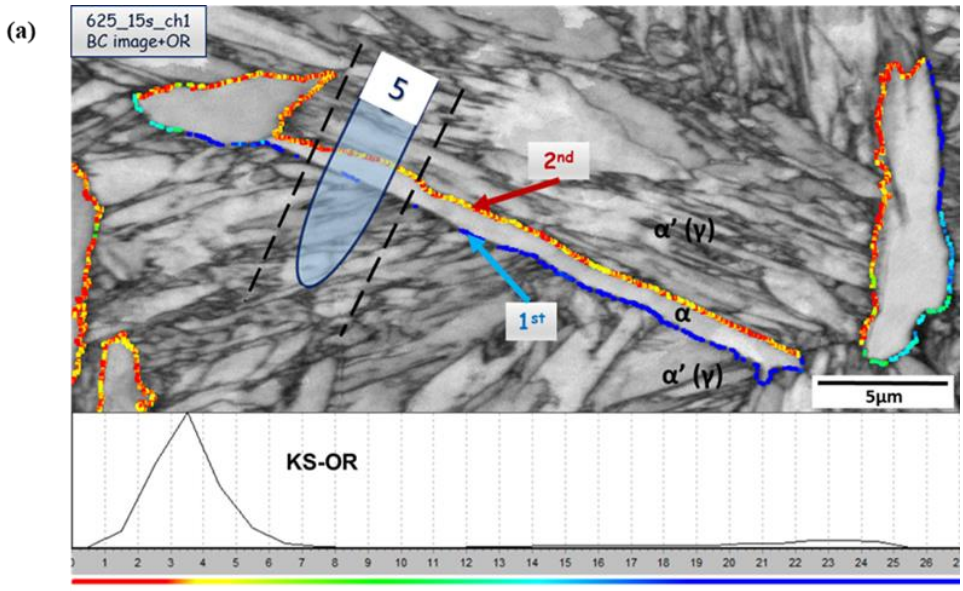

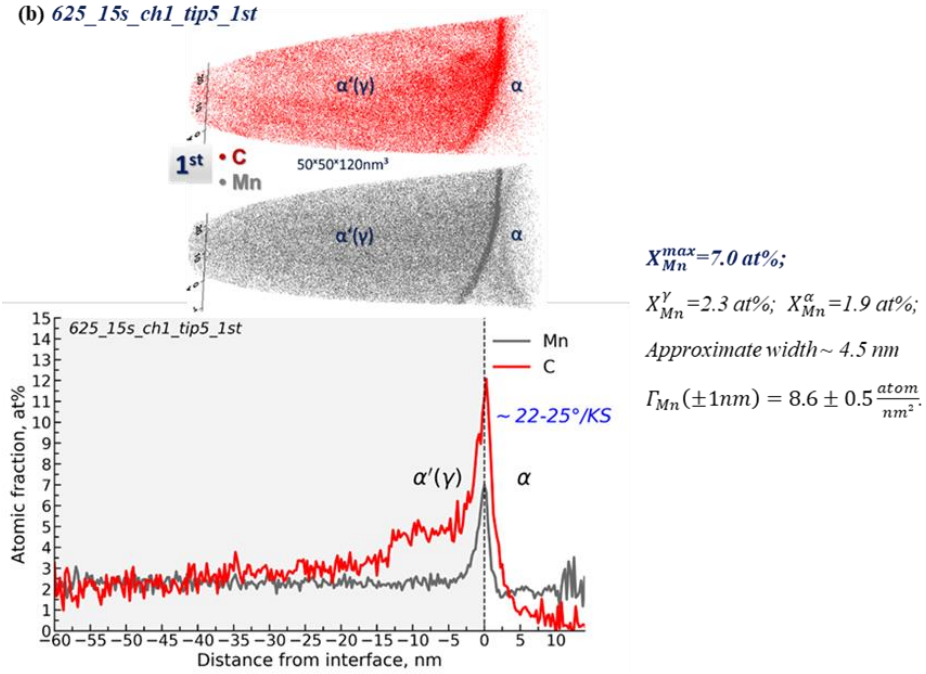

Figure 3.11. (a) *IQ map of the selected region with the allotriomorph ferrite formed after isothermal holding at 625°C during 15s (**625_15s_ch1**). Colors represent the orientation difference with respect to KS-OR of the initial ferrite–austenite orientation relationships at 625 °C.* ***(b)*** *3D reconstructions and concentration profiles of C and Mn atoms across the 1st interface of tip5.*

Another interesting observation can be noticed in the case of the next selected ferrite grain (see the IQ map and the measured ORs in **Figure 3.12**). The observed ferrite has a particular shape with the specific ORs redistribution at the two α'(γ)/α interfaces. It has a thin part of 'V' shape with the KS-ORs on both sites (right-top in **Figure 3.12**) and a thicker part with non-KS orientation (left-bottom in **Figure 3.12**). 3D reconstructions and concentration profiles across the 2nd interface for tip3 and tip5 are presented in **Figure 3.12**. The positions of tip3 and tip5 in **Figure 3.12** correspond to the initial locations of APT specimens along the selected ferrite–austenite interface. We can see that tip3 is located in the very thin ferrite part (width ~0.8 μm) of the 'V' shape with the KS-ORs on both sites, while the tip5 at the 2nd interface has the orientation difference with respect to KS orientation in the range of 11-15° (the width ~1.6 μm). Despite such differences in width and ORs, which most likely reflect different interface mobilities at different parts of the considered ferrite grain, the measured Mn concentration profiles at the 2nd interface for both tips are almost identical and similar to what was previously observed for the 5 s and 15 s of holding.

(a)

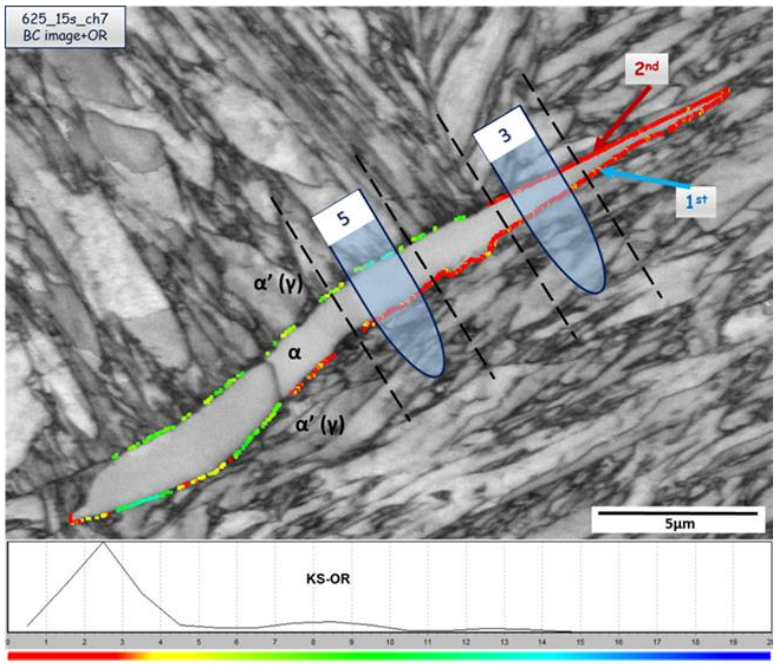

(b) *625_15s_ch7_tip3_2nd*

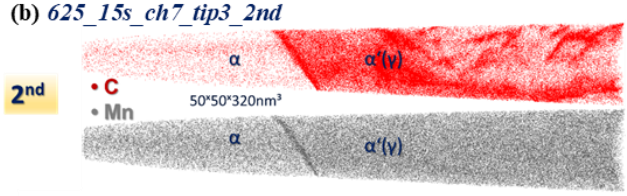

X_{Mn}^{max}=4.3 at%;

X_{Mn}^{α}=1.8 at%; X_{Mn}^{γ}=2.5 at%;
Approximate width ~ 4 nm

$$\Gamma_{Mn}(\pm 1nm) = 6.0 \pm 0.6 \frac{atom}{nm^2}$$

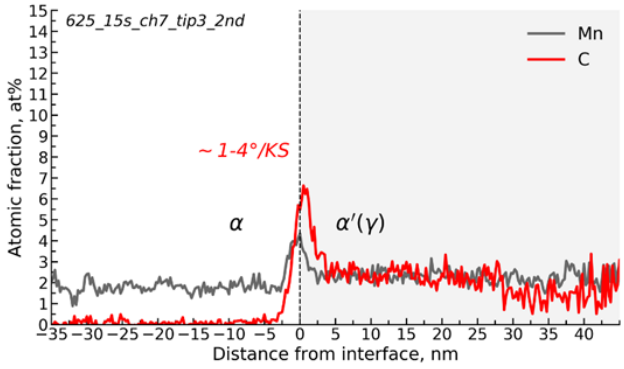

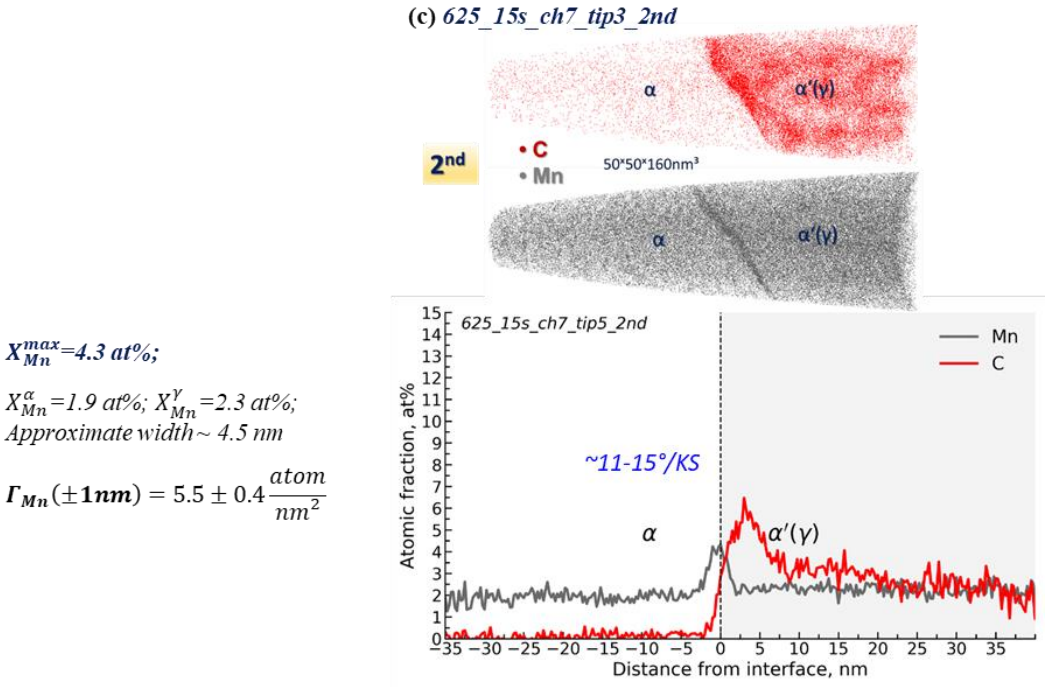

Figure 3.12. **(a)** *IQ map of the selected region with the allotriomorph ferrite formed after isothermal holding at 625°C during 15 s* ***(625_15s_ch7)****. Colors represent the orientation difference with respect to KS-OR of the initial ferrite–austenite orientation relationships at 625 °C.* ***(b)*** *3D reconstructions and concentration profiles of C and Mn atoms across the 2nd interface of tip3 and.* ***(c)*** *across the 2nd interface of tip5.*

3.5.3 Austenite/ferrite transformation interface after 30s at 625°C

In the case of the sample held 30 s at 625°C, two regions with thin allotriomorph ferrites have been chosen for the APT analyses. IQ maps with the measured ORs are shown in **Figure 3.13** (a) *625_30s_ch1*, and **Figure 3.14** (a) *625_30s_ch2*. The morphologies of both ferrite grains are very similar, in the way that they have straight shapes on both sides, with relatively small misorientations with respect to KS orientation relationships (<7°). Although both correspond to 30 s of transformation at 625°C, the width of formed ferrite in **Figure 3.13** (a) is twice bigger as in **Figure 3.14** (a), 3.4 µm vs. 1.7 µm. The length is around 30 µm and 24 µm for chunk1 and chunk2, respectively.

Nevertheless, the measured composition profiles somehow exhibit similar behaviors of solute across the investigated α'(γ)/α interfaces. The accumulations of Mn atoms at the interface in the case of *625_30s_ch1_tip3_2nd* (**Figure 3.13** (c)) and *625_30s_ch2_tip4_1st* (**Figure 3.14** (d)) are represented by the peaks of Mn with a maximum content of about 5.6 at% (excess – 7.7 atom/nm²) and 5.5 at% (excess – 4.7 atom/nm²), respectively. The composition profiles of *625_30s_ch1_tip5_1st* (**Figure 3.13** (d)) and *625_30s_ch2_tip2_2nd* (**Figure 3.14** (c)) have small peaks of Mn with a maximum content of about 3.4 at% (excess – 0.8 atom/nm²) and 3.2 at% (excess – 1.3 atom/nm²), respectively. However, in both cases, the Mn enrichment into

austenite and Mn depletion into ferrite in the close vicinity to the interface can be noticed. The profile of *625_30s_ch1_tip6_1st* (**Figure 3.13** (e) at the first view seems to be flat regarding the redistribution of Mn. However, the different average compositions from austenite and ferrite sides (X^{γ}_{Mn}=*2.2 at% vs.* X^{α}_{Mn}=*2.0 at%*) are measured.

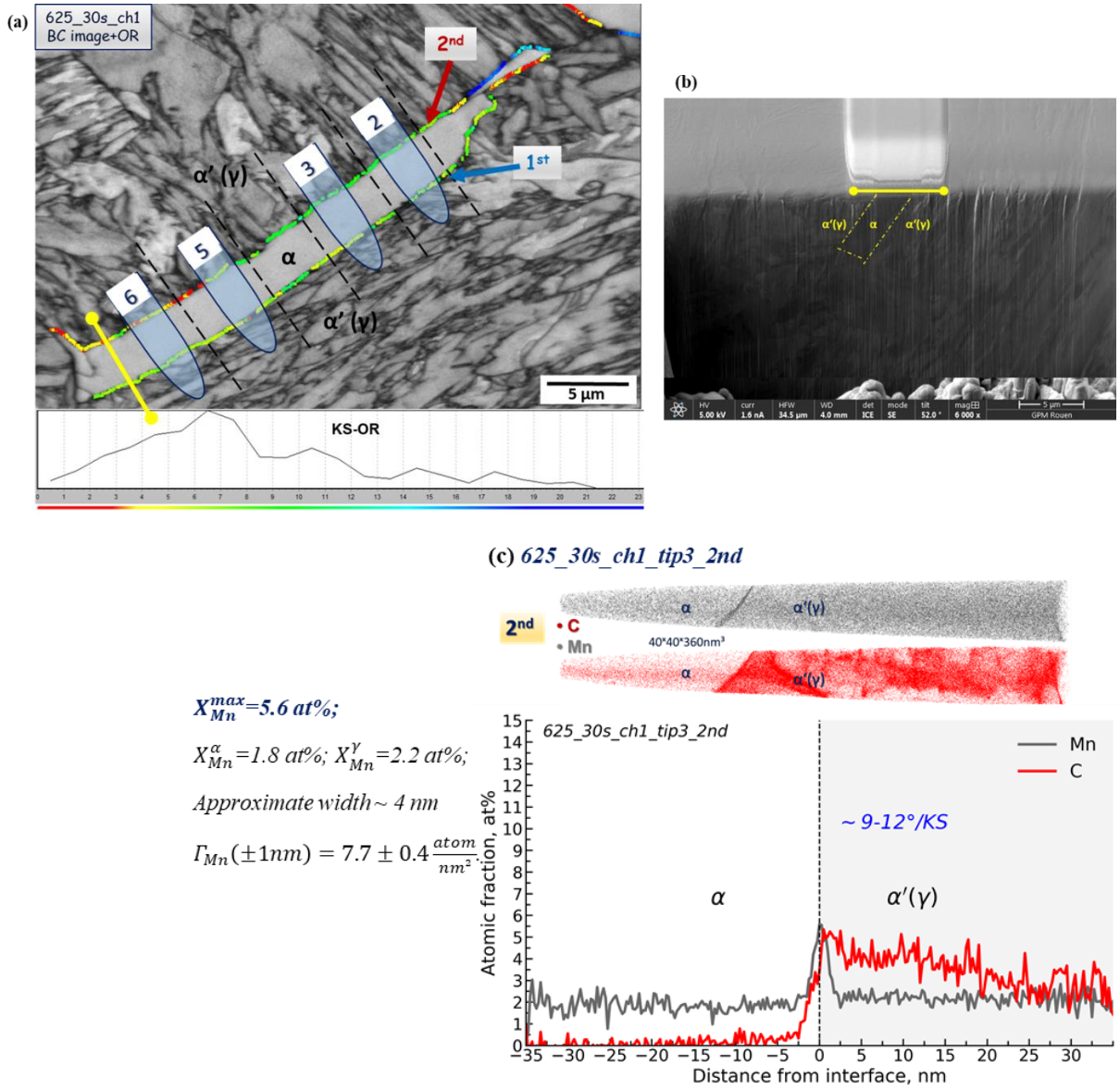

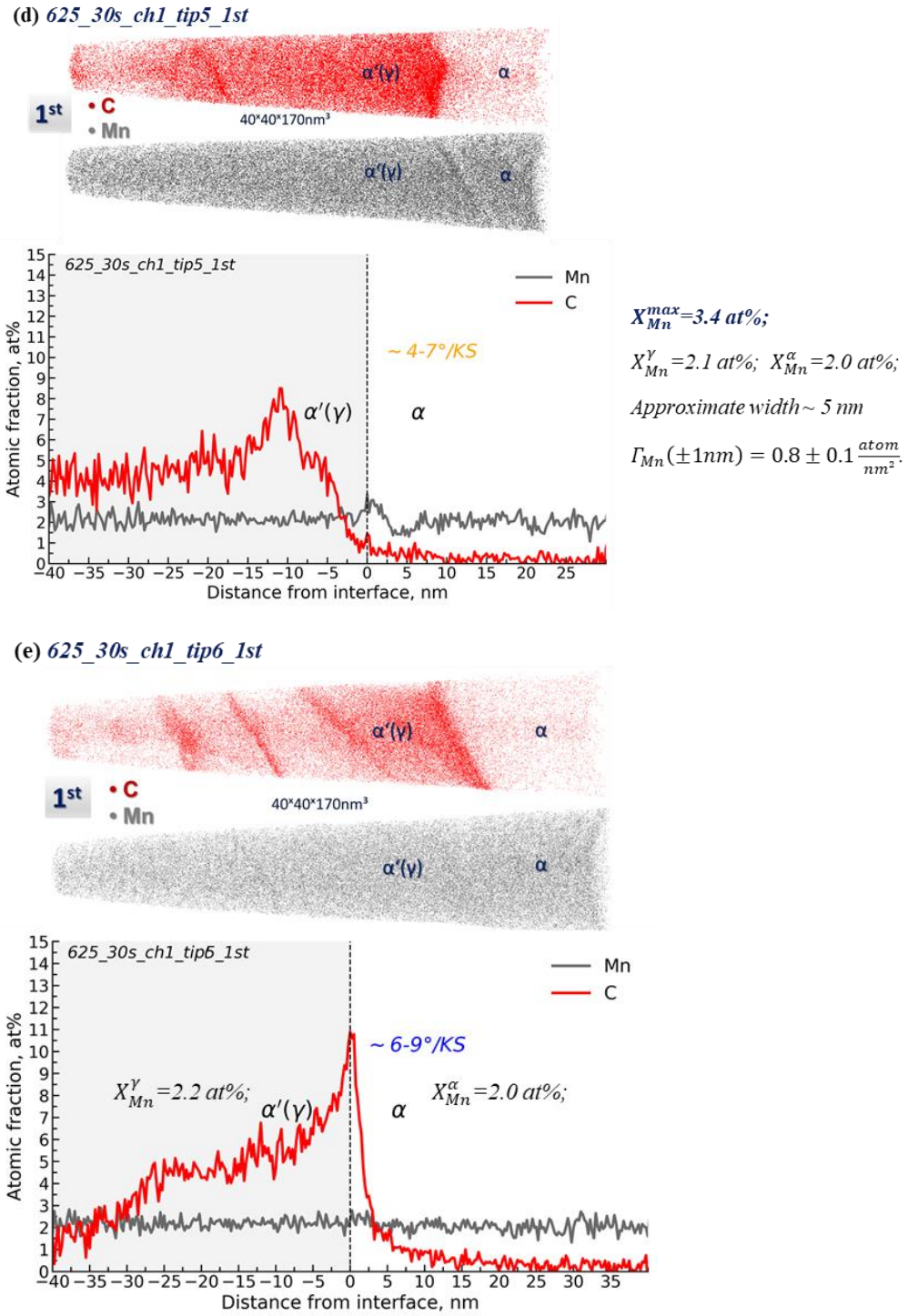

Figure 3.13. (a) *IQ map of the selected region with the allotriomorph ferrite formed after isothermal holding at 625°C during 30 s (**625_30s_ch1**). Colors represent the orientation difference with respect to KS-OR of the initial ferrite–austenite orientation relationships at 625 °C.* ***(b)*** *3D reconstructions and concentration profiles of C and Mn atoms across the 2nd interface of tip3 and.* ***(c)*** *across the 1st interface of tip5.*

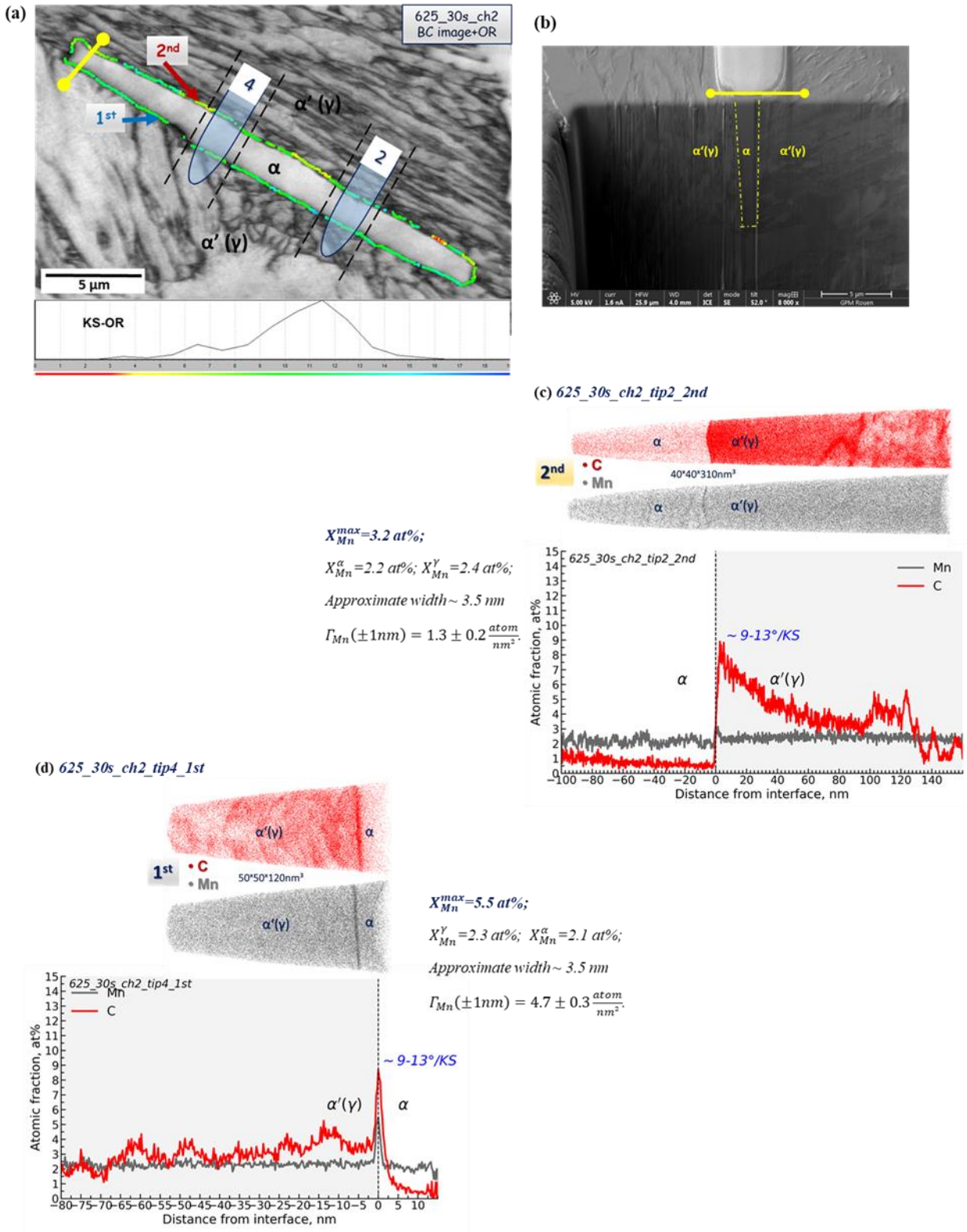

Figure 3.14. (a) *IQ map of the selected region with the allotriomorph ferrite formed after isothermal holding at 625°C during 30s (**625_30s_ch2**). Colors represent the orientation difference with respect to KS-OR of the initial ferrite–austenite orientation relationships at 625 °C.* ***(c)*** *3D reconstructions and concentration profiles of C and Mn atoms across the 2nd interface of tip2 and.* ***(c)*** *across the 1st interface of tip4.*

3.5.4 Austenite/ferrite transformation interface after 3h at 625°C

The next set of experimental results is related to the profiles obtained after isothermal holding at 625°C for 3h. The IQ maps with the measured ORs of the selected regions are shown in **Figure 3.15** (a) – chunk 3, **Figure 3.16** (a) – chunk 5, and **Figure 3.17** (a) – chunk 6. The ORs at the investigated interfaces are in the range of 15-25° misorientation with respect to KS-ORs. The lengths of the investigated grains are chunk 3 ~ 50 µm, chunk 5 ~ 75 µm, chunk 7 ~ 42 µm, and width 10 µm, 7.5µm, and 7 µm, respectively. These sizes have somewhat complicated the procedure of site-specific sample preparation because the chunk with such wide ROI can be too big for the lift-out procedure. However, since the fraction of the ferrite formed at this condition is about 33%, it was hard to find thinner ferrite grains. In consequence of such non-standard geometrical parameters of sample preparation (related to the procedure used in this work), a limited number of results were obtained: namely, the 2nd interfaces of the tip2 of chunk 3 and tip7 of chunk 5, and the 1st interface of the tip7 of chunk 6. 3D reconstruction of the analyzed volume for the C and Mn atoms with the corresponding composition profiles in **Figure 3.15** (b), **Figure 3.16** (b), and **Figure 3.17** (b), respectively.

In all the presented cases, the segregation of both Mn and C atoms is observed. The average contents of Mn in ferrite, austenite, at the peaks, with the calculated excess amount, are presented in **Table 8**. The average concentration of Mn is lower in ferrite and higher in austenite compared to the nominal one of 2.0 at%. In the case of **Figure 3.15** (b), the Mn peak of the profile has an abrupt shape on both sides of the interface. In comparison, the presence of a Mn composition gradient up to 15 nm away from the interface into the prior austenite side is apparent in **Figure 3.17** (b). As a consequence, the excess was not calculated in this case. The formation of the Mn content gradient from the austenite side in the case of **Figure 3.16** (b) just seems to appear in the very close vicinity (up to 5nm) of the interface. In the case of 625°C transformation temperature, the long-range diffusion is observed only for a longer holding time of 3h, besides clearly marked only in one of three measured cases.

Table 8. *The main parameters of observed profiles in the case of 625°C for holding time of 3h*

Condition	tip#	KS-OR	X^{α}_{Mn}, at%	X^{γ}_{Mn}, at%	~w, nm	X^{Max}_{Mn}, at%	Γ_{Mn} ($\pm 1nm$), $atom/nm^2$
T=625°C *t=3h*	**Chunk 3**						
	tip2_2nd	19-24°	1.7	2.3	2.5	8.5	10.4±0.7
	Chunk 5						
	tip7_2nd	12-18°	1.9	2.3	4.5	9.0	11.1±0.3
	Chunk 6						
	tip7_1st	21-25°	1.8	2.1	?	13.3	?

? – since the long-range diffusion of Mn into austenite is observed in the current compositions profiles, the Mn excess was not calculated in these cases (see more details in paragraph (2.7)).

(a) ***625_3h_ch3***

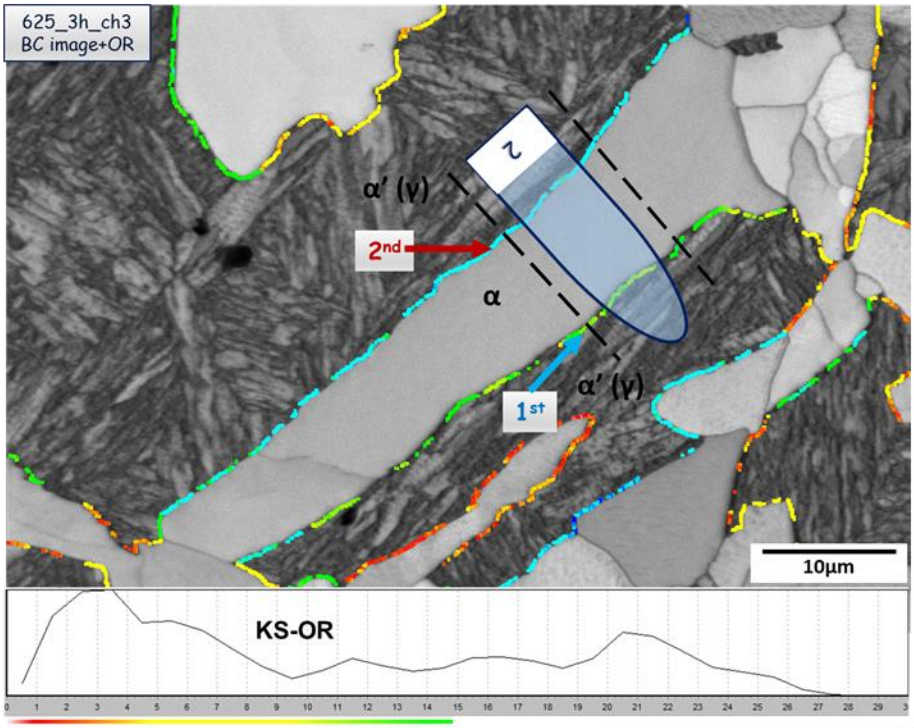

(b) ***625_3h_ch3_tip2_2nd***

X_{Mn}^{max}=8.5 at%;

X_{Mn}^{α}=1.7 at%; X_{Mn}^{γ}=2.30 at%;

Approximate width ~ 2.5 nm

$\Gamma_{Mn}(\pm 1nm) = 10.4 \pm 0.7 \frac{atom}{nm^2}$.

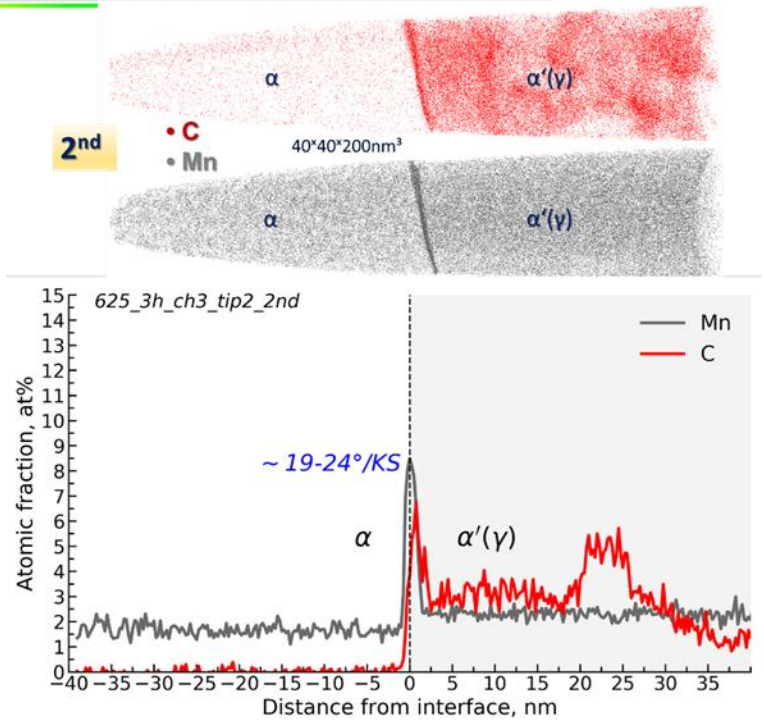

Figure 3.15. **(a)** *IQ map of the selected region with the allotriomorph ferrite formed at the prior austenite grain boundary after isothermal holding at 625°C for 3h* ***(625_3h_ch3)****. Colors represent the orientation difference with respect to KS-OR of the initial ferrite–austenite orientation relationships at 625 °C.* ***(a)*** *3D reconstructions and concentration profiles of C and Mn atoms across the 2nd interface of tip2.*

(a) ***625_3h_ch5***

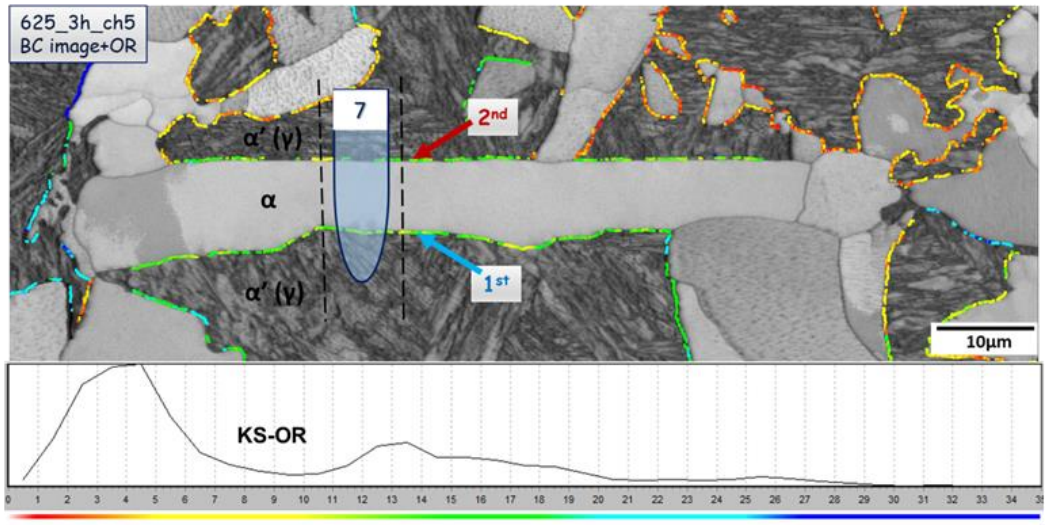

(b) ***625_3h_ch5_tip7_2nd***

X_{Mn}^{max} *=9.0 at%;*

X_{Mn}^{α}*=1.9 at%;* X_{Mn}^{γ}*=2.3 at%;*

Approximate width ~ 4.5 nm

$\Gamma_{Mn}(\pm 1nm) = 11.0 \pm 0.3 \frac{atom}{nm^2}$.

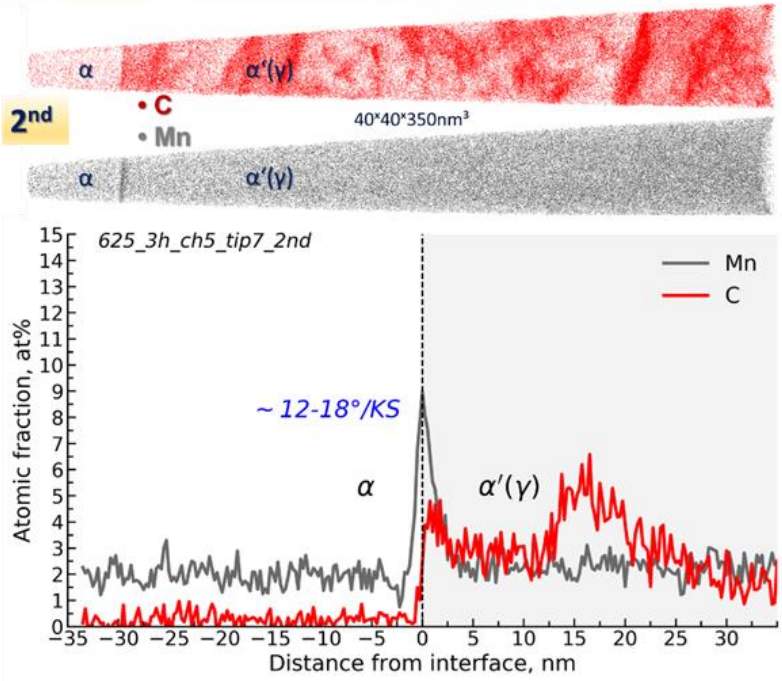

Figure 3.16. (a) *IQ map of the selected region with the allotriomorph ferrite formed at the prior austenite grain boundary after isothermal holding at 625°C for 3h (**625_3h_ch5)**. Colors represent the orientation difference with respect to KS-OR of the initial ferrite–austenite orientation relationships at 625 °C. **(a)** 3D reconstructions and concentration profiles of C and Mn atoms across the 2nd interface of tip7.*

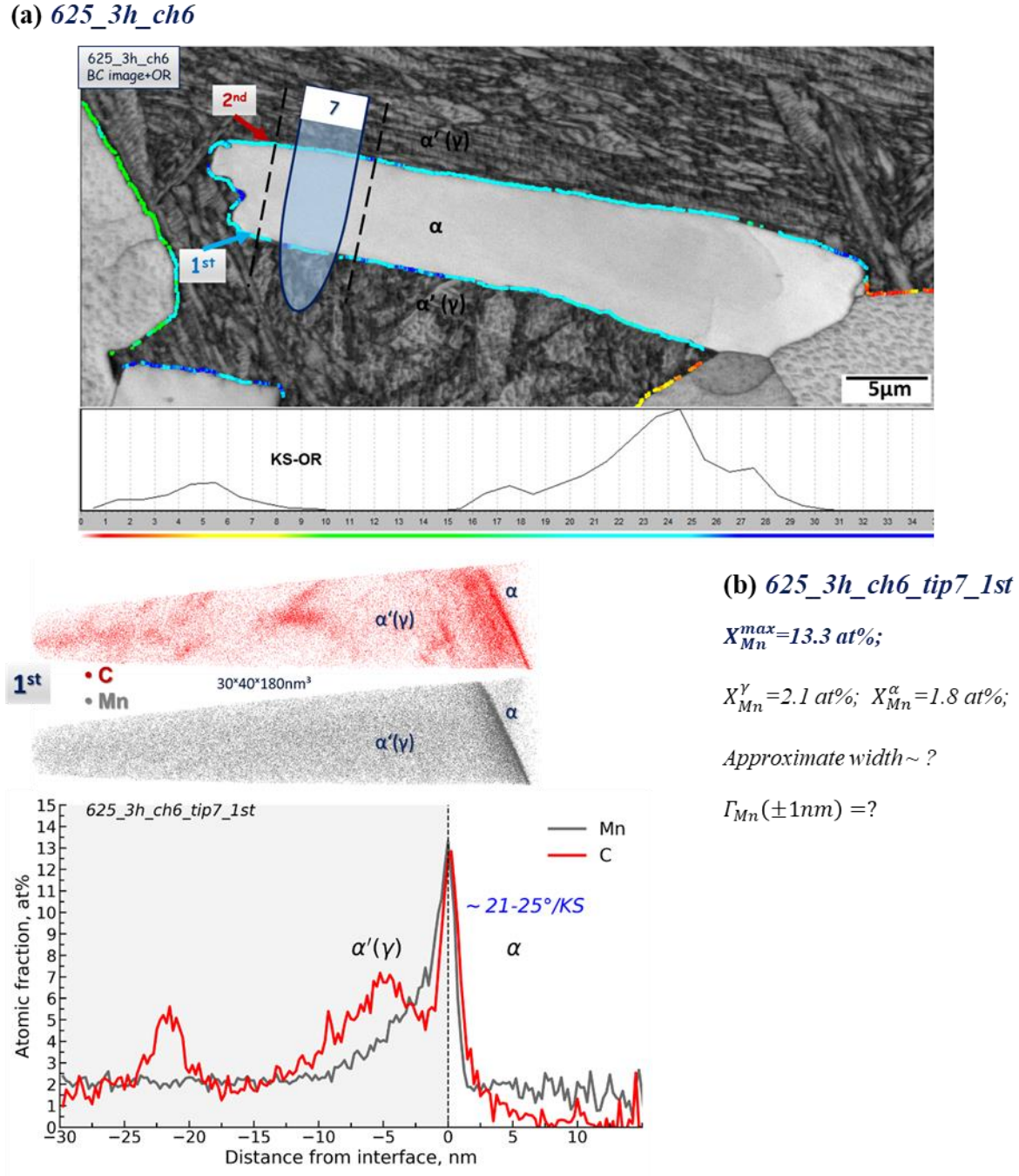

Figure 3.17. (a) *IQ map of the selected region with the allotriomorph ferrite formed at the prior austenite grain boundary after isothermal holding at 625°C for 3h* ***(625_3h_ch6)****. Colors represent the orientation difference with respect to KS-OR of the initial ferrite–austenite orientation relationships at 625 °C.* ***(a)*** *3D reconstructions and concentration profiles of C and Mn atoms across the 1st interface of tip7.*

3.6 Austenite/ferrite transformation interface after ageing at 680°

The next set of experimental observations is dedicated to the APT analyses of α'(γ)/α interfaces in the case of austenite-to-ferrite phase transformation that took place at 680°C. At this temperature, the situation is complementary as the competition of several regimes for ferrite growth can be observed, see **Figure 3.1** (b).

3.6.1 Austenite/ferrite transformation interface after ageing at 680° during 100s

In the case of the sample held at 680°C during 100s, two different regions with a thin allotriomorph ferrite film formed at a prior austenite grain boundary have been selected for investigation. The IQ map of the first selected film region with the measured ORs that correspond to the prior ORs at austenite/ferrite interfaces at 680°C are shown in **Figure 3.18** (*680_100s_ch1)*. The length of the observed ferrite film is about 33 µm, and its width varies smoothly from 3.6 µm (left) to 1.7 µm (right). The interfaces on both sides are relatively straight. The α'(γ)/α interface, noted as the 1st one, has an orientation difference with respect to KS orientation in the range of 13-18°, and the 2nd one shows a more closer orientation to the KS-OR (from 1° to 5° difference). The APT measurements were successful for both interfaces only for tip1, and for the rest (tip3, tip4, tip5), only 1st interfaces were analyzed. 3D reconstruction of the analyzed volumes for the C and Mn atoms with the corresponding concentration profiles are given in **Figure 3.19.**

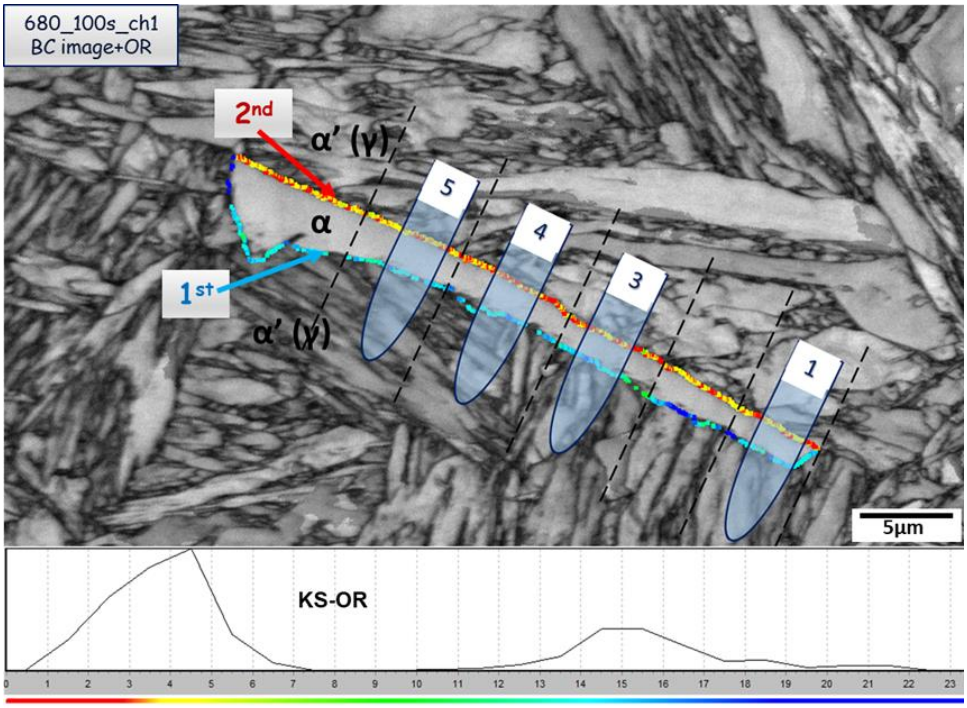

Figure 3.18. *IQ maps of the two selected regions with the allotriomorph ferrite films formed after isothermal holding at 680°C during 100* ***(680_100s_ch1).*** *Colors at α' (γ)/α interfaces represent the*

orientation relation between ferrite and prior austenite at 680 °C. It is expressed as the orientation difference with respect to the KS orientation relationship.

(a) ***680_100s_ch1_tip1_1st***

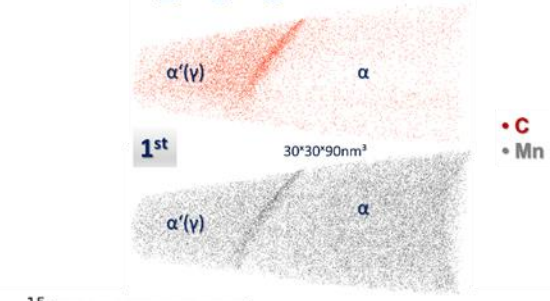

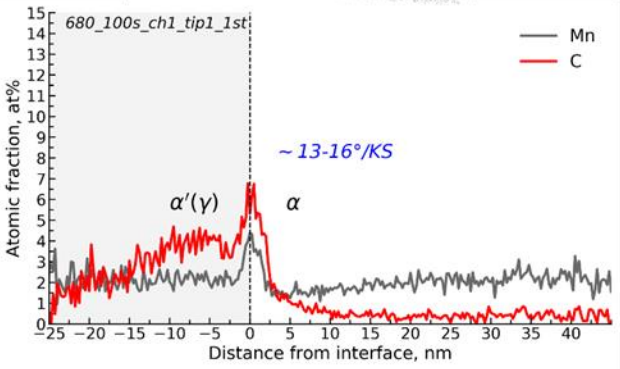

X_{Mn}^{max}=4.4 at%;
X_{Mn}^{γ}=2.2 at%; X_{Mn}^{α}=1.7 at%;
Approximate width ~ 4.5 nm
$\Gamma_{Mn}(\pm 1nm) = 3.6 \pm 0.4\ atom/nm^2$

(b) ***680_100s_ch1_tip1_2nd***

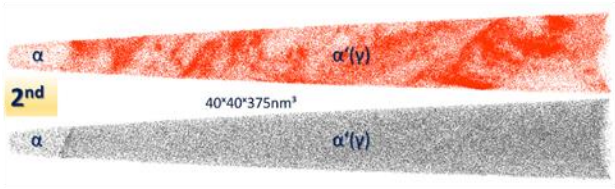

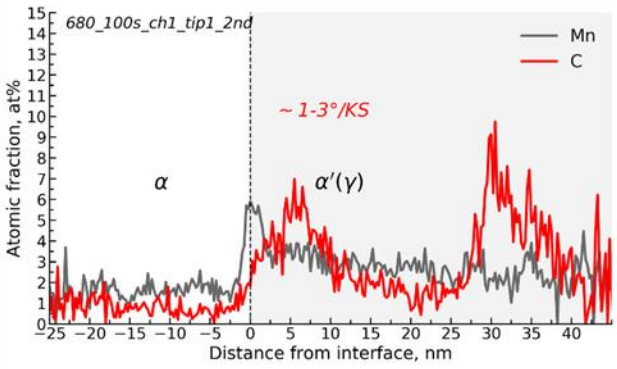

X_{Mn}^{max}=5.9 at%;
X_{Mn}^{α}=1.8 at%; X_{Mn}^{γ}=2.7 at%;
Approximate width ~ 4.5 nm
$\Gamma_{Mn}(\pm 1nm) = 7.9 \pm 1.2\ atom/nm^2$???

(c) ***680_100s_ch1_tip3_1st***

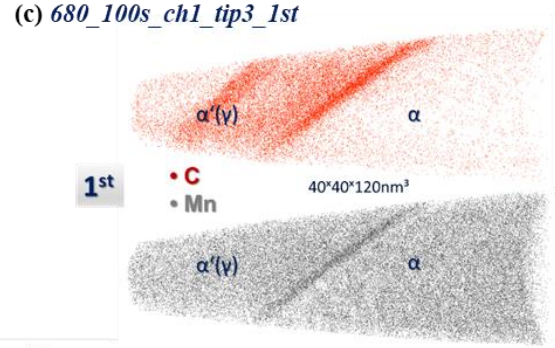

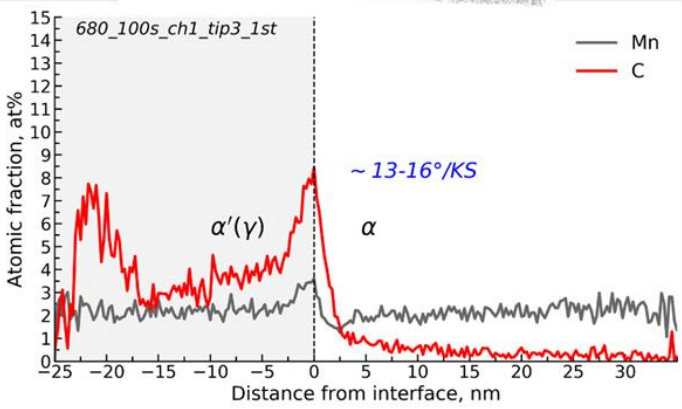

X_{Mn}^{max}=3.6 at%;
X_{Mn}^{γ}=2.2 at%; X_{Mn}^{α}=2.0 at%;
Approximate width ~ 4.5 nm
$\Gamma_{Mn}(\pm 1nm) = 2.0 \pm 0.2 \frac{atom}{nm^2}$.

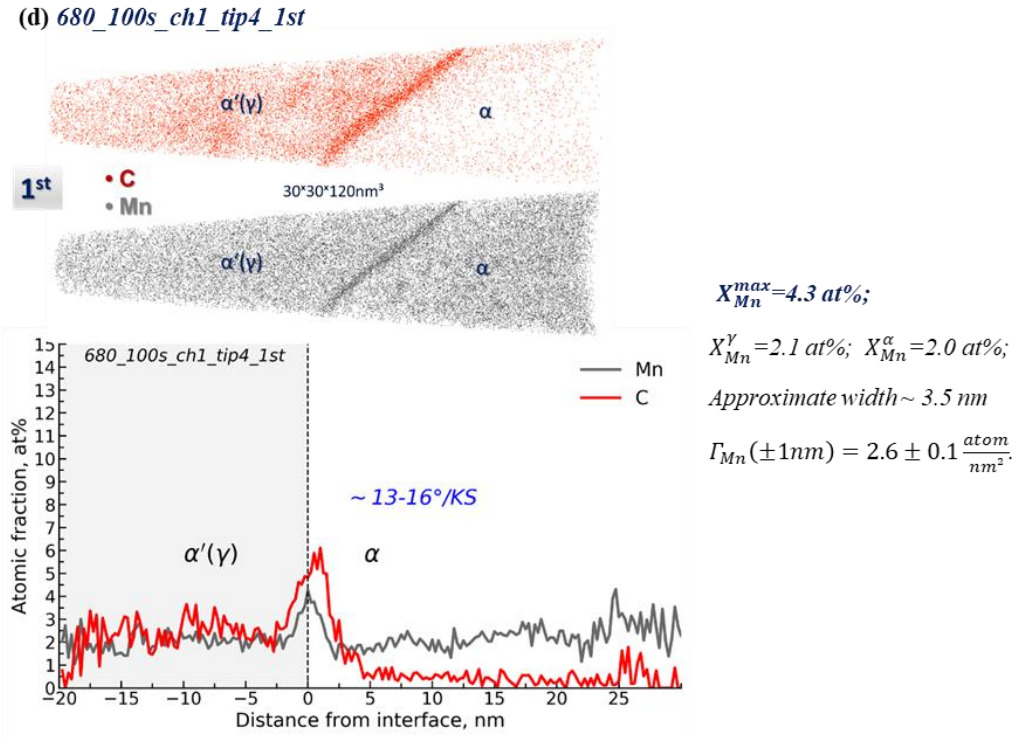

Figure 3.19. *3D reconstructions and concentration profiles of C and Mn atoms across the 1st interface of (**a**)tip1, (**c**)tip3, (**d**)tip4, and across the 2nd interface of (**b**)tip1 of the **680_100s_ch1** (see* **Figure 3.18***).*

The ferrite film from the second selected region, see **Figure 3.20** (*680_100s_ch3)*, similarly to the first one, has a straight morphology of the same length of about 33 µm, and a width of ~ 1.5 µm. The 2nd interface has a near KS orientation (deviation only of 1- 4°) while the 1st one can be separated into two regions, with orientation differences of 7-12° (yellow) with respect to KS-OR (the location of tip2 and tip3), and of 18-23° (light green, the location of tip6). Only information related to the 1st α'(γ)/α interface were collected, as only the first runs of tip2, tip3, and tip6 were successful during the APT analyses. 3D reconstruction of the analyzed volume for the C and Mn atoms with the corresponding concentration profiles are given in **Figure 3.21.**

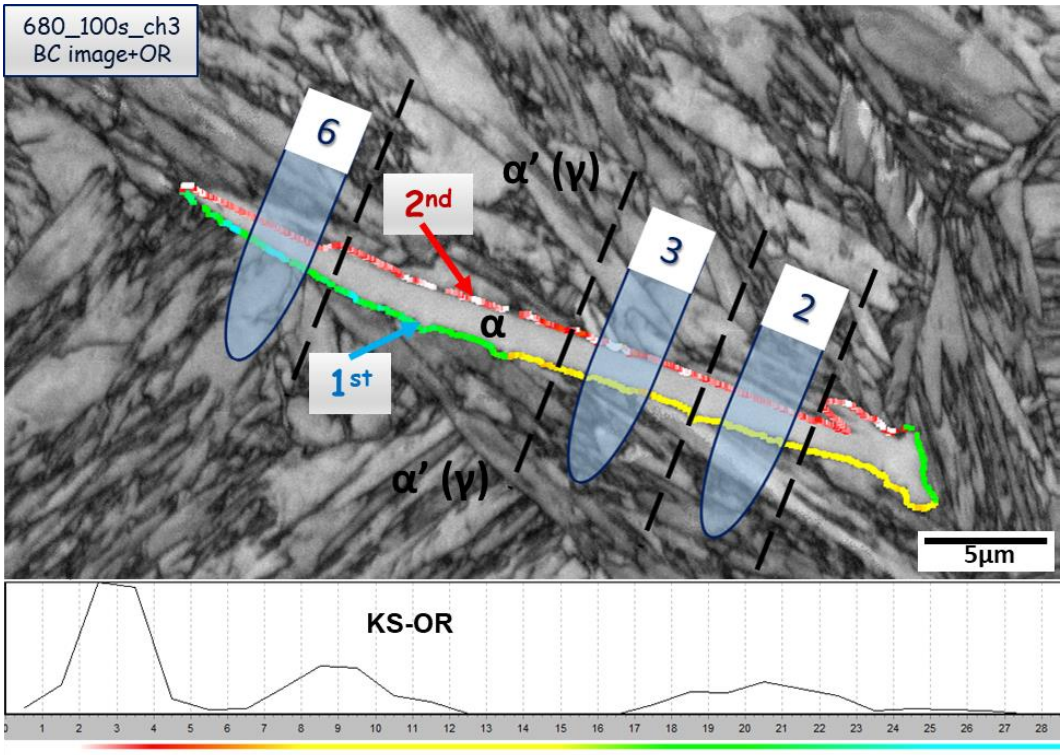

Figure 3.20. *IQ maps of the two selected regions with the allotriomorph ferrite films formed after isothermal holding at 680°C during 100s* ***(680_100s_ch3).*** *Colors at α' (γ)/α interfaces represent the orientation relation between ferrite and prior austenite at 680 °C. It is expressed as the orientation difference with respect to the KS orientation relationship.*

(a) ***680_100s_ch3_tip3_1st***

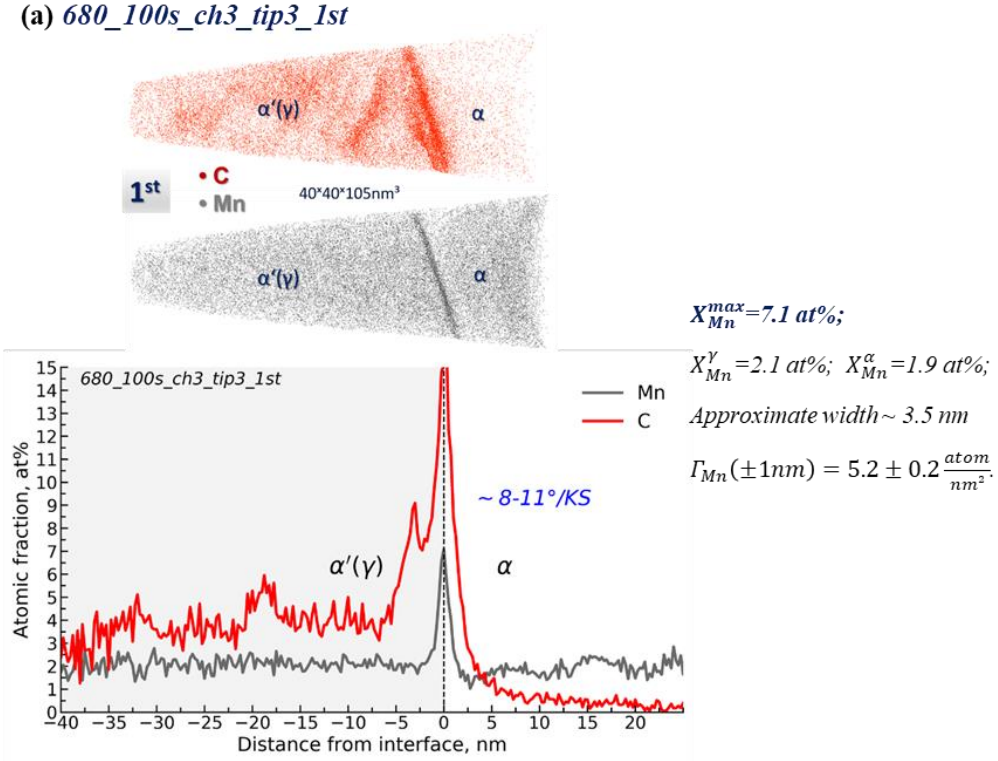

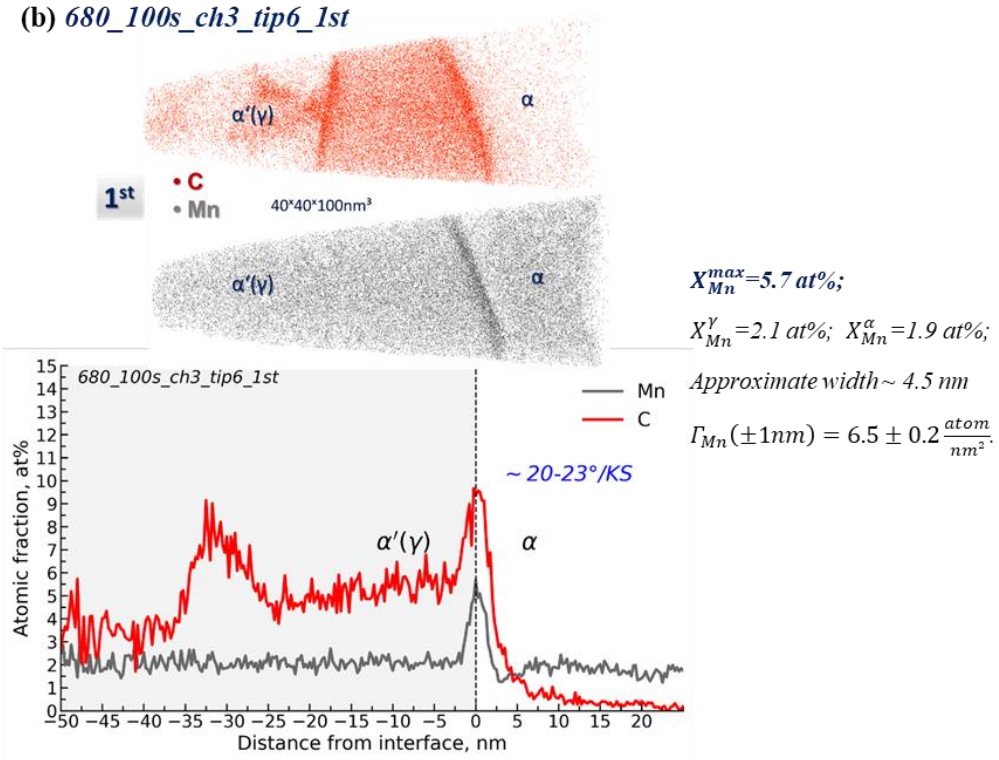

Figure 3.21. *3D reconstructions and concentration profiles of C and Mn atoms across the 1st interface of (**a**)tip3, (**b**)tip6 of the **680_100s_ch1** (see* **Figure 3.20***).*

In both cases, the observed profiles across the α'(γ)/α interfaces showing the larger misorientation with respect to KS-ORs indicate similar redistribution of Mn across the interface (see **Figure 3.19** and **Figure 3.21**). In all cases, the Mn depletion from the ferrite side can be observed; especially it is evident in the case of **Figure 3.19** (a), (c), and **Figure 3.21** (b). **Table 9** summarizes the set of the main measured and calculated parameters of all observed profiles for both examined ferrite grains, and it can be noticed that the segregated amount of Mn atom at the 1st interface of chunk 3 is higher compared to chunk 1 (see $\boldsymbol{X_{Mn}^{Max.}}$ and $\boldsymbol{\Gamma_{Mn}}$ values in the **Table 9** only for the interfaces noted as 1st one). Regarding the only concentration profile obtained across the 2nd interface of chunk 1, both Mn peak at the interface and long-range diffusion into austenite are observed. The Mn peak, in this case, reaches a maximum of 5.9 at%, but due to the redistribution of Mn into the austenite side, the calculated excess value is questionable.

Table 9. *The main parameters of observed profiles in the case of 680°C for holding time of 100s*

Condition	tip#	KS-OR	X_{Mn}^{α}, at%	X_{Mn}^{γ}, at%	Approximate width, nm	$X_{Mn}^{Max.}$, at%	Γ_{Mn} $(\pm 1nm)$, $atom/nm^2$
T=680°C t=100s	Chunk 1						
	tip1_1st	13-16	1.7	2.2	4.5	4.4	**3.6±0.4**
	tip3_1st	13-16	2.0	2.2	4.5	3.6	**2.0±0.2**
	tip4_1st	13-16	2.0	2.1	3.5	4.3	**2.6±0.1**

	tip5_1st	12-16	2.0	2.2	4.5	4.4	**4.5±0.2**
	tip1_2nd	1-3	1.8	2.7	4.5	5.9	**7.9±1.2?**
	Chunk 3						
	tip3_1st	8-11	1.9	2.1	3.5	7.1	**5.2±0.2**
	tip6_1st	20-23	1.9	2.1	4.5	5.7	**6.5±0.2**

3.6.2 Austenite/ferrite transformation interface after 600s at 680°C

The next set of APT experiments was performed for the sample isothermally held at 680°C during the 600s. The APT results obtained for five different allotriomorph ferrite grains will be presented in this section. **Table *10*** provides the main characteristics of each selected ferrite region. In these cases, one of α'(γ)/α interfaces has a near KS orientation, with a deviation in the range of 1- 4°, while the other one typically deviates from KS approximately 7-12° (except the case in **Figure 3.24**, where the deviation is in the range of 14-18°). The additional parameters, such as length, width, as well as the list of successful APT measurements for 1st and 2nd interfaces, are also given in Помилка! Джерело посилання не знайдено.

Table 10. *The main characteristics of the analysed ferrite regions in the case of 680°C and holding time of 600s*

#	*Code*	➢ **IQ map with ORs** ➢ **APT results (number of Figures)**	**ORs: misorientation from the KS relationship**	***L, w***
1	***680_600s_ch8*** *1st tips: 1, 2, 3, 4* *2nd: non*	➢ Figure *3.22* ➢ Figure *3.23*	*1st ~ 7-12°, wave-like* *2nd ~ 1-4°, straight*	*- length ~ 27 µm;* *- width varies ramdomly from 1.2 µm to 2.5 µm*
2	***680_600s_ch12*** *1st: non* *2nd tips: 2, 3, 5*	➢ Figure 3.24 ➢ Figure 3.24	*1st ~ 14-18°, slightly wave-like* *2nd ~ 1-4°, straight*	*length ~ 33 µm;* *width ~ 1.8-2.5 µm*
3	***680_600s_ch13*** *1st tip 3* *2nd tip 3*	➢ Figure *3.26* (a) ➢ Figure *3.26* (b-c)	*1st ~ 7-12°, straight* *2nd ~ 1-4°, straight*	*- length ~ 26 µm;* *- width varies ramdomly from 1.2 µm to 3.8 µm*
4	***680_600s_ch14*** *1st tips: 3, 4* *2nd: non*	➢ Figure *3.28* (a) ➢ Figure *3.28*(b-c)	*1st ~ 7-12°, straight* *2nd ~ 1-4°, straight*	*length ~ 31 µm;* *width ~ 0.9 µm*
5	***680_600s_ch15*** *1st tip 2* *2nd: non*	➢ Figure *3.27* (a) ➢ Figure *3.27* (b)	*1st ~ 1-7°, slightly straight* *2nd ~ 8-13°, slightly staight*	*length ~ 32.5 µm;* *width ~ 1.8-2.5 µm*

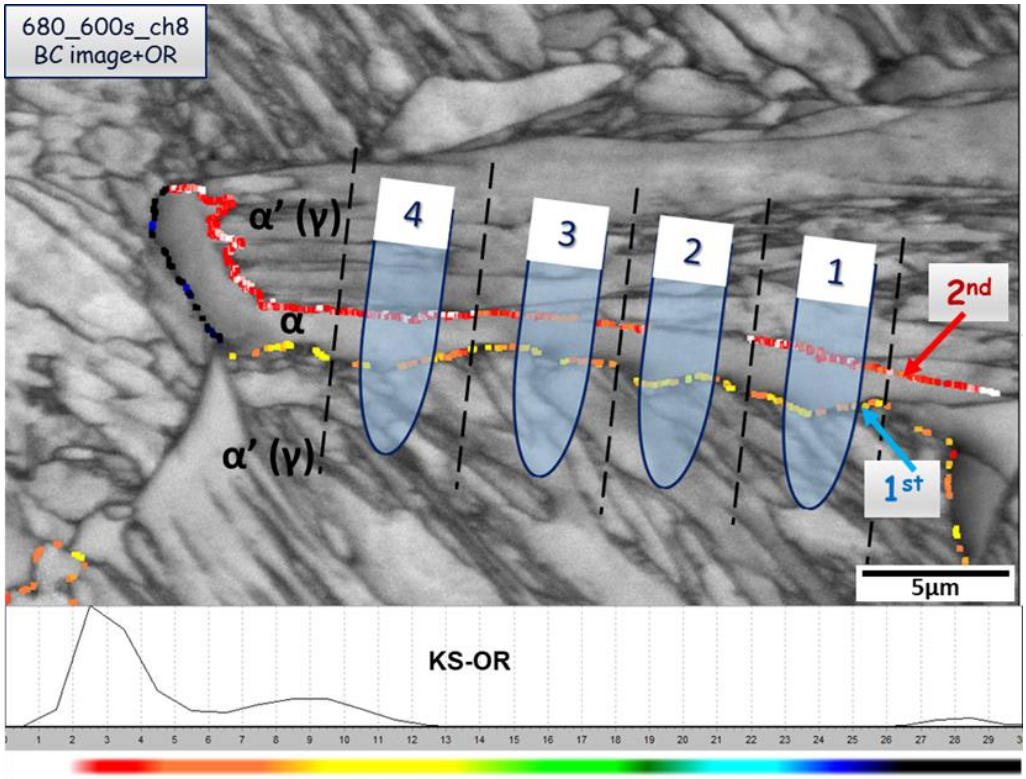

Figure 3.22. *IQ map of selected ROIs with the thin allotriomorph ferrite grains formed after isothermal holding at 680°C during 600s (**680_600s_ch8**). Colors at α'(γ)/α interfaces represent the orientation relation between ferrite and prior austenite at 680 °C. It is expressed as the orientation difference with respect to the KS orientation relationship.*

In the case of **Figure 3.22** (*680_600s_ch8*), APT analyses were successful for all four tips but only for the 1st interface. 3D reconstructions of the analyzed volume for the C and Mn atoms with the corresponding concentration profiles are given in **Figure 3.23**. The observed profiles in **Figure 3.23** show exactly the same behavior as observed after 100s for the 1st interfaces (with larger misorientation, see **Figure 3.21**, **Figure 3.19**). However, the increasing of the accumulated amount of Mn atoms at the interface can be noticed by comparing the $X_{Mn}^{Max.}$ and Γ_{Mn} values (see **Table 9** only for the interfaces noted as the 1st and **Table 11** for chunk8). The segregated amount of Mn atoms at the interface is becoming higher for the 600 s compared to the 100 s.

(a) ***680_600s_ch8_tip1_1st***

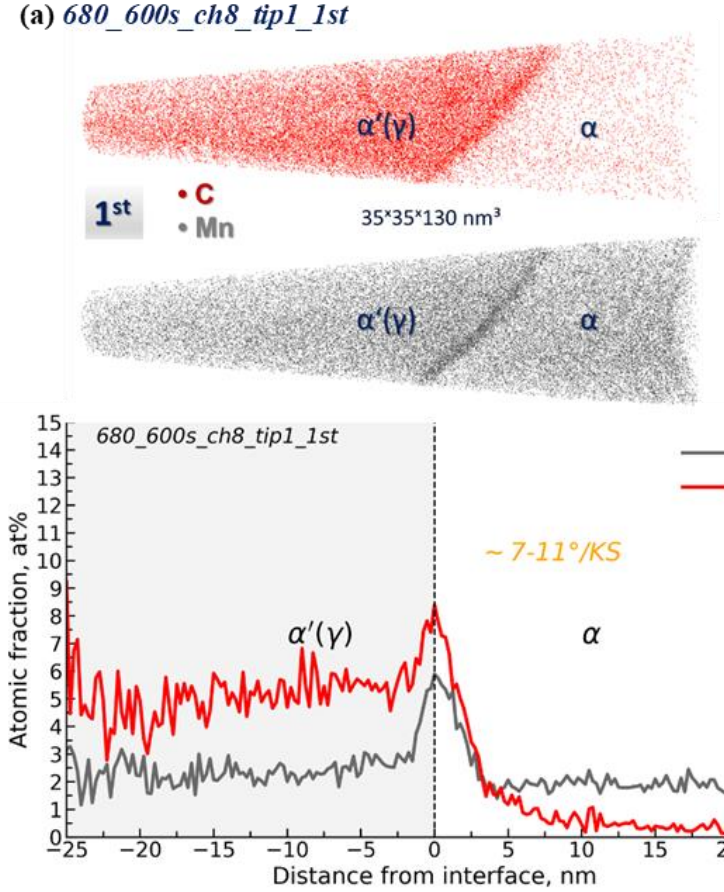

X_{Mn}^{max}=5.9 at%;

X_{Mn}^{γ}=2.3 at%; X_{Mn}^{α}=1.9 at%;

Approximate width ~ 5 nm

$\Gamma_{Mn}(\pm 1nm) = 11.9 \pm 0.4 \frac{atom}{nm^2}$.

(b) ***680_600s_ch8_tip2_1st***

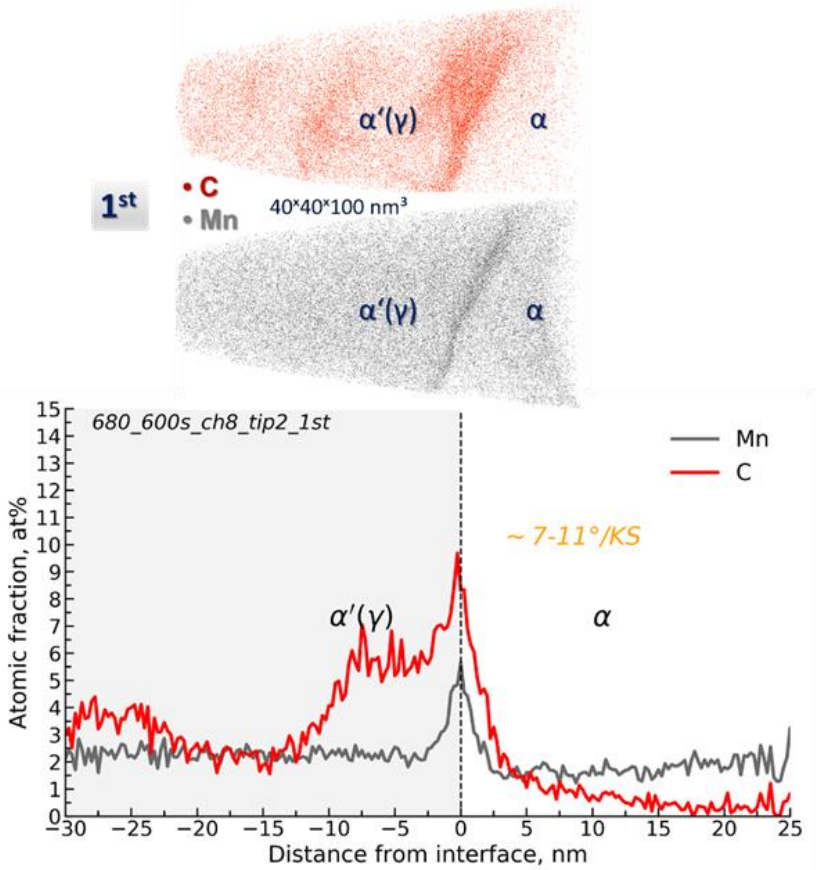

X_{Mn}^{max}=5.7 at%;

X_{Mn}^{γ}=2.3 at%; X_{Mn}^{α}=1.7 at%;

Approximate width ~ 5 nm

$\Gamma_{Mn}(\pm 1nm) = 6.1 \pm 0.6 \frac{atom}{nm^2}$.

(c) *680_600s_ch8_tip3_1st*

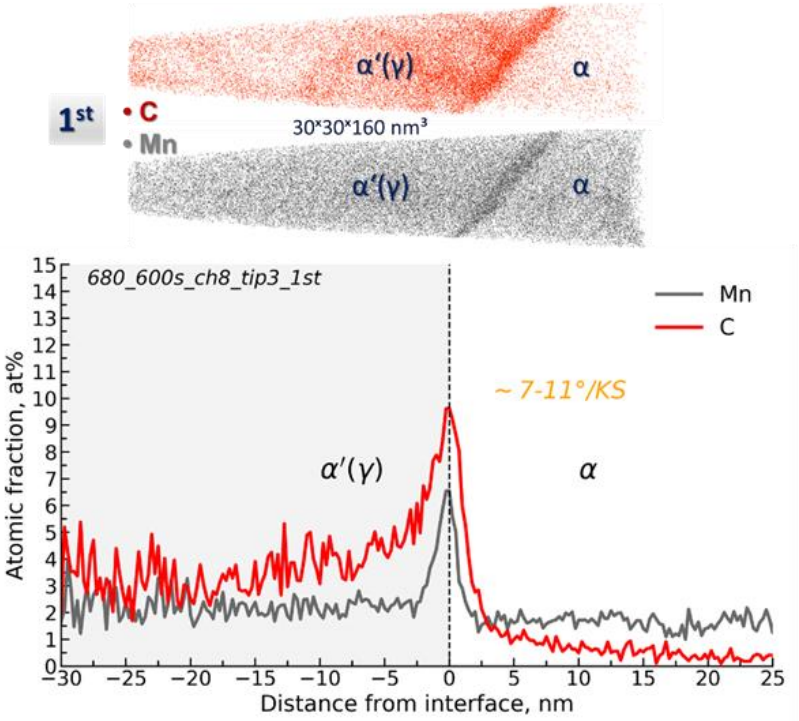

X_{Mn}^{max}=6.6 at%;

X_{Mn}^{γ}=2.2 at%; X_{Mn}^{α}=1.7 at%;

Approximate width ~ 4.5 nm

$\Gamma_{Mn}(\pm 1nm) = 9.7 \pm 0.6 \frac{atom}{nm^2}$.

(d) *680_600s_ch8_tip4_1st*

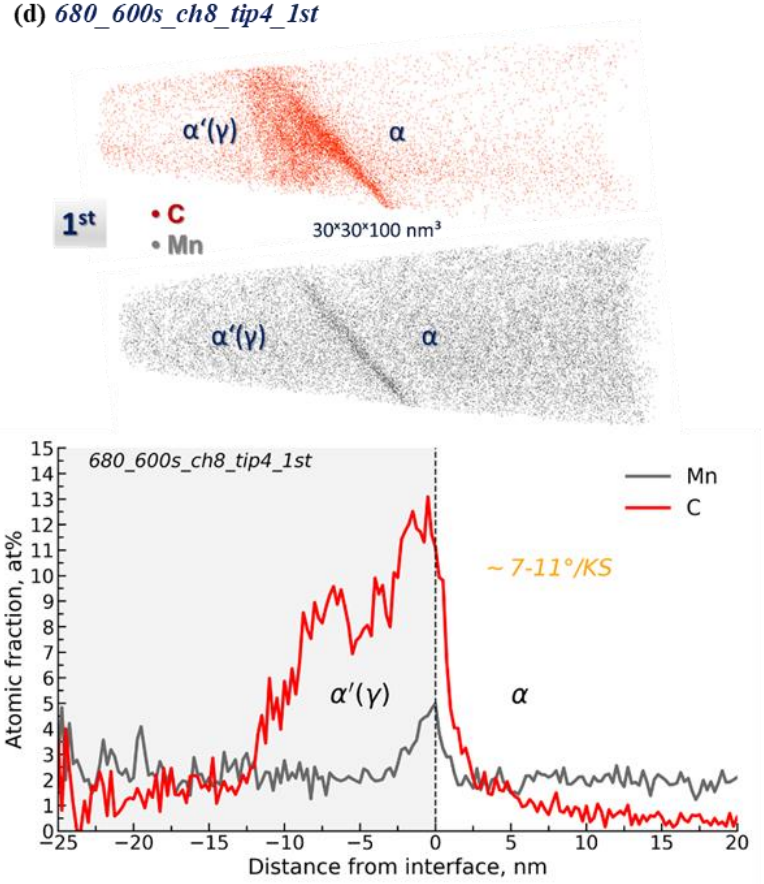

X_{Mn}^{max}=5.0 at%;

X_{Mn}^{γ}=2.2 at%; X_{Mn}^{α}=2.0 at%;

Approximate width ~ 4 nm

$\Gamma_{Mn}(\pm 1nm) = 7.1 \pm 0.2 \frac{atom}{nm^2}$.

Figure 3.23. *3D reconstructions and concentration profiles of C and Mn atoms across the 1st interface of 680_600s_ch8 of:* ***(a)*** *tip1_1st;* ***(b)*** *tip2_1st;* ***(c)*** *tip3_1st;* ***(d)*** *tip4_1st (see* **Figure 3.22***).*

Contrary to the previously described region (*680_600s_ch8*) for 600 s of transformation, in the case of another selected ferrite gain, shown in **Figure 3.24**, the APT measurements were successfully only for interface with the near KS-OR (noted as the 2nd) for tip2, tip3, and tip5 (see the results in **Figure *3.25***). The accumulation of the Mn atoms at the interface is observed in all three cases. The Mn content at the peak reaches ~ 5 at% (tip2), ~ 6 at% (tip3), and ~ 6.4% (tip5). The strong enrichment of Mn in austenite is present in all three cases. Moreover, in the case of tip2, both the Mn peak and the long-range diffusion into austenite can be observed.

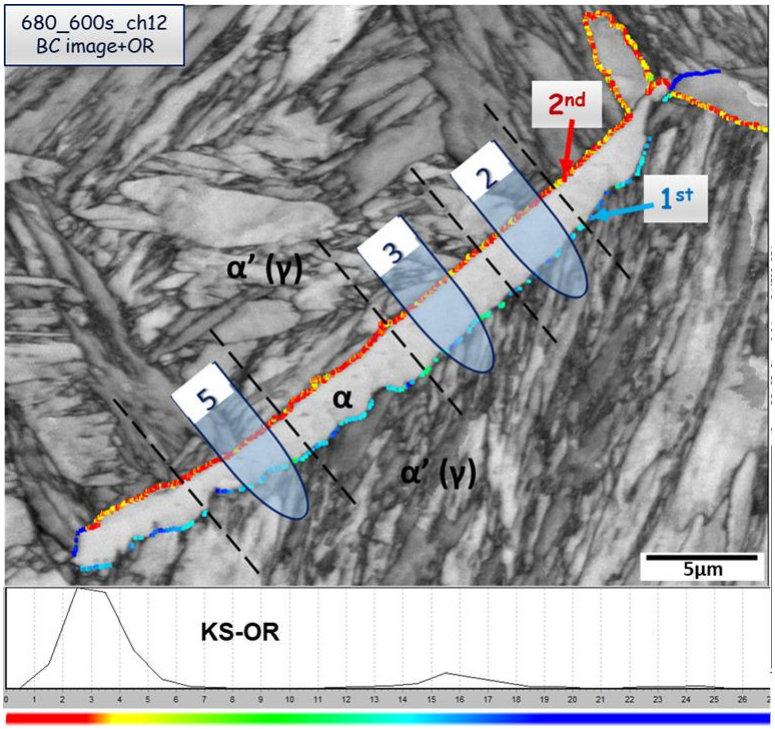

Figure 3.24. *IQ map of the selected allotriomorph ferrite grains formed after isothermal holding at 680°C during 600s (**680_600s_ch12**). Colors at α'(γ)/α interfaces represent the orientation relation between ferrite and prior austenite at 680 °C. It is expressed as the orientation difference with respect to the KS orientation relationship.*

(a) ***680_600s_ch12_tip2_2nd***

X_{Mn}^{max}=5.0 at%

X_{Mn}^{α}=1.8 at%; X_{Mn}^{γ}=2.4 at%

Approximate width ~ 4 nm

$\Gamma_{Mn}(\pm 1nm) = 14.1 \pm 0.5 \frac{atom}{nm^2}$.

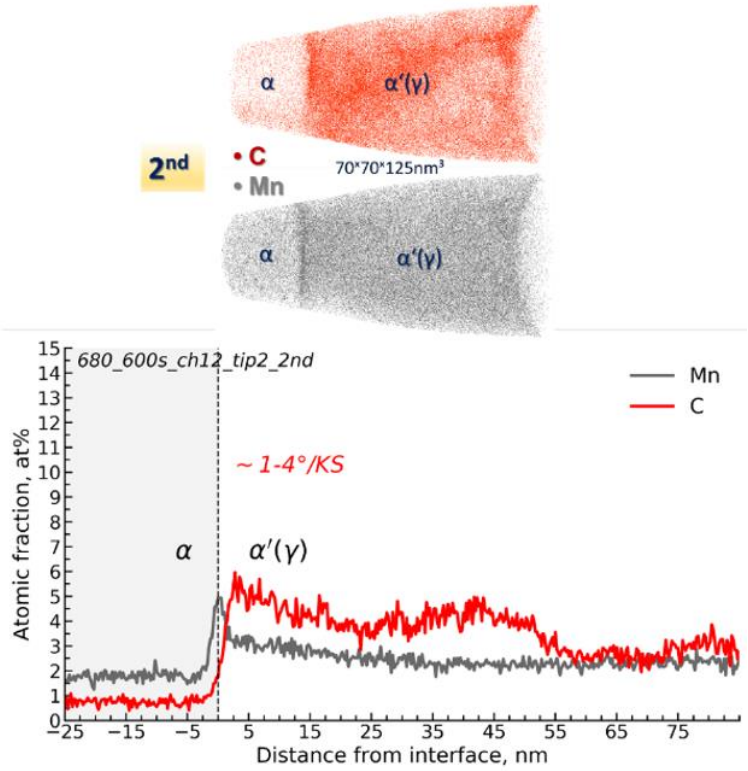

(b) ***680_600s_ch12_tip3_2nd***

X_{Mn}^{max}=6.0 at%

X_{Mn}^{α}=1.9 at%; X_{Mn}^{γ}=2.9 at%

Approximate width ~ 5 nm

$\Gamma_{Mn}(\pm 1nm) = 7.5 \pm 1.0 \frac{atom}{nm^2}$

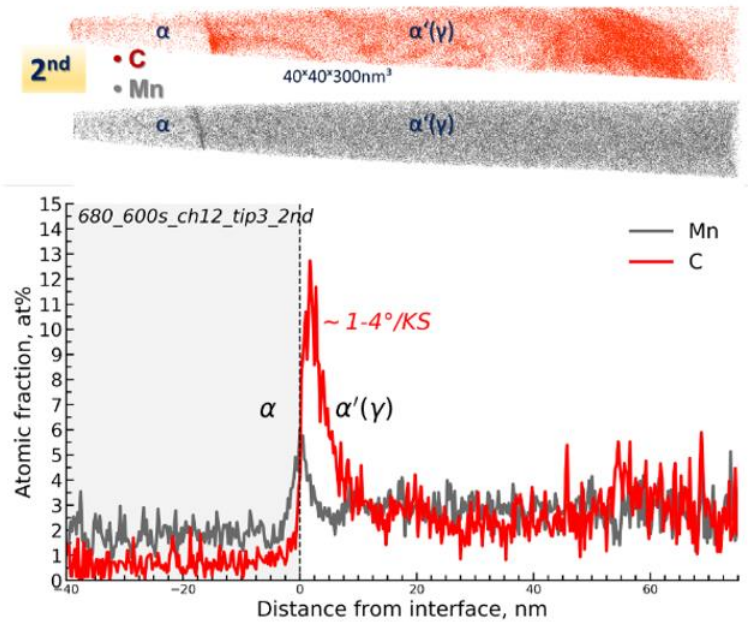

(c) ***680_600s_ch12_tip5_2nd***

X_{Mn}^{max}=6.4 at%

X_{Mn}^{α}=2.0 at%; X_{Mn}^{γ}=2.7 at%

Approximate width ~ 6 nm

$\Gamma_{Mn}(\pm 1nm) = 9.0 \pm 0.7 \frac{atom}{nm^2}$.

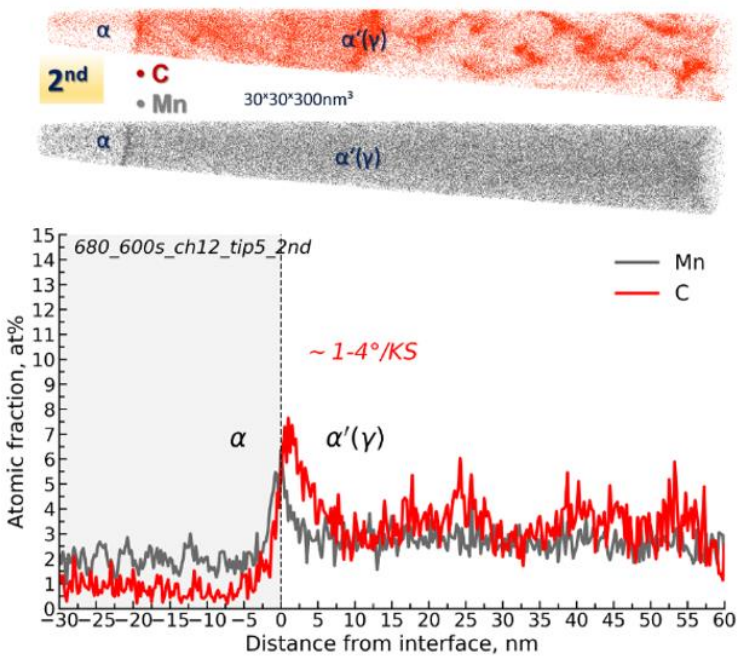

Figure 3.25. *3D reconstructions and concentration profiles of C and Mn atoms across the 2nd interface of 680_600s_ch12 of:* ***(a)*** *tip2_2nd;* ***(b)*** *tip3_2nd;* ***(c)*** *tip5_2nd; (see* ***Figure 3.24****).*

The results of the APT analyses of both interfaces of tip3 extracted from the region shown in **Figure 3.26** (a) are presented in **Figure 3.26** (b)-(c). Both profiles show a strong segregation of Mn at the interface with similar excess of 12.8 $atom/nm^2$ and 11.6 $atom/nm^2$ for tip3_1st and tip3_2nd, respectively. However, the slightly different shapes of the profiles can be noticed. In the case of tip3_1st, the Mn profile has a relatively sharp and symmetrical peak with a width of approximately 6 nm. The Mn content is equal from both austenite and ferrite sides (~ 2.1 at%), but the depletion of Mn just before the interface from the ferrite side is clearly observed. At the same time, the Mn peak, in the case of tip3_2nd, has a sharper shape from the ferrite side and extends over a distance of about 8-10 nm in austenite. Also, the average concentration in austenite side is clearly higher than in ferrite.

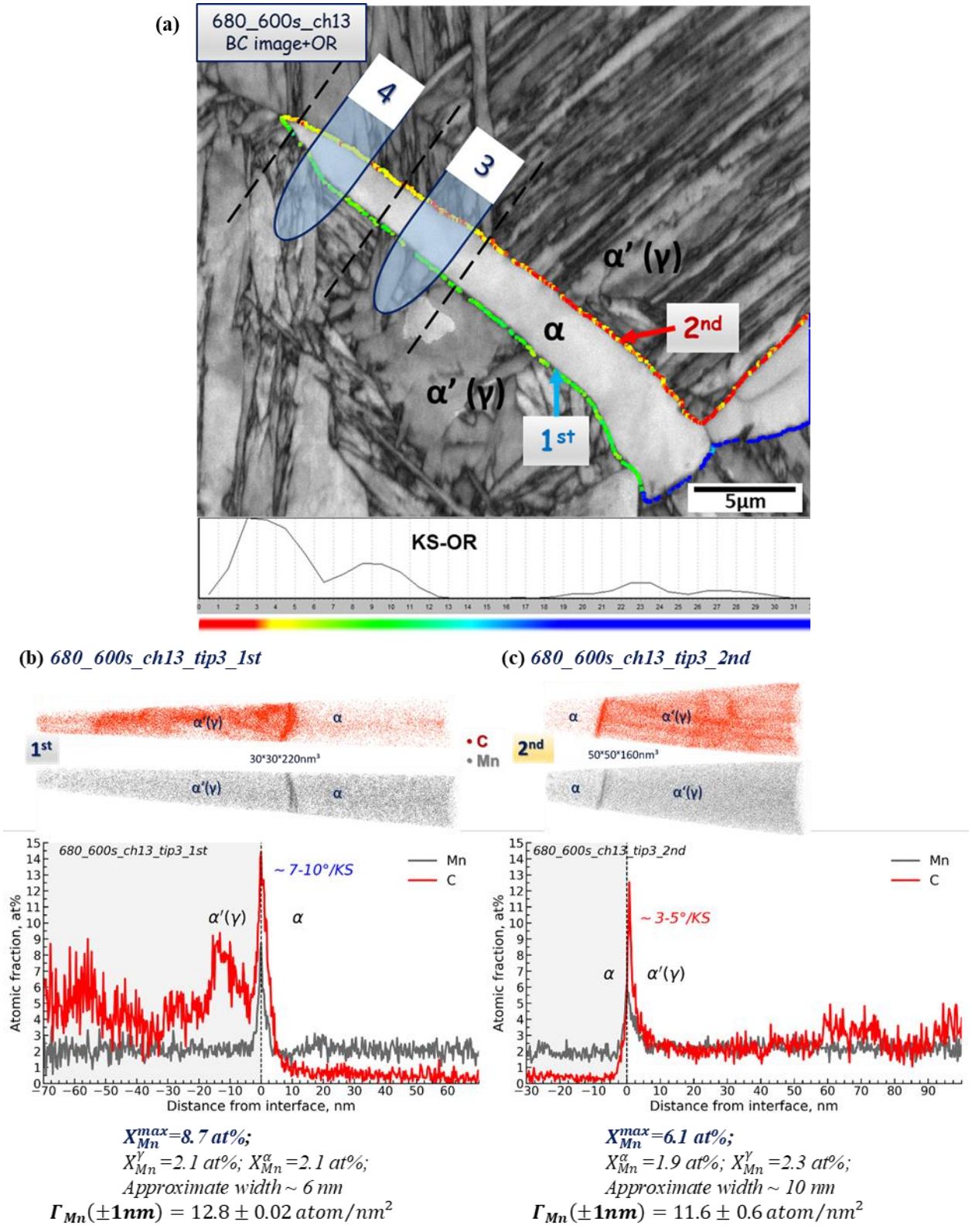

Figure 3.26. ***(a)*** *IQ map of selected ROIs with the thin allotriomorph ferrite grains formed after isothermal holding at 680°C during 600s (**680_600s_ch13**). Colors at α'(γ)/α interfaces represent the orientation relation between ferrite and prior austenite at 680 °C. It is expressed as the orientation difference with respect to the KS orientation relationship. 3D reconstructions and concentration profiles of C and Mn atoms across the 1st,* ***(b),*** *and 2nd (c) α/γ interfaces of tip3.*

Another example of strong Mn segregation at the interface during 600s isothermal holding at 680°C can be observed in **Figure 3.27** (b). The profile was measured for tip2 across the interface, noted as the 1st one in **Figure 3.27** (a).

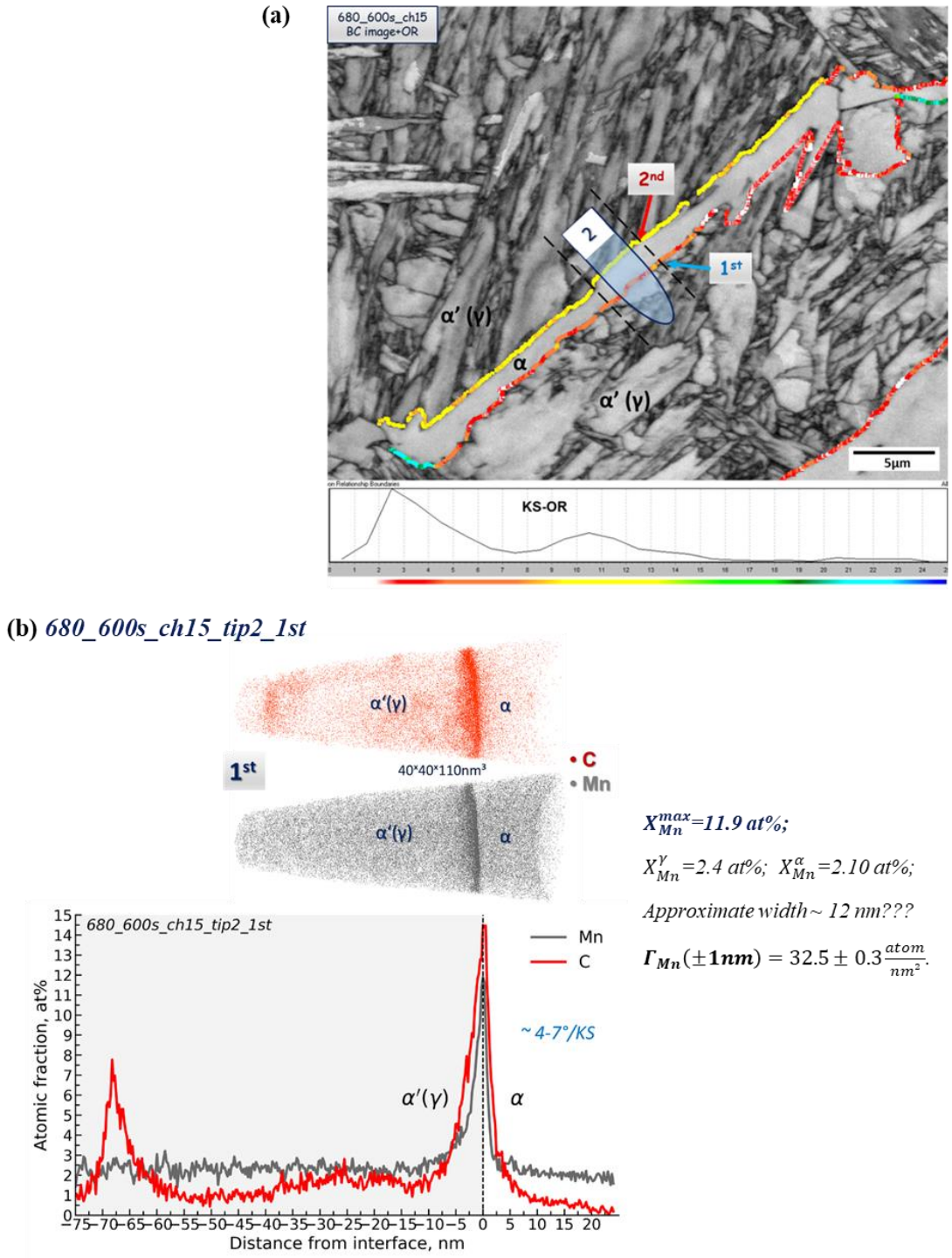

Figure 3.27. ***(a)*** *IQ map of selected ROIs with the thin allotriomorph ferrite grains formed after isothermal holding at 680°C during 600s (**680_600s_ch15**). Colors at α'(γ)/α interfaces represent the orientation relation between ferrite and prior austenite at 680 °C. It is expressed as the orientation difference with respect to the KS orientation relationship.* ***(b)*** *3D reconstructions and concentration profiles of C and Mn atoms across the 1st, of tip2.*

Figure 3.28 (b)-(c) illustrate two composition profiles measured for tip3 and tip4 by the APT analysis across the 1st interface shown in **Figure 3.28** (a). These composition profiles show a low amount of accumulated Mn atoms at the interface. They are very similar to the profiles observed in the case of 100 s (see **Figure 3.19** and **Figure 3.21**). Taking into account the dimension of the considered ferrite (width ~ 0.8 µm) and the behavior of the Mn profiles, it is possible to assume that the growing time of ferrite in **Figure 3.28** (a) does not correspond to 600 s. More likely, it was nucleated significantly after the beginning of holding time.

Table 11 summarises the main results of the observed composition profiles measured for 600 s at 680°C. All the presented composition profiles of Mn exhibit similar features. However, the observed variation in the shapes of Mn profiles at the same condition can indicate the different stages of Mn redistribution across the α'(γ)/α interfaces. The scattering of the amount of the Mn atoms accumulated at the interface can possibly be related to the different nucleation times of the in ferrite grains.

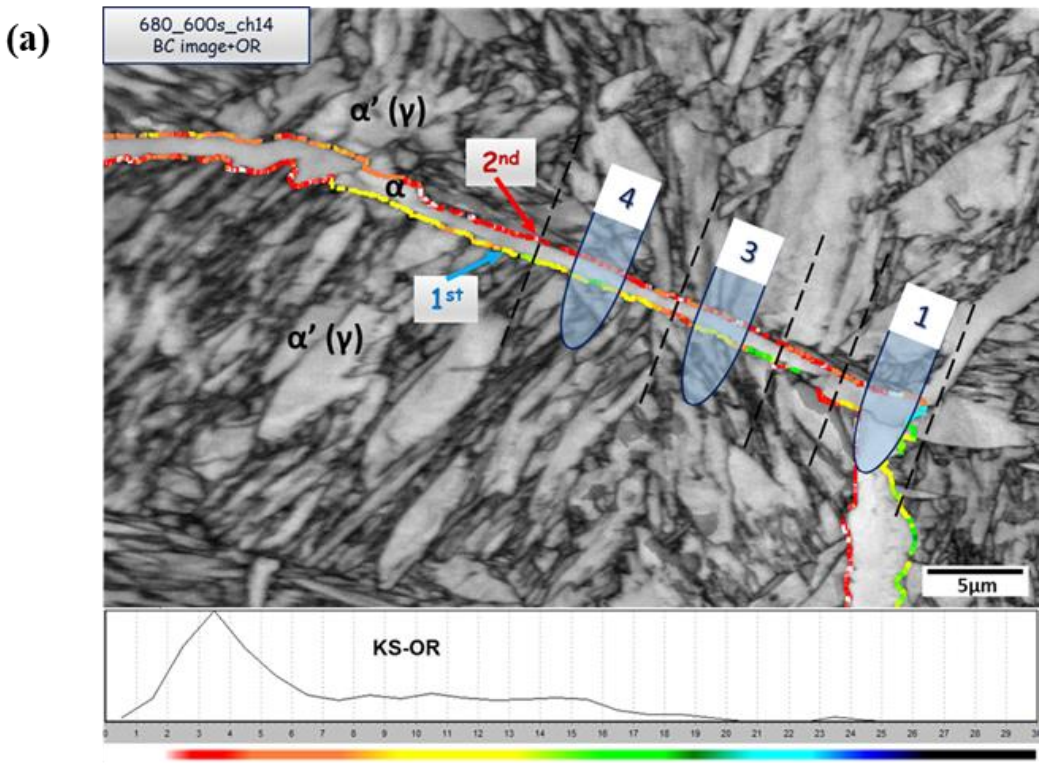

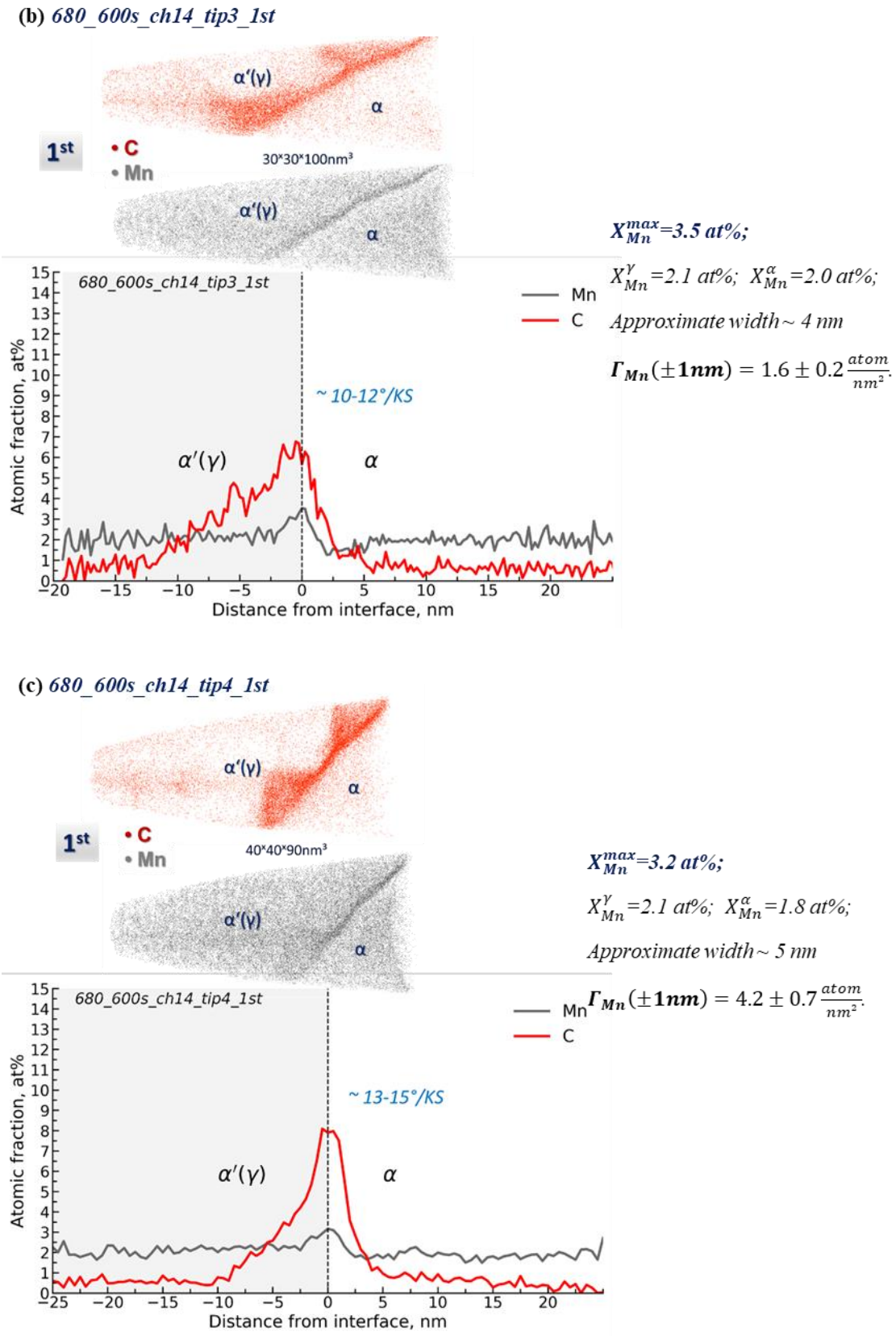

Figure 3.28. **(a)** *IQ map of selected ROIs with the thin allotriomorph ferrite grains formed after isothermal holding at 680°C during 600s (**680_600s_ch14**). Colors at α'(γ)/α interfaces represent the orientation relation between ferrite and prior austenite at 680 °C. It is expressed as the orientation difference with respect to the KS orientation relationship.* **(b)** *and* **(c)** *3D reconstructions and concentration profiles of C and Mn atoms across the 1st, of tip3 and tip 4, respectively.*

Table 11. *The main results of the observed composition profiles measured for 600 s at 680°C*

Condition	tip#	KS-OR	X^{α}_{Mn}, $at\%$	X^{γ}_{Mn}, $at\%$	~w, nm	X^{Max}_{Mn}, at%	Γ_{Mn} $(\pm 1nm)$, $atom/nm^2$
T=680°C t=600s	**Chunk 8**						
	tip1_1st	7-11	1.9	2.3	5	5.9	**11.9±0.4**
	tip2_1st	7-11	1.7	2.3	5	5.7	**6.1±0.6**
	tip3_1st	7-11	1.7	2.2	4.5	6.5	**9.7±0.6**
	tip4_1st	7-11	2.0	2.2	4	5.0	**7.1±0.2**
	Chunk 12						
	tip2_2nd	1-4	1.8	2.4	4	4.9	**14.1±0.5**
	tip3_2nd	1-4	1.9	2.9	5	6.0	**7.5±1.0**
	tip5_2nd	1-4	2.0	2.7	6	6.4	**9.0±0.7**
	Chunk 13						
	tip3_1st	7-10	2.1	2.1	6	8.7	**12.7±0.02**
	tip4_1st	7-10	1.4	2.1	4.5	4.3	**4.9±0.6**
	tip3_2nd	3-5	1.9	2.3	6	6.1	**11.6±0.6**
	Chunk 14						
	tip1_1st	α/α	2.0	1.8	4	3.7	**3.3±0.2**
	tip3_1st	10-12	2.0	2.1	4	3.5	**1.6±0.2**
	tip4_1st	13-15	1.8	2.1	5	3.2	**4.16±0.66**
	Chunk 15						
	tip2_1st	?	2.10	2.37	12???	11.90	**32.47±0.28?**

3.6.3 Austenite/ferrite transformation interface after 3h at 680°C

The set of results presented in this paragraph is dedicated to the analysis of the austenite/ferrite interfaces after the 3h of transformation at 680°C which is the longest at this temperatures. Again, several thin allotriomorph ferrites formed at prior austenite grain boundaries have been selected for APT analyses. The first selected region is shown in **Figure 3.29**. The ferrite film length is about 40 µm, while its width varies in the range of 1.4 – 1.7 µm. The interface noted as 2nd has a relatively straight morphology, with a near KS orientation relation between formed ferrite and prior austenite at 680°C. The 1st interface has a more wave-like shape with a wide spectrum of misorientations from KS (from 17° to 32°). APT analyses were very successful, as both interfaces (1st and 2nd) were analyzed for several tips along the considered ferrite grain. 3D reconstructions of the analyzed volumes for C and Mn with the corresponding composition profiles are shown in **Figure 3.30.**

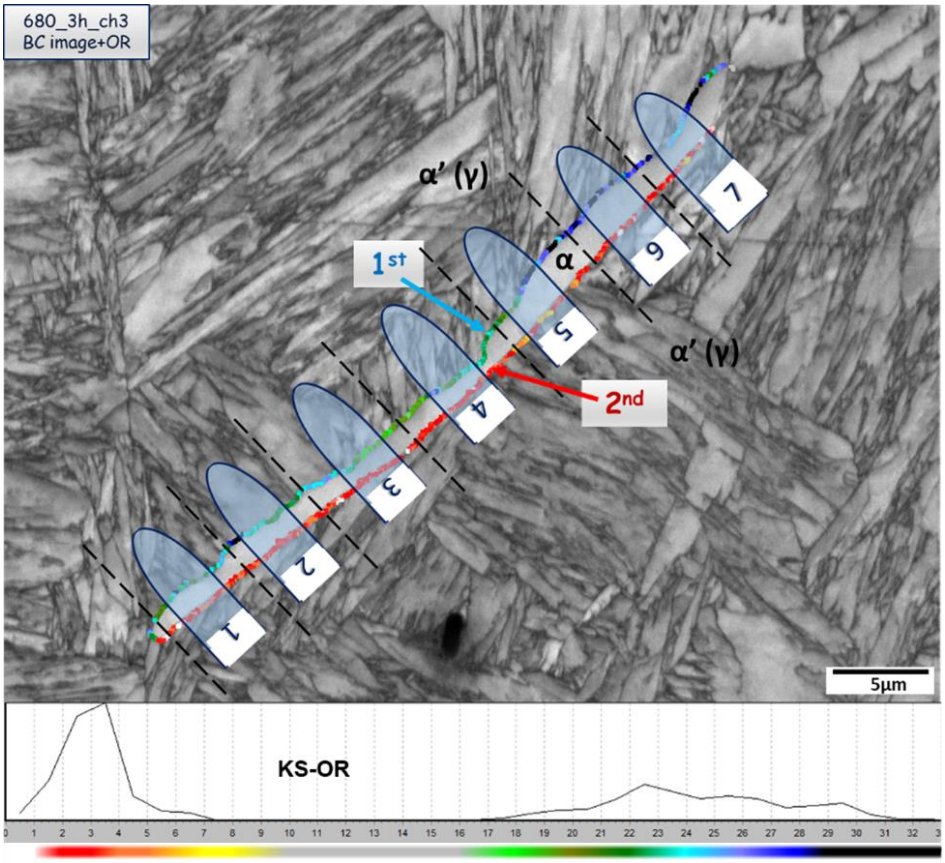

Figure 3.29. *Image quality (IQ) map of the selected region with the allotriomorph ferrite formed at the prior austenite grain boundary after isothermal holding at 680°C during 600s. This region is coded as* **680_3h_ch3**. *Colors at two α' (γ)/α interfaces (1st and 2nd) represent the orientation difference with respect to KS-OR of the initial ferrite – austenite interfaces at 680 °C.*

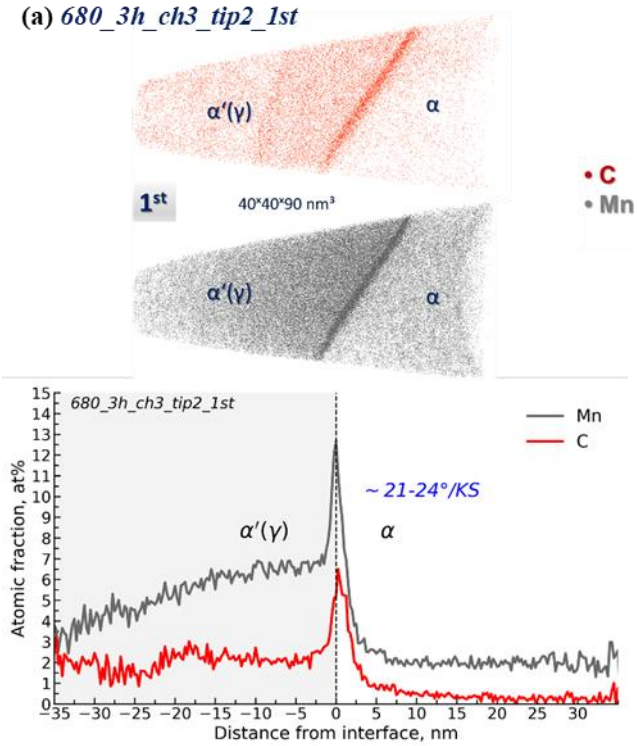

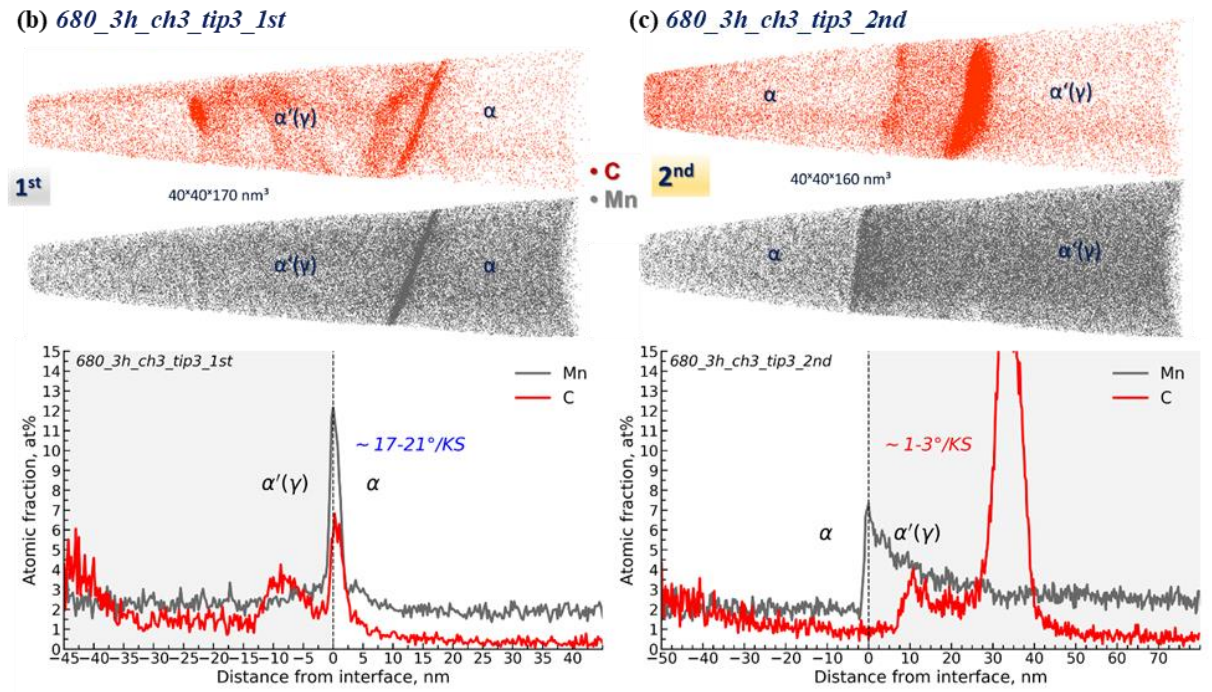
(b) 680_3h_ch3_tip3_1st
α'(γ)
α
1st
40*40*170 nm³
• C
• Mn
680_3h_ch3_tip3_1st
Mn
C
~ 17-21°/KS
Atomic fraction, at%
Distance from interface, nm
(c) 680_3h_ch3_tip3_2nd
2nd
40*40*160 nm³
680_3h_ch3_tip3_2nd
~ 1-3°/KS

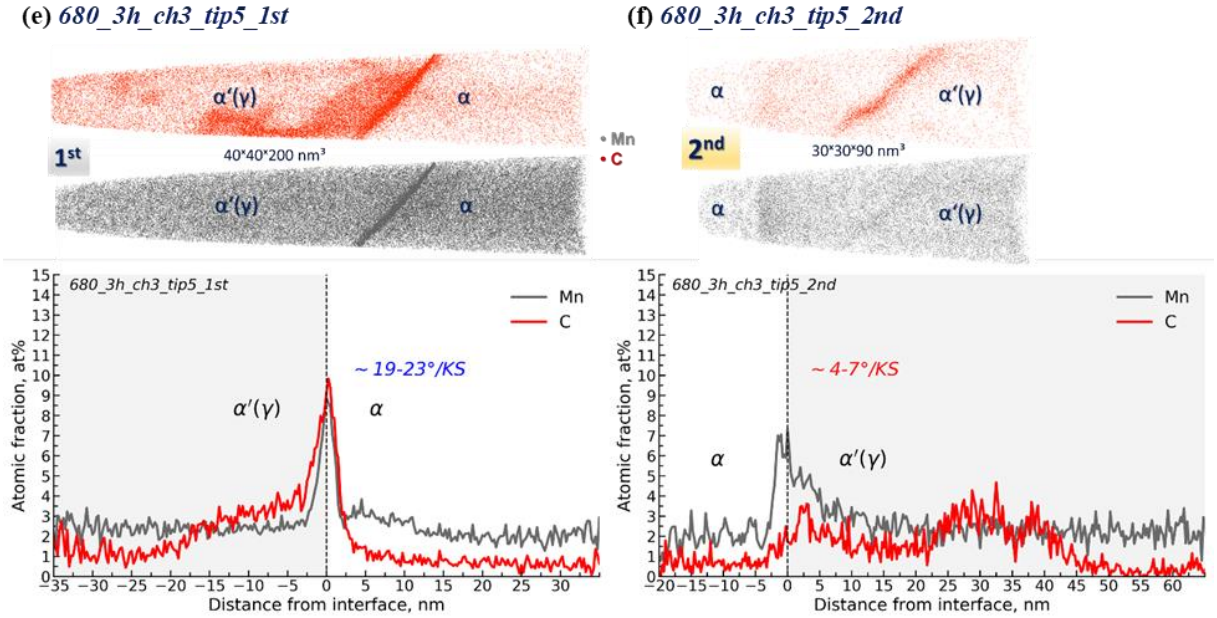
(e) 680_3h_ch3_tip5_1st
α'(γ)
α
1st
40*40*200 nm³
• Mn
• C
680_3h_ch3_tip5_1st
Mn
C
~ 19-23°/KS
Atomic fraction, at%
Distance from interface, nm
(f) 680_3h_ch3_tip5_2nd
2nd
30*30*90 nm³
680_3h_ch3_tip5_2nd
~ 4-7°/KS

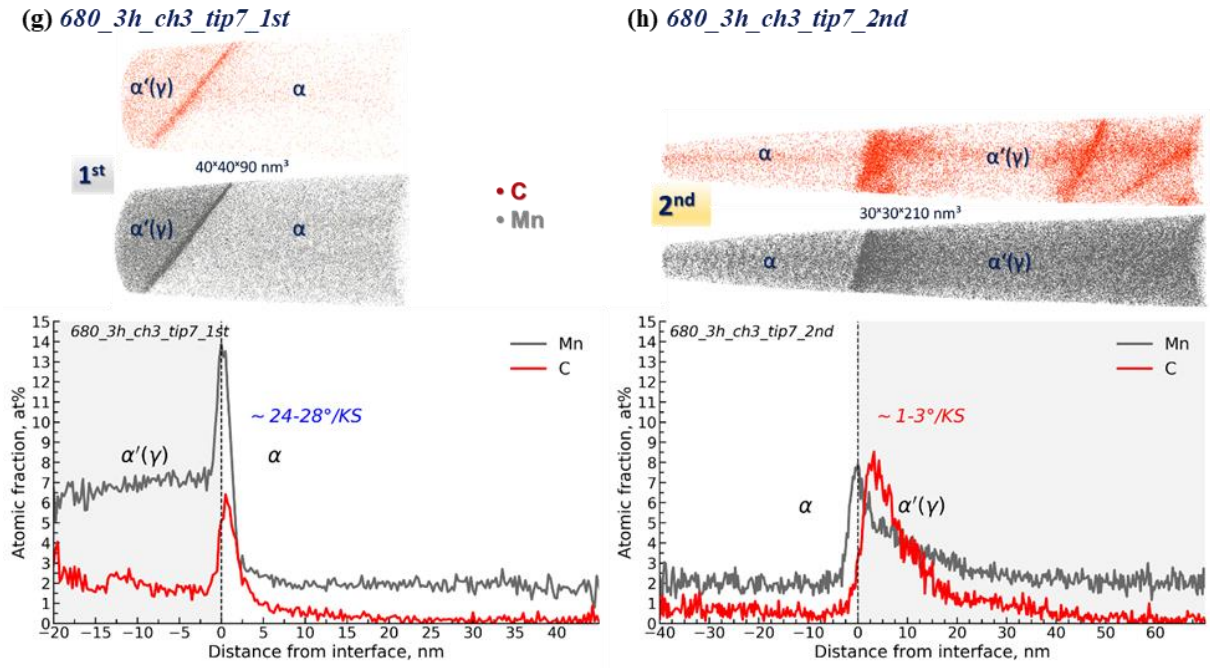

Figure 3.30. *3D reconstructions and concentration profiles of C and Mn atoms across the 1st, and 2nd α/γ interfaces of 680_3h_ch3, see* **Figure 3.29**.

The first observation from the profiles in **Figure 3.30** is that the Mn segregations are present at both interfaces (1st and 2nd). It indicates that both interfaces are mobile, but the significant difference between the Mn composition profiles may reflect different interface mobilities possibly connected to the ORs. Analyzing the Mn profiles across the 2nd interface with a near KS-OR, the long-range diffusion of Mn into austenite is clearly observed (see **Figure 3.30**(c, f, h)). All four profiles exhibit very similar features: (i) the gradients of Mn composition into austenite extend over more than 50 nm from the interface, (ii) Mn compositions reach about 7.5 at% at the interface, (iii) Mn peaks from the ferrite side are sharp, and the average Mn content in ferrite is lower as compared to the austenite one. Such a gradient of Mn composition into the parent austenite is expected for a slow ferrite growth and long times when Mn atoms have enough time for long-range diffusion into austenite.

Regarding the Mn profiles across the 1st interface (**Figure 3.30** (a,b,e,g)), two situations are observed. The first one is the presence of a sharp (relatively symmetrical) peak of Mn at the interface, **Figure 3.30** (b and e). The maximum composition of Mn at the interface reaches about 12.6 at% (**Figure 3.30** (b)) and 8.9 at% (**Figure 3.30** (e)), respectively. The second situation is the presence of both Mn peak at the interface and long-range diffusion into austenite**, Figure 3.30** (a and g). The maximum Mn contents at the interface are about 12.7 at% and 13.9 at% (again, the excesses can not be calculated for these types of profiles).

Similar Mn redistributions across the interface are observed in the second set of APT measurements that were performed for the interfaces (1st and 2nd) presented in Figure 3.31**.** The

examined ferrite grain has a length of about 30 µm, and the width varies in the range of 1.0 – 2.0 µm and a large misorientation with respect to KS OR from both sides. In addition, it can be noticed that the ferrite film consists of three ferrite grains (part 1 – schematically illustrated position of tip 1, part 2 – position of tips 2 and 3, part 3 – tips 4, 5, 6) with a slightly different crystallographic orientation (see the IPF Z color map). The results of the APT analyses are given in **Figure 3.32.**

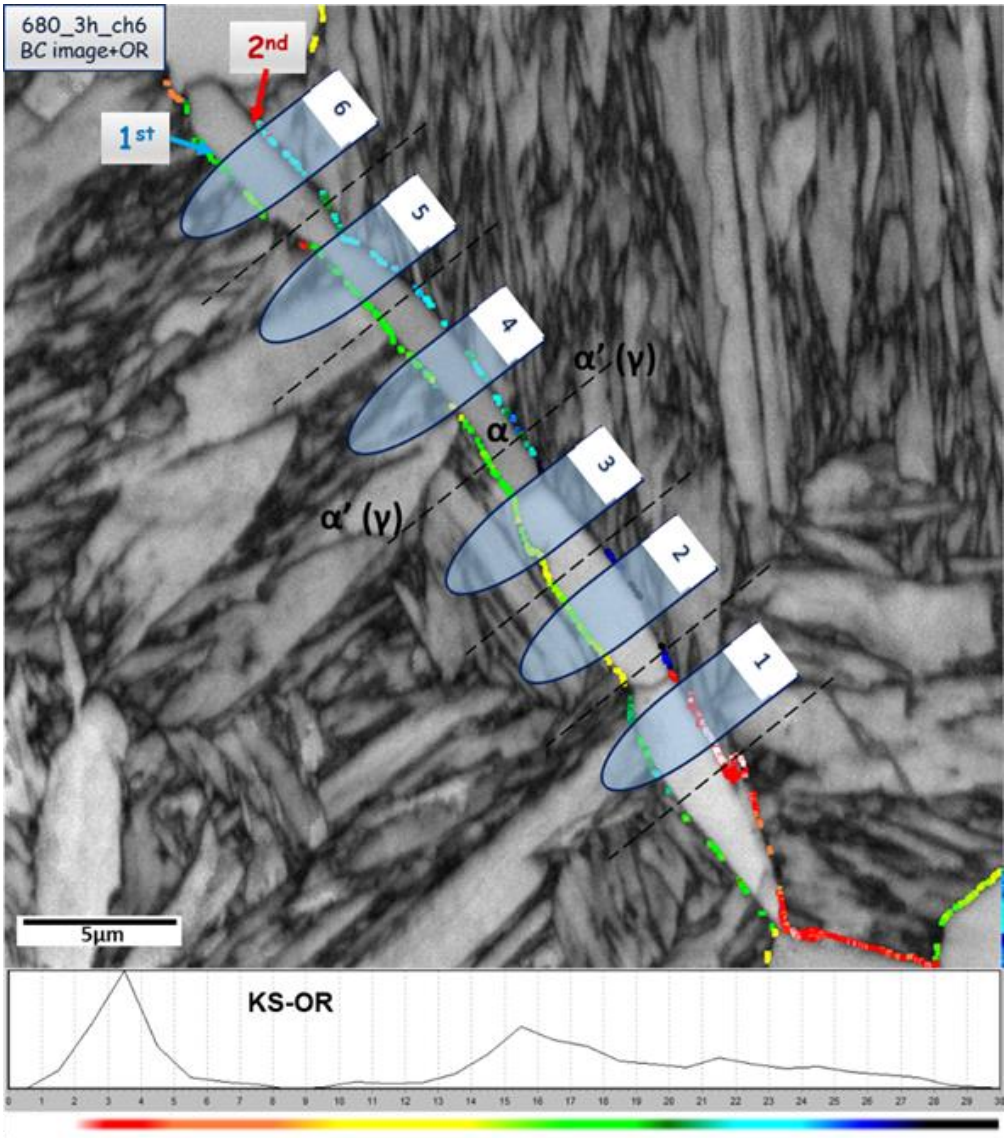

Figure 3.31. *Image quality (IQ) map of the selected region with the allotriomorph ferrite formed at the prior austenite grain boundary after isothermal holding at 680°C during 600s. This region is coded as* **680_3h_ch6.** *Colors at two α' (γ)/α interfaces (1st and 2nd) represent the orientation difference with respect to KS-OR of the initial ferrite – austenite interfaces at 680 °C.*

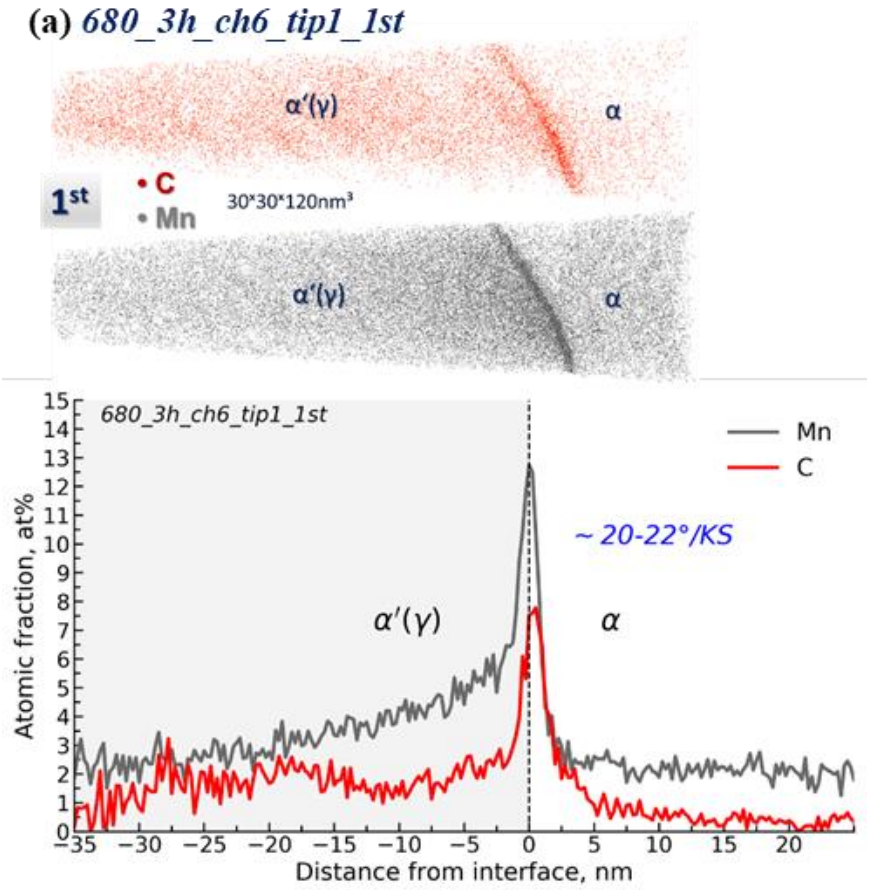
(a) 680_3h_ch6_tip1_1st
α'(γ)
α
1st
• C
• Mn
30*30*120nm³
α'(γ)
α
680_3h_ch6_tip1_1st
Mn
C
~ 20-22°/KS
α'(γ)
α
Atomic fraction, at%
Distance from interface, nm

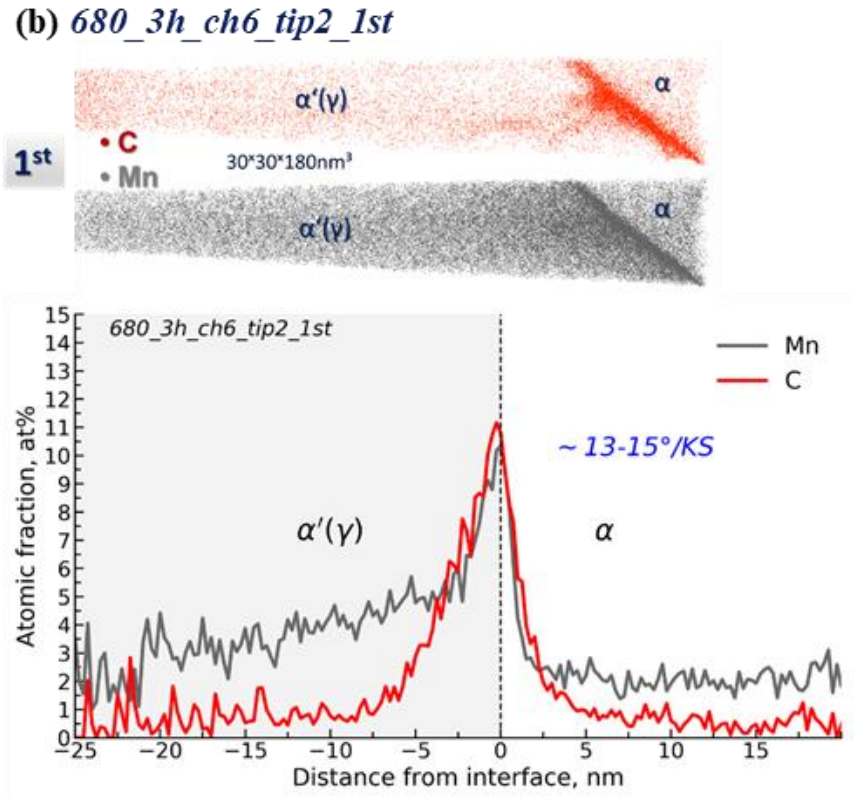
(b) 680_3h_ch6_tip2_1st
α'(γ)
α
1st
• C
• Mn
30*30*180nm³
α'(γ)
α
680_3h_ch6_tip2_1st
Mn
C
~ 13-15°/KS
α'(γ)
α
Atomic fraction, at%
Distance from interface, nm

(c) *680_3h_ch6_tip3_1st*

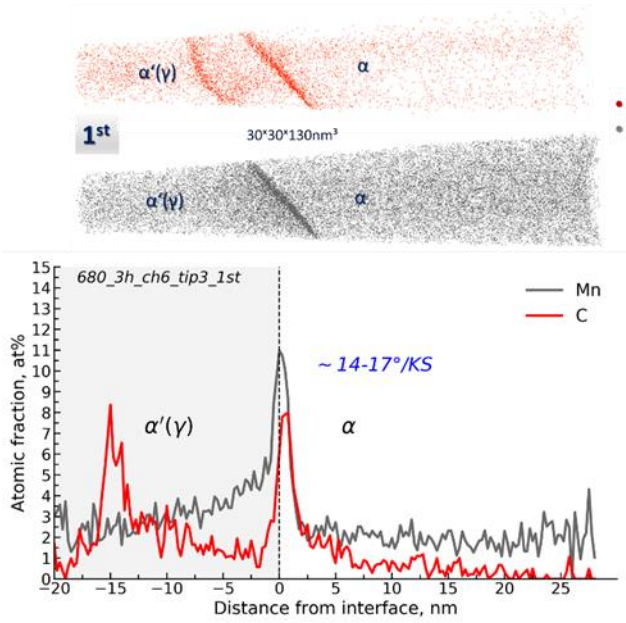

(d) *680_3h_ch6_tip3_2nd*

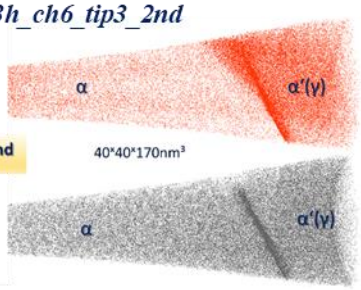

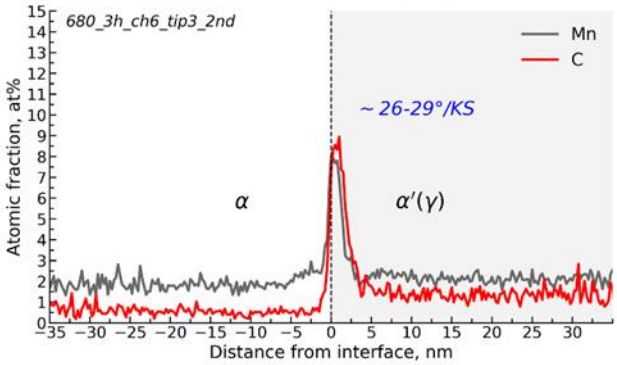

(e) *680_3h_ch6_tip4_1st*

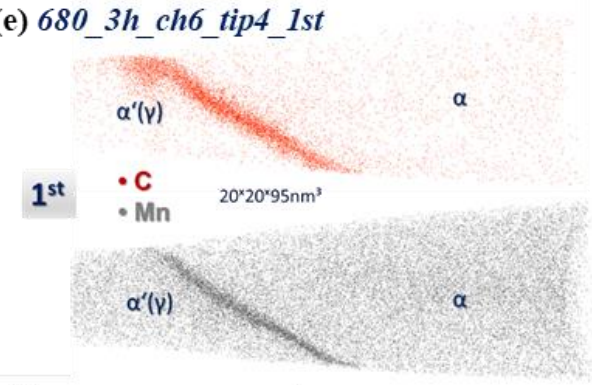

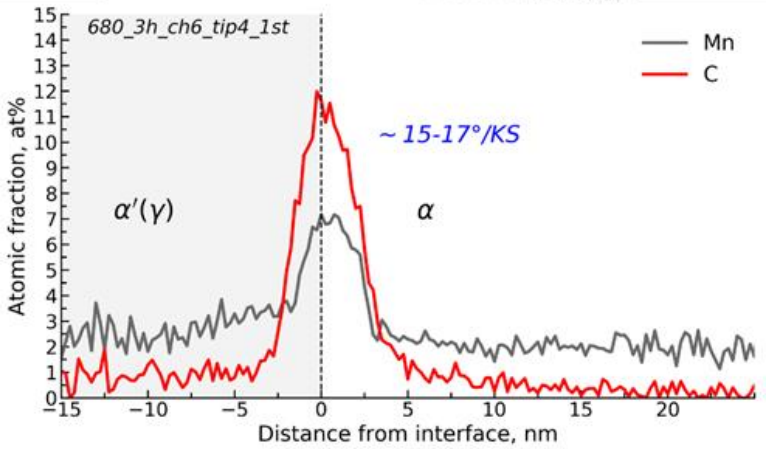

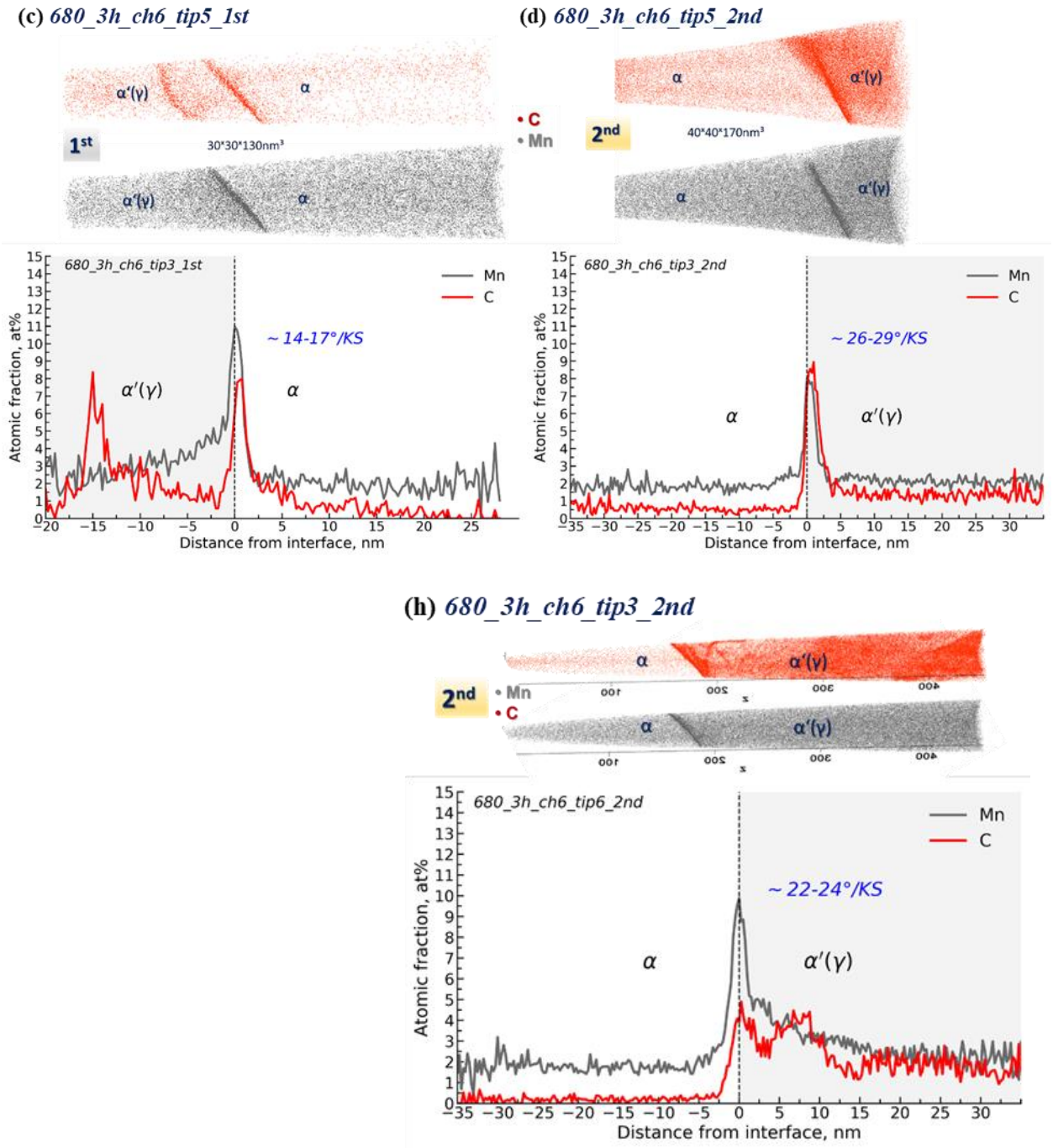

Figure 3.32. *3D reconstructions and concentration profiles of C and Mn atoms across the 1st, and 2nd α/γ interfaces of 680_3h_ch6, see* **Figure 3.31**.

The measured composition profiles across both interfaces show similar behaviors of Mn as across the 1st interfaces of chunk 3 (with the larger misorientation with respect to KS-ORs) **Figure 3.32**. Again two types of Mn redistribution across the interfaces are observed. The sharp Mn peak is observed in the case **Figure 3.32** (d). In addition, there are the presence of both Mn peak and long-range diffusion into austenite for the rest of the presented profiles in **Figure 3.32**. Moreover, the long-range diffusion is more pronounced in profiles a-c, g and somewhat less pronounced in profiles a-f, h. From these data, it is possible to assume that both interfaces are

mobile with a relatively similar rate, and the slight variations of Mn long-range diffusion can be related to the local variation of interface velocity. A similar redistribution of Mn atoms across the interfaces on both sides of the ferrite grain is observed in **Figure 3.33.** However, in this case (*680_3h_ch4)*, contrary to the *680_3h_ch6*, the ORs at the 2nd interface is near KS. **Table 12** summarises the main parameters of the observed composition profiles measured for the 3h of transformation at 680°C.

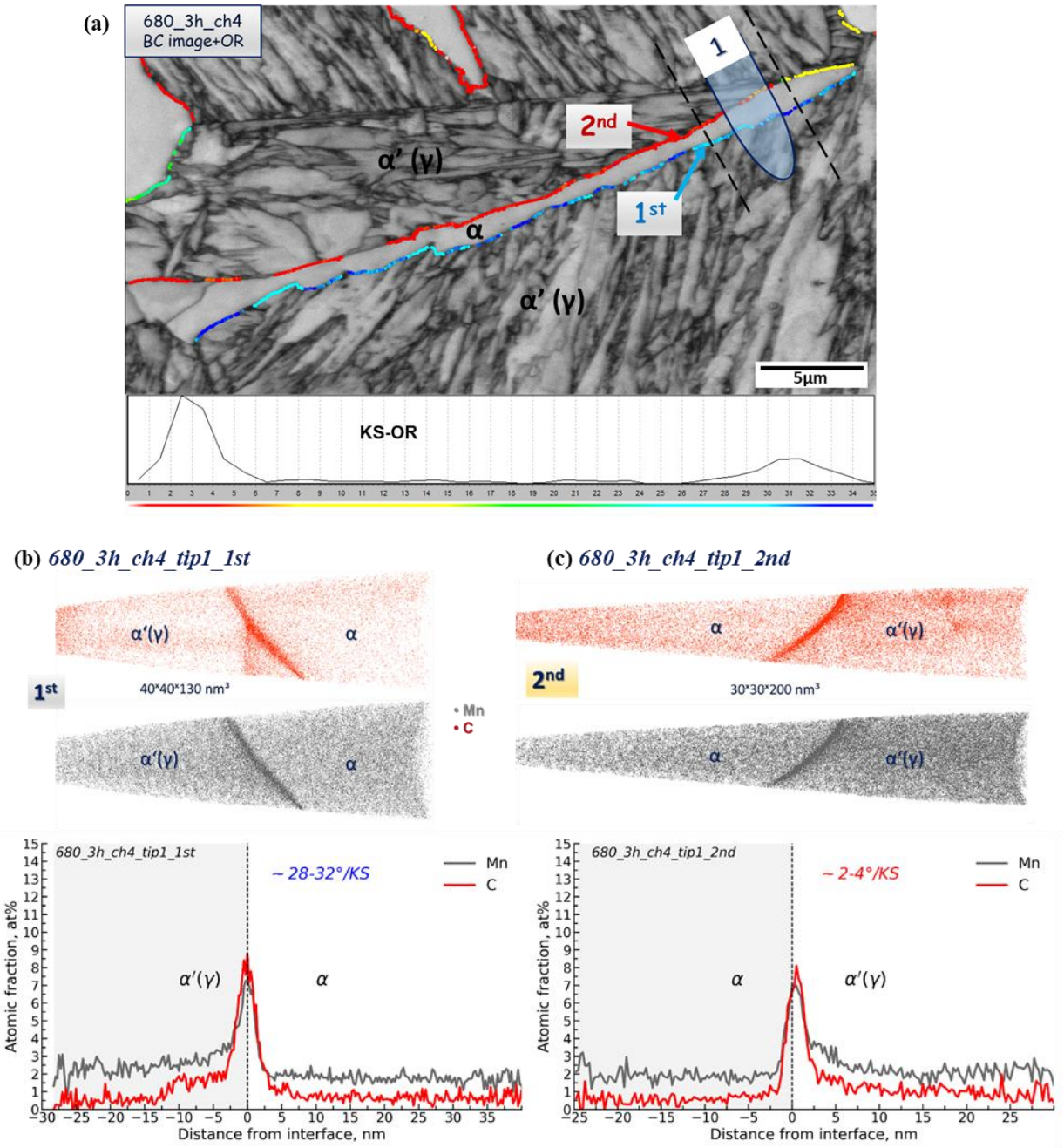

Figure 3.33. (a) *Image quality (IQ) map of the selected region with the allotriomorph ferrite formed at the prior austenite grain boundary after isothermal holding at 680°C during 3h. This region is coded as* **680_3h_ch4**. *Colors at two α'(γ)/α interfaces (1st and 2nd) represent the orientation difference with respect to KS-OR of the initial ferrite – austenite interfaces at 680 °C.* ***(b)*** *and* ***(c)*** *3D reconstructions and concentration profiles of C and Mn atoms across the 1st, and 2nd α/γ interfaces of tip 1, respectively.*

Table 12. *The main parameters of the observed composition profiles measured for the 3h of transformation at 680°C*

Condition	tip#	KS-OR	X^{α}_{Mn}, $at\%$	X^{γ}_{Mn}, $at\%$	~w, nm	X^{Max}_{Mn}, at%	Γ_{Mn} $(\pm 1nm)$, $atom/nm^2$
T=680°C t=3h	**Chunk 3**						
	tip2_1st	21-24	2.0	6.4?	?	12.7	?
	tip3_1st	17-21	2.2	2.5	4	12.2	**21.7±0.3**
	tip5_1st	19-23	2.6	2.4	5	8.9	**14.2±0.2**
	tip7_1st	24-28	2.0	6.9?	?	13.9	?
	tip3_2nd	1-3	2.0	3.0	?	7.3	?
	tip4_2nd	3-5	2.0	2.4	?	7.5	?
	tip5_2nd	4-7	2.0	2.3	?	7.3	?
	tip7_2nd	1-3	2.0	2.4	?	7.9	?
	Chunk 4						
	tip1_1st	28-32	1.8	2.6	6	7.3	**15.6±0.8**
	tip1_2nd	2-4	1.8	2.1	4.5	7.0	**17.3±0.4**
	Chunk 6						
	tip1_1st	20-22	2.22	4.0	?	12.7	?
	tip2_1st	13-15	2.03	4.1	?	10.3	?
	tip3_1st	14-17	2.01	3.0	?	11.0	?
	tip4_1st	15-17	2.10	2.8	5	7.2	**14.9±0.8**
	tip5_1st	17-20	2.08	2.6	6.5	8.9	**18.1±0.5**
	tip3_2nd	26-29	1.82	2.1	4	8.0	**19.1±0.4**
	tip5_2nd	22-24	1.78	2.5	?	9.4	?
	tip6_2nd	22-24	1.75	2.6	?	9.9	?

? – since the long-range diffusion of Mn into austenite is observed in the current compositions profiles, the Mn excess was not calculated in these cases (see more details in paragraph (2.7)).

3.6.4 Austenite/ferrite interfaces after 3 h at 720°C

The final set of results was obtained after holding for 3 h at 720°C. The kinetics of ferrite growth, as was it observed by dilatometry, is very slow at this condition. Even after 3 h of only about 2% of ferrite was formed, **Figure 3.2** (a). Therefore, data are only collected after this holding time (3h) since it will be experimentally difficult to localize and extract the region with the interface of interest for a shorter time.

Several regions with the thin allotriomorph ferrite grain formed at prior austenite grain boundaries were examined, and results are shown in **Figure 3.34**. The image quality (IQ) maps of the three selected ROIs with the measured ORs that corresponded to the prior OR at austenite/ferrite interfaces at 720°C are shown in **Figure 3.34** (**(a)** *720_3h_ch2*, **(c)** *720_3h_ch3* and **(e)** *720_3h_ch4*). In the case of ch2, only the 1st interface of tip1 was analyzed by APT (**Figure 3.34** (b)), and 2nd interface of tip2 (**Figure 3.34** (d)) and 1st interface of tip1 (**Figure 3.34** (f)) were analyzed in the case of ch3 and ch4, respectively.

The segregation of Mn can be observed in all the profiles shown in **Figure 3.34.** The gradient behavior of Mn profile into the parent austenite side is clearly observed in (b) and (d). In the case of **Figure 3.34** (b), the Mn content at the interface reaches around 4.5 at% and 5.5 at% - in **Figure 3.34** (b), while in both cases, the average Mn content in the ferrite is about 1.6 at% that is lower than in austenite (2.3 at%). Concerning the gradient of Mn composition into the prior austenite grain, it extends to several tens of nm (at least 30 nm and 60 nm in the case of *720_3h_ch2_tip1_1st* and *720_3h_ch3_tip2_2nd*, respectively. However, in both cases, the average Mn content at the last 10 nm of the profile from the austenite side is about 2.3 at%, which is higher than the nominal composition (2 at%). Therefore, it is possible that in both cases, the gradients of Mn extend further into austenite before the nominal composition is reached, which not be proved, due to the limited analyzed depth during the APT measurements.

A somewhat different Mn profile is observed in the cases shown in **Figure 3.34** (f), where the misorientation at the interface is 11-14° with respect to KS-OR. In this case, there is no long-range diffusion of Mn into austenite. Only the peak of Mn with the maximum content of 5.1 at% at the interface is observed. The mean Mn concentration in ferrite is about 1.8 wt% and in austenite is 2.2 at%.

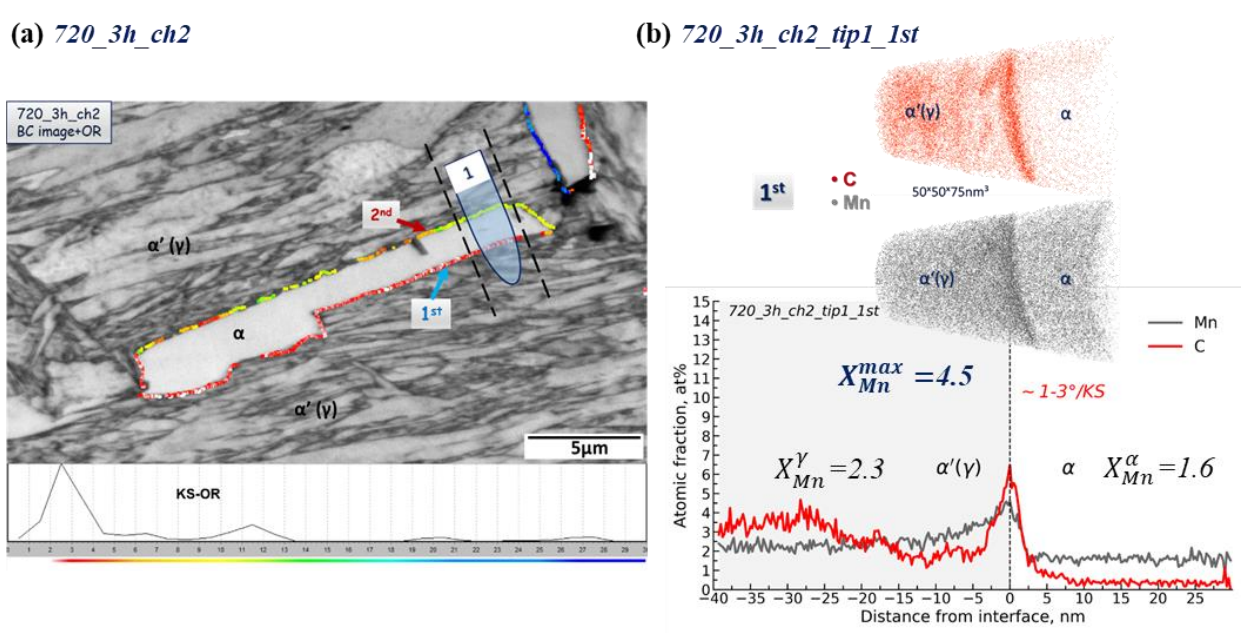

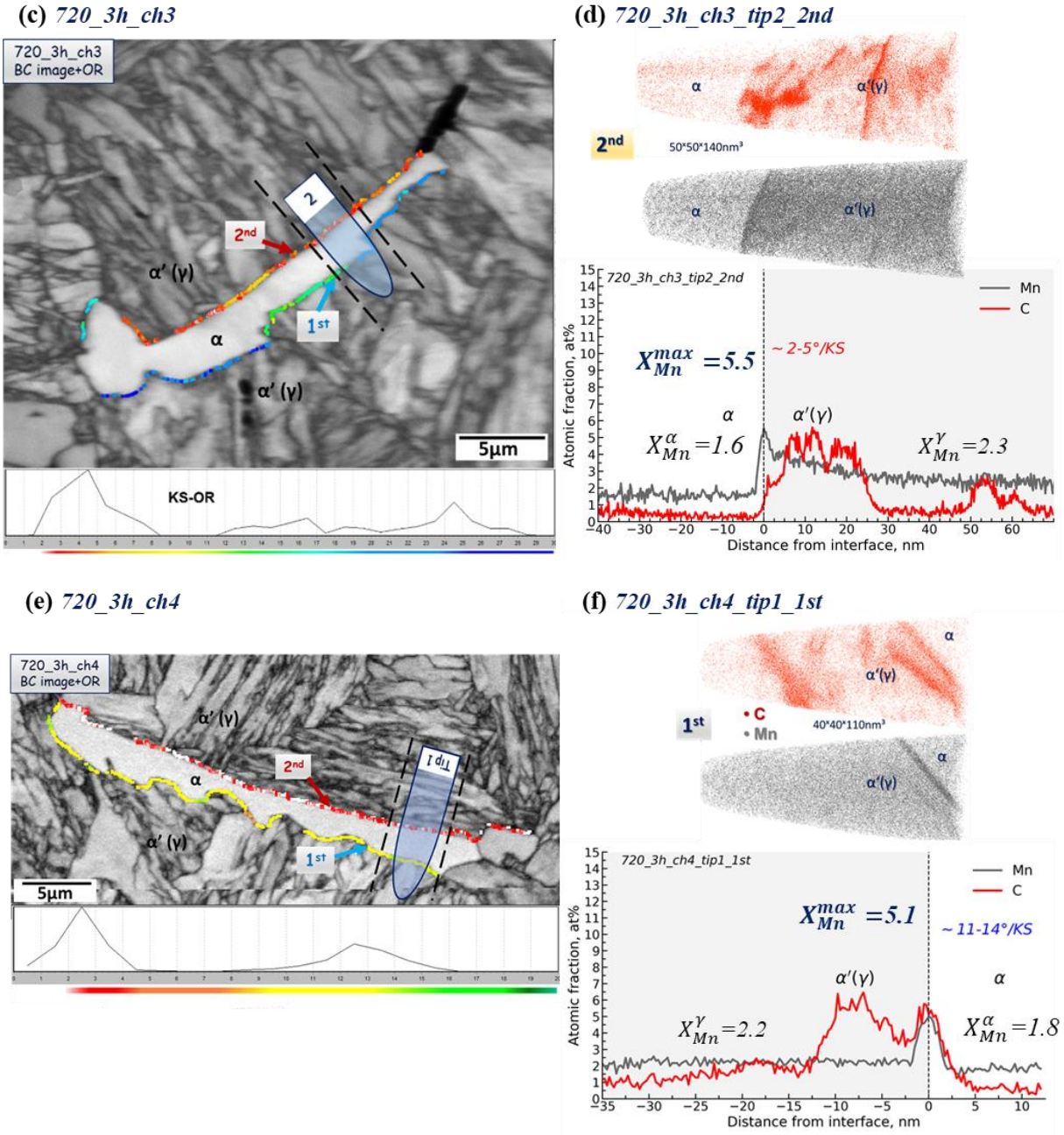

Figure 3.34. ***(a)*** *Image quality (IQ) map of the selected allotriomorph ferrite formed at the prior austenite grain boundary after isothermal holding at 720°C for 3h and 3D reconstructions with concentration profiles of C and Mn atoms across the α/γ interfaces:* ***(a-b)*** ***720_3h_ch2****,* ***(c-d)*** ***720_3h_ch3****,* ***(e-f)*** ***720_3h_ch4****. Colors at two α′(γ)/α interfaces (1st and 2nd) represent the orientation difference with respect to KS-OR of the initial ferrite – austenite interfaces at 720 °C.*

3.7 Conclusions

The experimental results of the austenite/ferrite interfaces investigation at the nanoscale using APT in the domain of three transformation temperatures: 625 °C, 680°C, and 720 °C were presented in this chapter. The segregation of both Mn and C at the α'(γ)/γ interface was founded in most successfully analyzed samples within this work (except only a few samples).

ORs between the parent austenite and formed ferrite have been determined by reconstructing EBSD data measured at room temperature (for martensite-ferrite microstructure) using Merengue2 software. The obtained data demonstrated the tendency for α/γ interfaces to satisfy the KS-ORs. In most of the considered ferrite within this work, at one side, the α/γ interface with the adjusted prior austenite grain had a near KS orientation with deviation in the range of 0 - 4°, while the other one typically deviates with respect to KS approximately in the range of 7-15° (or less). The small number of interfaces with the larger misorientation with respect to the KS-OR have also been found. Similar observations have been reported from the in-situ EBSD investigation in [48]. In addition, from the investigated cases within this work, it can be noticed that interfaces with near KS-ORs tend to have more straight (planar) morphology, while the morphology of the interfaces with higher misorientation variate from case to case. Also, at the lower transformation temperature of 625 °C (compared to 680 °C and 720 °C), more ferrite grains did not have a near KS-OR at any of the interfaces but had a relatively flat shape at both sides: see **Figure 3.13** -**Figure 3.17** (a).

Although various interface morphologies were found, exploring all the data, some common tendencies for the Mn behaviors across the α/γ interface are observed, and several types of Mn profiles can be defined:

- *homogeneous Mn distribution through the interface*: see examples in **Figure 3.7** (e), **Figure 3.8** (b, c), **Figure 3.10** (d), **Figure 3.13**(e);
- *the initial stage of Mn partitioning through the interface* that is characterized by the enrichment into austenite and depletion into ferrite: see nice example in **Figure 3.13** (d), **Figure 3.14** (c), **Figure 3.19** (c), **Figure 3.28** (b-c);
- *Mn accumulation at the interface*, when the relatively symmetrical peaks of Mn are observed;
- *the presence of both Mn peak and long-range diffusion of Mn into austenite*: see **Figure 3.17** (b), **Figure 3.19** (b), **Figure 3.25** (a), **Figure 3.30** (a, g), **Figure 3.32** (a, c, h), **Figure 3.34** (c);
- *only the long-range diffusion of Mn into austenite*: see **Figure 3.30** (c, f, h), **Figure 3.34** (a).

At 680°C and 720°C, the long-range diffusion of Mn into austenite almost always was observed at the interfaces with near KS-ORs. In contrast, it was observed only for a longer transformation (3h) time at the interfaces with larger misorientation with respect to KS. This tendency wasn't observed at 625°C.

Chapter 4

Atomistic modeling of fcc-to-bcc phase transformation

In the previous chapters, it was emphasized that the mobility of the α/γ transformation interface is one of the crucial parameters controlling the kinetic of austenite to ferrite phase transformation. This mobility depends on many factors such as a complex interaction of the alloying elements with a moving interface, the orientation relationship between phases at the interface and interface properties (coherency, thickness, shape). The movement of this interface involves a collective movement of atoms at a distance smaller than interatomic space. The available experimental techniques can not track this dynamic, while the atomistic simulations can significantly contribute to understanding the atomic rearrangement at the interface during fcc/bcc phase transformations.

Molecular Dynamic (MD) modelling is a frequently used approach to study the fcc-bcc phase transformation. This method allows to follow the movements of each individual atom in the system and to investigate the migration of the interface. However, the MD approach is limited to a small length and time scale. The recently developed Quasi-Particle (QP) approach based on the Atomic Density Function theory (ADF) has been applied to model the fcc-to-bcc phase transformation [38][174][175]. It was shown that using this approach, it is possible to describe the atomic structure of the α/γ interface and follow its propagation at a large time scale. The following sections provide a brief overview of the QP approach and its application for modelling fcc/bcc phase transformation in the system of pure iron.

4.1 Quasi-Particle approach: Atomic Fragment Theory (AFT)

The Quasi-Particle (QP) approach used in this work is a continuous version of the discrete Atomic Density Function (ADF) theory. The ADF approach was proposed by Khachaturyan in the 1970s. In this method, the atomic configuration is described by the density probability function $\rho(\boldsymbol{r})$, which is the probability of finding an atom α at lattice site $\boldsymbol{r}$ at a given time t. The parameter Δx defines the size of a simulation grid. In the ADF theory $\Delta x = a$, where a is a lattice parameter. Then, $\sum_{\boldsymbol{r}} \rho(\boldsymbol{r}) = N_{atoms}$, where N_{atoms} is a total number of atoms in a system. The atomic configuration in the ADF method is shown in **Figure 4.1** (a). In this case,

the underlined Ising lattice coincides with the atomic position in the crystal lattice, and the atoms occupy each site with different probabilities. The different level of grey indicates the different values of the probability function, which varies from 0 (white colour) to 1 (black colour).

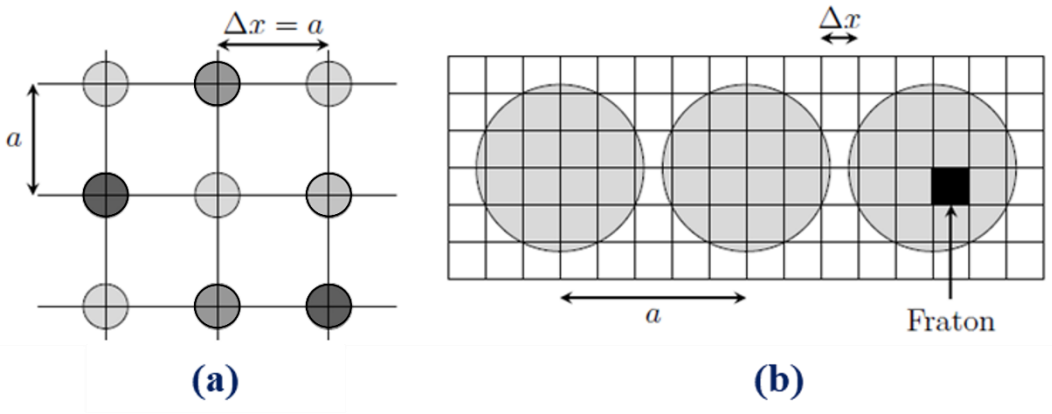

Figure 4.1. (a) *Illustration of the ADF theory on a rigid Ising lattice,* **(b)** *illustration of AFT model with fraton approach* [176].

The discrete ADF model has been widely used to model the isostructural phase transformation [177]. However, this approach cannot be applied to study displacive phase transformations. In 2006 the continuous version of the ADF model was proposed by A.G. Khachaturyan and Y. Jin [178]. The extended version of this approach, introducing the quasi-particles, was developed in 2014 by A.G. Khachaturyan, H. Zapolosky, and M. Larvskyi [38][179]. This new version of ADF is known as the Quasiparticle Approach (QA). In this method, the size of the simulation grid is much smaller than the interatomic distance. Then each atom can be represented as a sphere comprised of a finite number of simulation grids. The simulations grids which belong to the atomic spheres were called fratons (**Figure 4.1** (b)). Since the size of simulation grids is smaller than the distance between two atoms, the QA approach can be used to model displacive phase transformations.

The position of the fraton at time t is described by the configuration number, $c(\boldsymbol{r}, t)$. It is a stochastic variable describing two possible events:

$$c(\boldsymbol{r}, t) = \begin{cases} 1 & if\ site\ r\ is\ occupied\ by\ fraton \\ 0 & otherwise \end{cases} \qquad (4.1)$$

The dynamics of the system can be described by the creation or annihilation of a fraton at each point of the simulation box. The creation of a fraton corresponds to the situation when the configuration number $c(\boldsymbol{r}, t)$ is turned out from zero to one. It indicates that the point, $\boldsymbol{r}$, which was outside of any atomic sphere, becomes inside of it. This event is related to atomic displacement to position $\boldsymbol{r}$. The annihilation of a fraton corresponds to the contrary process.

The averaging of $c(\boldsymbol{r},t)$ over the time-dependent ensemble gives the occupation probability function: $\rho_\alpha(\boldsymbol{r},t)=\langle c(\boldsymbol{r})\rangle_t$ or so-called fraton density function. The function $\rho_\alpha(\boldsymbol{r},t)$ is defined as the probability of finding a fraton of the type α at the site $\boldsymbol{r}$ and at a given time t. At temperature, T, the values of $\rho_\alpha(\boldsymbol{r},t)$ vary between 0 and 1. For a multi-component system the $\rho_\alpha(\boldsymbol{r},t)$ has to be defined for each chemical element.

4.1.1 Kinetic equation

In a general case, the temporal evolution of fraton density function for the multi-component system can be described by a microscopic diffusion equation [178]:

$$\frac{\partial\rho_\alpha(\boldsymbol{r},t)}{\partial t}=\sum_{\boldsymbol{r}'}\sum_{\beta}L_{\alpha\beta}(\boldsymbol{r}-\boldsymbol{r}')\frac{\delta F}{\delta\rho_\beta(\boldsymbol{r}',t)} \tag{4.2}$$

where indexes α,β label the fratons corresponding to two different atomic species. F is the free energy of system and $L_{\alpha\beta}(\boldsymbol{r})$ is the kinetic coefficients matrix. This kinetic equation assumes a linear proportionality between the density rate $\frac{\partial\rho_\alpha(\boldsymbol{r},t)}{\partial t}$ and the transformation driving force $\frac{\delta F}{\delta\rho_\beta(\boldsymbol{r}',t)}$. To assure the conservation of the number of fratons next condition should be satisfied: $\sum_{\boldsymbol{r}}{\partial\rho_\alpha(\boldsymbol{r},t)}/{dt}=0$. This condition leads to the next condition for the kinetic coefficients:

$$\sum\nolimits_{\boldsymbol{r}}L_{\alpha\beta}(\boldsymbol{r}-\boldsymbol{r}')=0 \tag{4.3}$$

The free energy functional in the QA approach (F, see eq.(4.2)) can be written as:

$$F=F(\{\rho_\alpha(\boldsymbol{r})\},T)=U-TS \tag{4.4}$$

where U is the internal energy and S is the configurational entropy. In the mean-field approximation, this energy is:

$$\begin{aligned}F(\{\rho_\alpha(\boldsymbol{r})\},T)=&\frac{1}{2}\sum_{\boldsymbol{r},\boldsymbol{r}'}\sum_{\alpha=1}^{\alpha=m}\sum_{\beta=1}^{\beta=m}\omega_{\alpha\beta}(\boldsymbol{r}-\boldsymbol{r}')\,\rho_\alpha(\boldsymbol{r})\rho_\beta(\boldsymbol{r}')\\&+k_BT\sum_{\boldsymbol{r}}\left[\sum_{\alpha=1}^{\alpha=m}\rho_\alpha(\boldsymbol{r})\ln\,\rho_\alpha(\boldsymbol{r})\right.\\&\left.+\left(1-\sum_{\alpha=1}^{\alpha=m}\rho_\alpha(\boldsymbol{r})\right)ln\left(1-\sum_{\alpha=1}^{\alpha=m}\rho_\alpha(\boldsymbol{r})\right)\right]\end{aligned} \tag{4.5}$$

where k_B is a constant of Boltzman, T is the temperature of the system and $\omega_{\alpha\beta}(\boldsymbol{r})$ is a pairwise interaction potential.

To describe a system with a given symmetry, the interatomic potential should assure, first, the condensation of fratons to the atomic spheres and then its periodic arrangement. It was proposed to divide this interaction into two parts [179]: short-range (SR) and long-range (LR). Then, the short-range part of interaction induces the auto assembling of fratons into the atomic spheres, while the long-range interaction is responsible for the periodic arrangement of these atomic spheres. In general, the total interaction potential, $\widetilde{\omega}_{\alpha\beta}(\boldsymbol{k})$, can be written as:

$$\widetilde{\omega}_{\alpha\beta}(\boldsymbol{k}) = \lambda^{SR} V^{SR}(\boldsymbol{k}) + \lambda^{LR} V^{LR}(\boldsymbol{k}) \qquad (4.6)$$

where λ^{SR} and λ^{LR} are the parameters that define the strength of the SR, $V^{SR}(\boldsymbol{k})$, and LR part $V^{LR}(\boldsymbol{k})$ of the interactions, respectively.

One of the simple choices for the short-range fraton-fraton interaction $V^{SR}(\boldsymbol{r})$ is a step function:

$$V^{SR}(\boldsymbol{r}) = \begin{cases} -1 & if \quad r < r_i \\ \xi & if \quad r \le r + \Delta r \\ 0 & if \quad r > r_i + \Delta r \end{cases} \qquad (4.7)$$

Then the SR interaction, $V^{SR}(\boldsymbol{r})$, schematically represented in **Figure 4.2** (a) and has attractive and repulsive parts. The attractive part is represented by the negative part of the step function (4.7) and define the size (radius r_i) of different sort of atoms. While a repulsive part of the SR interaction, with the height, ξ, and width, Δr, prevents the coarsening between two atomic spheres.

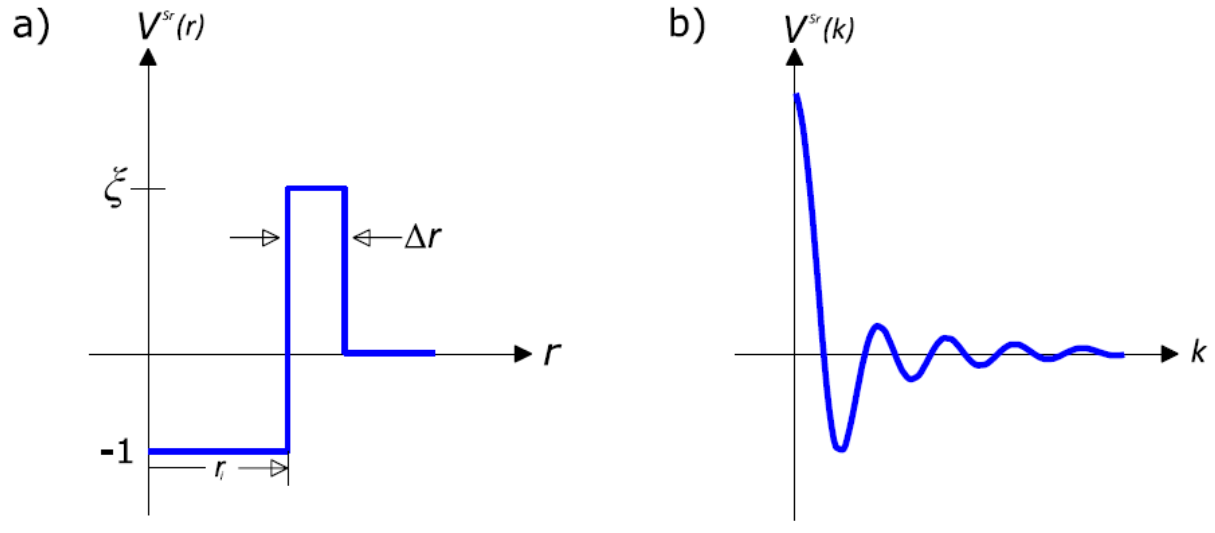

Figure 4.2 (a) *The short-range potential in real space,* **(b)** *the short-range potential in reciprocal space.*

The Fourier transform (FT) of the SR potential (4.7) is schematically shown in **Figure 4.2** (b) and is:

$$V^{SR}(k) = \frac{4\pi}{k^3}\{-\sin(kr_i) + kr_i\cos(kr_i) + \xi[\sin(k(r_i + \Delta r)) - k(r_i + \Delta r)\cos(k(r_i + \Delta r)) - \sin(kr_i) + kr_i\cos(kr_i)]\} \quad (4.8)$$

The long-range potential was introduced using the cluster a cluster function, $V_{clstr}^{\alpha\beta}(r)$, which can be written in k-space as:

$$V_{\alpha\beta}^{LR}(\boldsymbol{k}) = \sum_{\boldsymbol{r}} V_{\alpha\beta}^{clst}(\boldsymbol{r})\, e^{-i\boldsymbol{kr}} \quad (4.9)$$

where, the summation is carried out over all lattice sites, and the wave vector, $\boldsymbol{k}$, is defined in the first Brillouin zone of the computational grid. There are different ways to define the LR potential depending on the system of interest.

The task of this work is to model fcc-to-bcc transformation. Therefore, the LR part of interaction potential has to provide the formation of the fcc and bcc structures. In this study, the LR potential was represented by a Gaussian function. As was discussed in [38], the bcc structure can be stabilized using only one Gaussian function. However, the superposition of two Gaussian functions is needed to obtain fcc crystal. In the case of the bcc structure, the minimum of Gaussian function corresponds to the distance between (110) planes, while for the fcc structure, the position of the minima of the two Gaussian functions corresponds to the distances between (111) and (200) planes. In other words, the position of the minima corresponds to the distance between the first neighings that is schematically shown in **Figure 4.3**.

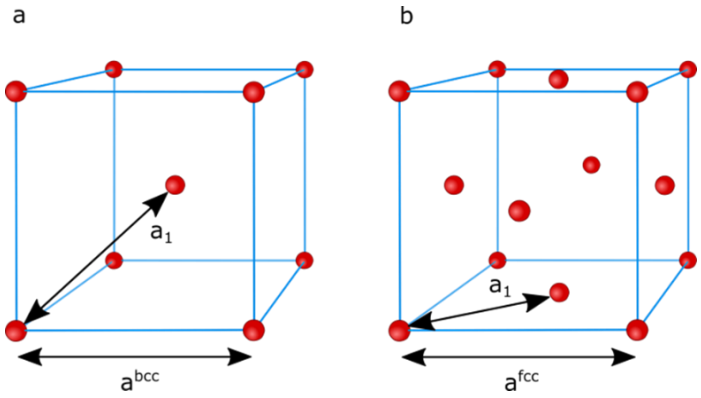

Figure 4.3. *Schematic representation of the distance a_1 to the first neighbors in* **(a)** *bcc and* **(b)** *fcc lattices with the lattice parameter a^{bcc} and a^{fcc}, respectively* [38].

For computational efficiency, the interaction potential is implemented in reciprocal space using the Fourier transforms. The long-range potential in the k-space for the bcc structure can be written as:

$$V_{bcc}^{LR}(k) = \exp\left(-\frac{(k-k_1^{bcc})^2}{2\left(\sigma_1^{bcc}\right)^2}\right) \tag{4.10}$$

and for the fcc structure:

$$V_{fcc}^{LR}(k) = \exp\left(-\frac{(k-k_1^{fcc})^2}{2\left(\sigma_1^{fcc}\right)^2}\right) + \exp\left(-\frac{(k-k_2^{fcc})^2}{2\left(\sigma_2^{fcc}\right)^2}\right) \tag{4.11}$$

where σ_1^{bcc}, σ_1^{fcc}, σ_2^{fcc} are the standard deviations of the Gaussian functions and k_1^{bcc}, k_1^{fcc}, k_2^{fcc} are the extremums of these functions. In the case of the bcc structure, the potential (4.10) reaches the minimum at $k_1^{bcc} = \frac{2\pi}{a^{bcc}}\sqrt{2}$. In the case of the fcc structure, the potential (4.11) has two minima at $k_1^{fcc} = \frac{2\pi}{a^{fcc}}\sqrt{3}$ and $k_2^{fcc} = \frac{2\pi}{a^{fcc}}2$. The long-range potentials for both fcc and bcc structures are schematically shown in **Figure 4.4**.

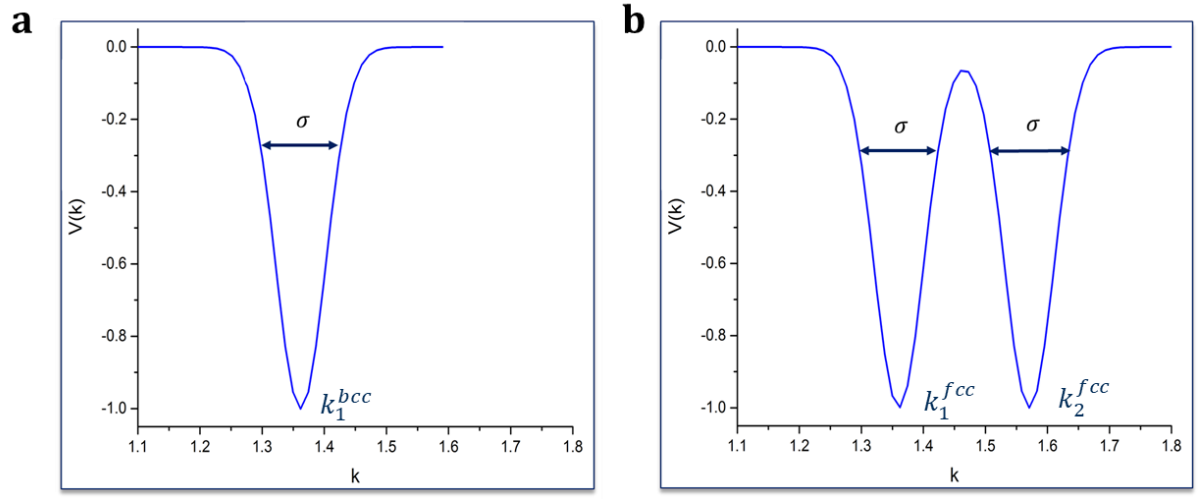

Figure 4.4. *The schematic illustration of the long-range potential for* **(a)** *bcc and* **(b)** *fcc structures in reciprocal space.*

The values of standard Gaussian deviations (σ_1^{bcc}, σ_1^{fcc}, σ_2^{fcc}) considered in eqs. (4.10) and (4.11) can be used to adjust the elastic properties. In order to choose these parameters and to check the validity of interaction potentials for the fcc and bcc phases in pure iron, the elastic constants of these phases can be evaluated. In the case of cubic crystals, there are only three independent elastic constants (ECs): C_{11}, C_{12}, C_{44}. The calculation details of these ECs using the energy approach related to the changes in the elastic energy density caused by a small

deformation and their compliance with experimental constants for iron fcc and bcc crystals are described in **Appendix A.**

4.2 Modeling of fcc-to-bcc phase transformation by QP approach: Simulation details

The modeling of fcc-to-bcc transformation consisted of a few steps: (i) the formation of the equilibrium fcc and bcc phases; (ii) the construction of the initial configuration where a thin slice of bcc structure was introduced into the centre of the box filled by the fcc phase; (iii) the modelling of the fcc-to-bcc phase transformation itself.

The first step is the modelling of equilibrium fcc and bcc structures. The fcc and bcc lattice parameters ($a^{fcc}$and a^{bcc}) were chosen to satisfy the condition of constant volume per atom during fcc/bcc phase transformation. The values of lattice parameres of the fcc and bcc structures extracted from experimental data [35] give the ratio: $\frac{a_{exp}^{fcc}}{a_{exp}^{bcc}} = \frac{0.356nm}{0.286nm} \approx 1.245$. The lattice parameters used in the simulation was chosen as follow: $a^{fcc} = 8.0\Delta x$ and $a^{bcc} = 6.5\Delta x$ that give the close ratio to experimental one: $\frac{a_{model}^{fcc}}{a_{model}^{bcc}} = \frac{8.0\Delta x}{6.5\Delta x} = 1.231$. The rest of the used simulation parameters are presented in **Table 13**. Let us note that the average concentration of fraton ($\bar{\rho}$) was chosen according to the minimization of the free energy of the system. Simulations were performed in three dimensions with a simulation box containing 256^3 grids.

Table 13. *The simulation parameters used in the simulation used in formulas*

a^{fcc}/a^{fcc}	r_i	Δr	ξ	λ^{SR}	λ^{LR}	$\sigma_1^{bcc} = \sigma_1^{fcc} = \sigma_2^{fcc}$	k_BT	$\bar{\rho}$	L
8.0/6.5	2.82	$0.17r_i$	4.0	1.0	0.2	0.04	-0.05	0.17	256

To check the validity of interaction potentials for the bcc (4.10) and fcc (4.11) phases in pure iron using the simulation parameters presented in **Table 13**, the elastic constants of these phases were calculated. The calculated elastic constants in this work and the experimentally measured values are given in **Table 14.** Since the calculated elastic constants are presented in dimensionless units, it is more convenient to compare the experimental and simulated ratio of the elastic constants for the bcc and fcc lattices.

Table 14. *Elastic constants for the bcc and fcc lattice structures: calculated via simulations (used in this work) and experimentally measured*

Calculated elastic constant via simulation in the dimensionless units			Experimentally measured elastic constants for the iron, GPa		
$C_{11}^{bcc} = 1.593$	$C_{11}^{fcc} = 1.403$	$\boldsymbol{C_{11}^{bcc}/C_{11}^{fcc} = 1.135}$	$C_{11}^{bcc} = 226$	$C_{11}^{fcc} = 154$	$\boldsymbol{C_{11}^{bcc}/C_{11}^{fcc} = 1.467}$
$C_{12}^{bcc} = 0.741$	$C_{12}^{fcc} = 0.416$	$\boldsymbol{C_{12}^{bcc}/C_{12}^{fcc} = 1.781}$	$C_{12}^{bcc} = 140$	$C_{12}^{fcc} = 122$	$\boldsymbol{C_{12}^{bcc}/C_{12}^{fcc} = 1.475}$
$C_{44}^{bcc} = 0.578$	$C_{44}^{fcc} = 0.386$	$\boldsymbol{C_{44}^{bcc}/C_{44}^{fcc} = 1.497}$	$C_{44}^{bcc} = 116$	$C_{44}^{fcc} = 77$	$\boldsymbol{C_{44}^{bcc}/C_{44}^{fcc} = 1.506}$

The bcc structure modeling requires additional attention since the fcc-to-bcc transformation occurs following a specific crystallographic orientation relationship (OR) (see paragraph 1.2.3). Therefore, the bcc crystal has to be initially rotated with respect to the fcc crystal. Its rotation can be performed using the rotation matrix that can be calculated for each particular OR. In our work, the systems with Bain, Pitsch, Nishiyama-Wassermann (NW) Kurdjumow-Sachs (KS) ORs had been simulated. **Table 15** contains the list of these ORs (given by the common crystallographic plane and direction in the two phases) and the corresponding rotation matrix. The example of the rotation matrix calculation is provided in **Appendix B.**

Table 15. *The ORs list and corresponding rotation matrices considered in this study*

Name of ORs	{Plane} ⟨Direction⟩	Rotational matrices
Bain (B)	$\{010\}_\gamma \parallel \{010\}_\alpha$ $\langle 001\rangle_\gamma \parallel \langle 101\rangle_\alpha$	$\begin{pmatrix} 0.707 & -0.707 & 0.0 \\ 0.707 & 0.707 & 0.0 \\ 0.0 & 0.0 & 1.0 \end{pmatrix}$
Pitsch (P)	$\{001\}_\gamma \parallel \{\bar{1}01\}_\alpha$ $\langle 110\rangle_\gamma \parallel \langle 111\rangle_\alpha$	$\begin{pmatrix} 0.986 & 0.0 & 0.169 \\ 0.120 & 0.707 & 0.697 \\ -0.120 & 0.707 & 0.697 \end{pmatrix}$
Kurdjumov-Sachs: KS-V1	$\{111\}_\gamma \parallel \{011\}_\alpha$ $\langle \bar{1}01\rangle_\gamma \parallel \langle \bar{1}\bar{1}1\rangle_\alpha$	$\begin{pmatrix} 0.742 & -0.667 & -0.075 \\ 0.650 & 0.742 & -0.167 \\ 0.167 & 0.075 & 0.983 \end{pmatrix}$
Nishiyama-Wassermann: NW-V1	$\{111\}_\gamma \parallel \{011\}_\alpha$ $\langle 10\bar{1}\rangle_\gamma \parallel \langle 100\rangle_\alpha$	$\begin{pmatrix} 0.707 & 0.0 & -0.707 \\ 0.696 & -0.169 & -0.120 \\ 0.120 & 0.986 & 0.120 \end{pmatrix}$

After the generation of the equilibrium fcc and bcc structures, the initial configuration to model fcc/bcc phase transformation was constructed as follows: the thin slice of the rotated bcc structure was introduced into the centre of the simulation box initially filled by the fcc phase. Then, such an initial configuration contains two planar fcc/bcc interfaces that propagate in opposite directions. It should be noted that the initial size of the bcc slice has to be large enough to overcome the energetic barrier for the fcc-to-bcc transformation. The bcc slice with the width of $64\Delta x$ was embeded in the centre of simulation box ($256^3\Delta x$) filled initially by the fcc matrix.

The initial configuration with Bain OR as an example is shown in **Figure 4.5** (a). This figure displays the 3D view of the simulation box with the initial configuration using Common Neighboring Analysis (CNA) of OVITO software [180]. The fcc structure is represented by green and bcc by blue colour. The grey colour corresponds to any other local configurations of atoms, such as the transformation interfaces between fcc and bcc phases in this case. **Figure 4.5** (b) shows the 2D slice view of the $\{010\}_\gamma$ plane, which is a common plane for the fcc and bcc phase with Bain OR. Then, the two phases can be easily identified as well as the position of the fcc/bcc interface.

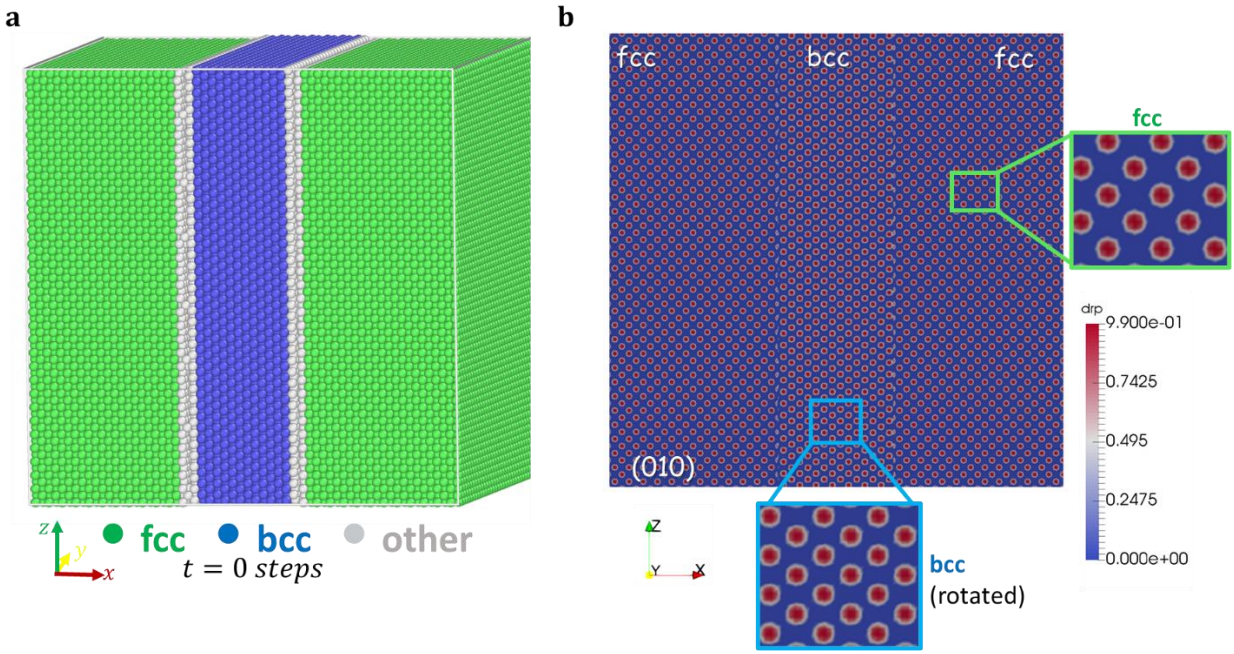

Figure 4.5. *Initial configuration with Bain OR (t=0 simulation steps):* **(a)** *3D view using CAN of OVITO software;* **(b)***2D slice visualization of the* $\{010\}_\gamma$ *plane using ParaView software (the* $\{010\}_\gamma$ *plane is demonstrated as the common plane for fcc and bcc phases in the case of Bain OR).*

Finally, to model the fcc/bcc transformation process, it is necessary slightly destabilise the fcc phase with respect to bcc. It was done by decreasing the depth of the second peak in the LR potentials (4.11) for the fcc structure by multiplying it by the factor 0.1. Therefore, the LR potential for the modelling of the fcc-to-bcc transformation is:

$$V^{LR}(k) = \exp\left(-\frac{(k-k_{01})^2}{2\sigma^2}\right) + 0.1\exp\left(-\frac{(k-k_{02})^2}{2\sigma^2}\right) \qquad (4.12)$$

All simulations were performed with periodic boundary conditions in adimensional units (reduced time units). The kinetics equation (4.2) was solved using the semi-implicit Fourier-spectral method [181] since it provides better stability during numerical calculation and requires less computational time. In addition, the definition of interatomic potential is somewhat

simplified in the k-space. The results of QP simulation were post-treated with the *fratons2atoms package* [182] to determine with good precision the position of the centre of the atom that can be shifted due to the numerical fluctuation of the fratons density field.

4.3 Modeling of fcc-to-bcc phase transformation by QP approach: Numerical results

4.3.1 Bcc growth kinetic during fcc-to-bcc transformation

One of the characteristics of fcc-to-bcc transformation is the kinetics of bcc growth that can be extracted from the simulations results using CNA. The fcc/bcc system with Bain, Pitsch, NW and KS ORs (see **Table 15**) was compared. The 3D view of the growing bcc phase in the fcc matrix at different simulation time steps, in the case of the system with KS OR as an example, is shown in **Figure 4.6.** The temporal evolution of the volume fraction of the bcc phase for the systems with considered ORs in this work is shown in **Figure 4.7**. As mentioned in (1.2.3), there are a different number of possible variants of the considered OR due to the crystal symmetry. Therefore, in the case of KS OR, three variants (KS-V1, KS-V2, KS-V3 see **Table 20**, **Appendix B**) were compared. It was done to check if there is an effect of different variants of a particular OR on the fcc-to-bcc transformation.

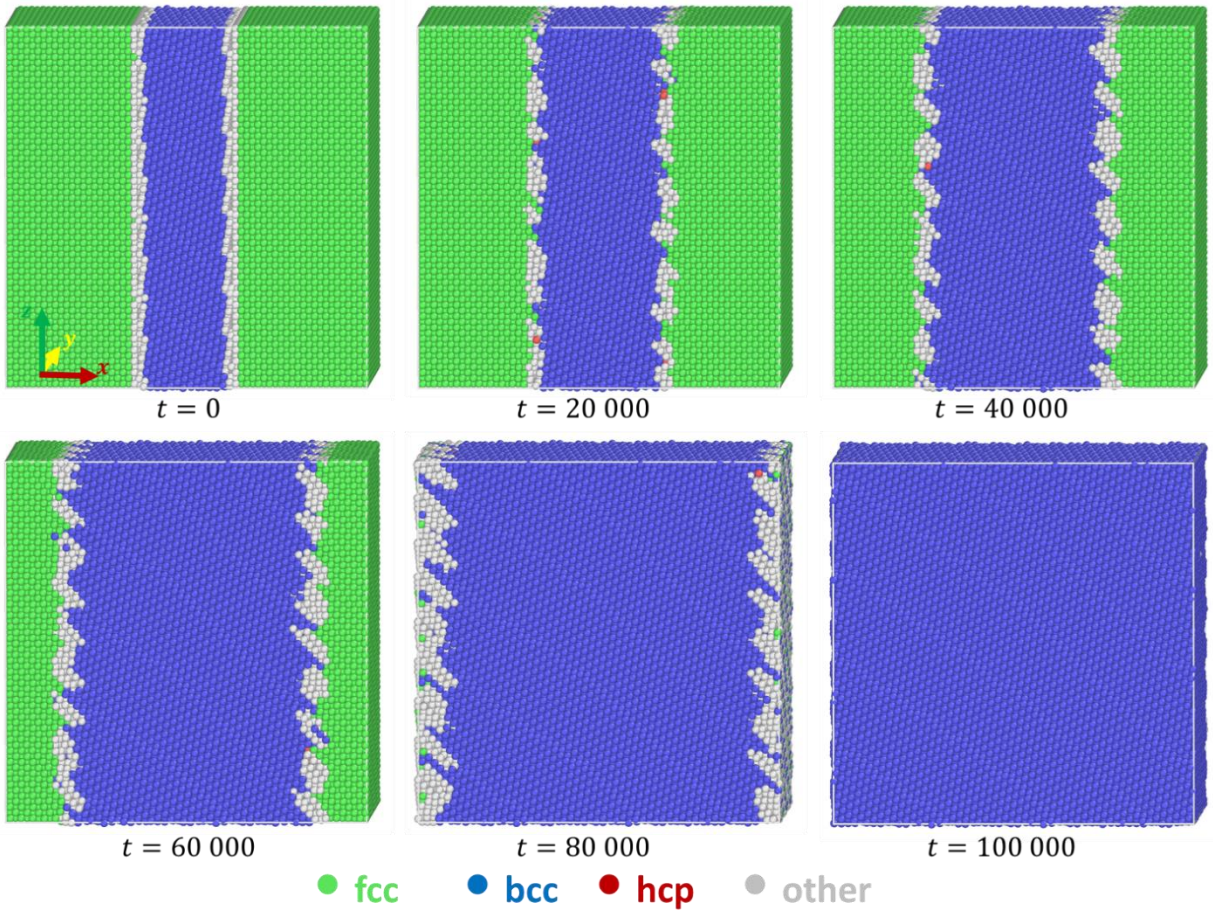

Figure 4.6. *Growth of the bcc phase in fcc matrix (system with KS-V1 OR).*

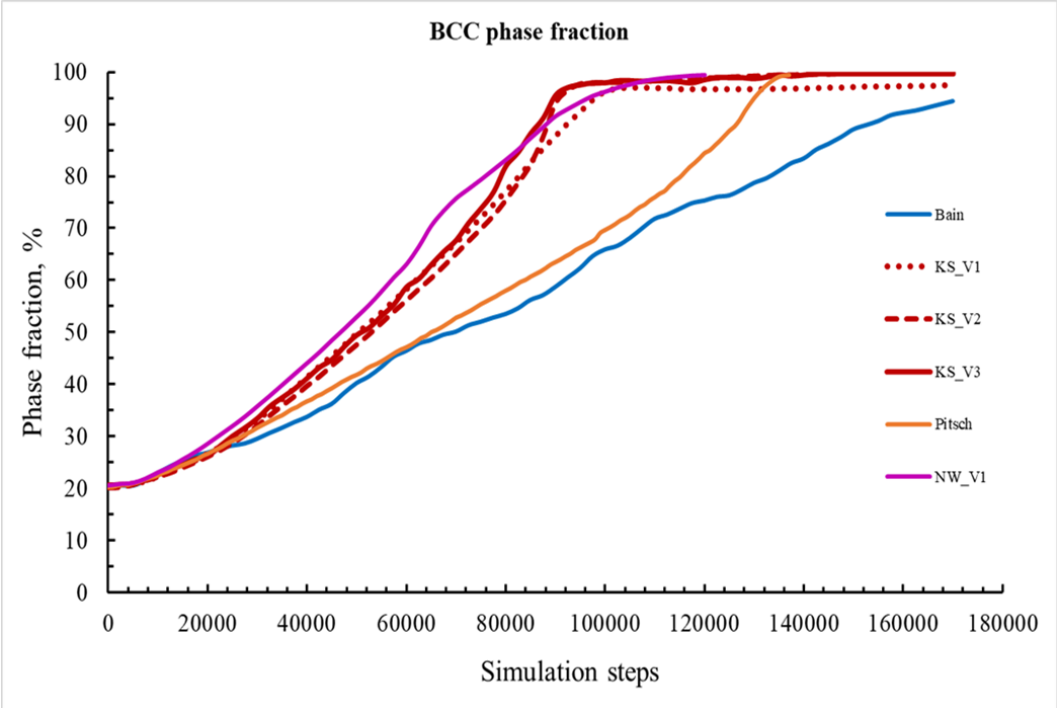

Figure 4.7. *Temporal evolution of the bcc phase fraction in the systems with different ORs.*

The systems with the first three variants of KS ORs (KS-V1 dotted red curve, KS-V2 dashed red curve, KS-V3 red curve) show similar results, which are very close to the evolution of the system with one of the NW ORs (NW-V1 purple curve). It can be seen that the modeled systems with such ORs demonstrate higher interface mobility in comparison with Bain and Pitsch ORs. The bcc-structure completely filled the simulation box after ~ 90 000 simulation steps in the case of KS and NW ORs, while 135 000 steps and 180 000 steps were needed for the systems with Pitsch and Bain ORs, respectively. It is expected that such a difference in mobility can be related to the atomic structure of the interface and the mechanism of its propagation, which require a more detailed analysis.

4.3.2 Atomic structure of fcc/bcc interface

The fcc-to-bcc phase transformation is accompanied by the crystal structure rearrangement from fcc to bcc lattice. Due to the atomic misfit between these lattices, the semi-coherent interface is energetically preferable to be formed. In general, a semi-coherent interface is characterized by the presents of misfit dislocations, which are expected to be highly mobile during the phase transformation. The slip mechanism occurs during the dislocation movement. Since less energy is required to move atoms along the more dense atomic planes, slip occurs along a close-packed plane and direction [183]. The close-packed plane in fcc crystals is $\{111\}_\gamma$ and $\langle 1\bar{1}0\rangle_\gamma$ is close-packed direction. There is no close-packed plane in the bcc crystal, but the slip predominantly takes place in $\{110\}_\alpha$ plane and $\langle \bar{1}11\rangle_\alpha$ direction that have higher atomic density. Combining these planes with high atomic density in both phases imposes the ORs between two phases. The orientation relationships discussed in this work is presented in **Table 15**.

Figure 4.8 shows the atomic configuration at t=30 000 for the systems with different ORs. The visualization plane is the common plain for the fcc and bcc structures defined by the ORs (see the relationships in **Table 15**). In the case of Bain and Pitsch ORs, this plane is $\{010\}_\gamma$, while for KS and NW ORs it corresponds to the – $\{111\}_\gamma$ plane. It can be see that depending on the considered ORs, the atomic structures of interfaces are quite different.

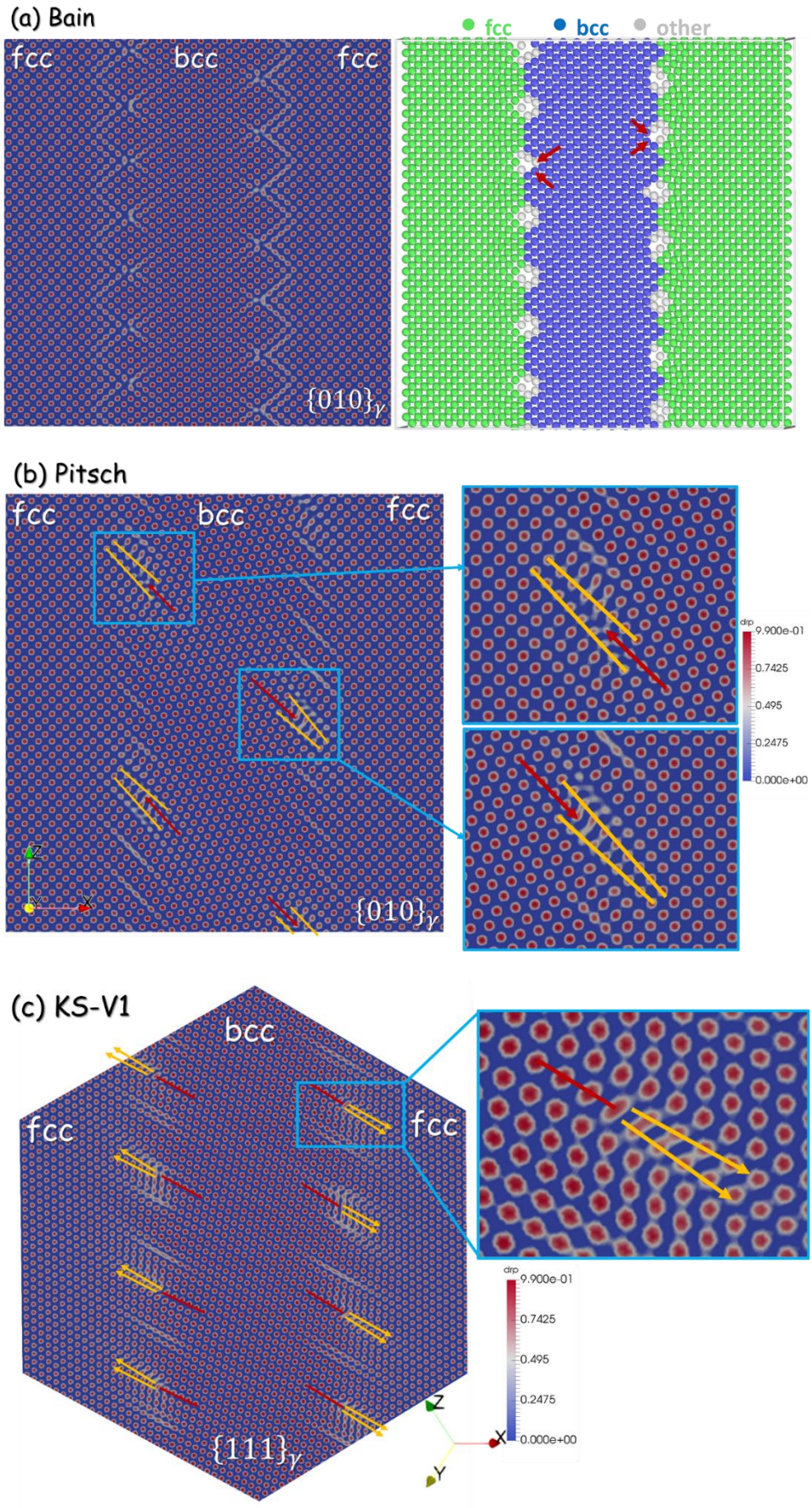
(a) Bain
fcc
bcc
fcc
{010}γ
fcc
bcc
other
(b) Pitsch
fcc
bcc
fcc
{010}γ
drp
9.900e-01
0.7425
0.495
0.2475
0.000e+00
(c) KS-V1
bcc
fcc
fcc
{111}γ
drp
9.900e-01
0.7425
0.495
0.2475
0.000e+00

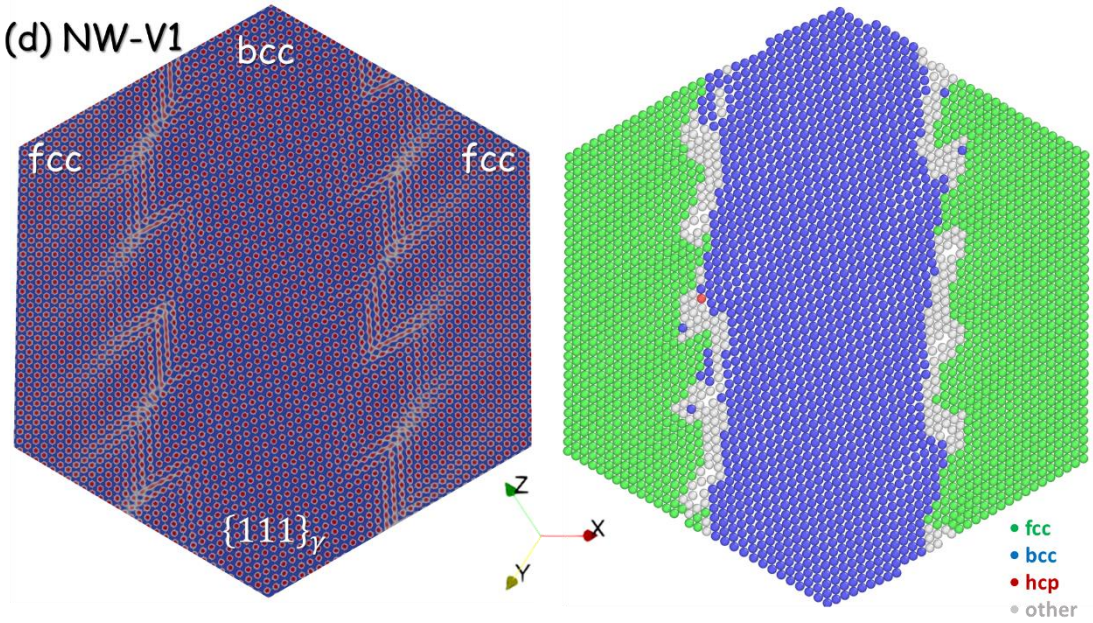

Figure 4.8. *The atomic density profile at t=30 000 in the* $\{010\}_\gamma$ *plain for the system with* **(a)** *Bain and* **(b)** *Pitch ORs and* $\{111\}_\gamma$ *plain for* **(c)** *KS-V1 and* **(d)** *NW-V1.The red and yellow arrows highlight the presence of structural defects at the fcc/bcc intricate.*

Figure 4.8 (a) shows the fcc/bcc interface with Bain OR. It can be observed that two types of slip shear modes are operating at the transformation interface during the fcc-to-bcc crystal lattice rearrangement under the Bain distortion. The first slip mode represents the displacement in the $\langle 0\bar{1}1\rangle$ slip direction of $\{011\}_{bcc}$ plane and the second one is the displacement in the $\langle 011\rangle$ slip direction of $\{0\bar{1}1\}_{bcc}$plane. The Bain strain compensation by the $\{011\}_{bcc}$ slip mechanism schematically ilustreted in **Figure 4.9**. The mechanism of Bain transformation was described in [177].

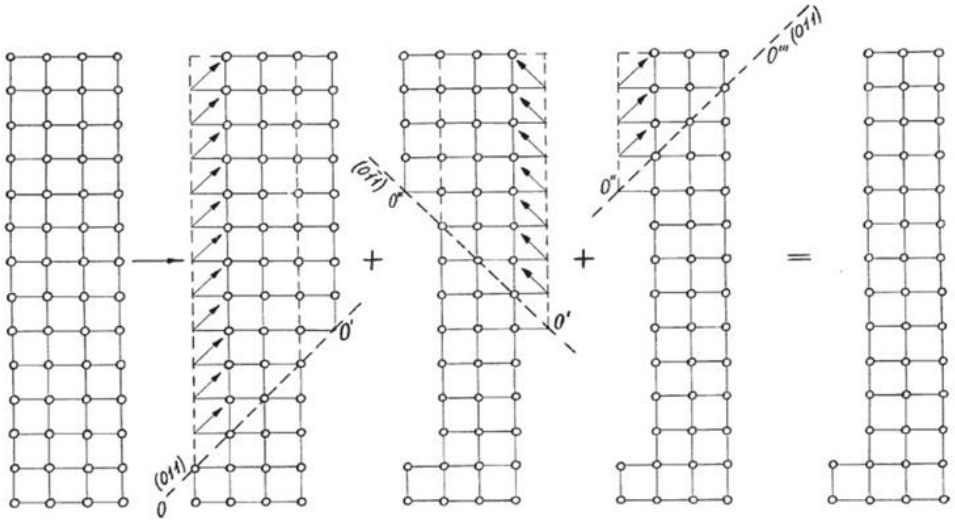

Figure 4.9. *Schematic representation of the shape change of a bcc lattice caused by the two-slip modes. Arrows indicate the slip direction* [177].

The Bain transformation process could not be employed to describe the hole fcc/bcc transformation since it does not satisfy the conditions of the invariant plane formation. It can explain the fact that the Bain OR is not reported experimentally in steels.

Others consider ORs based on a similar process to the Bain but mainly different in the shear direction that leads to the formation of periodic dislocations at the interface that are highlighted as red and yellow arrows in **Figure 4.8**. Such differences in atomic structures lead to different interfacial energy. The energy of the interface was calculated for each considered ORs. In the case of KS and NW ORs it was very close, but compared to Bain and Pitsch, it was 15% lower. The lower interfacial may explain the higher interface mobility.

In [184][185][186], lower interfacial energy in the case of KS and NW was connected with the presence of a special step-ledge disconnection structure at the interface (interface containing misfit dislocation and step characteristic). It was shown that disconnections act as the nucleation center for the bcc structure. Thus, its higher concentration enhances the fcc-to-bcc transformation rate. Therefore, the transformation path KS and NW ORs are energetically preferable and is confirmed by the fact that these two ORs are the most frequently reported experimentally [48][49]. Particular interest in this study has KS ORs since they were experimentally observed with this work. Therefore, the interface propagation with this OR will be considered in more detail.

4.3.3 System with KS-V1 OR

In the literature [177], the mechanism of the fcc-to-bcc phase transformation with KS-OR is described in two steps:

- *The first step* is the slip in $\langle 11\bar{2}\}\rangle_{fcc}$direction of $\{111\}_{fcc}$ plane that produces the stacking fault. That means that from the ABCABC consequences of the plane, it will produce the ABABAB consequences that will give a compact hexagonal structure.
- *The second step* is the homogeneous deformation that leads to the formation of the bcc phase from the intermediate hexagonal phase.

Let us consider the results of modelling in the system with KS-OR. **Figure 4.10** shows the planar fcc/bcc interface with KS-V1 OR at t=0, t=5000 and t=10000 simulation steps in $\{111\}_{\gamma}$ plane using the CNA and redistribution of elastic strain field. The elastic strain field is visualized via the Voronoi analysis in the OVITO software. It is done by the calculation of the volume per atom in the whole simulation box. This information can be used to identify the area under compression or dilatation. In **Figure 4.10**, the distribution of the elastic field is associated

with a color map gradient, where the blue color indicates the dilatation (higher volume) and red – compression (lower volume).

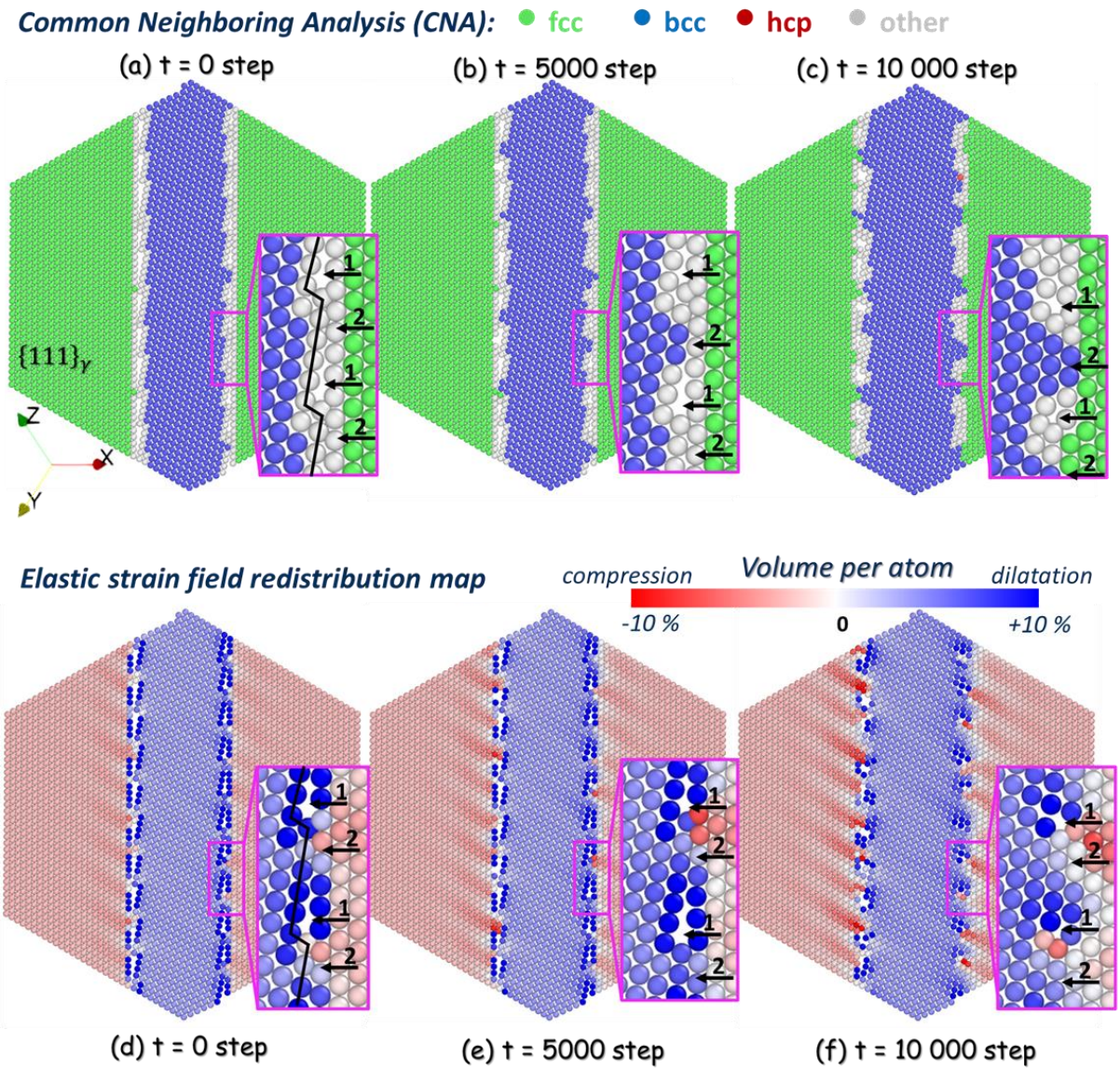

Figure 4.10. *Propagation of the fcc-to-bcc interface with respect to the KS-V1 OR, visualization in* $\{111\}_\gamma$ *plain at different simulation time steps (t=0, 5 000 and 10 000 simulation steps):* **(a)**, **(b)**, **(c)** *the 2D slices of CNA (green – fcc, blue – bcc, grey – unknown structure) and* **(d)**, **(e)**, **(f)** *elastic strain field redistribution map (using Voronoi analysis) are shown.*

As can be seen in **Figure 4.10**, the fcc/bcc interface can be characterised by the periodic distribution of the step disconnections that induce the periodic elastic field. The areas of the high and low misfits between fcc and bcc structures noted as 1 and 2, respectively, can be observed in **Figure 4.10** (a)). These areas correspond to the areas with high and low elastic stress in **Figure 4.10** (d)). Then combining the images of CNA (**Figure 4.10** (b-c)) and strain field distribution (**Figure 4.10** (e-f)), it can be seen that the bcc phase preferentially starts to grow in the area with low elastic stress (areas noted as 2). Then the growth of bcc develops in the high energy areas of the line dislocations formed in the area of higher misfit between two lattices (areas noted as 1).

The distribution of the elastic field around the interface highlights the presents of periodic dislocations. The more detailed view of the interface at t =30 000 simulation steps is shown in **Figure 4.11**. In addition to CNA and elastic strain field distribution, a dislocation analysis implemented into OVITO software, the so-called Dislocation Extraction Algorithm (DXA), is used to identify dislocation line defects and to determine their Burgers vectors [187][188]. It is necessary to note that such an algorithm works well for the dislocations identification in the fcc or bcc structures separately, but this approach is less adapted for analysis of the fcc-bcc interface. Nevertheless, the dislocation analysis in OVITO software detected at the interface the Shockley dislocations with burger vector 1/6 (112), which is normally expected for this kind of interface. The Burger contour around one of the Shockley dislocations is presented in **Figure 4.11**.

The results of modeling correlate with the first step of the fcc-to-bcc phase transformation with KS-OR described in the literature, which may confirm the slip in $\langle 11\bar{2}\}\rangle_{fcc}$direction of $\{111\}_{fcc}$ plane. Regarding the second step, the pereodic deformations are observed along the interface and defenetly play a critical role in the fcc-to-bcc transfromation. However, the existence of the intermediate hexagonal phase is under discussion since the CAN of OVITO detected an insignificant presence of the hcp structure (~ 0.1% of volume fraction).

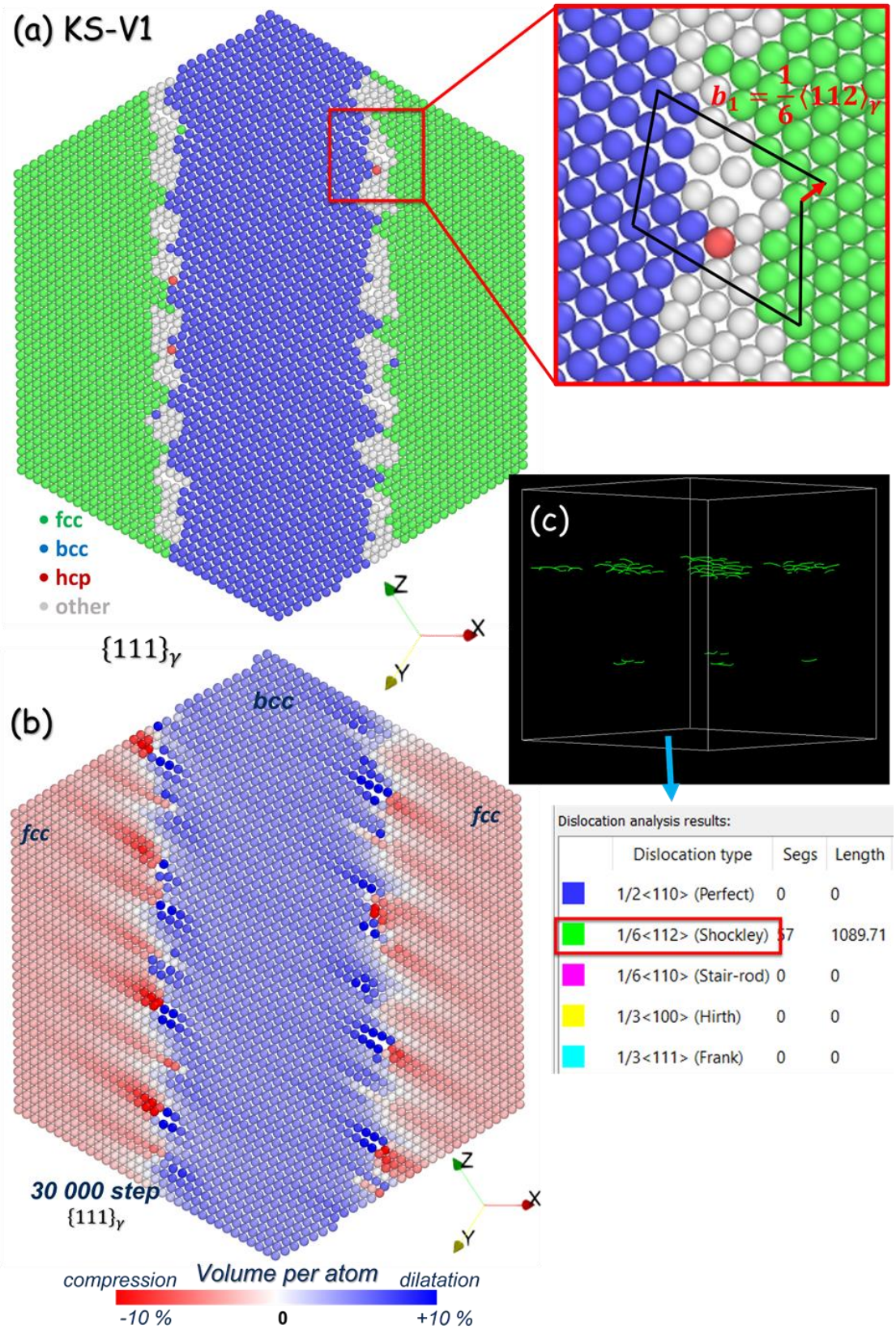

Figure 4.11. *The fcc-to-bcc transformation with the KS-V1 OR at t=30 000 simulation steps in* $\{111\}_\gamma$ *plain.* **(a)** *2D slice visualization using CNA of OVITO software (green – fcc, blue – bcc, grey – unknown structure).* **(b)** *The gradient color map of Voronoi analysis in the range from 150 to 150 atomic volume that corresponds to the regions of dilatation (blue color) and compression (red color), respectively.* **(c)** *The dislocation analysis in OVITO software: the Shockley dislocations with burger vector 1/6 (112) are detected at the interface.*

4.4 Simulated diffraction patterns

To obtain additional information about the fcc/bcc interface, the atomistic configurations obtained in our simulation were used to simulate the diffraction patterns. It is one of the advantages of the QP approach since these results can be directly compared with the experimental data. Using the simulated diffraction patterns, dark-field or high-resolution dark-field images can also be simulated. These images can be used to highlight different regions in the simulation box, which are difficult to identify otherwise.

Figure 4.12 (a) demonstrates the simulated diffraction pattern of the atomic configuration with KS-V1 ORs in $\{111\}_\gamma$ plane at $t = 30\,000$. Diffraction spots corresponding to the fcc phase are presented in green color, and the rotated bcc phase – blue color. All other reflections correspond to the interface. Considering only the interface reflexions, a dark-field image can be generated (**Figure 4.12**(b)).

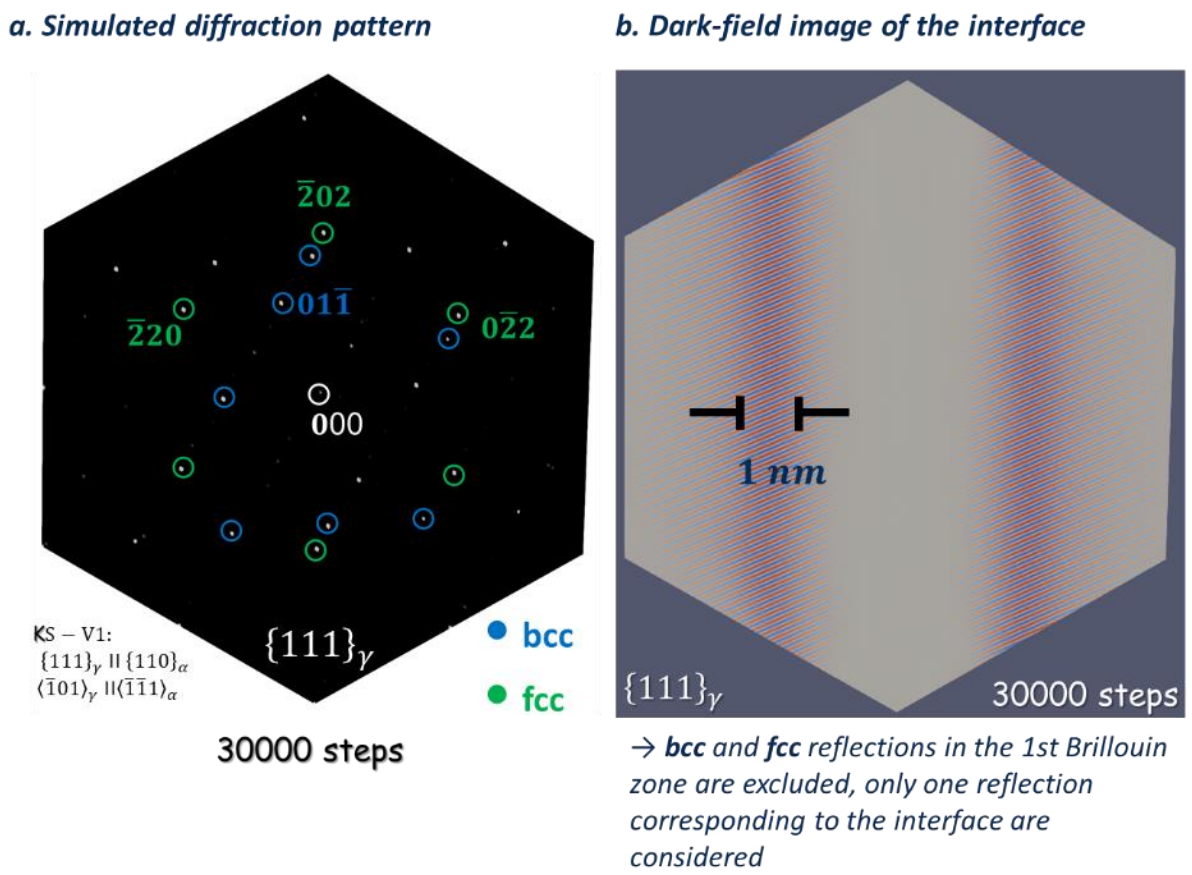

Figure 4.12. (a) *Simulated diffraction pattern in the* $\{111\}_\gamma$ *plane. Green spots correspond to the fcc structure and blue - bcc.* **(b)** *Simulated dark-field images. The example demonstrated for the system with KS-V1 OR at* $t = 30\,000$.

In this study, the dark-filed image of the interface has a particular interest because it gives an idea about the interface width, which is the important input parameter for many theoretical calculations of ferrite growth. In the case of KS-V1, OR thickness of the interface is around 1nm

(Помилка! Джерело посилання не знайдено. (b)). Similar values were obtained in the case of N W-V1 and Pitsch ORs, while in the case of Bain, it was around 2 nm. The value of 1 nm estimated from the modeling results for KS OR (experimentally observed in this work) was used as a starting interface thickness for the theoretical calculation presented in the last chapter of this work.

4.5 Conclusions

In this chapter, the QP approach was introduced. Then this approach was used to model the propagation of the α/γ interface. It was shown that this new method open a way to describe the atomic structure of the mobile fcc/bcc interface and follow the interface migration at large time and space scales.

Using this approach, the kinetics and structure of the α/γ interface have been investigated in pure iron. Systems with different orientation relationships between the face-centered cubic austenite phase and body-centered cubic ferrite phase have been considered, with Bain, Pitch, KS, and NW ORs. In all considered orientations, the propagation of the planar fcc/bcc interfaces was observed. However, the fcc/bcc interfaces with KS and NW ORs demonstrated higher interface mobility compared with Bain and Pitsch ORs. The more detailed analysis of the atomic structure of interfaces shows that in the case of KS interfaces contain certain numbers of periodic step disconnections. This defect structure provides lower interfacial energy. Moreover, it was noticed that disconnection plays a critical role in bcc phase growth and interface propagation. Because the growth of bcc preferentially starts at the area of low lattices misfit following the dislocation movement in the area of higher misfit regions. In the case of KS OR, the phase transformation is happened by the dislocation slip mechanism that is caused by the sliding of Shockley partial dislocations along $\langle 11\bar{2}\} \rangle_{fcc}$direction in $\{111\}_{fcc}$ plane.

The simulated dark-field image has been used to estimate the interface thicknesses, which in the case of KS, NW, and Pitsch ORs was about 1 nm, while about 2 nm in the case of Bain.

The QP modeling has shown great potential in investigating transformation interfaces since it can significantly contribute to the understanding of the atomic structure of the interface and link this structure with interface mobility.

Chapter 5

Discussion

The aim of this study was to understend the austenite-to-ferrite phase transformation through the analysis of α/γ interfaces at the nanometric scale and quantify the local solute enrichment. This study can help to identify the operative mode of ferrite growth during austenite-to-ferrite phase transformation. A large set of experimental results have been presented in Chapter 3. In order to compare the experimentally observed Mn profiles with the ones theoretically expected assuming local transformation conditions, the austenite-to-ferrite phase transformation was in parallel modeled using both the commercial software DICTRA (the diffusive module of Thermo-Calc) and a recently developed model by D. Huin (ArcelorMittal SA), which is a new formalism of the Purdy&Brechet model. The calculation results, and their comparison with experimental data, are presented in the following chapter. However, none of these two approaches considers the different orientation relationships at the interface that may potentially affect the segregation of Mn and interface propagation, as seen in Chapter 3. Therefore, the observations regarding this point are also discussed with respect to our experimental results.

5.1 LENP vs. Solute Drag at 625°C and 680°C

It was mentioned previously that to investigate the different possible mechanisms of austenite/ferrite transformation, the transformation temperatures and nominal composition had been chosen in the domains where several regimes can compete (LEP, LENP, PE or SD). Therefore, it is useful again to refer to the Fe-C-Mn ternary phase diagram. Its isothermal sections at each investigated transformation temperature (625°C, 680°C and 720°C) are presented in **Figure 5.1**. The red points represent the nominal composition (0.17w%C-2wt%Mn), and the red tie-lines are the operative tie-lines.

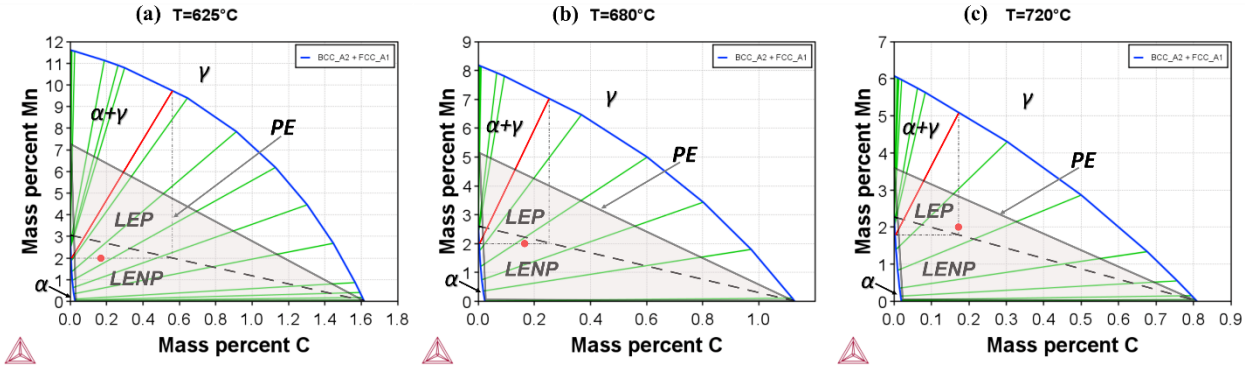

Figure 5.1. *The isothermal section at **(a)** 625° **(b)** 680° **(c)** 720°C in the Fe-C-Mn phase diagrams. The nominal composition is given as a red point, and the red tie-line is the operative tie-line.*

The majority of experimental results were obtained for 625°C and 680°C transformation temperatures and will be discussed first. At these conditions, LENP, PE, or SD are possible transformation mechanisms. In the case of the PE regime, the Mn composition profile is expected to be flat since the substitutional solutes are assumed to be immobile with respect to high interface velocity (more details in paragraph (1.4.3)). The homogeneous Mn distribution through the interface was observed only in a few cases: **Figure 3.7** (e), **Figure 3.8** (b, c), **Figure 3.10** (d), **Figure 3.13** (e). These cases will be discussed a bit later in this chapter as they do not represent the common tendency of the observed results since the Mn peak at the interface was found in most investigated samples at 625°C and 680°C. The majority of experimental data show a Mn partition that can be described by either LENP or SD model. LENP model predicts the existence of Mn "spike" at the interface in order to respect the local equilibrium conditions (see paragraph (1.4.2)). In the case of SD, the segregation of the Mn atoms at the interface caused by the interaction of the moving interface with alloying elements is expected to be more important than a simple spike (see paragraph (1.5)). Therefore, one of the main questions of this study is if the observed Mn peaks at 625°C and 680°C could correspond to LENP spike or they represent the segregation due to the SD effect. To answer this question, it is necessary to compare the experimentally obtained Mn profiles with the theoretically expected ones. Therefore, in parallel to the experimental investigation, the austenite-to-ferrite phase transformation was modeled using the commercial software DICTRA (the diffusive module of Thermo-Calc) and a recently developed model by D. Huin (ArcelorMittal SA, Metz), which is a new formalism of the Purdy&Brechet model.

5.1.1 DICTRA calculation at 625°C and 680°C

DICTRA module of Thermo-Calc commercial software is widely used to simulate diffusion controlled transformations in multicomponent systems, including the diffusion problems with a moving transformation interface. Its calculations are based on the solutions of the diffusion equations assuming local thermodynamic equilibrium at transformation interfaces [189]. In this work, DICTRA was used to simulate the austenite-to-ferrite phase transformation. The kinetics of the ferrite phase fraction evolution and the solute composition profile across the interface have been calculated for the considered transformation temperatures. In DICTRA simulation, the diffusion equations are solved by a 1D finite element method. It means that the solutions of the diffusion equations are obtained along one spatial coordinate, but the geometry of the simulated system can be planar, cylindrical or spherical [190]. The initial configuration of the simulated system is shown in **Figure 5.2**. As we can see from this figure, the planar geometry has been chosen in the current study. It was motivated by the fact that the allotriomorphic ferrite (investigated in this work) preferentially nucleates at the austenite grain boundary and then rapidly grows along this boundary. Basically, its growth can be treated as one-dimensional thickening normal to the boundary plane (see more details in (1.2.4)). The growth of ferrite (bcc) into austenite (fcc) was simulated with a total austenite grain size of 15 μm which is equivalent to an actual grain size of 30 μm. The austenite is considered to be initially homogeneous with the composition Fe-0.17wt%C-2.0wt%Mn (nominal composition). The initially very thin ferrite (20 nm) is also present at the start of the simulation, which means that the nucleation of ferrite is not treated.

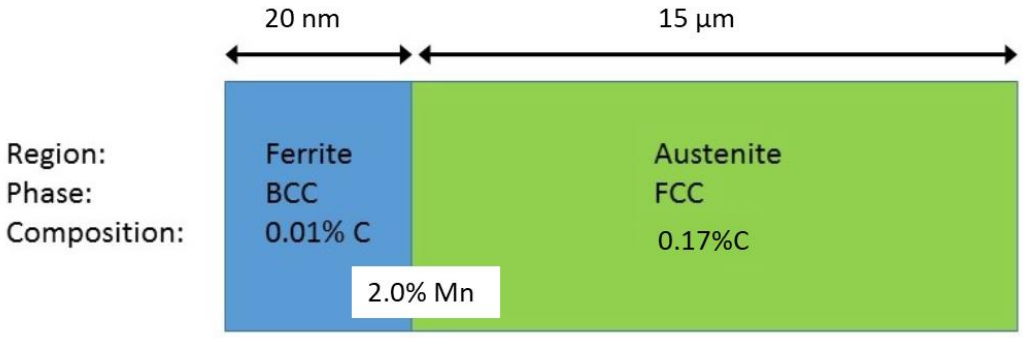

Figure 5.2. *The initial state of the DICTRA simulation system used for modeling austenite-to-ferrite phase transformation. There are two regions, Ferrite and Austenite, consisting of bcc and fcc phases, respectively.*

Before presenting the results of DICTRA calculation, it is important to note that during the calculation process, the effects of the mesh type and the number of points on the width of the simulated Mn profile and thus Mn excess at the interface were observed. In DICTRA, there is the possibility to choose between linear (L), geometric (G) or double geometric (DG) mesh

types. For the linear mesh type, the mesh point spacing is constant, while for the geometric one, it changes by a constant factor between every grid point. For example, the ratio factor of r = 1.05 is often used and means that spacing increases by 5% from the lower left side for each grid point. In the case of double geometric, there are geometrical meshes from both sides of the considered phase. It is usually good practice to have a denser mesh close to moving boundaries where the composition profiles are expected to vary more significantly during the simulation [190].

Different mesh types with different numbers of points have been tested, and the width of the simulated Mn profiles and Mn excess for 625°C, as an example, are presented in **Table 16**. The Mn excess was calculated as the area under the Mn peak. The obtained data demonstrate that, depending on the chosen mesh type and the number of points, the width of the predicted Mn spike by DICTRA can differ by several orders of magnitude. For example, (see the column in **Table 16** for 5 s) spike width is equal to 143.34 nm for 100 points in linear mesh vs 0.04 nm in the case of 200 points with geometrical mesh (highlighted in yellow). Moreover, in all the cases, the width of the Mn peak decreases with time. Normally, from a numerical point of view, the final result should not depend on the number of points and mesh type if the mesh is fine enough (in this case, fine enough with respect to the diffusion length of Mn). However, if we significantly increase the number of points, the software returns an error. Therefore, further in this work, the results of the DICTRA simulation will be presented only for the case highlighted in yellow in **Table 16**, which means:

ferrite – 20 nm thickness, geometrical mesh with 50 points and ratio r=0.95,

austenite – 15 µm thickness, geometrical mesh with 200 points and ratio r=1.05.

These conditions provide the finest possible spacing reached in this work: the distance between the points in close vicinity to the interface is ~ 0.02 nm. In any case, the appropriate mesh definition remains an open problem in the specific task of solute spike determination expected under the LENP condition. We are not fully convinced that the selected geometry is correct, but at least it is the finest of the considered one.

Table 16. *Tested mesh types with different numbers of points in the case of 625°C.*

625°C							
Number of points and mesh type*		Peak width, nm			Mn_excess, atom/nm²		
Ferrite (F)	Austenite (A)	5s	100s	1000s	5s	100s	1000s
N=10_L	N=100_L	143.34	123.69	70.09	472.74	407.93	231.16
N=10_L	N=150_L	95.48	82.16	48.73	314.89	270.96	160.71
N=10_L	N=200_L	70.51	62.49	35.34	232.54	206.09	116.55
N=20_L	N=150_L	95.95	82.36	47.31	316.44	271.62	156.03

N=20_L	N=150_G, r=1.05	0.503	0.4	0.24	1.66	1.32	0.79
N=20_G, r=0.95	N=150_G, r=1.05	0.50	0.4	0.24	1.65	1.32	0.79
N=**50_G, r=0.95**	**200_G, r=1.05**	**0.04**	**0.03**	**---**	0.13	0.10	**---**
N=100_G, r=0.95	N=300_G, r=1.05	Softwere send an error with more points.					
N=100_G, r=0.95	N=500_G, r=1.05						

*__N__ – number of points, **L** – linear mesh type, **G** – geometric mesh type, **r** – ratio factor of the adaptive (geometric) mesh, **---** means the presents of long-range diffusion, thus it is difficult to determine the peak width.

The result of the DICTRA simulations at both 625°C and 680°C transformation temperatures are shown in **Figure 5.3. Figure 5.3** (a) shows the temporal evolution of the α/γ interface position predicted by DICTRA. As expected, we can see that the α/γ interface initially propagates faster at 625°C than at 680°C because of the higher driving force at lower transformation temperature. The comparison of experimentally measured kinetics of ferrite growth (from image analysis and dilatometry) and kinetics predicted by DICTRA is shown in **Figure 5.3** (b). For the transformation temperature of 680°C, the kinetics predicted by DICTRA corresponds to the experimentally observed one for the holding times shorter than about 1000 s, and it became slower for the longer time. After 3 h of transformation, the calculation predicted ~17 % of volume ferrite fraction vs ~ 25 % experimentally observed. For the transformation temperature of 625°C, the experimentally observed kinetici is significantly slower than predicted by the calculation. In both cases, we see that the experimentally observed ferrite growth kinetics cannot be well predicted using the model with conditions fixed by local equilibrium at the transformation interface.

To check the evolution of the simulated Mn profile by DICTRA and to be able to compare it with the profiles measured by APT, the Mn profiles were calculated for several transformation times, mainly: 5 s, 15 s, 30 s, 100 s, 600 s, 1000 s, 5000 s and 3 h (according to the experimentally investigated one, mentioned in **Table 5**), but only those for 5 s and 3 h are shown in **Figure 5.3**.

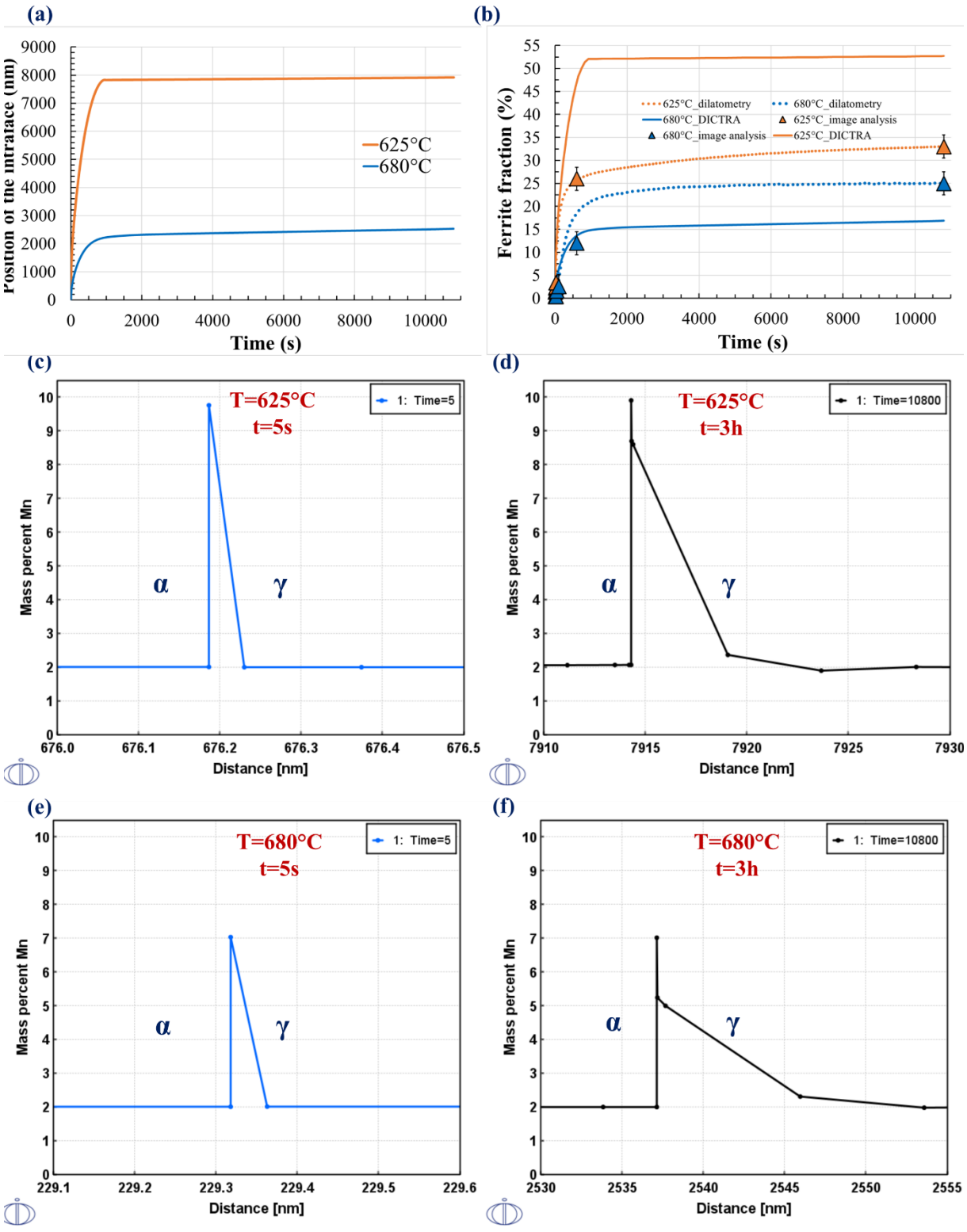

Figure 5.3. *The results of DICTRA calculation for the Fe-C-Mn model alloy with the nominal composition of 0.17 wt%C and 2.0 wt%Mn:* ***(a)*** *temporal evolution of the ferrite/austenite interface position,* ***(b)*** *predicted and measured ferrite growth kinetics,* ***(c-d)*** *and* ***(e-f)*** *Mn profiles predicted by DICTRA at 5s and 3h of transformation at 625°C and 680°C, respectively.*

In the case of both transformation temperatures, the simulated Mn profiles demonstrate the presence of the Mn spike at the transformation interface at the beginning of the phase transformation. Long-range diffusion of Mn into austenite started to be observed for a longer

transformation time. The detailed views of the Mn profiles at α/γ interface after 5s (early beginning) and 3 h (long time) of transformation at 625°C is shown in **Figure 5.3** (c-d) and **Figure 5.3**(e-f) at 680°C. The maximum values of the Mn content at the interface reached about ~ 9.8 at% in the case of 625°C and about ~ 7.0 at% in the case of 680°C. These maximum values are independent of the type of mesh and the number of points since there are defined by the phase diagrams shown in **Figure 5.1** (a-b).

The width of the Mn peak and calculated Mn excess are presented in **Table 17**. It should be noted that these values were calculated only for the transformation times before long-range diffusion of Mn into austenite was observed. It can be seen that, at 680°C, the Mn spike's width slightly decreased from 0.044 nm (5s) to 0.039 nm (1400 s). At 625°C, the long-range diffusion of Mn into austenite is observed after 1400 s, and after the 3 h the Mn gradient extends into austenite up to 17 nm (**Figure 5.3** (f)). The situation is quite surprising at 625°C as the Mn spike's width decreases by a factor of two with time: from 0.044 nm to 0.023 nm. Therefore such behaviour is more likely linked with calculation artefacts caused by the mesh definition (problem mentioned earlier in this paragraph). At 625°C, long-range diffusion of Mn into austenite started to be observed after 600 s of transformation and after 3 h extended up to 13 nm (**Figure 5.3** (d)). The length of Mn diffusion into austenite is smaller at 625° than at 680°C since the diffusion of Mn is slower at lower temperatures.

Table 17. *The peak width of the simulated Mn profile by DICTRA and calculated Mn excess at the interface for both 625°C and at 680°C TT.*

<table>
<tr><th rowspan="2">time, s</th><th colspan="2">625°C
Mn_max=9.82%at</th><th colspan="2">680°C
Mn_max=7.04%at</th></tr>
<tr><th>Peak width, nm</th><th>Mn_excess, atom/nm²</th><th>Peak width, nm</th><th>Mn_excess, atom/nm²</th></tr>
<tr><td>5</td><td>0.044</td><td>0.144</td><td>0.045</td><td>0.113</td></tr>
<tr><td>15</td><td>0.042</td><td>0.140</td><td>0.044</td><td>0.112</td></tr>
<tr><td>30</td><td>0.041</td><td>0.135</td><td>0.044</td><td>0.111</td></tr>
<tr><td>100</td><td>0.037</td><td>0.123</td><td>0.043</td><td>0.108</td></tr>
<tr><td>600</td><td>0.023</td><td>0.077</td><td>0.039</td><td>0.099</td></tr>
<tr><td>1000</td><td colspan="2" rowspan="3">After the 600s, long-range diffusion of Mn into austenite is presented</td><td>0.039</td><td>0.098</td></tr>
<tr><td>1400</td><td>0.039</td><td>0.098</td></tr>
<tr><td>1500</td><td colspan="2">After the 1400s, long-range diffusion of Mn into austenite is presented</td></tr>
</table>

The width of the Mn spike (0.04 - 0.02 nm) measured by DICTRA simulation, which is commensurate with the values obtained in [191][192], is quite small and, to some extent, unphysical. It means that the diffusion zone is one order of magnitude smaller than the lattice parameter, so it can exist only mathematically since there is no possibility of defining such a

narrow concentration spike at the interface. However, the artefacts that were observed during the DICTRA simulation, namely that the results depend on mesh type and the number of points, as well as the fact that the interface thickness decreases with time, questions the obtained results. Therefore, in addition to DICTRA, an alternative way to estimate the thickness of the Mn was used. It is based on the relationship proposed by Coates [16] that was obtained considering local equilibrium assumptions and the diffusive character of the phase transformation (the same as DICTRA calculation are based).

5.1.2 LENP spike thickness: estimation according to Coates

Assuming local equilibrium at the interface, Coates [16] established the relationship between interface velocity and diffusion zone thickness as follows:

$$v = \frac{2D_i}{\Delta S} \tag{5.1}$$

where v is the interface velocity, ΔS is the spike thickness, and $D_i$is the diffusion coefficient of the slow diffuser (Mn in our case). To estimate the width of the diffusion zone, ΔS, it is necessary first to determine the values of v and D_i.

The evolution of the diffusion coefficient with temperature is expressed by Arrhenius law as follows:

$$D(T) = D_0 e^{\frac{-E_a}{RT}} \tag{5.2}$$

where, D_0 is the pre-exponential factor (m^2/s), E_a is the activation energy (J/mol), R is the gas constant $(J/mol\ K)$, T – temperature (K). The values of D_0 and E_a parameters found in the literature [193][194] are:

for ferrite: D_0=1.49•10^{-4}, $[m^2/s]$, $E_a = 233kJ/mol$;

for austenite: D_0=1.6•10^{-4}, $[m^2/s]$, $E_a = 261kJ/mol$;

Substituting these parameters into equation (5.2), the Mn diffusion coefficients were calculated for each considered transformation temperature. Then to calculate the Mn spike thicknesses, ΔS, using eq. (5.1), it is necessary to determine the interface velocity.

The average velocity of the interface migration during phase transformation is the derivative of ferrite volume fraction with respect to time. Therefore, it was calculated from the experimentally obtained dilatometry data using the following expression:

$$v_\alpha = x_i \frac{df_\alpha}{dt} \tag{5.3}$$

where v_α is interface velocity, f_α is volume fraction, df_α/dt is the rate of change in the volume fraction over time, and x_i is the interface displacement that has to be estimated. The estimation of the average interface displacement differs depending on the considered geometry of ferrite growth. As mentioned earlier, the growth of allotriomorphic ferrite can be treated as one-dimensional thickening. Therefore, in this study, the "1D" geometry of interface propagation has been considered. Its schematical illustration is shown in **Figure 5.4**.

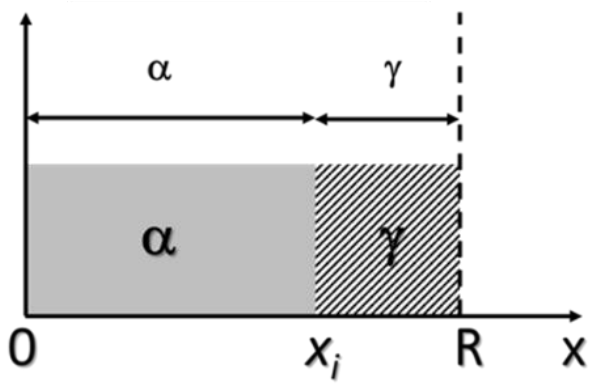

Figure 5.4. *Schematic views of 1D geometries of interface propagation during ferrite growth at the austenite grain boundary considered in this study.*

The estimated velocities derived from dilatometry curves using equation (5.3), considering a grain size (2R) equal to 30 μm, are shown in **Figure 5.5**. The obtained data were approximated by the following function:

$$v(t) = \frac{a}{(b+t)^2} \tag{5.4}$$

The fitting parameters a and b with the maximum velocity values for each considered case are given in **Table 18**.

Table 18. *Fitting parameters with the maximum velocity values*

T, °C	1D propagation		
	a	b	v_{max}, μm/s
625	319.028	69.841	0.056
680	2472.408	509.031	0.009
720	1.408E-05	0.308	1.14E-0.7

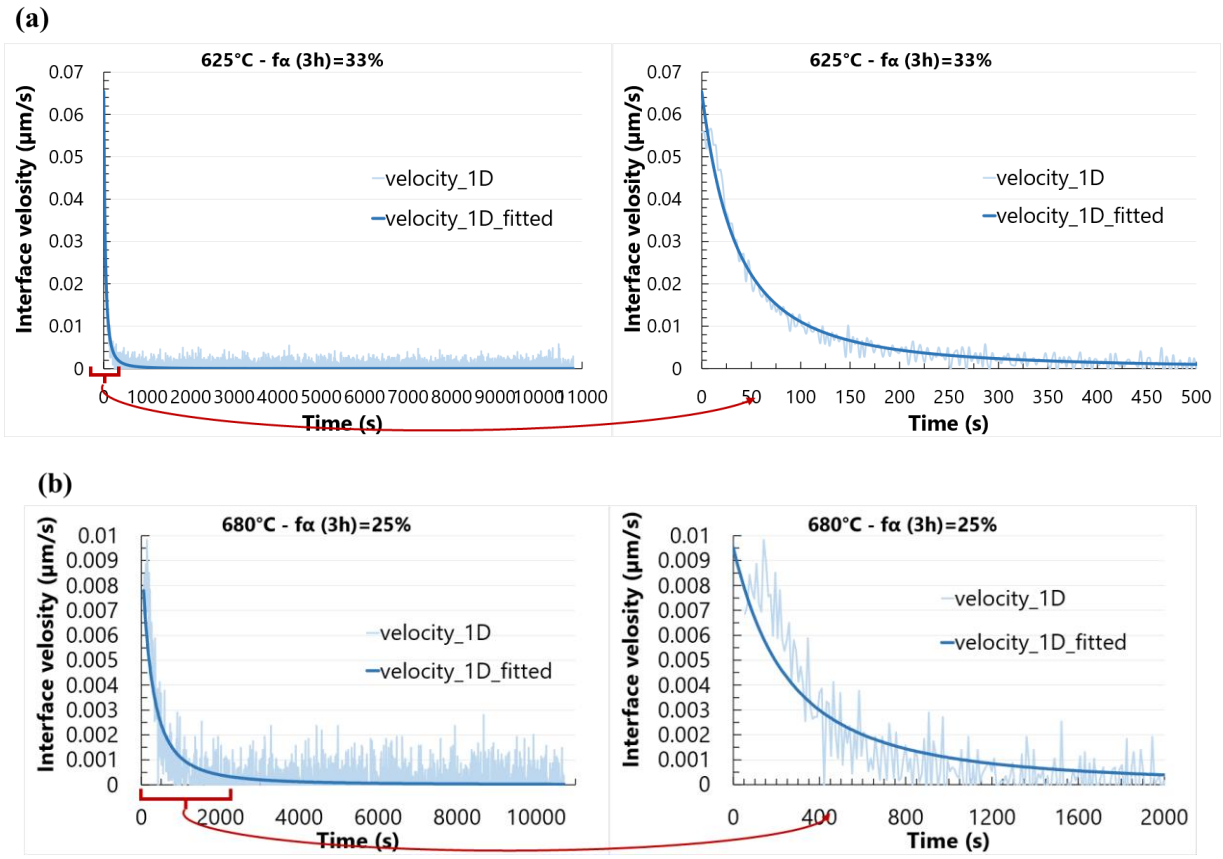

Figure 5.5. *Average interface velocities estimated from the dilatometry data for transformation temperature* ***(a)*** *625°C and* ***(b)*** *680°C.*

Finally, the temporal evolution of spike thickness using the relationship (5.1) can be calculated. The results are shown in **Figure 5.6** and demonstrate that the thickness of the spike changes very little at the beginning of the transformation when the interface velocity is quite high. The expected Mn excess was calculated as an area of a triangle with a base equal to the obtained spike thickness and with a height equal to the maximum Mn content at the interface defined by the operative tie-lines (**Figure 5.1**) minus the nominal Mn composition (2wt%). The Mn excess is noted as *Coates_v=1D* and reported in **Figure 5.7**.

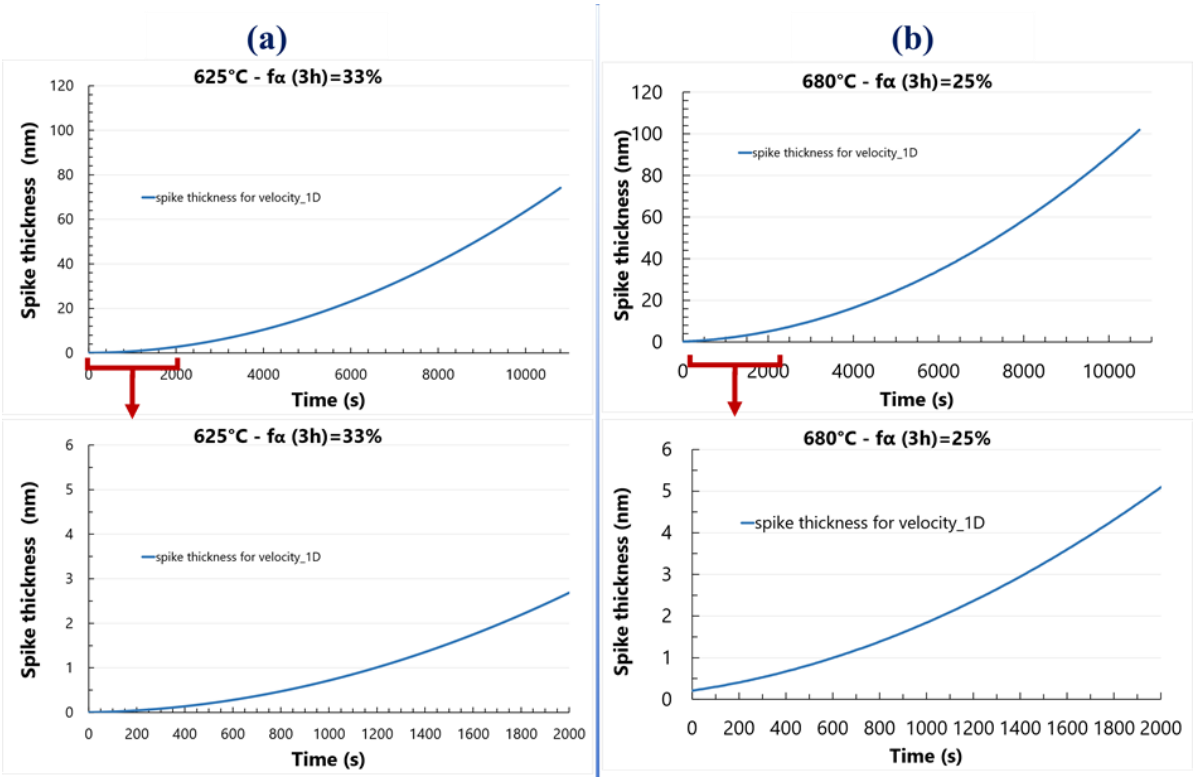

Figure 5.6. *The evolution of spike thickness estimated from the relationship established by Coates for* ***(a)*** *625°C and* ***(b)*** *680°C of transformation temperature.*

5.1.3 Comparison of APT data at 625°C and 680°C with theoretically expected under LENP condition

The Mn excess determined from the experimentally measured profiles by APT were compared with the Mn excess obtained from DICTRA calculation and using Coates approach. The results of this comparison are shown in **Figure 5.7** (a) and (b) for transformation temperatures of 625°C and 680°C, respectively. Note that considering the possible influence of orientation relationships at the transformation interface on the amount of segregation, the experimental data were separated into two groups: obtained for the interfaces with near KS-ORs (*APT_KS* – red squares) and with the large misorientation with respect to KS-ORs (*APT_non-KS* – blue triangles).

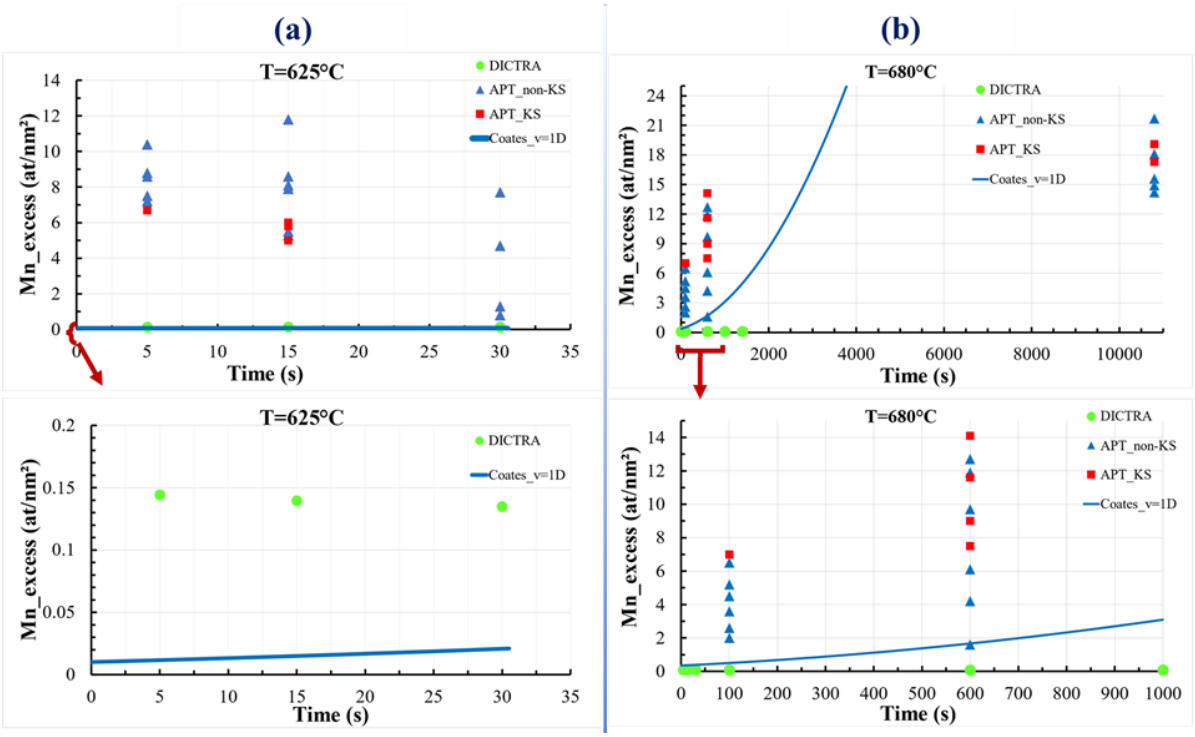

Figure 5.7. *Comparison of theoretically calculated Mn excess with the Mn excess determined from APT data at* ***(a)*** *625°C and* ***(b)*** *680°C.*

The calculated Mn excess by DICTRA (green circles) at both considered transformation temperatures are almost constant at the beginning of the transformation and significantly smaller than the measured Mn excess by APT. From the presented data, it is clear that the results of DICTRA id not describe the experimentally observed tendency. In any case, we have to keep in mind the problem with the mesh definition mentioned above. The Mn excesses estimated using the Mn peak width obtained according to Coates approach (*Coates_v=1D* – blue line) gives a slightly better tendency with respect to experimental data, but still show that amount of accumulated Mn at the interface should not vary a lot at the beginning of phase transformation in contrast with what is experimentally observed. However, it is also necessary to keep in mind that the calculations proposed by Coates are an approximation.

Both calculations show that the excess of Mn at the interface under the local equilibrium condition is expected to be almost constant or slightly increasing at the beginning of the transformation, which is not the case regarding the experimental data. It is a fundamental point that can help differentiate the LENP mode from other transformation models (LEP and SD) for ferrite growth (at least at the early stage of growth). Since the measured Mn excess is relatively high (>2 at/nm²) compared to the calculated one, it becomes evident that the observed Mn peaks experimentally at 625°C and 680°C can not be treated as LENP spikes. Therefore, the LENP is not the right mode to describe austenite-to-ferrite phase transformation at investigated condition.

The measured Mn excess evolution at the interface well demonstrates increasing segregation over time, which rather corresponds to the Solute Drag. In order to support the SD as a possible mode for ferrite growth, the calculations using the model for the prediction of interfacial conditions developed by D. Huin have been performed.

5.2 Model of D. HUIN, ArcelorMittal SA

5.2.1 Model overview

Introduction

A new formalism based on the Purdy&Brechet model was developed by D. Huin (ArcelorMittal SA) and, further, will be called the 'Huin' model. This model has been used in this work to predict the evolution of the solute composition profile across the moving α/γ interface. Similar to the P&B approach, the transformation interface in the proposed model is considered as a particular phase with a certain thickness and properties. The idea is to describe the evolution of the substitutional element profile (Mn in this work) through three different zones: ferrite, interface, and austenite (see **Figure 5.8** (a)). The first zone with an initial thickness L_1 corresponds to the initial ferrite phase. The second zone represents an interface between the ferrite and austenite phases. In the 'Huin' approach, the transformation interface is considered as a particular phase (with a certain thickness and diffusion properties). Therefore, the zone of the interface has two sides, one in contact with the ferrite phase (α/I1) and one with austenite (I2/γ). In this approach, the thickness of the interface phase is assumed to be constant over time with a given thickness, L_2. Therefore both sides of the interface (I1 and I2) are moving with the same velocity, $\vec{v}$. The third zone is the parent austenite phase, with a thickness L_3. The total length, L, ($L = L_1 + L_2 + L_3$) is constant.

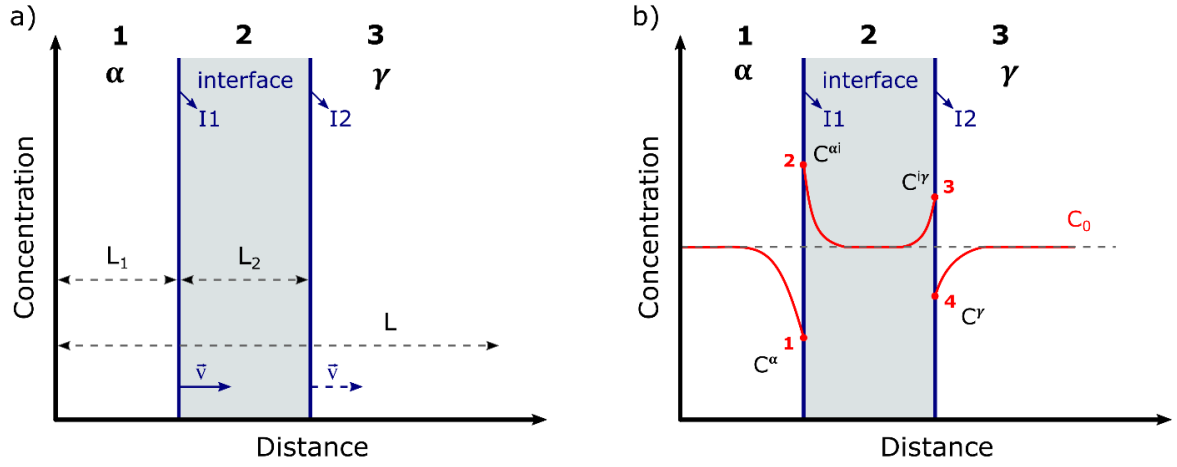

Figure 5.8. ***(a)*** *Geometrical configuration of the 'Huin' model and* ***(b)*** *schematic representation of the initial profile of the substitutional element.*

To describe the evolution of the profile for the substitutional element in the system, the diffusion equation (5.5) has to be solved for each of the three zones:

$$\frac{\partial C}{\partial t} = D\frac{\partial^2 C}{\partial^2 x} \qquad (5.5)$$

where C and D are the concentration and diffusion coefficient of the substitutional element.

To solve eq. (5.5), it is first necessary to consider the boundary conditions at the interface between each zone. In the general case, the McLean equation for each phase and the mass balance equation for the initial profile are used to create the initial conditions.

McLean equation

Due to the difference in the chemical potential of Mn between ferrite, interface and austenite, the McLean equation can be used to calculate the initial concentrations of the alloying element at the interface in ferrite and austenite phases (see points 1,2 and 3,4 in red in **Figure 5.8** (b)). In this case, the chemical potential can be expressed as a function of the concentration:

$$\mu = \mu_0 + RT\ln C(x) + E(x) \qquad (5.6)$$

where μ is the chemical potential of the solute in the alloy, μ_0 - the chemical potential of pure solute and $E(x)$ is the profile of chemical potential (se**e Figure 5.9**). Purdy&Brechet [92] assumed that $E(x)$ has a "V" shape (in red in **Figure 5.9**). In the 'Huin' model, it will induce an additional term in the diffusion equation (1.15) which will be responsible to the evolution of the chemical potential inside the interface. Unlike the P&B model, where a quasi-steady-state velocity is assumed, the current model considers the unsteady regime. The time required to establish segregation on the interface has to be taken into account, and the unsteady diffusion equation has to be independently solved in each subdomain, respecting mass balance. In the 'Huin' model, the "U" shape (in blue in **Figure 5.9**) of chemical potential is postulated. This shape simplifies the resolution of the diffusion equations and eases establishing a relationship between the concentration on both sides of the interface.

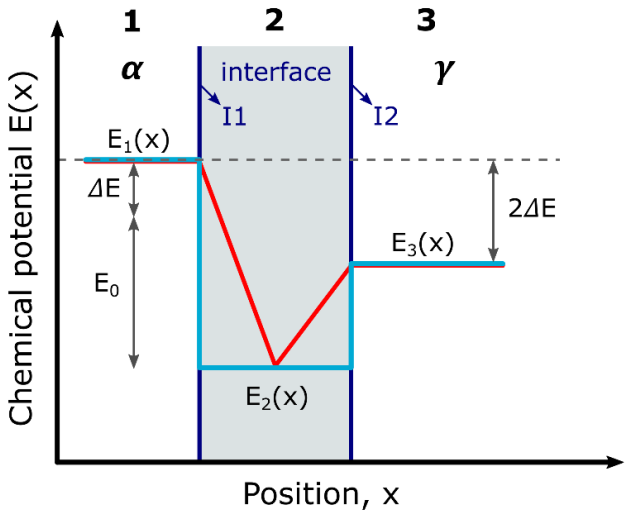

Figure 5.9. *Chemical potential profile of the substitution element across the transformation interface: E_0 – binding energy, ΔE – the half of the Mn chemical potential difference between austenite and ferrite.*

In the case of "U" shape, the chemical potential for each point 1, 2, 3, and 4 in **Figure 5.8** (b) can be written as:

$$\mu_1^{\alpha} = \mu_0 + RTlnC_1 + E_1(x) \quad (5.7)$$

$$\mu_2^{\alpha i} = \mu_0 + RTlnC_2 + E_2(x) \quad (5.8)$$

$$\mu_3^{i\gamma} = \mu_0 + RTlnC_3 + E_2(x) \quad (5.9)$$

$$\mu_4^{\gamma} = \mu_0 + RTlnC_4 + E_3(x) \quad (5.10)$$

where $C_1 = C^{\alpha}$, $C_2 = C^{\alpha i}$, $C_3 = C^{i\gamma}$, $C_4 = C^{\gamma}$. Considering the equality of the chemical potential on each side of the interface (local equilibrium condition):

$$\mu_1^{\alpha} = \mu_2^{\alpha i}$$
$$\mu_3^{i\gamma} = \mu_4^{\gamma} \quad (5.11)$$

combining eqs. (5.7-5.10) it comes:

$$RT(lnC_2 - lnC_1) = E_1(x) - E_2(x) = \Delta E_{12} \quad (5.12)$$

$$RT(lnC_4 - lnC_3) = E_2(x) - E_3(x) = \Delta E_{23} \quad (5.13)$$

As a result, the following relations can be obtained for each phase:

$$\frac{C_2}{C_1} = exp\left(\frac{\Delta E_{12}}{RT}\right) = k_{12} \quad (5.14)$$

$$\frac{C_3}{C_4} = exp\left(\frac{\Delta E_{23}}{RT}\right) = k_{34} \quad (5.15)$$

The factors k_{12} and k_{34} determine the ratio of Mn concentrations on each side of the interface. At a constant temperature, k_{12} and k_{34} are fixed and given by the local gap on the

chemical potential chosen for the calculation. This approximation is the simplest way to solve the McLean equation. The next step is the definition of the initial profile of the substitutional element.

Mass balance conditions

The initial profile of the substitutional element is expected to be flat at the beginning of the transformation. However, to satisfy the condition (5.14) and (5.15), the concentrations at the interface should be different for the different interfaces. It can be assumed that for a very short initial time, $t = \varepsilon$, close to zero, the transformation interface is fixed (non-mobile). As a consequence, the initial profile can be taken according to the solution of the diffusion equation for a static interface [195], which can be written as

$$C(x,t) = (\mathrm{C}_i - \mathrm{C}_0) * (1 - \mathrm{erfc}\left(\frac{\mathrm{x}}{2\sqrt{\mathrm{D}_n \mathrm{t}}}\right) \qquad (5.16)$$

where $i = 1,..,4$; $n = \alpha, i, \gamma$ and C_0 is the nominal concentration of the substitutional element in bulk. Then, the initial profile is schematically illustrated in **Figure 5.10**.

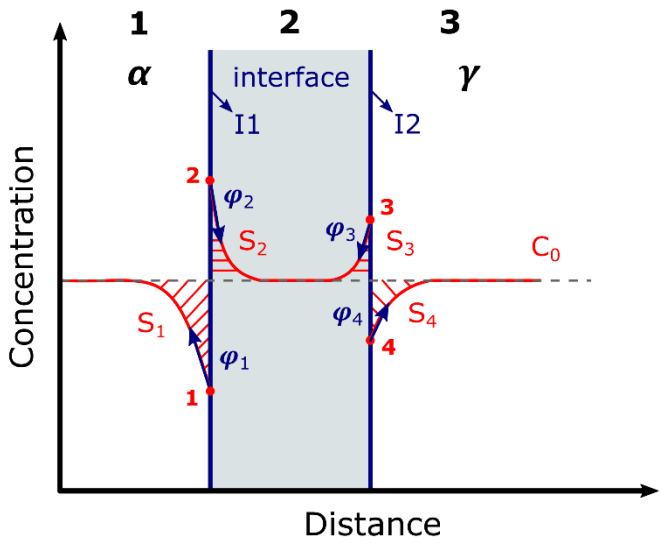

Figure 5.10. *The schematic illustration of the initial profile.*

Simultaneously with the McLean conditions (5.14) and (5.15), the mass balance has to be respected. It means that area S_1 has to be equal to S_2 and S_3 equal to S_4. Those areas could be calculated by considering the flux $\varphi(x,t)$ of the substitutional element with time. For example, for areas S_1 and S_2 it can be written:

$$\varphi_1(x,t) = D_\alpha \frac{\partial C}{\partial x}\Big|_{t=0} \qquad (5.17)$$

$$\varphi_2(x,t) = D_i \frac{\partial C}{\partial x}\Big|_{t=0} \tag{5.18}$$

where D_α and D_i are the diffusion coefficients of the substitutional element in ferrite and the interface phase, respectively. The integration of eqs. (5.17) and (5.18), from t=0 to t=ε, can be used to calculate these areas:

$$\int_0^{t=\varepsilon} \varphi_1(x,t)dt = 2(C_0 - C_1)\sqrt{\frac{D_\alpha \varepsilon}{\pi}} = S_1 \tag{5.19}$$

$$\int_0^{t=\varepsilon} \varphi_2(x,t)dt = 2(C_0 - C_2)\sqrt{\frac{D_i \varepsilon}{\pi}} = S_2 \tag{5.20}$$

Combining the mass balance ($S_1 = S_2$) and McLean ${}^{C_2}/_{C_1} = k_{12}$ conditions, the following equations can be obtained:

$$2(C_0 - C_1)\sqrt{\frac{D_\alpha \varepsilon}{\pi}} = 2(C_2 - C_0)\sqrt{\frac{D_i \varepsilon}{\pi}} \tag{5.21}$$

$$C_2 = k_{12} C_1 \tag{5.22}$$

$$\sqrt{D_\alpha}(C_0 - C_1) = \sqrt{D_i}(k_{12} C_1 - C_0) \tag{5.23}$$

Using $B_1 = \frac{D_i}{D_\alpha}$, the C_1 and C_2 for the initial profile can be expressed as:

$$C_1 = C_0 \frac{1 + \sqrt{B_1}}{1 + k_{12}\sqrt{B_1}}; \qquad C_2 = C_0 k_{12} \frac{1 + \sqrt{B_1}}{1 + k_{12}\sqrt{B_1}} \tag{5.24}$$

The concentrations C_3 and C_4 ban be obtained in the same way:

$$C_3 = C_0 \frac{1 + \sqrt{B_2}}{1 + k_{34}\sqrt{B_2}}; \qquad C_4 = C_0 k_{34} \frac{1 + \sqrt{B_2}}{1 + k_{34}\sqrt{B_2}}, \tag{5.25}$$

where $B_2 = \frac{D_\gamma}{D_i}$ and $k_{34} = \frac{C_4}{C_3}$.

More details of the numerical solving of the eq. (5.5) are given in **Appendix C.**

5.2.2 'Huin' model: simulation details

'Huin' model was recently developed. Therefore, the first step of calculating the evolution of the concentration profile across the austenite/ferrite interface using this approach is to choose the initial parameters for simulation and to estimate the influence of each of these parameters on the final results. A short overview of the main parameters that can be modified are:

- ***Temperature, T*: –** 625°C, 680°C and 720°C (investigated in this work).
- ***Initial thickness of ferrite zone, L_1*:–**was taken as 20 nm for all calculations (similarly to DICTRA). The modification of L_1 did not affect the simulation results.
- ***Interface thickness, L_2***: – within this work 1nm, 3 nm and 5nm were tested. Most of the calculations were performed with an interface thickness of 1 nm because this value was obtained from atomistic simulation using the Quasi-Particle approach (see (4.4)). The interface thicknesses 3 nm and 5nm were tested to investigate its effect.
- ***Thickness of austenite zone, L_3***: – was taken as 30 μm for all calculations, as the same taken value for DICTRA calculation, and estimation of interface velocity from dilatometry data. In any case, the austenite zone's thickness L_3 did not affect the results.
- ***Interface velocity, v***: – two types of calculations, with constant and variable interface velocities with transformation time, have been performed.
- ***Diffusion coefficients, D^{α}_{Mn}:*** – diffusion of Mn in ferrite, D^{int}_{Mn} – diffusion of Mn through the interface, D^{γ}_{Mn}– diffusion of Mn in austenite.

In the Huin' model, the variation of the diffusion coefficient with temperature is defined by Arrhenius law expressed by eq. (5.2). In this work, the calculation has been performed with two sets of diffusion coefficients ($D^{\gamma}_{Mn}, D^{\alpha}_{Mn}, D^{int}_{Mn}$). The first set of diffusion coefficients was calculated with the D_0 and E_a parameters found in the literature [193][194] and were noted as *Dif_liter*. The second set of Mn diffusion coefficients was obtained from DICTRA simulation using FEDEMO (Iron Demo Database v4.0) and MFEDEMO (Fe-alloys Mobility demo databases v2.0) databases of the Demo Steels and Fe alloys package, and was referred as *Dif_DICTRA.* However, the diffusion coefficient of Mn through the interface is unkonown, and it is an open question. In this work, its values were calculated with the next set of parameters: D_0=1.0•$10^{-4}\ m^2/s$ and $E_a = 155kJ/mol$. The values of diffusion coefficients used in this work are presented in **Table 19**.

Table 19. *The values of the Mn diffusion coefficients used for calculation within this work*

T, °C	D(T), *DICTRA* calculation *Dif_DICTRA*		D(T) defined by Arrhenius law *Dif_liter.*		
	ferrite, $10^{-18}, [m^2/s]$	**austenite,** $10^{-19}, [m^2/s]$	**ferrite,** $10^{-18}, [m^2/s]$	**austenite,** $10^{-19}, [m^2/s]$	**interface,** $10^{-13}, [m^2/s]$
625	1.044	0.164	4.165	1.051	0.963
680	10.964	1.103	25.524	7.907	3.192
720	54.615	3.866	82.466	29.804	7.018

- ***Binding energy:*** E_0 (J/mol)

The solute binding energy (attraction energy of a solute atom to a site at a grain boundary) is one of the fitting parameters of the SD based models. Since the binding energy of solute atoms to the transformation interface is the result of a variety of factors, its value is difficult to determine experimentally [196][197]. However, binding energy can be estimated from the accurately quantified amount of segregated atoms at the transformation interface, as segregation is a function of binding energy. According to Cahn [86], in the case of quasi-stationary interface, the binding energy can be linked to the ratio between bulk composition and the peak composition at the interface by the following expression:

$$\frac{C_{max}}{C_0} = exp^{\frac{(E_0-\Delta E)}{RT}} \qquad (5.26)$$

with C_{max} – the peak composition at the interface, C_0 – bulk composition, E_0 – binding energy, ΔE – the half of the Mn chemical potential difference between austenite and ferrite calculated from ThermoCalc, R – gas constant, T – temperature. Since the value of $C_{max}$is dependent on the used instrument, such an approach should be used with caution. Van Landeghem [22] suggested an alternative approach and proposed to estimate C_{max} from the measured Mn excess using the relationship of Maugis and Hoummada [119]: $C_{ex} = (C_{max} - C_0) \cdot l$ and considering a rectangular shape of Mn peak with thickness $l = 1\ nm$.

The results using the measured values of C_{max} (Mn_max, blue dots) and estimated values using Mn excess (Mn_excess, red dots) are shown in **Figure 5.11**. The large scatter of experimentally obtained values of C_{max} and C_{ex} due to the investigation of the different transformation interfaces (different ORs, shape…) led to a large scatter in binding energy calculated for both transformation temperatures. It is difficult to define a precise value of binding energy from the presented data in **Figure 5.11**, but the average value of $7\ kJ/mol$ have been used for the simulations. It is necessary to mention that this chosen average value is in good agreement with experimental measurements on austenite grain boundaries ($E_0 = 8 \pm 3\ kJ/mol$

[198]) on ferrite grain boundaries ($E_0 = 5.5\ kJ/mol$ [199]) and with the binding energy at α/γ transformation interface in the Fe-C-Mn system reported to be around $E_0 = 6\ kJ/mol$ in [21][65]. In addition, the twice bigger value of 14 kJ/mol has been used for testing purposes.

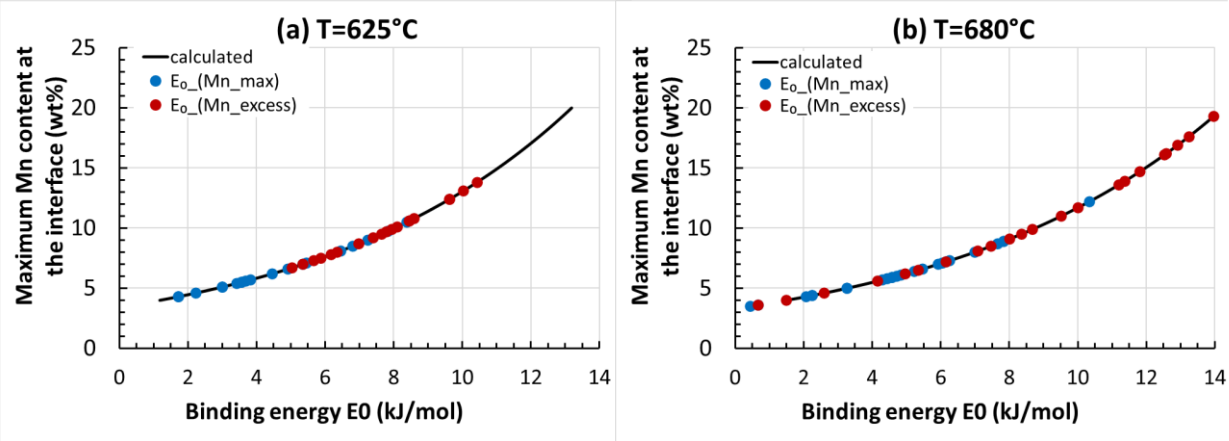

Figure 5.11. *Evolution of the maximum Mn content within the interface as a function of binding energy E_0 at **(a)** 625°C and **(b)** 680°C.*

5.2.3 Constant interface velocities

It is well known that the velocity of the transformation interface is slowing down over time, which is once again confirmed by the estimated interface velocity observed in this study (**Figure 5.5**). However, before considering the calculations with variable velocities, the simulation with constant velocities is useful in order to understend the sole effect of interface mobility on Mn partitioning through the α/γ transformation interface. Several constant values of interface velocity ($v_1 = 0.01\,\mu m/s\,, v_2 = 0.001\,\mu m/s\,, v_3 = 10^{-4}\,\mu m/s\,, v_4 = 10^{-7}\,\mu m/s$) have been used to simulate the segregation profile at both 625°C and 680°C.

The Mn composition profiles obtained as the results of the interface phase motion using the 'Huin' model for the constant velocities at 625°C and 680°C are shown in **Figure 5.12** and **Figure 5.13**, respectively. The profiles are shown at the beginning of the transformation (t_1*=4.9s* – blue, t_2*=14.4s* – red, t_3*=32.4s* – green, t_4*=102.4s* – magenta,), as well as at longer transformation times (t_5*=608.4s* – yellow, t_6*=10758.4s* – black). The times where chosen to be close to those that were investigated experimentally (**Table 5**). Here, it will probably be useful to remind that in the 'Huin' approach, the transformation interface is considered as a particular phase (with a certain thickness and diffusion properties). Therefore, now the α/γ transformation interface consists of "two interfaces" (α/I1 and I2/γ) and the region between them (see **Figure 5.8**).

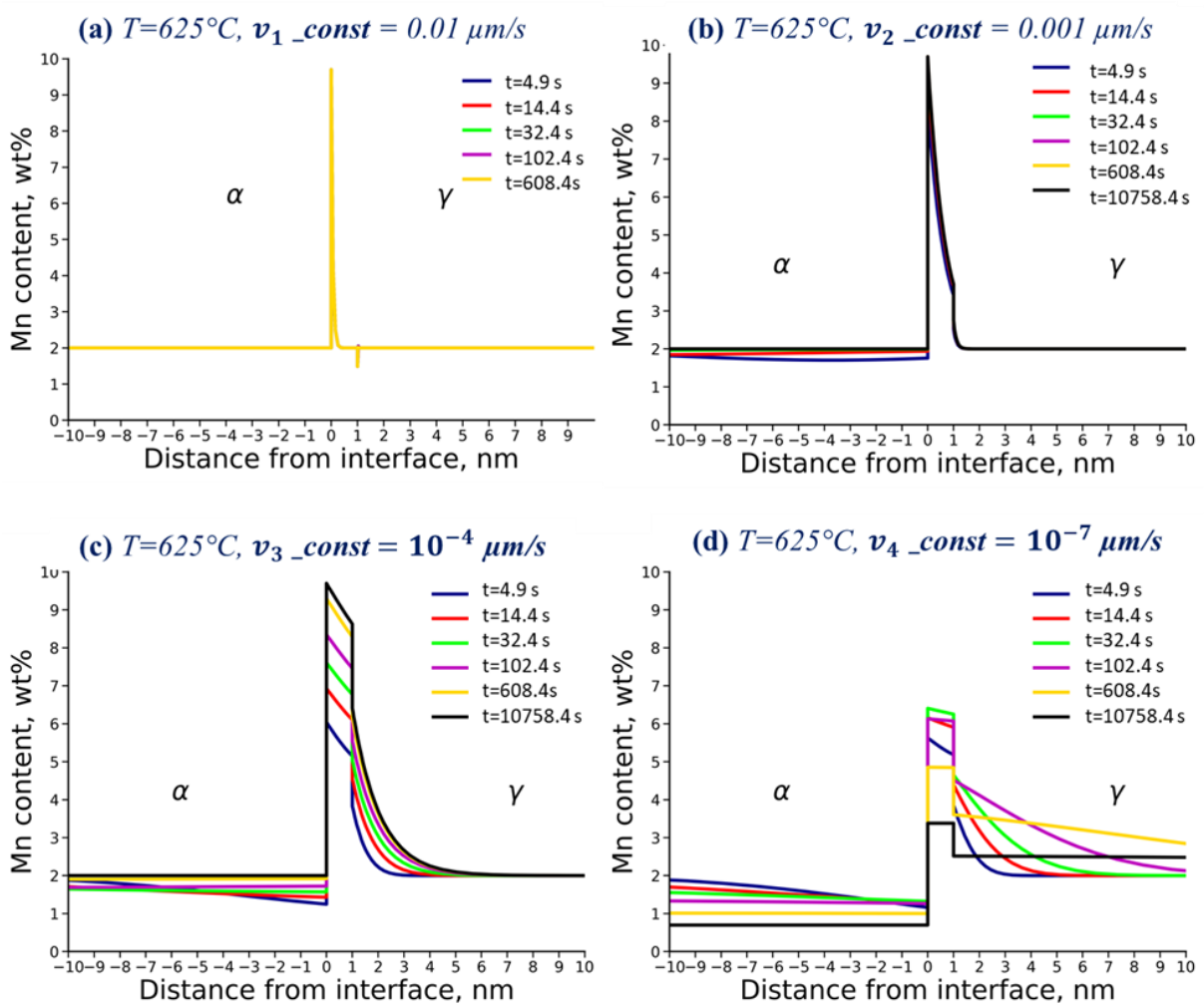

Figure 5.12. *Mn profiles at T=625°C f simulated with constant velocities using 'Huin' model: Dif_1iter.,* $\boldsymbol{E_0} = 7\ kJ/mol$, $\boldsymbol{L_2}$*=1 nm.*

At 625°C, at very high interface velocity ($v_1 = 0.01\,\mu m/s$), only the Mn peak that satisfies initially imposed conditions (McLean conditions and mass balance) is observed (**Figure 5.12** (a)). The maximum Mn content at the α/I1 interface is about 9.8 wt%. In this case, the interface is too fast, and there is no time for Mn diffusion. Therefore, the shape and maximum value of the observed Mn peak do not evolve with time and only propagate in space as ferrite is growing.

With decreasing of the interface velocity to $v_2 = 0.001\,\mu m/s$, the Mn has time to accumulate a bit at the interfacial zone. This is reflected by the increase of the maximum value of Mn content at I2/γ interface up to 4 wt%, while at α/I1 it does not change because the maximum value imposed by McLean is already reached (**Figure 5.12** (b)). Like in the previous case, the Mn peak propagates with time but with little evolution in shape. The segregation process at the interfacial zone is very rapid since the accumulation of Mn is observed from the early beginning of transformation (see *t=4.9s*). Still, a full partition has no time to be established

because of the high interface velocities. These results are similar to the steady-state results of the P&B model [92].

In the case of the intermediate velocity, $v_3 = 10^{-4}\,\mu m/s$ (**Figure 5.12** (c)), the partition of Mn from ferrite into austenite becomes more obvious, and extends over larger distances with transformation times. The transformation begins with Mn partitioning (see *t=4.9s*). However, the velocity is still high enough and segregated Mn at the interfacial zone does not have time for full partitioning into austenite. Therefore, it accumulates in the interfacial region, which may explain the increase of Mn peak over time. The depletion of Mn from the ferrite side next to the interface can be noticed from the early stages of transformation. At longer transformation times, the Mn content in ferrite close to the interface becomes equal to the nominal composition (2 wt%).

Finally, for the very low velocity, $v_4 = 10^{-7}\,\mu m/s$ (**Figure 5.12** (d)), the segregation inside the interfacial zone takes place, but the partitioning of Mn from ferrite into austenite becomes more pronounced. A lower peaks values of Mn in the interface zone than in the previous cases is observed, but the long-range diffusion into austenite extent over a larger distance with time. In addition, it can be noticed that the drop of Mn content in ferrite for all transformation times becomes even more pronounced than in the case of the previous faster velocities. At $v_4 = 10^{-7}\,\mu m/s$, the interface phase can be considered as immobile, so the ferrite domain remains very limited in size during all the transformation under this condition. The imposed constraints of the Mn interaction with the interracial region (expressed throughout the binding energy) lead to the Mn enrichment at the interface but Mn depletion in the ferrite, which becomes more evident for the limited ferrite domain. Consequently, Mn content in ferrite decreases but also decreases the levels of Mn content in the interface due to McLean law.

A similar tendency for the Mn profile evolution as was described above 625°C can be observed from the simulation results obtained in the case of 680°C (**Figure 5.13)**, but with stronger Mn partitioning since, due to higher temperature, the diffusion is faster.

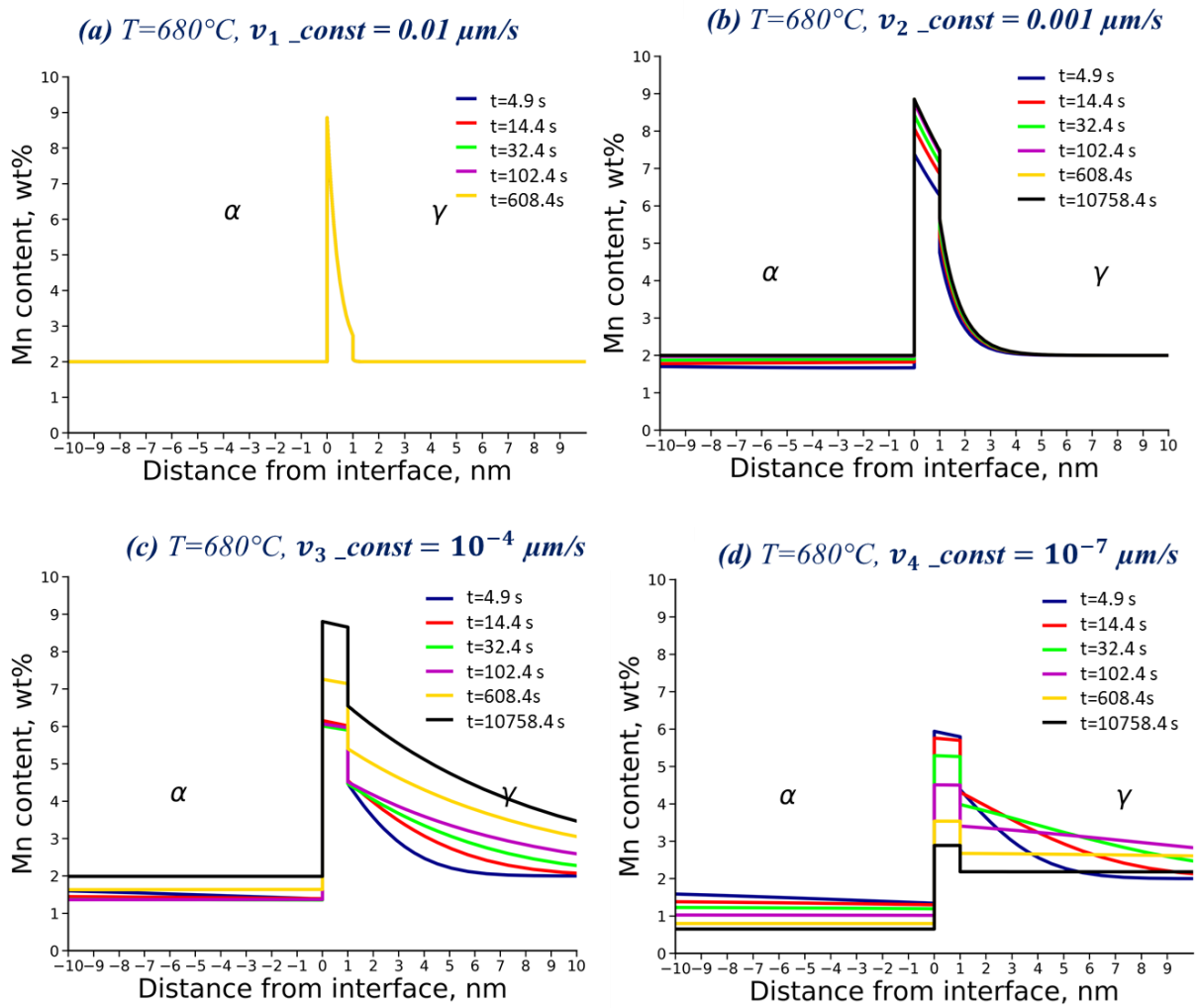

Figure 5.13. *Mn profiles at T=680°C f simulated with constant velocities using 'Huin' model: Dif_1iter., $E_0 = 7\ kJ/mol$, L_2=1 nm.*

The simulations with constant interface velocities demonstrate the competition between Mn segregation at the interfacial zone and Mn partitioning from ferrite into austenite. The obtained results show a critical influence of the interface velocity on the local condition that leads to different shapes of the Mn profile. Therefore, it is important to perform the simulation with the variable interface velocity (starting with a high velocity that decreases with time) that will better represent the real process during phase transformation. In this case, a mix of all observed effects with constant velocities is expected.

5.2.4 Variable interface velocity

The next set of simulations is dedicated to the investigation of the evolution of the Mn composition profiles using the variable interface velocity in the 'Huin' model. Our ultimate goal is to compare the modelling results with experimental data. Therefore, it is necessary for the simulation to use the evolution law of interface mobility variation obtained based on our

experimental results using dilatometry data as presented in paragraph (5.1.2), **Figure 5.5**. As mentioned earlier in this chapter, the variable velocity considering "1D" geometries of interface propagation (the same as DICTRA calculation, 1D modeling) will be discussed in this work. In addition, the influence of different parameters, such as diffusivities, binding energy, and interface thicknesses, are investigated. As previously mentioned, two sets of diffusion coefficients ($D_{Mn}^{\gamma}, D_{Mn}^{\alpha}, D_{Mn}^{int}$) noted as *Dif_liter.* and *Dif_DICTRA* (see **Table 19**), as well as two values of binding energy: 7 kJ/mol and 14 kJ/mol have been used. Interfacial zone thicknesses 1 nm, 2 nm and 5 nm have been considered. These parameters' changes lead to similar characteristics of the Mn profiles for both considered temperatures (625 °C and 680 °C). Therefore, only the results of calculations at one temperature (680 °C) are presented in detail. For the other temperature, only a brief overview of the results will be presented.

First of all, let us consider the position evolution of the interfacial zone (α/I1 interface position) with time for the variable velocities that is shown in **Figure 5.14**. As we impose the variable velocity that decreases with time, the propagation of the interfacial zone is also slowing down significantly with time.

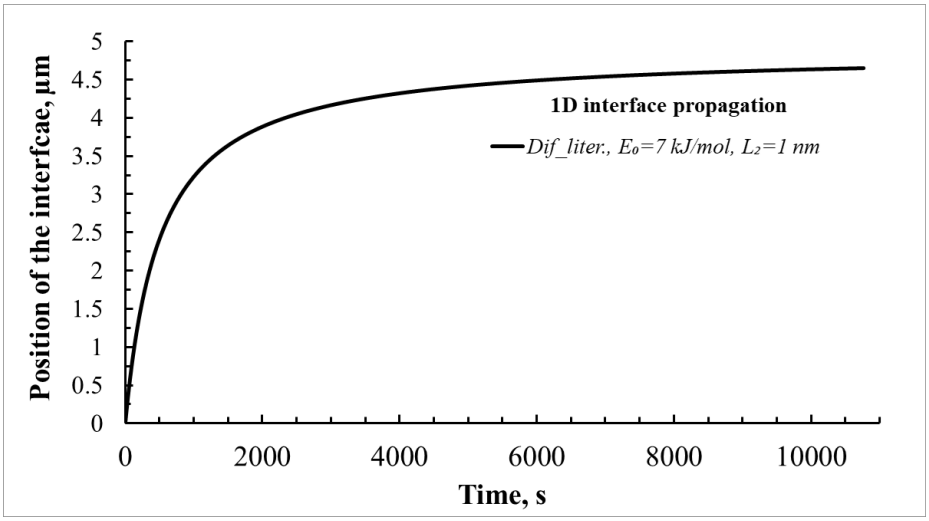

Figure 5.14. *Temporal evolution of the interfacial zone propagation at T=680°C with variable velocity considering "1D" interface propagation simulated using 'Huin' model: Dif_1iter.,* $\boldsymbol{E_0} = 7\ kJ/mol$, $\boldsymbol{L_2}$*=1 nm.*

The Mn profiles obtained at 680°C for different transformation times and with different sets of parameters using the 'Huin' model are shown in **Figure 5.15.** The profiles were plotted for the exact transformation times as in the case of constant velocities. **Figure 5.15** (a), (b) and (c) show the Mn profiles considering the interfacial zone thicknesses 1 nm, 3 nm and 5 nm, respectively. In these cases, the simulations were performed with 7 kJ/mol binding energy and with the *Dif_liter* set of diffusion coefficients. The simulation results with the diffusion

coefficient obtained from DICTRA (*Dif_DICTRA)* for comparison are shown in **Figure 5.15** (d). Finally, the Mn profiles obtained with the binding energy of 14 kJ/mol are shown in **Figure 5.15** (e).

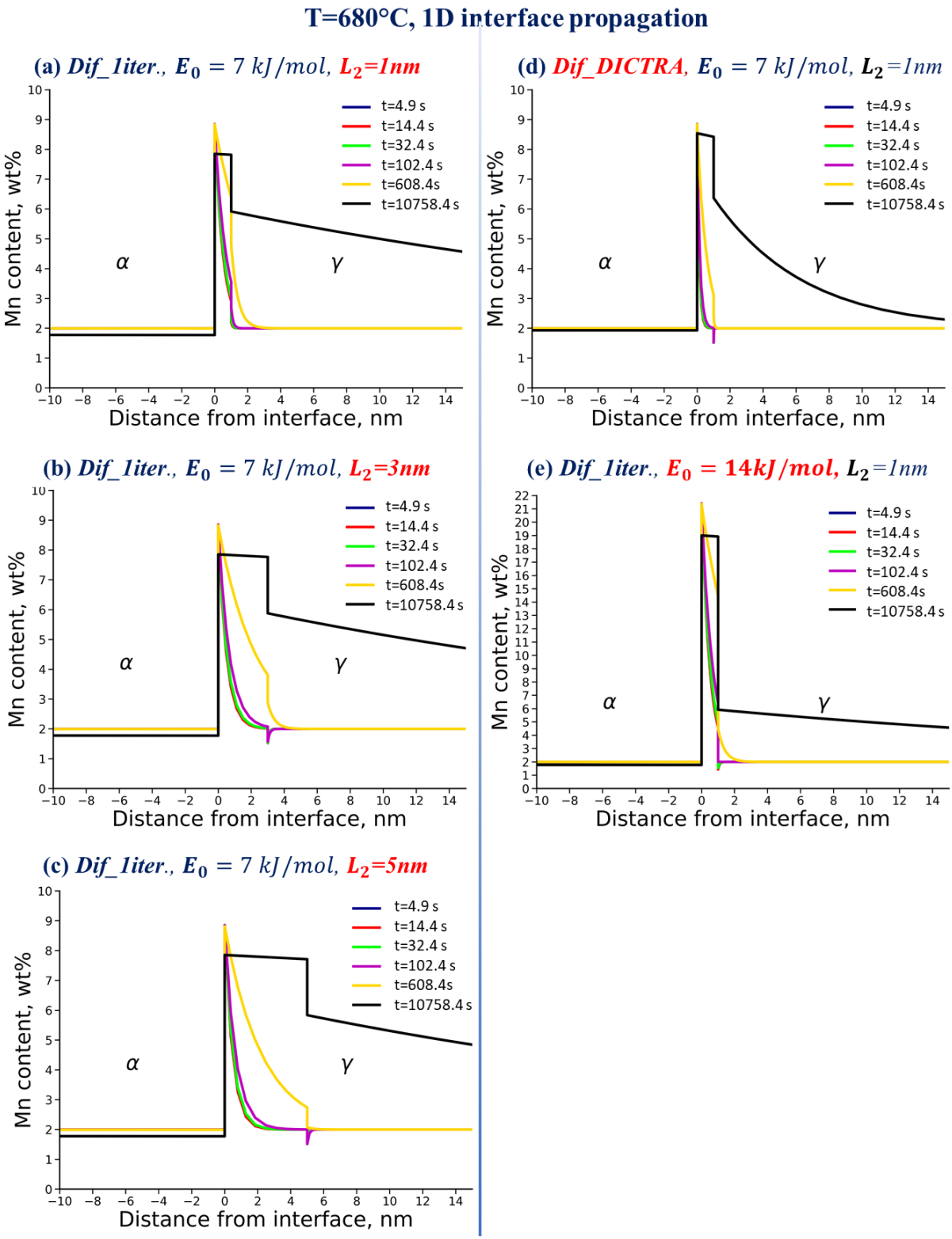

Figure 5.15. *Mn profiles simulated at T=680°C with variable velocity considering "1D" interface propagation using 'Huin' model with different diffusion coefficients (Dif_liter and Dif_DICTRA), binding energy values (7 and 14 kJ/mol) and thicknesses of the interfacial zone (1 nm, 3 nm and 5 nm).*

In all the cases, several steps of profile evolution can be observed. At the early beginning of transformation, the average interface velocity is very high (see first 100 s in **Figure 5.5** (b), "1D" case – blue curve). Therefore, as previously shown, the initially formed profile (see profiles at *t=4.9 s, 14.4 s, 32.4 s, and 102.4 s*) only propagates in space without significant accumulation of Mn in the interfacial zone (because of the fast propagation, there is no time for Mn segregation). Only very slight variations of Mn content values at α/I1 and I2/γ interfaces can be observed. Then, when the interface velocity slows down enough, Mn has time to accumulate at the interfacial phase, leading to the increase of the Mn content at the I2/γ interface, while the amount of Mn at α/I1 does not change. In most of the cases presented in **Figure 5.15**, this stage occurs approximately between 100 and 600 s of transformation. Then, the interface velocity is low enough for the long-range diffusion of Mn into austenite to occur. This stage can be observed in **Figure 5.15,** typically after 600 s (yellow curves) of transformation. For even longer transformation time, Mn has more and more time to diffuse and partition over longer distance into the austenite, progressively leading to the thermodynamic equilibrium of the system (equilibrium composition and thus immobile interface). Of course, equilibrium is only reached for "infinite" time.

As can be seen from **Figure 5.15**, the considered parameters (diffusivities, binding energy, and interface thicknesses) have no major influence on the evolution of the Mn profile shapes during phase transformation. However, segregation energy and interface thickness will influence the amount of Mn segregation in the interface phase. It is especially evident comparing **Figure 5.15** (a) and **Figure 5.15** (f). Therefore, the Mn excesses were calculated to compare the Mn segregation predicted by 'Huin' model with values obtained from the APT measurements and DICTRA simulations.

5.2.5 Comparison of APT data at 625°C and 680°C with the results of 'Huin' model

Using simulation profiles presented in **Figure 5.15**, Mn excess is calculated as the area under the Mn composition profile minus the area corresponding to the nominal composition. Since in the 'Huin' model, the width of the interfacial zone is fixed, the Mn excesses related to Mn peak and Mn long-range diffusion into austenite (when it present) can be easily separated. Then, the Mn excess related to Mn peak includes the area only under the Mn peaks of the fixed interface thickness (1 nm, 2 nm, or 5 nm). The tail value corresponds to the area under the tail of long-range diffusion from the right border of the interface (depending on the fixed interface width) up to the distance where Mn value is back to the nominal composition. However, in the case of experimentally measured Mn profiles by APT, it's impossible to define the interface

limit (see more details in paragraph (2.7)). Besides, it would also be impossible to measure the 'tail' value because often, experimental profiles do not extend enough due to the limited analysed volume by APT. Therefore, the Mn excess for the experimental data was calculated only for the profiles without long-range diffusion. Taking into account this fact, in the case of theoretical data, only Mn excess related to the peak are presented.

The comparison of the experimentally measured Mn excess and simulated ones are shown in **Figure 5.16**. The evolution of Mn excesses obtained from the simulation using the 'Huin' model clearly shows the increasing tendency for Mn excess with time (at least when $t < 1000\ s$). This behaviour is similar to what is observed experimentally. We can see that the different diffusivities (*Dif_liter.* and *Dif_DICTRA*, **Table 19**) do not affect the results significantly. On the other hand, the values of the binding energy and interface thicknesses significantly influenced the amount of Mn excess at the interface. In the case of different interface thicknesses, the asymptotic values (5 at/nm^2, 15 at/nm^2 and 25 at/nm^2) are proportional to these thicknesses (1 nm, 3 nm and 5 nm, see solid, dot and dashed black curves in **Figure 5.16**). However, taking into account a significant scatter of experimental data, it is difficult to define the appropriate values of the binding energy and interface thicknesses.

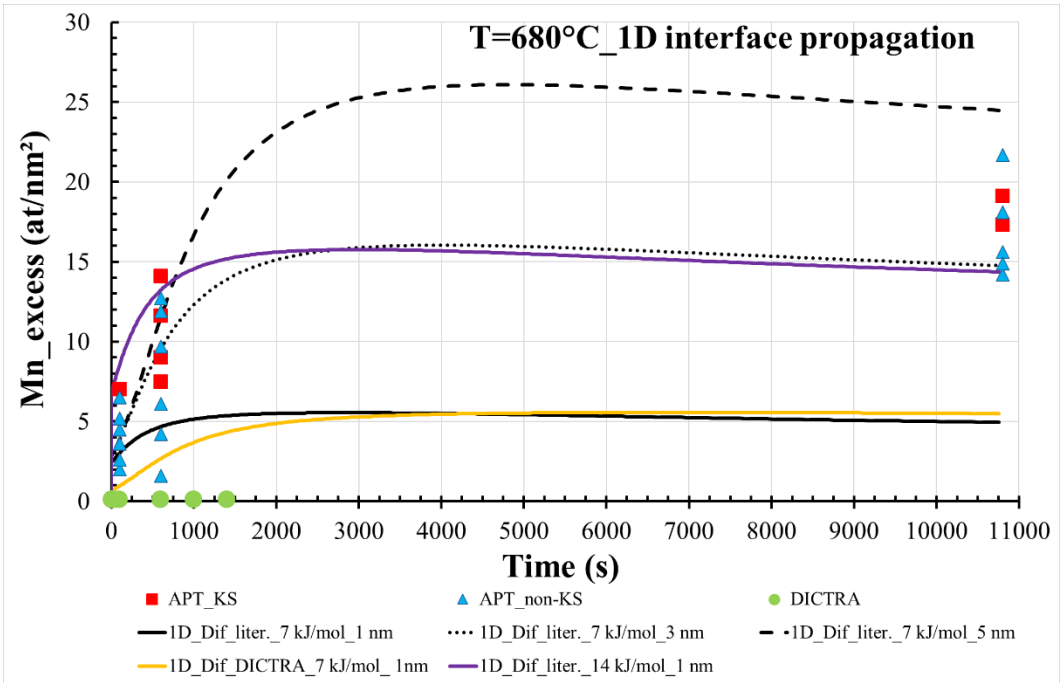

Figure 5.16. *Mn excess calculated from the results of simulations ('Huin' model considering the experimental velocity for 1D ferrite growth, and DICTRA) vs APT measured Mn excess at 680°C.*

As was mentioned earlier, the simulations performed at 625 °C show a similar tendency of the Mn profile evolution as observed at 680 °C. Therefore, it was decided not to show all the detailed results at 625 °C. Only as an example, the Mn profiles obtained for the simulation with

"1D" geometry of interface propagation, with the diffusion coefficient from literature *(Dif_liter.)*, $\boldsymbol{E_0} = 7\ kJ/mol$, and $\boldsymbol{L_2}$=1 nm are shown in **Figure 5.17**. The comparison of calculated Mn excess and measured by APT is also shown in **Figure 5.17**. At this temperature, most experimental data were obtained for short transformation time (5 s, 15 s and 30 s), and only two after 3 h. Therefore, comparison of the simulated data with experimentally obtained ones is more challenging. The analysis of the simulation results at 625°C shows similar tendencies as observed for 680°C, and the 'Huin' model results seem to be more realistic than the predictions of DICTRA.

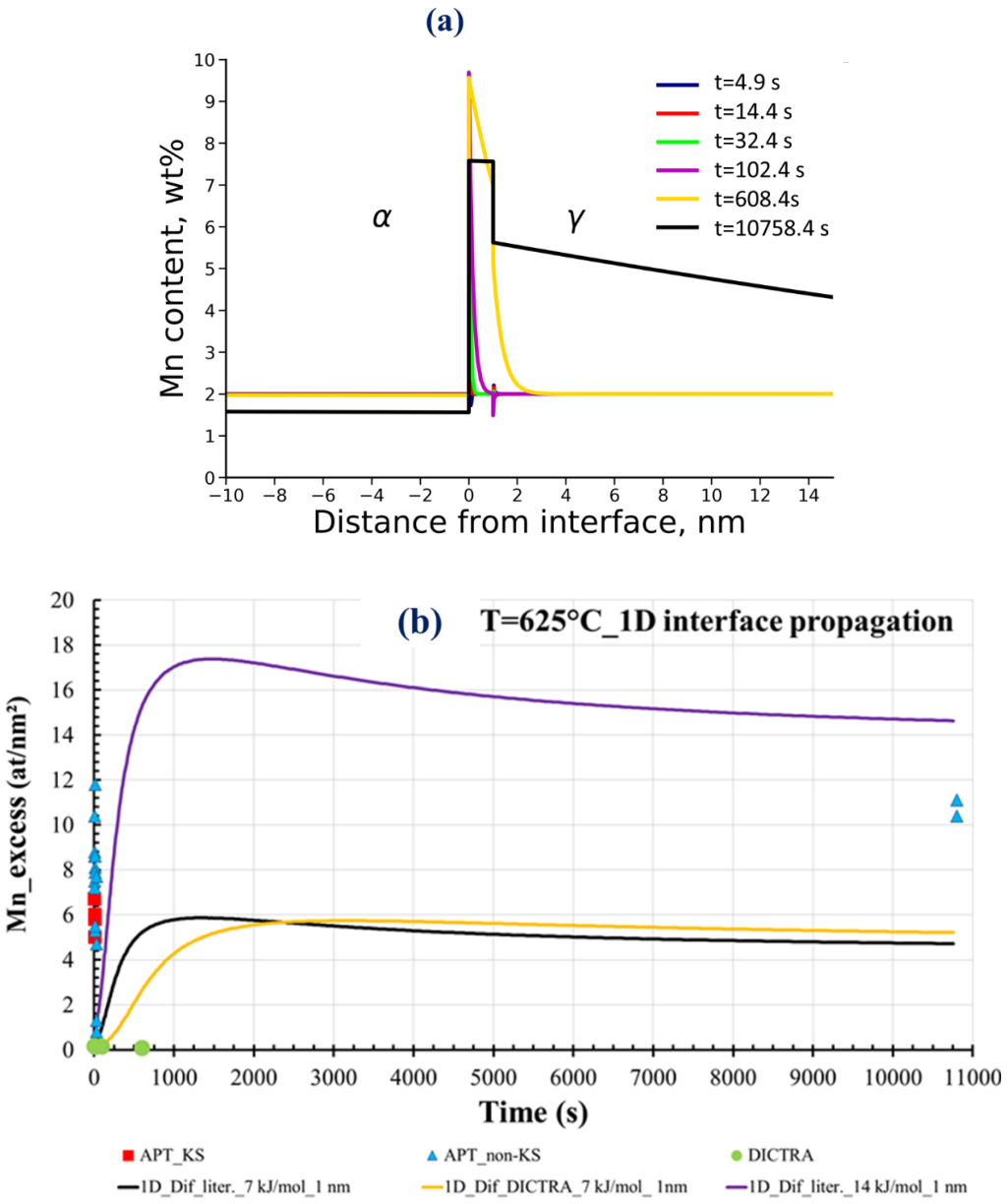

Figure 5.17. (a) *Mn profiles simulated at T=625°C with variable velocity considering "1D" interface propagation using 'Huin' model: Dif_1iter.,* $\boldsymbol{E_0} = 7\ kJ/mol$, $\boldsymbol{L_2}$*=1 nm.* **(b)** *Mn excess calculated from the results of simulations ('Huin' model considering the velocity for 1D ferrite growth and DICTRA) vs APT measured Mn excess at 625°C.*

Finally, we can conclude that the 'Huin' model has been successfully used for the prediction of the Mn composition profile evolution across the moving α/γ transformation interface. Analysing the simulation results shows that this approach describes much better the experimentally observed Mn excesses at 625°C and 680°C than the model with the sole assumption of local equilibrium (DICTRA calculation and estimation using Coats approximation). Here, to avoid confusion, we must clarify that we do not compare the results of DICTRA calculations with the results obtained using the 'Huin' model because these two calculations are based on different assumptions regarding the phase transformation mechanism. However, comparing the results of each calculation independently with the experimentally measured one, it can be concluded that the experimental results qualitatively support the Solute Drag as the effective mode that operates during austenite-to-ferrite phase transformation at 625 and 680°C. One of the main arguments for this conclusion is based on the comparison of predicted and measured Mn excess evolution. For both temperatures, the tendency of Mn excess to increase with time is clearly observed experimentally and predicted by the 'Huin' model.

Another question is the choice of the model parameters to describe as accurately as possible the real systems. As was shown and discussed before, the interface propagation velocity has critical effects on the partitioning processes during phase transformation by influencing the shapes of the Mn composition profile across the transformation interface. Nevertheless, despite some simplifications, average interface velocity can be realistically estimated from the dilatometry experiments that are representative of the real kinetics. More challenging is the definition of binding energy, the estimation of which is also one of the goals of the experimental part of this work. However, due to the larger scatter in experimental data, its value remains quite uncertain, and is still a fitting parameter in simulation. Last but not least is the determination or estimation of the diffusion coefficient of Mn in the interface. Its effect was not explored in this study but may have an influence and should be investigated in more detail.

Despite some open questions related to the choice of input parameters, the model developed by D. Huin seems to be a promising approach to predicting the shape of solute profiles close to and across the transformation interface and, thus, leads to a better understanding of the phase transformation process. A set of experimental composition profiles after 3h of transformation at 680°C is shown in **Figure 5.18** for comparison. It is a very interesting example showing the complexity of the selection, as, along the same ferrite grain (shown in the right bottom part in **Figure 5.18**), very different types of Mn profiles were observed: the presence of only Mn peaks (b) and (d), presence of both Mn peaks and Mn long-range diffusion in austenite (a) and (f), mostly Mn long-range diffusion in austenite (c, e, g).

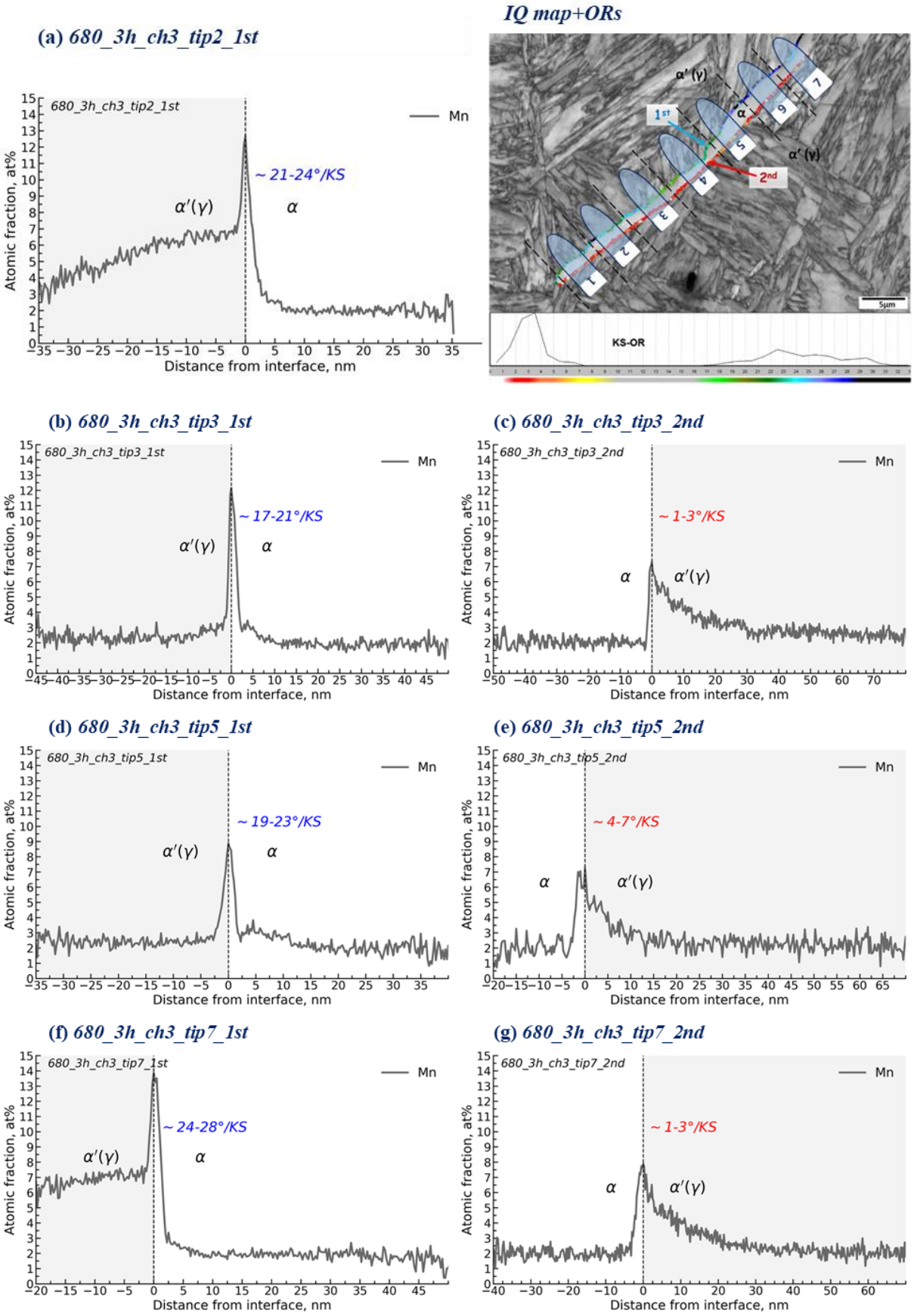

Figure 5.18. *Composition profiles of Mn across the 1st and 2nd α/γ interfaces of 680_3h_ch3, see more details in* **Figure 3.29** *and* **Figure 3.30.**

As we can see in **Figure 5.18**, the Mn long-range diffusion in austenite is observed at the interfaces with ORs close to KS (2nd interface, **Figure 5.18** (c, e, g)). Similar Mn profiles were observed during the simulation using the 'Huin' model at 680°C with very low constant interface velocities (**Figure 5.13** (d)). In comparison, only the peak of Mn during the simulation was observed in the case of high interface velocity (**Figure 5.13** (a)) that is close to profiles in **Figure 5.18** (b and d) obtained across the interface with non-KS ORS (1st interface). The presence of both Mn peak and Mn long-range diffusion was obtained from the simulation with variable velocity for longer transformation time (**Figure 5.15**) or with intermediate constant interface velocities (**Figure 5.13** (b or c)). That is similar to experimental profiles in **Figure 5.18** (a and f). In our experimental investigation, we do not know the exact local value of the interface velocity. Thus, comparing the simulated and measured profiles can only be made some assumptions. The presence of only long-range diffusion of Mn in austenite may indicate very low local interface velocity, while the profiles only with Mn peak indicate high interface velocity. Such observation may help us to explain the different Mn profiles obtained experimentally along the same ferrite grain due to the variation of local interface velocities, and potentially to understend better the effect of ORs on the segregation processes.

5.2.6 Homogeneous Mn distribution through the interface

One of the uncertain points of the experimental investigation of γ/α interfaces is the lack of the Mn peak observed only at the transformation temperature 625°C. As previously mentioned, the segregation of Mn atoms at the interface was found in most of the observed samples except for a few cases (**Figure 3.7** (e), **Figure 3.8** (b, c), **Figure 3.10** (d), **Figure 3.13**(e)). Different explanations can be done in these cases: one of them is that the interface is immobile and thus do not generate a solute drag effect. Definitely, it can not be the case for both interfaces in **Figure 3.8**(b-c), because at least one of the interfaces has to be mobile. From the other side we can suggest that the interface velocity is so big at 625°C that Mn atoms don't have time to segregate at the interface.

Another situation can be found in the two cases shown in **Figure 3.7** (e) and **Figure 3.10** (d), where the Mn segregation was observed at the neighbouring tips of the interface where flat Mn profiles were observed. Here, two assumptions can be considered. The first one is that can exist a variation of the interface velocity along the same ferrite grain caused by compositional or structural local variations. The second assumption is that the austenite/ferrite interface position can be shifted during the quenching to the RT. This cannot be excluded and has already been observed during decarburizing experiments [200]. Thus, the observed interfaces in the

analyzed APT volumes may not be exactly the initial interface of interest. The C redistribution in the close vicinity to the interface from the ferrite side in both considered cases is not typical for pure of C ferrite regions. It can indicate that the ferrite continues partly to grow during the martensite transformation, and the original interface with Mn segregation was not analyzed within these APT volumes. Regarding the last case of the homogeneous Mn distribution through the interface observed in **Figure 3.13** (e), the higher Mn content in the prior austenite side can indicate the early stage of the Mn partitioning across the interface, as observed for the neighbouring tips in **Figure 3.13** (d).

5.3 LEP vs. Solute Drag at 720°C

The final result to be discussed is the case of 720°C. The isothermal section of the phase diagram at 720°C is shown in **Figure 5.19** (a). The LEP, PE or SD are possible transformation mechanics at this transformation temperature. The experimentally measured kinetics of ferrite growth (from image analysis and dilatometry) is very slow at this temperature (**Figure 5.19** (b) as compared to 625°C and 680°C (**Figure 5.3** (b)). This can be easily explained in terms of the dropping of transformation driving force with increasing temperature. Thus, the interface velocity, estimated from the dilatometry data, is very low (see **Figure 5.19** (c)), but the diffusion process is faster at a higher temperature. Therefore, the PE regime is not likely to be operated. Moreover, segregation at the interfaces was observed under this condition that can be described by either LEP or SD model. Under LEP conditions, a long-range diffusion profile of Mn atoms into austenite with a maximum Mn content defined from the phase diagram is expected. As was already mentioned, the segregation at the transformation interface can be caused by the solute drag. Therefore, similar to the previous cases, DICTRA and 'Huin' calculations have been performed to model the Mn profiles in order to find a mechanism that operates during phase transformation at 720°C.

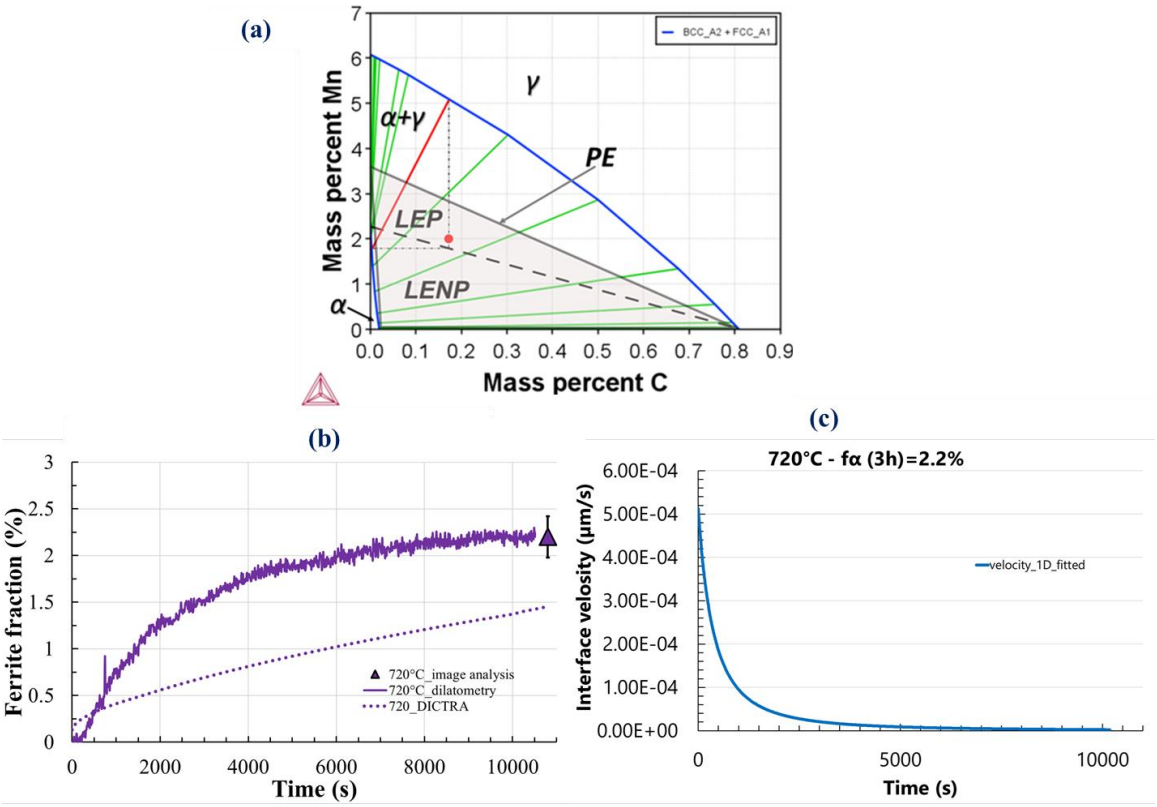

Figure 5.19. *Investigation of austenite-to-ferrite at 720°C:* **(a)** *the isothermal section of Fe-C-Mn phase diagram;* **(b)** *predicted and measured ferrite growth kinetics;* **(c)** *average interface velocities estimated from the dilatometry data.*

The Mn composition profiles predicted by DICTRA at 720 °C are shown in **Figure 5.20** and were plotted for several holding times (5s, 100s, 600s and 3h) to illustrate their evolution with time. Since phase transformation kinetics are very slow, Mn diffusion plays an important role in establishing the composition profiles. Therefore significant gradients of Mn in austenite (corresponding to the long-range diffusion) are presented since the beginning of the transformation (see profiles at 100s – magenta and 600s – orange curves). After 3h of transformation, the DICTRA predicts an expansion of Mn composition gradient in austenite up to 150 nm. The maximum Mn content at the interface is about ~5.0 at%, and the lower Mn content from the ferrite side is ~1.7 wt%, which corresponds to the values defined according to the operative tie-line shown in red in **Figure 5.19** (a).

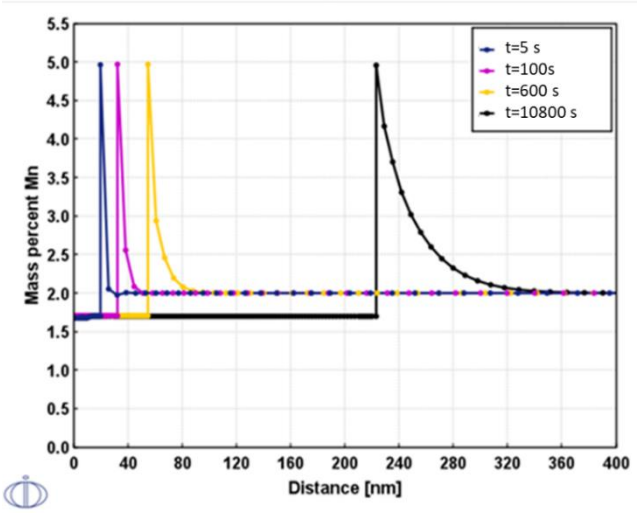

Figure 5.20. *Mn composition profiles predicted by DICTRA calculation at 720°C.*

The evolution of the Mn composition profiles simulated using the 'Huin' model at 720°C with variable velocity considering 1D interface propagation (**Figure 5.19** (c)) is shown in **Figure 5.21**. Since interface velocity is very low, the Mn partitioning from ferrite into austenite is dominant at this condition. The long-range diffusion of Mn into austenite started to be observed even after t=4.9s. The content of Mn in ferrite is lower compared to austenite.

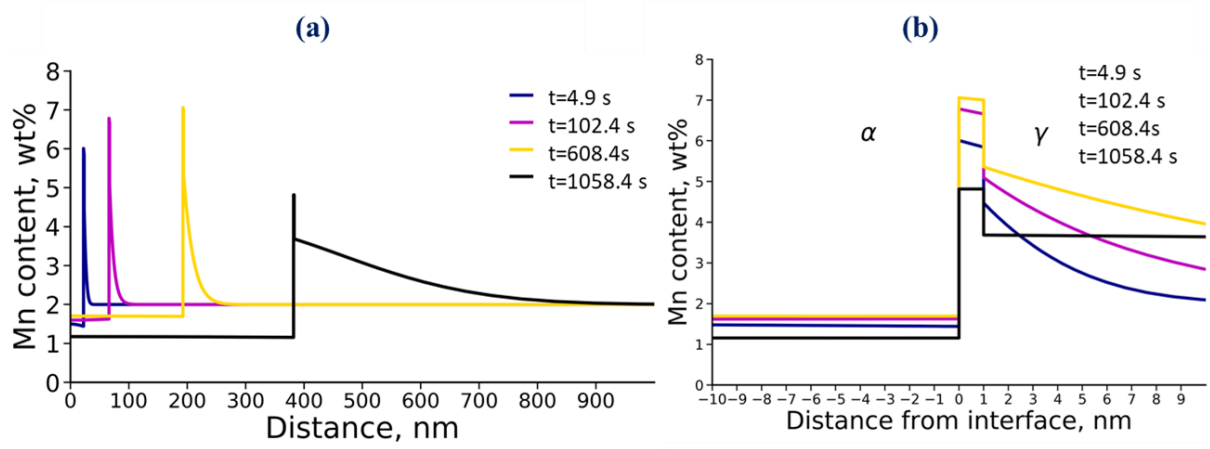

Figure 5.21. *Mn profiles with variable velocity considering "1D" interface propagation simulated at 720°C using 'Huin' model: Dif_1iter.,* $\boldsymbol{E_0} = 7\ kJ/mol$, $\boldsymbol{L_2}$*=1 nm.* **(a)** *the evolition of Mn profile with time;* **(b)** *detailed views of Mn profiles at the interface.*

There are not a lot of APT data in the case of 720°C (see **Figure 3.34**). The experimentally obtained Mn concentration profiles in **Figure 3.34** (b) and (d) are in good agreement with the profile predicted by the DICRA calculation (**Figure 5.20**). First of all, the gradient of Mn concentration into the parent austenite side is clearly observed in both cases. It indeed extends to several tens of nm (30 nm in **Figure 3.34** (b) and 60 nm in **Figure 3.34** (d))

vs 150 nm predicted by DICTRA. Nevertheless, the experimentally observed Mn gradients possibly extend further into austenite but can not be seen due to the limited analyzed depth during the APT measurements. In both cases, the Mn content at the interface is near 5 at%, and the average Mn content in the ferrite is about 1.6 at%. These values are in good agreement with the value predicted by the DICTRA calculation. However, it can be noticed that in the case of **Figure 3.34** (b), we see only long-range diffusion of Mn into austenite. While in the case of **Figure 3.34** (d), we can notice the presence of both Mn peak and long-range diffusion that is closer to the profiles obtained using the 'Huin' approach propagation (**Figure 5.21**). Moreover, the third experimentally observed Mn profile (**Figure 3.34** (f)) demonstrates the presence of only the Mn peak. It is not predicted by LEP but can be obtained using the 'Huin' model considering faster interface velocity.

Indeed, both DICTRA and 'Huin' modeling could fit the observed results in **Figure 3.34** (b and d). However, the result in **Figure 3.34** (f) is questionable. In any case, there is limited experimental data in this case. Therefore, in order to be able to conclude about the operating regime (LEP vs SD) at 720°, additional experimental investigations are required.

5.4 Mobile interface of transformation. ORs influence

In most cases, the nucleation and growth of allotriomorph ferrite from austenite occurs with respect to well-defined ORs. In particular, KS-ORs are one of the most frequently reported experimentally. Typically, ferrite grain has KS-ORs with the parent austenite grain from one side and a larger misorientation with respect to KS-ORs from the other side. Note that double-KS at both sides of ferrite grain) was also be observed [21][48]. It should be noted that the interface with near KS-OR has a semi-coherent structure, while non-KS can be described as incoherent (disordered structure). Such different interface structures may reflect different interface parameters such as thickness, biding energy, and interfacial diffusivity that can affect the interfacial energy dissipation due to the solute partitioning through an interface and thus affect the Solute Drug process. Therefore, the possibility of ORs influence on the solute segregation during phase transformation has been discussed by many authors [10][21][22] and will also be discussed with respect to our experimental results.

It was mentioned earlier in this work that we don't know which of the two interfaces of the ferrite grain is the mobile one. It was reported [1][37] that ferrite preferentially grows into austenite with a larger deviation from KS. Nevertheless, the situation that both interfaces are mobile and ferrite grows in both directions is not excluded. That's why the composition profiles were measured on both sides of the ferrite grain. It was assumed that the presence of Mn

segregation at the interface could be the indicator of interface mobility. However, it should be kept in mind that the Mn may not have time to accumulate at transformation interfaces with very high velocity. In that case, the Mn profile across such kind of interfacthe will be flat. At the same time, the possibility for the equilibrium segregation at the immobile interface for a longer holding time, especially in the case of 720 °C when the diffusivity of Mn atoms is higher compared to the 680°C and 625°C, was not exulted as well.

Our experimental results show the presence of Mn segregation at the interfaces from both sides of investigated ferrite grains. Therefore, the experimental observation may indicate that both interfaces (with near KS-ORs and non-KS) are mobile. Moreover, in situ TEM and EBSD observations of austenite-ferrite interface migration [48], [49], [201]–[203] confirm this conclusion. However, it was shown that, depending on the ORs, austenite-ferrite interfaces have different mobility rates. In particular, it was shown that planar (straight) interfaces with KS or NW ORs have lower mobility than those with a larger misorientation [48][49][201][202]. Also was shown that this difference became less pronounced as the transformation temperature is reduced[202].

The influence of different ORs on the interaction of Mn atoms with the α/γ interface can be clearly seen at 680° at different holding times: 100 s (**Figure 3.19**, **Figure 3.21**), 600 s (**Figure 3.23**, **Figure 3.25**) and especially in the case of 3 h (**Figure 3.30**). In the most observed cases at these conditions, the observed Mn profiles across the α' (γ)/α interfaces with a larger misorientation from the KS-ORs demonstrate the relatively symmetrical peak of Mn atoms at the interface. In addition, the Mn depletion from the ferrite side is often observed. In comparison, the Mn profiles across the interfaces with near KS-ORs are characterized by the presence of long-range diffusion profiles in the austenite side. It is becoming even more clear for the longer holding time, for example 3 h. Similar observations can be seen at 720 °C (**Figure 3.34**). However, it is not the case for the Mn profile at α' (γ)/α interfaces observed at 625 °C. For example, the results presented in **Figure 3.12** demonstrate that independent of the ORs, similar Mn profiles are obtained. At these conditions, the long-range diffusion profile started to be observed only for the longer holding time of 3h.

Summarizing the above observations, it is possible to assume that the ORs affect the Mn segregation at the γ/α interface due to the different interface mobilities. The presence of the interface with the larger deviation from KS exhibits a rapid migration compared to the interface with near KS. The fact that both interfaces are mobile explains the presence of Mn segregation in both cases. The variation of the Mn profile shape observed at near KS and non-KS can be explained by the different velocities depending on ORs. In addition, it can be noticed that OR

has a more pronounced influence at the higher transformation temperatures (720°C and 680°C), whereas it is less evident at 625°C. It can be explained that at a lower transformation temperature, the driving force is higher, so the effect of OR becomes less dominant. Besides, the diffusion process is slow and influences less the shape of the Mn profile.

Summarizing the experimental results mentioned above, it is possible to assume that the ORs influence the behavior of the Mn profile across the γ/α interface due to the different interface mobilities depending on the different misorientation. The presence of the interface with the large deviation from KS exhibit a rapid migration compere to the interface with near KS. However, as both interfaces are mobile, Mn atoms are segregated at both sides. The variation of the shape of the Mn profile observed for the KS and non-KS ORs can be explained by the different velocities of these interfaces. In addition, it can be noticed that OR can influence the segregation kinetics transformation temperature between 720°C and 680°C, whereas it is less evident at 625°C. At a low temperature, the driving force of transformation is higher, which induces faster kinetics. So the effect of OR becomes less pronounced.

5.5 Conclusions

Two approaches of austenite-to-ferrite phase transformation modeling have been presented and discussed in this chapter. The first one is based on the diffusive character of the phase transformation and uses the standard local equilibrium assumptions. The diffusive module DICTRA of commercial Thermo-Calc software has been used to investigate this approach. The second approach is a Solute Drag based model developed by D. Huin from ArcelorMittal SA, Metz, which is a new formalism of Purdy and Brechet model. The aim of the chapter was to compare the experimentally obtained Mn profiles with the ones theoretically expected and, based on this comparison, to identify the most likely operative mode of ferrite growth during austenite-to-ferrite phase transformation in the investigated temperature domain (625 °C, 680°C, 720 and for a nominal composition of Fe-0.17wt%C-2wt%Mn).

In the case of 625°C and 680°C, it was shown that theoretically predicted Mn profiles according to LENP assumption (DICTRA calculation) showed an extremely small width Mn spike at the α/γ interface (~0.04 nm), remaining unchanged throughout the transformation sequence up to 1000 s of holding. A long-range diffusion of Mn into austenite was observed for a long transformation time. The calculated Mn excess was far lower than the experimentally one measured at both temperatures. Therefore, it was concluded that the experimentally observed Mn peaks can not be interpreted in the framework of the LENP model at 625°C and 680°C. In turn, the characteristics of the predicted Mn profiles using ‘Huin’ model showed the same

evolution tendency across the transformation interface as observed experimentally. Depending on the interface velocity and temperature, several types of Mn profiles were obtained: the initial partitioning of Mn, accumulation of Mn at the interface, the presence of both peak and long-range diffusion of Mn into austenite, the drop of Mn peak and the increasing long-range diffusion tail with time. Moreover, for both temperatures, the evolution of Mn excess obtained from the simulation using the 'Huin' model exhibits similar behaviour as observed experimentally. Based on this presented calculation and experimental data, it can be concluded that the Solute Drag is operating mode during austenite-to-ferrite phase transformation at 625°C and 680°C.

However, the situation is not so clear at 720°C. From the presented modeling and limited experimental data, it is impossible to conclude which regime, LEP or SD, operates at this temperature. Therefore, more APT experiments are required at this temperature to make a final conclusion.

Another uncertain point is related to the observed homogeneous Mn profile. Some explanation was proposed in this chapter for each particular case, but it can be under discussion.

The influence of the ORs on the Mn redistribution at the α/γ interfaces was discussed based on the literature review of the in-situ tracking of interfaces propagation by EBSD and TEM. It was observed that at a higher temperature, the interfaces with the larger misorientation with respect to the well-defined ORs (KS in our case) are faster than the interfaces with well-defined ORs. Therefore, the Mn profile shape variation observed at near KS and non-KS at 720°C and 680°C was explained by the different interface velocities depending on ORs.

Conclusions and suggestions for further work

Conclusions based on experimental work

The austenite-to-ferrite phase transformation plays a key role in tailoring the final steel microstructure, especially during the processing of modern AHSS. It has been long observed that the interaction between the alloying elements and the migrating transformation interface affects directly the kinetics of ferrite growth. Thus, a better understanding of the redistribution processes of alloying elements across the transformation interface is critical for a profound knowledge of the austenite-to-ferrite phase transformation mechanism.

Many different models have been developed accounting for the interfacial partitioning of alloying elements during the austenite-to-ferrite transformation in Fe-C-X alloys. The models of Local Equilibrium with Partitioning (LEP) or with Non-Partioning (LENP), as well as ParaEqulibrium (PE) have been widely used to describe the behaviour of solutes atoms at and close to the fcc/bcc interface. A brief overview of these models was presented in Chapter 1. However, deviations from the predictions of these models were often observed experimentally, which was attributed to the interaction of the solute atoms with the moving transformation interface, through a phenomenon called Solute Drag (SD). SD approach was also presented in Chapter 1. Although the SD approach used to describe the ferrite growth in steels is widely discussed in the literature, there are only few experimental data that directly demonstrate solute interactions with a moving ferrite/austenite interface. Thus, accurate measurement of the solute composition profiles across transformation interfaces down to the nanoscale is an important element to understand the phase transformation better. Therefore, the aim of this thesis was to investigate experimentally the redistribution of alloying elements in the close vicinity to α/γ interface and quantify the solute enrichment at the interface. Atom probe tomography (APT), because of its high spatial resolution and sensitivity, is one of the most promising techniques for this kind of investigation. It was, therefore, the central technique used in the current study.

In this work, a Fe-C-Mn ternary model alloy with a nominal composition of 0.17 wt%C and 2.0 wt%Mn (0.787 at%C and 2.0 at%Mn) was investigated. This composition was selected in order to 'explore' the different potential modes of γ to α phase transformation in the selected temperature range (625-720°C). The intercritical annealing treatments were performed in a

dilatometer, which provided a controlled heat treatment procedure and allowed to estimate the kinetics of ferrite growth from the dilatation curves. The potential SD effect vs. LEP/LENP or PE was investigated for three transformation temperatures: 720°C, 680°C, and 625°. In order to identify the operative mode of ferrite growth at these temperatures, the evolution of the Mn composition profiles at the transformation interface with time was investigated. Analysis of a large number of α/γ interfaces was necessary to assure the representativity of the experimental results. The standard lift-out procedure for the site-specific APT sample preparation was modified to increase the number of successful APT runs. The TKD technique was used to control the final position of the interface with respect to the apex of APT tip. In addition, to investigate the possible influence of ORs on the transformation rate, SEM-EBSD measurements with a special post-treatment were used before lift-out to identify the ORs between parent γ and daughter α phases. The description of the experimental procedures used in this study, and details of experimental data treatments were given in Chapter 3. The measured APT profiles are possibly affected by well known biases such as the local magnification effect or the spatial resolution. Therefore, the Mn segregation at the interface was characterised quantitatively by the Mn excess and Mn excess was calculated from the integral profile that is not affected by these biases. The details of Mn excess calculation at the interface between two different phases were also discussed.

Despite all the challenges of the experimental procedures and data treatments, about a hundred Mn profiles were successfully measured at the nanoscale using APT and post-treated within this work. The overview of the observed results was given in Chapter 4. The segregation of both Mn and C at the α'(γ)/γ interface was found in most of the analyzed samples within this study. In this work, we were focused only on the interpretation of Mn segregation since the origin of C segregation is questionable due to its high diffusivity even at room temperature. However, due to the low carbon solubility in ferrite, the C composition profiles and 3D reconstructions of C were very helpful for the α'(γ)/α interface identification.

Several types of Mn composition profiles were observed in APT reconstructions:

- homogeneous Mn distribution through the interface (no visible Mn peak)
- the initial partitioning of Mn through the interface
- Mn segregation at the interface,
- the presence of both Mn peak and long-range diffusion of Mn into austenite
- only the long-range diffusion of Mn into austenite.

The experimentally obtained Mn profiles were compared with the ones theoretically predicted profiles under local equilibrium using DICTRA software (Thermo-Calc) and a SD

model developed by D. Huin from ArcelorMittal SA. The calculation results and their comparison with experimental data were presented in Chapter 5.

The majority of the Mn profiles were measured for 625°C and 680°C transformation temperatures. Based on the isothermal sections of the Fe-C-Mn ternary phase diagram at these temperatures, LENP/PE or SD was expected to operate during the austenite/ferrite phase transformation. Therefore, one of the main questions was whether the observed Mn peaks measured at these temperatures correspond to the predicted LENP spike or represent the accumulation of Mn atoms at the interface due to the SD effect. According to the relationship established by Coates and obtained from DICTRA calculation, the spike thickness should not evolve significantly at the beginning of phase transformation. Therefore, under LENP conditions, the calculated Mn excess at the interface should be almost constant with time, and the related Mn excess insignificant. It is important to note that the physical meaning of Mn spike thickness (about ~0.04 nm) predicted by DICTRA is questionable, especially considering the problem of the appropriate mesh definition relative to the Mn diffusion in the particular case of LENP. The experementally measured Mn excess for different holding times demonstrated rapid evolution, which is not in agreement with the predicted results under LENP conditions. Therefore, from the presented results in Chapter 5, it is evident that the observed Mn peaks at 625°C and 680°C can not be explained as LENP spike, and SD is therefore a more realistic model for ferrite growth at these temperatures.

The SD as an operative mode for ferrite growth at 625°C and 680°C was confirmed using the 'Huin' model. Two types of calculations, with constant and variable interface velocities, have been performed. It was shown that the interface velocity affects the Mn redistribution across the interface. For a given interface velocity, a competition between the Mn segregation at the interface and Mn partitioning in austenite was observed. Based on these calculations results, it can be assumed that the different experimental Mn profiles obtained along the same ferrite grain might be linked to local variations of interface velocities. The calculations with variable interface velocity (defined relatively to dilatometer measurements) represented a more realistic situation, since the transformation interface propagation is slowing down with time during the phase transformation. In this condition, the simulated Mn profiles generally showed the same tendency of Mn redistribution across the transformation interface than was observed experimentally. Finally, the evolution of Mn excess obtained using the 'Huin' model demonstrates similar behavior as was observed experimentally at 625°C and 680°C. Such results support the conclusion that Solute Drag is the transformation mode that operates during austenite-to-ferrite phase transformation under these temperature. However, the definition of the calculation

parameters such as binding energy, interface width, and diffusivity remains an open question and requires more investigations.

In the case of 720°C, LEP and SD mode are potentially expected. However, due to the limited experimental data, it was difficult to conclude regarding the operative regime of ferrite growth at this condition. Therefore, more APT measurements should be done for this temperature.

In this study, the obtained data of crystallographic identification of the α/γ interfaces confirmed the tendency that at least one of the α/γ interfaces of the ferrite grain has near KS-ORs, while the other one typically has a larger misorientation with respect to KS-ORs. The segregation of Mn was found on both sides of the examined ferrite grains, independently of the ORs. However, at 680°C and 720°C, the long-range diffusion of Mn into austenite was always observed at the interfaces with near KS-ORs. At the same time, in the case of the larger misorientation of the interface from KS-ORs, this kind of Mn profile was observed only in some cases of long transformation time. In the literature, it is reported that interfaces with larger misorientation to well-defined ORs are more mobile. Therefore, it was assumed that different shapes of Mn profiles reflect the different interface mobilities, depending on the ORs. This tendency wasn't observed at 625°C when the phase transformation is faster.

Prospective regarding the experimental work

The experimental investigations of a model Fe-C-Mn alloy presented in this work allowed us to gather a large number of data that confirms the influence of interface velocity on the segregation phenomena that take place at α'(γ)/γ interface. These results also give some ideas for the further development of the SD based models. However, two important points can be highlighted regarding the experimental study. The first one is related to the actual growth kinetic of individual ferrite grain. We know the holding time in our experience but we don't know when ferrite grain was nucleated and started to grow. Then it's difficult to define exactly a real "growth time". Therefore, the large scattering of experimental data of Mn excess evolution can partly be connected to this problem. The second open question is the actual interface velocity. The calculation using 'Huin' model clearly demonstrated the effect of interface velocities on the shape of Mn profile across the interface. Based on these calculations and the in-situ EBSD and TEM experiments reported in the literature, it is possible to make some assumptions about the link between the shape of Mn profiles observed experimentally and the interfaces velocities. However, this link is not direct and remains based on extrapolations. To solve this problem, in-situ-EBSD or in-situ TEM experimental studies can be considered as a perspective for further work.

Another open question is related to the role of C segregation at the interface. The question is whether C atoms also segregate at the interface due to the SD effect, and if it affects the Mn segregation at the interface by a coupled-solute drag effect. Unfortunately, up to now, we can not answer these questions from the experimentally obtained data in this study because the observed segregation of carbon may be at least partly caused by carbon redistribution at room temperature and thus not be related to the high temperature process. The investigation of the role of carbon clearly requires additional experimental and theoretical work.

Conclusions based on QP modelling

In addition to the experimental investigation, the recently developed Quasi-Particle (QP) approach was also used to describe the fcc-to-bcc phase transformation. This atomistic approach provides the possibility of describing the displacive phase transformation when atoms move at distances smaller than interatomic space and keep the time scale typical for the fcc/bcc interfaces propagation. Using this method, the propagation of the fcc/bcc interfaces with different orientation ralationships (ORs) were simulated. It was shown that the interfaces with KS and NW ORs demonstrate higher mobilities compared to the interfaces with Bain and Pitsch ORs. It was also shown that the interfaces with KS and NW ORs had lower interfacial energy due to a special step disconnection structure formed at these interfaces. It was reported that the areas at the interface with smaller misfits (low energy areas due to smaller atomic stress) are preferential for the growth of the bcc phase, while dislocations were observed to be formed in the areas of larger misfits (the high energy areas). Thus the presence of disconnections at the interface is an important factor that affects the transformation rate. The slip mechanism of phase transformation with a primary shear in $\langle 11\bar{2}\} \rangle_{fcc}$ direction of $\{111\}_{fcc}$ plane and further homogeneous deformation were observed in the case of KS OR.

Prospective regarding the atomistic modelling using QP approach

The propagation of the fcc/bcc interface was successfully modeled at the atomic scale using the QP approach in a pure Fe system. Relevant information about the fcc/bcc interfaces atomic structures, propagation mobility, and mechanism of phase transformation with different ORs was obtained. However, the observed dislocations at the interfaces and their movements require more profound analysis, which is one of the prospects for further work. In addition, there is another concern related to the fact that the simulation results based on the QP approach demonstrated the faster migration of the interfaces with well-defined ORs (KS and NW) with respect to the large misorientation interfaces. It is somewhat contrary to the experimental

observations where the interfaces with a larger misorientation demonstrate higher mobility. Here, is important one more time to note that at this stage, the modeling was performed only for one component system (pure Fe), without taking into account diffusion phenomena at the transformation interface. For example, it can be expected that the segregation of solute atoms will be high at an incoherent interface that contains more free volume than a coherent one. Therefore, it will be important to understand the migration mechanism of fcc/bcc interfaces and their interaction with solute atoms in multicomponent systems. Consequently, the main step to further advance the work in this direction is to develop the QP for the case of ternary alloys and to model the fcc/bcc phase transformation in Fe-C-Mn systems.

Appendix A. Elastic constant calculation

Elastic properties are fundamental properties of solid materials. In particular, elastic constants are of interest because they are related to the interatomic forces in the solid. For small deformation, these forces are linearly proportional to the displacement of the atoms from the equilibrium position. At the same time, elastic constants can derive such elastic properties like shear modulus, G, Young's modulus, E, and bulk modulus, B. Therefore, the elastic constants can be represented as a connection between the atomic and macroscopic scale and can be used to adjust the validity and accuracy of the simulated system to the physical one.

A.1. Elastic constants of a cubic crystal

A general form of Hooke's law for a linear elasticity (small deformation) of the continuous elastic material mathematically can be expressed as follows [204]:

$$\sigma_{ij} = \sum_{kl} C_{ijkl}\, \varepsilon_{kl} \qquad (0.1)$$

C_{ijkl} is the fourth-order tensor of elastic constants related to the linear connection between the second-rank strain, ε_{kl}, and the stress, σ_{ij}, tensors. In the general form, tensor C_{ijkl} has 81 components. The number of independent constants is usually reduced to 36 due to the symmetry elements of crystals.

In a particular case of cubic crystals, taking to account that diagonal shear components are zero and mixed components does not occur, there are only three independent elastic constants: $C_{11}, C_{12}, C_{44.}$ (Constants C_{ijkl} denote by C_{mn}, where indices one through six have the following definition $1 = xx, 2 = yy, 3 = zz, 4 = yz, 5 = zx, 6 = zz$). So the matrix Hooke's law for the cubic system can be written as:

$$\begin{pmatrix} \sigma_{xx} \\ \sigma_{yy} \\ \sigma_{zz} \\ \sigma_{yz} \\ \sigma_{zx} \\ \sigma_{xy} \end{pmatrix} = \begin{pmatrix} C_{11} & C_{12} & C_{12} & 0 & 0 & 0 \\ C_{12} & C_{11} & C_{12} & 0 & 0 & 0 \\ C_{12} & C_{12} & C_{11} & 0 & 0 & 0 \\ 0 & 0 & 0 & C_{44} & 0 & 0 \\ 0 & 0 & 0 & 0 & C_{44} & 0 \\ 0 & 0 & 0 & 0 & 0 & C_{44} \end{pmatrix} \begin{pmatrix} \varepsilon_{xx} \\ \varepsilon_{yy} \\ \varepsilon_{zz} \\ 2\varepsilon_{yz} \\ 2\varepsilon_{zx} \\ 2\varepsilon_{xy} \end{pmatrix} \qquad (0.2)$$

A.2. Calculation of elastic constant

Elastic constants are a response function to the external forces and can be derived by two approaches. The first one, known as the stress theorem proposed by Nielsen and Martin [205],

and it is based on the stress-strain relation. The second one used in this work is the energy approach related to the changes in the elastic energy density caused by a small deformation [206].

For small deformation in the regime of Hook's law, the total free energy can be calculated by expanding it in a Taylor series up to the second-order about the unstrained state [207]:

$$F(\{\varepsilon_k\}) = F_0 + V_0\left(\sum_{m=1}^{6}\sigma_m\,\varepsilon_m\ + \frac{1}{2}\sum_{m,n=1}^{6}C_{mn}\varepsilon_m\,\varepsilon_n\right) \tag{0.3}$$

where, F_0 and V_0, are the total free energy and the initial volume of the system before deformation, respectively. Then, elastic constants can be found from the second-order partial derivation of the free energy, Eq. (0.3), at zero strain

$$C_{mn} = \frac{1}{V_0}\left[\frac{\partial^2 F}{\partial\varepsilon_m\partial\varepsilon_n}\right]_{\{\varepsilon_k\}=0} \tag{0.4}$$

To define three independent elastic constants C_{11}, C_{12}, C_{44} of cubic crystal, it is necessary to apply three independent strains (ε). The initial cubic system can be deformed by applying the following deformation:

$$\hat{A}_{cubic} = \begin{pmatrix} 1+\varepsilon & 0 & 0 \\ 0 & 1+\varepsilon & 0 \\ 0 & 0 & 1+\varepsilon \end{pmatrix};$$
$$\hat{A}_{orthor} = \begin{pmatrix} 1+\varepsilon & 0 & 0 \\ 0 & 1-\varepsilon & 0 \\ 0 & 0 & 0 \end{pmatrix};\ \hat{A}_{shear}(\varepsilon) = \begin{pmatrix} 1 & \varepsilon & 0 \\ 0 & 1 & 0 \\ 0 & 0 & 0 \end{pmatrix} \tag{0.5}$$

where $\hat{A}_{cubic}$ is a volumetric cubic deformation and $\hat{A}_{orthor}$ *and* $\hat{A}_{shear}$ are distortional orthorhombic and simple shear deformation, Figure 0.1.

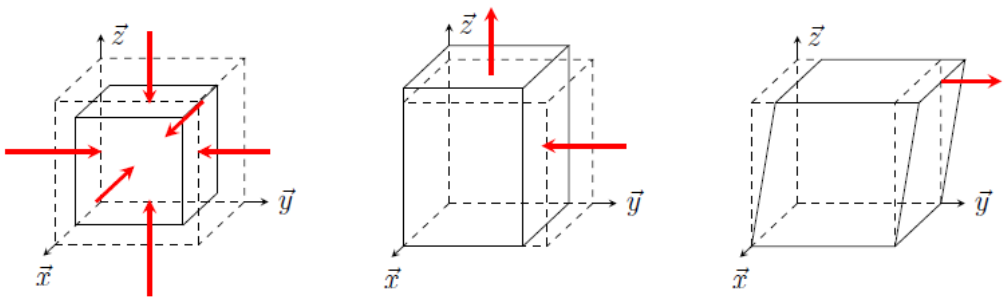

(a) *Déformation cubique.* (b) *Déformation orthorombique.* (c) *Déformation monoclinique.*

Figure 0.1. *Three types of deformations* [176].

According to the equation (0.3) the energy of the system with respect to these three deformations (0.5) can be express as follows:

$$F_{cubic}(\varepsilon) = F_0 + V_0 \frac{3}{2}(C_{11} + 2C_{12})\varepsilon^2 + O(\varepsilon^4) \tag{0.6}$$

$$F_{orthor}(\varepsilon) = F_0 + V_0(C_{11} - C_{12})\varepsilon^2 + O(\varepsilon^4) \tag{0.7}$$

$$F_{monoc}(\varepsilon) = F_0 + V_0 \frac{C_{44}}{2}\varepsilon^2 + O(\varepsilon^4) \tag{0.8}$$

The change in the free energy per unit volume can be written as:

$$\Delta F_{bulk}(\varepsilon) = \frac{9}{2} B\varepsilon^2 + O(\varepsilon^4) \tag{0.9}$$

$$\Delta F_{dev}(\varepsilon) = 2C'\varepsilon^2 + O(\varepsilon^4) \tag{0.10}$$

$$\Delta F_{shear}(\varepsilon) = \frac{C_{44}}{2}\varepsilon^2 + O(\varepsilon^4) \tag{0.11}$$

where $B = (C_{11} + 2C_{12})/3$ is a bulk modulus and $C' = (C_{11} - C_{12})/2 = G$ is a shear modulus related to elastic constants.

The elastic anisotropy of a cubic crystal can also be characterized by the Zener anisotropy ratio A, which represents the ratio of the two extreme elastic-shear coefficients [208].

$$A = \frac{2C_{44}}{C_{12} - C_{12}} = \frac{C_{44}}{C'} \tag{0.12}$$

In the case of AFT approach, deformation of the system, according to the (0.5), can be defined by the displacement of the interaction potential as [38], [209]:

$$\omega(\boldsymbol{r}) \to \omega\left(\left(\hat{I} + \bar{\varepsilon}\right)\boldsymbol{r}\right) \tag{0.13}$$

where $\left(\hat{I} + \bar{\varepsilon}\right) = \hat{A}$ is the deformation matrix and $\bar{\varepsilon}$ is the strain vector.

In real space, the position of the displacement atom after deformation can be defined by the vector $\boldsymbol{r'}$ with respect to the initial position given by vector $\boldsymbol{r}$. Since the interaction potential in QP approach is used in FT form, it is necessary to define the position vector $\boldsymbol{k}$ before and $\boldsymbol{k'}$ after the deformation in Fourier space. The product of vector $\boldsymbol{r}$ in real space and corresponding vector $\boldsymbol{k}$ in reciprocal space is equal to 2π. It defines that $\boldsymbol{kr} = \boldsymbol{k'r'}$**.** So

$$\boldsymbol{kr} = \boldsymbol{k}\left(\hat{A}^{-1}\hat{A}\right)\boldsymbol{r} = \left(\boldsymbol{k}\hat{A}^{-1}\right)\left(\hat{A}\boldsymbol{r}\right) = \boldsymbol{k'r'} \tag{0.14}$$

Thus, the vector $\boldsymbol{k}'$ of the deformed system in reciprocal space is $\boldsymbol{k}' = \boldsymbol{k}\,\hat{A}^{-1}$ and the corresponding deformation matrix are,

$$\hat{A}^{-1}_{cubic} = \begin{pmatrix} \frac{1}{1+\varepsilon} & 0 & 0 \\ 0 & \frac{1}{1+\varepsilon} & 0 \\ 0 & 0 & \frac{1}{1+\varepsilon} \end{pmatrix};\quad \hat{A}^{-1}_{otrhor} = \begin{pmatrix} \frac{1}{1+\varepsilon} & 0 & 0 \\ 0 & \frac{1}{1-\varepsilon} & 0 \\ 0 & 0 & 0 \end{pmatrix};$$
$$\hat{A}^{-1}_{shear} = \begin{pmatrix} 1 & -\varepsilon & 0 \\ 0 & 1 & 0 \\ 0 & 0 & 0 \end{pmatrix} \qquad (0.15)$$

Then the elastic constants can be found from the second derivations of the free energy change with respect to the change of intern strain energy. The calculated elastic constants used in this work and the experimentally measured values for the comparisons are given in **Table A.1**. Since the calculated elastic constants via simulations are presented in dimensionless units, it is more convenient to compare the experimental and simulated ratio of the elastic constants for bcc and fcc lattices.

Table A.1. *Elastic constants for the bcc and fcc lattice structures: calculated via simulations (used in this work) and experimentally measured for the comparisons. The ratio* $C_{ij}^{bcc}/C_{ij}^{fcc}$ *is under interest.*

Calculated elastic constant via simulation in the dimensionless units			Experimentally measured elastic constants for the iron, GPa		
$C_{11}^{bcc} = 1.593$	$C_{11}^{fcc} = 1.403$	$\boldsymbol{C_{11}^{bcc}/C_{11}^{fcc} = 1.135}$	$C_{11}^{bcc} = 226$	$C_{11}^{fcc} = 154$	$\boldsymbol{C_{11}^{bcc}/C_{11}^{fcc} = 1.467}$
$C_{12}^{bcc} = 0.741$	$C_{12}^{fcc} = 0.416$	$\boldsymbol{C_{12}^{bcc}/C_{12}^{fcc} = 1.781}$	$C_{12}^{bcc} = 140$	$C_{12}^{fcc} = 122$	$\boldsymbol{C_{12}^{bcc}/C_{12}^{fcc} = 1.475}$
$C_{44}^{bcc} = 0.578$	$C_{44}^{fcc} = 0.386$	$\boldsymbol{C_{44}^{bcc}/C_{44}^{fcc} = 1.497}$	$C_{44}^{bcc} = 116$	$C_{44}^{fcc} = 77$	$\boldsymbol{C_{44}^{bcc}/C_{44}^{fcc} = 1.506}$

Appendix B. The orientation transformation matrix

From a crystallographic point of view, phase transformation describes a crystal rearrangement from one lattice to another. In the case of austenite to ferrite phase transformation, it involves the crystal rearrangement from parent fcc to the product bcc lattice structure. There is various ways for atoms movement to achieve such crystallographic rearrangement. However, to reduce the internal strain stress caused by the mismatch between these two structures and provide the best fit at the interface, the transformation occurs following specific orientation relationships that predict the existence of a pair of parallel or nearly parallel close-packed planes in both phases. It means that the coordinates of the atoms of the bcc lattice can be found from the coordinates of atoms in fcc. Therefore, the ORs between austenite and ferrite can be described by a transformation matrix. In this case, the direction of the lattice vector $R_{\gamma n}$ (here, n refers to each variant of the specific ORs) can be related to the α coordinate system using a simple rotation matrix $(\alpha T \gamma)$ by the next expression:

$$\frac{R_\alpha}{|R_\alpha|} = (\alpha_n T \gamma) \frac{R_{\gamma n}}{|R_{\gamma n}|} \qquad (0.1)$$

A brief overview of one of the methods for calculating such a rotation matrix is given below. An example is done for the first variant (V1) of NW-ORs.

The first step is to establish a set of parallel vectors of the three lattices:

$$[111]_\gamma \parallel [011]_\alpha \qquad [10\bar{1}]_\gamma \parallel [100]_\alpha \qquad [1\bar{2}1]_\gamma \parallel [01\bar{1}]_\alpha \qquad (0.2)$$

The lengths of the parallel vectors in two different lattices presented (0.2) must remain invariant to a coordinate transformation. Thus it is necessary to equalize the magnitudes of those vectors by defining the constant k, g and m as:

$$k = \frac{a_0^{fcc}\sqrt{3}}{a_0^{bcc}\sqrt{2}} \qquad g = \frac{a_0^{fcc}}{a_0^{bcc}}\sqrt{2} \qquad m = \frac{a_0^{fcc}\sqrt{6}}{a_0^{bcc}\sqrt{2}} \qquad (0.3)$$

Substituting expressions (0.3) and (0.2) in (0.1), the following relations will be obtained:

$$\begin{aligned} [0kk] &= (\alpha_1 T \gamma)[111] \\ [g00] &= (\alpha_1 T \gamma)[10\bar{1}] \\ [0m\bar{m}] &= (\alpha_1 T \gamma)[1\bar{2}1] \end{aligned} \qquad (0.4)$$

Equations (0.4) can be written as:

$$\begin{pmatrix} 0 & g & 0 \\ k & 0 & m \\ k & 0 & \bar{m} \end{pmatrix} = \begin{pmatrix} T_{11} & T_{12} & T_{13} \\ T_{21} & T_{22} & T_{23} \\ T_{31} & T_{32} & T_{33} \end{pmatrix} \begin{pmatrix} 1 & 1 & 1 \\ 1 & 0 & \bar{2} \\ 1 & \bar{1} & 1 \end{pmatrix} \tag{0.5}$$

It follows that:

$$\begin{aligned} (\alpha_1 T \gamma) &= \frac{1}{6} \begin{pmatrix} 3g & 0 & -3g \\ 2k+m & 2k-m & -2k+m \\ 2k-m & 2k+2m & 2k-m \end{pmatrix} \\ &= \frac{a_0^{fcc}}{a_0^{bcc}} \begin{pmatrix} 0.707 & 0 & -0.707 \\ 0.696 & -0.169 & -0.120 \\ 0.120 & 0.986 & 0.120 \end{pmatrix} \end{aligned} \tag{0.6}$$

Finally, the desired rotation matrix $(\alpha_1 T \gamma)$ is:

$$(\alpha_1 T \gamma) = \hat{T}_1 = \begin{pmatrix} 0.707 & 0 & -0.707 \\ 0.696 & -0.169 & -0.120 \\ 0.120 & 0.986 & 0.120 \end{pmatrix} \tag{0.7}$$

It is important to note that the direction of the γ basis vectors always change in relation to the α coordinate system according to each of the possible variants of the considered OR. Hence the rotation matrix has to be obtained for each possible variant. Due to the crystal symmetry, there are 12 variants of NW-ORs (table) while 24 variants of KS-ORs (table). The rotation matrix for the 24 variants of KS and 12 variants of NW ORs is presented in the tables below.

Table 20. *The 24 crystalographic variants of the KS ORs. Various Bain groups (BG) and misorientation angle (Θ) of variant V2 to V24 relative to V1 are given* [210].

KS-ORs variant	Plane parallel	Direction parallel	BG	Misorientation from V1 (θ)
V1	$\{111\}_\gamma \parallel \{011\}_\alpha$	$\langle\bar{1}01\rangle_\gamma \parallel \langle\bar{1}\bar{1}1\rangle_\alpha$	B1	-
V2		$\langle\bar{1}01\rangle_\gamma \parallel \langle\bar{1}1\bar{1}\rangle_\alpha$	B2	60°
V3		$\langle 01\bar{1}\rangle_\gamma \parallel \langle\bar{1}\bar{1}1\rangle_\alpha$	B3	60°
V4		$\langle\bar{1}01\rangle_\gamma \parallel \langle\bar{1}1\bar{1}\rangle_\alpha$	B1	10.5°
V5		$\langle 1\bar{1}0\rangle_\gamma \parallel \langle\bar{1}\bar{1}1\rangle_\alpha$	B2	60°
V6		$\langle 1\bar{1}0\rangle_\gamma \parallel \langle\bar{1}1\bar{1}\rangle_\alpha$	B3	49.5°
V7	$\{1\bar{1}1\}_\gamma \parallel \{011\}_\alpha$	$\langle 10\bar{1}\rangle_\gamma \parallel \langle\bar{1}\bar{1}1\rangle_\alpha$	B2	49.5°
V8		$\langle 10\bar{1}\rangle_\gamma \parallel \langle\bar{1}1\bar{1}\rangle_\alpha$	B1	10.5°
V9		$\langle\bar{1}\bar{1}0\rangle_\gamma \parallel \langle\bar{1}\bar{1}1\rangle_\alpha$	B3	50.5°
V10		$\langle\bar{1}\bar{1}0\rangle_\gamma \parallel \langle\bar{1}1\bar{1}\rangle_\alpha$	B2	50.5°
V11		$\langle 011\rangle_\gamma \parallel \langle\bar{1}\bar{1}1\rangle_\alpha$	B1	14.9°
V12		$\langle 011\rangle_\gamma \parallel \langle\bar{1}1\bar{1}\rangle_\alpha$	B3	57.2°
V13	$\{\bar{1}11\}_\gamma \parallel \{011\}_\alpha$	$\langle 0\bar{1}1\rangle_\gamma \parallel \langle\bar{1}\bar{1}1\rangle_\alpha$	B1	14.9°
V14		$\langle 0\bar{1}1\rangle_\gamma \parallel \langle\bar{1}1\bar{1}\rangle_\alpha$	B3	50.5°
V15		$\langle\bar{1}0\bar{1}\rangle_\gamma \parallel \langle\bar{1}\bar{1}1\rangle_\alpha$	B2	57.2°
V16		$\langle\bar{1}0\bar{1}\rangle_\gamma \parallel \langle\bar{1}1\bar{1}\rangle_\alpha$	B1	20.6°
V17		$\langle 110\rangle_\gamma \parallel \langle\bar{1}\bar{1}1\rangle_\alpha$	B3	51.7°
V18		$\langle 110\rangle_\gamma \parallel \langle\bar{1}1\bar{1}\rangle_\alpha$	B2	47.1°
V19	$\{11\bar{1}\}_\gamma \parallel \{011\}_\alpha$	$\langle\bar{1}10\rangle_\gamma \parallel \langle\bar{1}\bar{1}1\rangle_\alpha$	B3	50.5°
V20		$\langle\bar{1}10\rangle_\gamma \parallel \langle\bar{1}1\bar{1}\rangle_\alpha$	B2	57.2°
V21		$\langle 0\bar{1}\bar{1}\rangle_\gamma \parallel \langle\bar{1}\bar{1}1\rangle_\alpha$	B1	20.6°
V22		$\langle 0\bar{1}\bar{1}\rangle_\gamma \parallel \langle\bar{1}1\bar{1}\rangle_\alpha$	B3	47.1°
V23		$\langle 101\rangle_\gamma \parallel \langle\bar{1}\bar{1}1\rangle_\alpha$	B2	57.2°
V24		$\langle 101\rangle_\gamma \parallel \langle\bar{1}1\bar{1}\rangle_\alpha$	B1	21.1°

Table 21. *The rotation matrices for the 24 variants of KS ORs* [38].

The rotation matrices for the 24 variants of KS ORs		
$\hat{T}_1 = \begin{pmatrix} 0.742 & -0.667 & -0.075 \\ 0.650 & 0.742 & -0.167 \\ 0.167 & 0.075 & 0.983 \end{pmatrix}$	$\hat{T}_2 = \begin{pmatrix} 0.075 & 0.667 & -0.742 \\ -0.167 & 0.742 & 0.650 \\ 0.983 & 0.075 & 0.167 \end{pmatrix}$	$\hat{T}_3 = \begin{pmatrix} -0.667 & -0.075 & 0.742 \\ 0.742 & -0.167 & 0.650 \\ 0.075 & 0.983 & 0.167 \end{pmatrix}$
$\hat{T}_4 = \begin{pmatrix} 0.667 & -0.742 & 0.075 \\ 0.742 & 0.650 & -0.167 \\ 0.075 & 0.167 & 0.983 \end{pmatrix}$	$\hat{T}_5 = \begin{pmatrix} -0.075 & 0.742 & -0.667 \\ -0.167 & 0.650 & 0.742 \\ 0.983 & 0.167 & 0.075 \end{pmatrix}$	$\hat{T}_6 = \begin{pmatrix} -0.742 & 0.075 & 0.667 \\ 0.650 & -0.167 & 0.742 \\ 0.167 & 0.983 & 0.075 \end{pmatrix}$
$\hat{T}_7 = \begin{pmatrix} -0.075 & 0.667 & 0.742 \\ -0.167 & -0.742 & 0.650 \\ 0.983 & -0.075 & 0.167 \end{pmatrix}$	$\hat{T}_8 = \begin{pmatrix} -0.742 & -0.667 & 0.075 \\ 0.650 & -0.742 & -0.167 \\ 0.167 & -0.075 & 0.983 \end{pmatrix}$	$\hat{T}_9 = \begin{pmatrix} 0.742 & 0.075 & -0.667 \\ 0.650 & 0.167 & 0.742 \\ 0.167 & -0.983 & 0.075 \end{pmatrix}$
$\hat{T}_{10} = \begin{pmatrix} 0.075 & 0.742 & 0.667 \\ -0.167 & -0.650 & 0.742 \\ 0.983 & -0.167 & 0.075 \end{pmatrix}$	$\hat{T}_{11} = \begin{pmatrix} -0.667 & -0.742 & -0.075 \\ 0.742 & -0.650 & -0.167 \\ 0.075 & -0.167 & 0.983 \end{pmatrix}$	$\hat{T}_{12} = \begin{pmatrix} 0.667 & -0.075 & -0.742 \\ 0.742 & 0.167 & 0.650 \\ 0.075 & -0.983 & 0.167 \end{pmatrix}$
$\hat{T}_{13} = \begin{pmatrix} 0.667 & 0.742 & -0.075 \\ -0.742 & 0.650 & -0.167 \\ -0.075 & 0.167 & 0.983 \end{pmatrix}$	$\hat{T}_{14} = \begin{pmatrix} -0.667 & 0.075 & -0.742 \\ -0.742 & -0.167 & 0.650 \\ -0.075 & 0.983 & 0.167 \end{pmatrix}$	$\hat{T}_{15} = \begin{pmatrix} 0.075 & -0.667 & 0.742 \\ 0.167 & 0.742 & 0.650 \\ -0.983 & 0.075 & 0.167 \end{pmatrix}$
$\hat{T}_{16} = \begin{pmatrix} 0.742 & 0.667 & 0.075 \\ -0.650 & 0.742 & -0.167 \\ -0.167 & 0.075 & 0.983 \end{pmatrix}$	$\hat{T}_{17} = \begin{pmatrix} -0.742 & -0.075 & -0.667 \\ -0.650 & -0.167 & 0.742 \\ -0.167 & 0.983 & 0.075 \end{pmatrix}$	$\hat{T}_{18} = \begin{pmatrix} -0.075 & -0.742 & 0.667 \\ 0.167 & 0.650 & 0.742 \\ -0.983 & 0.167 & 0.075 \end{pmatrix}$
$\hat{T}_{19} = \begin{pmatrix} 0.742 & -0.075 & 0.667 \\ 0.650 & -0.167 & -0.742 \\ 0.167 & 0.983 & -0.075 \end{pmatrix}$	$\hat{T}_{20} = \begin{pmatrix} 0.075 & -0.742 & -0.667 \\ -0.167 & 0.650 & -0.742 \\ 0.983 & 0.167 & -0.075 \end{pmatrix}$	$\hat{T}_{21} = \begin{pmatrix} -0.667 & 0.742 & 0.075 \\ 0.742 & 0.650 & 0.167 \\ 0.075 & 0.167 & -0.983 \end{pmatrix}$
$\hat{T}_{22} = \begin{pmatrix} 0.667 & 0.075 & 0.742 \\ 0.742 & -0.167 & -0.650 \\ 0.075 & 0.983 & -0.167 \end{pmatrix}$	$\hat{T}_{23} = \begin{pmatrix} -0.075 & -0.667 & -0.742 \\ -0.167 & 0.742 & -0.650 \\ 0.983 & 0.075 & -0.167 \end{pmatrix}$	$\hat{T}_{24} = \begin{pmatrix} -0.742 & 0.667 & -0.075 \\ 0.650 & 0.742 & 0.167 \\ 0.167 & 0.075 & -0.983 \end{pmatrix}$

Table 22. *The rotation matrices for the 12 variants of NW ORs.*

The rotation matrices for the 12 variants of NW ORs		
$\hat{T}_1 = \begin{pmatrix} 0.707 & 0.0 & -0.707 \\ 0.696 & -0.169 & -0.120 \\ 0.120 & 0.986 & 0.120 \end{pmatrix}$	$\hat{T}_2 = \begin{pmatrix} -0.707 & 0.707 & 0.0 \\ 0.120 & -0.120 & 0.986 \\ 0.697 & 0.697 & 0.169 \end{pmatrix}$	$\hat{T}_3 = \begin{pmatrix} 0.0 & -0.707 & 0.707 \\ 0.986 & 0.120 & 0.120 \\ -0.169 & 0.697 & 0.697 \end{pmatrix}$
$\hat{T}_4 = \begin{pmatrix} 0.707 & 0.0 & 0.707 \\ -0.120 & 0.986 & 0.120 \\ -0.697 & 0.169 & 0.697 \end{pmatrix}$	$\hat{T}_5 = \begin{pmatrix} -0.707 & 0.707 & 0.0 \\ -0.697 & 0.697 & -0.169 \\ -0.120 & 0.120 & 0.986 \end{pmatrix}$	$\hat{T}_6 = \begin{pmatrix} 0.0 & 0.707 & 0.707 \\ -0.986 & 0.120 & 0.120 \\ 0.169 & 0.697 & 0.697 \end{pmatrix}$
$\hat{T}_7 = \begin{pmatrix} 0.707 & 0.0 & -0.707 \\ 0.696 & -0.169 & -0.120 \\ 0.120 & 0.986 & 0.120 \end{pmatrix}$	$\hat{T}_8 = \begin{pmatrix} 0.707 & 0.707 & 0.0 \\ 0.120 & -0.697 & -0.169 \\ 0.697 & -0.120 & 0.986 \end{pmatrix}$	$\hat{T}_9 = \begin{pmatrix} 0.0 & -0.707 & 0.707 \\ 0.986 & 0.120 & 0.697 \\ 0.169 & 0.697 & -0.120 \end{pmatrix}$
$\hat{T}_{10} = \begin{pmatrix} -0.707 & 0.0 & -0.707 \\ -0.697 & 0.986 & -0.120 \\ -0.120 & 0.169 & -0.697 \end{pmatrix}$	$\hat{T}_{11} = \begin{pmatrix} 0.707 & -0.707 & 0.0 \\ 0.697 & 0.697 & 0.169 \\ 0.120 & 0.120 & -0.986 \end{pmatrix}$	$\hat{T}_{12} = \begin{pmatrix} 0.0 & 0.707 & 0.707 \\ 0.986 & 0.120 & -0.120 \\ -0.169 & 0.697 & -0.697 \end{pmatrix}$

Appendix C. Numerical resolution of the diffusion equation

C.1. The adaptive mesh for the space discretization

Considering the initial conditions described in paragraph (5.2.1), the diffusion equation (5.5) has to be solved for each zone. The resolution of this equation is based on the Finite Element Method (FEM). In this method, the space discretization should be done first. Different positions of nodes can be chosen for each zone, and the diffusion equation (5.5) should be solved at each node. Then to optimize the numerical resolution, the adaptive mesh algorithm is used. It means that a higher density of nodes is set closer to the interface. The schematic representation of the nodes' position for each zone (subdomain) is illustrated in **Figure 0.1**.

Three different cases are considered. In the first case for the ferrite zone, the position of the left node is fixed, and only the right hand is mobile. In the case of the interface zone, both, left and right nodes are mobile. In the last case for the austenite zone, the left node is mobile, and the right hand is fixed. In general, the position of the nodes characterized by the parameters: $\xi_i = \frac{x_i}{X} \in [0,1]$ and:

fixed interface : $x = 0 \quad \rightarrow \quad \xi_1 = 0$

mobile interface: $x = X \quad \rightarrow \quad \xi_{n+1} = 1$

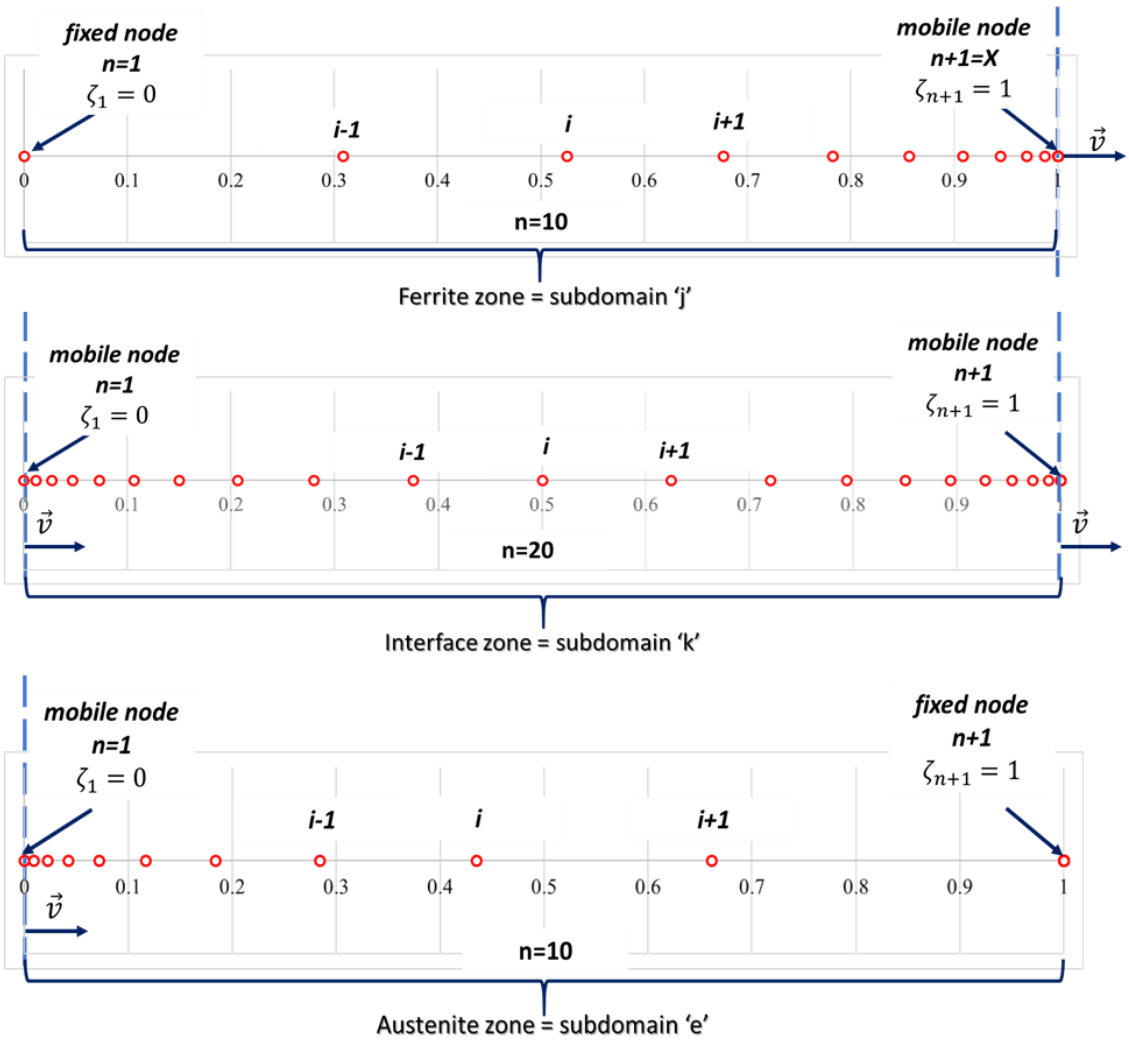

Figure 0.1 *Schematic representation of nodes position for each subdomain.*

C.2. Numerical resolution of the diffusion equation

Using the approximation of linear segments, the continuous concentration profile can be replaced by the combination of linear segments. In that case, the function $C(x,t)$ can be represented by the product of two functions with separate variables:

$$C(x,t) = C_j(t)\Phi_j(x) \qquad (0.1)$$

Using the definition (0.1), the derivatives of the left and right part of the eq. (5.5) can be written as:

- the left part:

$$\frac{\partial C}{\partial t} = \dot{C}_j(t)\Phi_j(x) - C_j(t)\Phi'_j(x)\frac{x}{X}V \qquad (0.2)$$

where: $\dot{C}_j(t) = \frac{dC_j(t)}{dt}$, $\Phi'_j(x) = \frac{\partial \Phi_j(x)}{\partial x}$, $V = \dot{X}$;

- the right part:

$$\frac{\partial^2 C}{\partial x^2} = C_j(t)\Phi_j''(x) \tag{0.3}$$

where $\Phi_j''(x) = \frac{\partial^2 \Phi_j(x)}{\partial x^2}$.

Substituting the equations (0.2) and (0.3) into eq. (5.5) gives:

$$\dot{C}_j(t)\Phi_j(x) - C_j(t)\Phi_j'(x)\frac{x}{X}V - DC_j(t)\Phi_j''(x) = 0 \tag{0.4}$$

Then both sides of the eq. (0.3), multiplied by $\Phi_i(x)$ and integrated over the subdomain $\mathcal{D}$:

$$\dot{C}_j(t)\int_{\mathcal{D}} \Phi_i(x)\Phi_j(x)\,dx - C_j(t)\frac{V}{X}\int_{\mathcal{D}} x\,\Phi_i(x)\Phi_j'(x)\,dx - DC_j(t)\int_{\mathcal{D}} \Phi_i(x)\,\Phi_j''(x) = 0 \tag{0.5}$$

The last term of the eq. (0.5) can be rewritten as:

$$\int_{\mathcal{D}} \Phi_i(x)\,\Phi_j''(x) = \left[\Phi_i(x)\Phi_j'(x)\right]_{\mathcal{D}} - \int_{\mathcal{D}} \Phi_i'(x)\Phi_j'(x)\,dx \tag{0.6}$$

Finally, eq. (0.5), using eq. (0.6), is:

$$\dot{C}_j(t)\int_{\mathcal{D}} \Phi_i(x)\Phi_j(x)\,dx - \frac{V}{X}C_j(t)\int_{\mathcal{D}} x\,\Phi_i(x)\Phi_j'(x)\,dx - DC_j(t)\int_{\mathcal{D}} \Phi_i'(x)\Phi_j'(x)\,dx = DC_j(t)\left[\Phi_i(x)\Phi_j'(x)\right]_{\mathcal{D}} \tag{0.7}$$

The eq. (0.7) is solved using the Finite Element Method (FEM), where the approximation function $\Phi_i(x)$ is a first order polinom:

$$\Phi_i(x) = \begin{cases} 0 & \\ \dfrac{x - x_{i-1}}{x_i - x_{i-1}} & x < x_{i-1} \\ \dfrac{x_{i+1} - x}{x_{i+1} - x_i} & x_{i-1} < x < x_i \\ 0 & x_i < x < x_{i+1} \\ & x_{i+1} < x \end{cases} \tag{0.8}$$

REFERENCES

[1] H. Bhadeshia and R. Honeycombe, *STEELS: Microstructure and Properties*, 4th ed. Elsevier Ltd., 2017.

[2] R. Rana and S. B. Singh, *Automotive Steels: Design, Metallurgy, Processing and Applications*, 1st ed. Elsevier Ltd., 2017.

[3] M.Y. Demeri, *Advanced High-Strength Steels—Science, Technology, and Application*. ASM International, 2013. doi: 10.31399/asm.tb.ahsssta.t53700071.

[4] N. Fonstein, *Advanced high strength sheet steels: Physical metallurgy, design, processing, and properties*. Springer International, 2015. doi: 10.1007/978-3-319-19165-2.

[5] *EU Commission, A European Strategy for Low-Emission Mobility*. Brussels, 2016.

[6] M. F. Ashby and D. R. H. Jones, *Engineering Materials 1: An Introduction to Properties, Applications, and Design*. Elsevier Ltd, 2012. doi: 10.1016/B978-0-08-096665-6.00030-1.

[7] A. C. Serrenho, J. B. Norman, and J. M. Allwood, "The impact of reducing car weight on global emissions: The future fleet in Great Britain," *Philosophical Transactions of the Royal Society A: Mathematical, Physical and Engineering Sciences*, vol. A375, 2017, doi: 10.1098/rsta.2016.0364.

[8] A. I. Taub and A. A. Luo, "Advanced lightweight materials and manufacturing processes for automotive applications," *MRS Bulletin*, vol. 40, no. 12, pp. 1045–1053, 2015, doi: 10.1557/mrs.2015.268.

[9] M. Singh, "Application of Steel in Automotive Industry," *International Journal of Emerging Technology and Advanced Engineering*, vol. 6, no. 7, pp. 246–253, 2016.

[10] M. Gouné *et al.*, "Overview of the current issues in austenite to ferrite transformation and the role of migrating interfaces therein for low alloyed steels," *Materials Science and Engineering R: Reports*, vol. 92, pp. 1–38, 2015, doi: 10.1016/j.mser.2015.03.001.

[11] C. Zener, "Kinetics of the decomposition of austenite.," *Transactions of the American Institute of Mining and Metallurgical Engineers*, 1946.

[12] S. Crusius, L. Hoglund, U. Knoop, and G. Inde, "On the growth of ferrite allotriomorphs in Fe-C alloys.," *International Journal of Materials Research*, vol. 83, no. 10, pp. 729–738, 1992.

[13] J. R. Bradley, J. M. Rigsbee, and H. I. Aaronson, "Growth kinetics of grain boundary ferrite allotriomorphs in Fe-C alloys," *Metallurgical Transactions A*, vol. 8, no. 2, pp. 323–333, 1977, doi: 10.1007/BF02661647.

[14] G. Purdy *et al.*, "ALEMI: A ten-year history of discussions of alloying-element interactions with migrating interfaces," *Metallurgical and Materials Transactions A:*

Physical Metallurgy and Materials Science, vol. 42, no. 12, pp. 3703–3718, 2011, doi: 10.1007/s11661-011-0766-0.

[15] H. K. D. H. Bhadeshia, "Diddusional formation of ferrite in iron and its alloys," *Progress in materials sience*, vol. 29, pp. 321–386, 1985.

[16] D. E. Coates, "Diffusion-controlled precipitate growth in ternary systems I," *Metallurgical Transactions*, vol. 3, pp. 1203–1212, 1972.

[17] A. Van der Ven and L. Delaey, "Models for precipitate growth during the gamma-> alpha+ gamma transformation in Fe-C and Fe-CM alloys," *Progress in materials sience*, vol. 40, pp. 181–264, 1996.

[18] A. Béché, H. S. Zurob, and C. R. Hutchinson, "Quantifying the solute drag effect of Cr on ferrite growth using controlled decarburization experiments," *Metallurgical and Materials Transactions A: Physical Metallurgy and Materials Science*, vol. 38 A, no. 12, pp. 2950–2955, 2007, doi: 10.1007/s11661-007-9353-9.

[19] C. Qiu, "The ' Solute - Drag ' Effect on Migrating Interfaces during Solid-State Phase Transformations," 2013. doi: 10.4225/03/58ae5f304d89d.

[20] C. Qiu, H. S. Zurob, D. Panahi, Y. J. M. Brechet, G. R. Purdy, and C. R. Hutchinson, "Quantifying the solute drag effect on ferrite growth in fe-c-x alloys using controlled decarburization experiments," *Metallurgical and Materials Transactions A: Physical Metallurgy and Materials Science*, vol. 44, no. 8, pp. 3472–3483, 2013, doi: 10.1007/s11661-012-1547-0.

[21] F. Danoix, X. Sauvage, D. Huin, L. Germain, and M. Gouné, "A direct evidence of solute interactions with a moving ferrite/austenite interface in a model Fe-C-Mn alloy," *Scripta Materialia*, vol. 121, pp. 61–65, 2016, doi: 10.1016/j.scriptamat.2016.04.038.

[22] H. P. V. Landeghem *et al.*, "Investigation of solute/interphase interaction during ferrite growth," *Acta Materialia*, vol. 124, pp. 536–543, 2017.

[23] K. Olsson, M. Gladh, J. E. Hedin, and J. Larsson, "Microalloyed high-strength steels," *Advanced Materials and Processes*, vol. 164, no. 8, pp. 44–46, 2006.

[24] B. Yan *et al.*, "A new dual phase steel for automotive body panels," *SAE Technical Papers 2003-01-0518*, 2003, doi: 10.4271/2003-01-0518.

[25] M. S. Rashid, "GM 980X-A unique high strength sheet steel with superior formability," *SAE Technical Papers 760206*, vol. 85, no. c, pp. 938–949, 1976, doi: 10.4271/760206.

[26] S. Hayami and T. Furukawa, "A Family of High-Strength, Cold- Rolled Steels, MicroAlloying," *Union Carbide Corp.*, vol. 75, pp. 311–320, 1977.

[27] S. Krajewski and J. Nowacki, "Dual-phase steels microstructure and properties consideration based on artificial intelligence techniques," *Archives of Civil and Mechanical Engineering*, vol. 14, pp. 278–286, 2014, doi: 10.1016/j.acme.2013.10.002.

[28] Y. Granbom, "Structure and mechanical properties of dual phase steels – An experimental and theoretical analysis," 2010.

[29] G. Krauss, *Steels—Processing, Structure, and Performance*, 2nd ed. ASM International, 2015.

[30] Z. P. Xiong, A. G. Kostryzhev, N. E. Stanford, and E. V. Pereloma, "Microstructures and mechanical properties of dual phase steel produced by laboratory simulated strip casting," *Materials and Design*, vol. 88, no. October 2017, pp. 537–549, 2015, doi: 10.1016/j.matdes.2015.09.031.

[31] I. A. Soomro, M. I. Abro, and M. M. Baloch, "Effect of Intercritical Heat Treatment on Mechanical Properties of Plain Carbon Dual Phase Steel," *Mehran University Research Journal of Engineering and Technology*, vol. 37, no. 1, pp. 149–158, 2018, doi: https://doi.org/10.22581/muet1982.1801.13.

[32] W. Bleck and K. Phiu-On, "Microalloying of Cold-Formable Multi Phase Steel Grades," *Materials Science Forum*, vol. 500–501, pp. 97–114, 2005, doi: 10.4028/www.scientific.net/msf.500-501.97.

[33] H. K. D. H. Bhadeshia, "Phase transformations contributing to the properties of modern steels," *Bulletin of the Polish Academy of Sciences: Technical Sciences*, vol. 58, no. 2, pp. 255–265, 2010, doi: 10.2478/v10175-010-0024-4.

[34] I. K. Razumov, Y. N. Gornostyrev, and M. I. Katsnelson, "Towards the ab initio based theory of phase transformations in iron and steel," *Physics of Metals and Metallography*, vol. 118, no. 4, pp. 362–388, 2017, doi: 10.1134/S0031918X16130032.

[35] W. D. Callister and D. G. Rethwisch, "Fundamentals Materials science and Engineering : An Integrated Approach," *Fundamentals of Materials Science and Engineering:An Integrated Approach*, no. 5th Edition, pp. 1–964, 2015, [Online]. Available: 9781119230403

[36] "https://www.tf.uni-kiel.de/matwis/amat/iss/kap_6/illustr/s6_1_2.html."

[37] D. A. Porter, K. E. Easterling, and M. Y. Sherif, *Phase transformations in metals and alloys, third edition*. 2009.

[38] M. Lavrskyi, "Modélisation en fonctionnelle de la densité atomique des transformations de phases dans le système Fe-C à basse température," 2017. doi: https://tel.archives-ouvertes.fr/tel-01537116.

[39] E. Pereloma and D. V. Edmonds, *Phase transformations in steels Volume 1: Fundamentals and diffusion-controlled transformations*. Woodhead Publishing Limited, 2012.

[40] J. Yin, M. Hillert, and A. Borgenstam, "Morphology of Proeutectoid Ferrite," *Metallurgical and Materials Transactions A: Physical Metallurgy and Materials Science*, vol. 48, no. 3, pp. 1425–1443, 2017, doi: 10.1007/s11661-016-3903-y.

[41] S. S. Babu and H. K. D. H. Bhadeshia, "A direct study of grain boundary allotriomorphic ferrite crystallography," *Materials Science and Engineering A*, vol. 142, no. 2, pp. 209–219, 1991, doi: 10.1016/0921-5093(91)90660-F.

[42] C. Cayron, "One-step theory of fcc-bcc martensitic transformation," *Acta Crystallographica Section A: Foundations of Crystallography*, vol. 69, pp. 498–509, 2013, doi: 10.1107/S0108767313019016.

[43] A. Muehlemann, K. Koumatos, and A. Muehlemann, "A Theoretical Investigation of Orientation Relationships and Transformation Strains in Steels," *arXiv:1604.05270 [cond-mat.mtrl-sci]*, pp. 1–27, 2016, doi: https://doi.org/10.48550/arXiv.1604.05270.

[44] Bowles J.S and Wayman C.M., "The Bain Strain, Lattice Correspondences, and Deformations Related to Martensitic Transformations," *Metall Mater Trans B*, vol. 3, no. May, pp. 1113–1121, 1972, doi: https://doi.org/10.1007/BF02642442.

[45] K. Verbeken, L. Barbé, and D. Raabe, "Evaluation of the Crystallographic Orientation Relationships between FCC and BCC Phases in TRIP Steels," vol. 49, no. 10, pp. 1601–1609, 2009, doi: https://doi.org/10.2355/isijinternational.49.1601.

[46] G. Miyamoto, N. Takayama, and T. Furuhara, "Accurate measurement of the orientation relationship of lath martensite and bainite by electron backscatter diffraction analysis," *Scripta Materialia*, vol. 60, no. 12, pp. 1113–1116, 2009, doi: 10.1016/j.scriptamat.2009.02.053.

[47] G. Nolze, "Determining the fcc / bcc orientation relationship in plessite regions of iron meteorites," *HKL Technology*, vol. App.8, pp. 40–45, 2005.

[48] K. Hata *et al.*, "In situ EBSD analysis on the crystal orientation relationship between ferrite and austenite during reverse transformation of an Fe-Mn-C Alloy," *Materials Transactions*, vol. 57, no. 9, pp. 1514–1519, 2016, doi: 10.2320/matertrans.MAW201602.

[49] G. Miyamoto, R. Hori, B. Poorganji, and T. Furuhara, "Crystallographic analysis of proeutectoid ferrite/austenite interface and interphase precipitation of vanadium carbide in medium-carbon steel," *Metallurgical and Materials Transactions A: Physical Metallurgy and Materials Science*, vol. 44, no. 8, pp. 3436–3443, 2013, doi: 10.1007/s11661-013-1702-2.

[50] C. Zener, "Theory of Growth of Spherical Precipitates from Solid Solution," *Journal of Applied Physics*, vol. 20, pp. 950–953, 1949, doi: https://doi.org/10.1063/1.1698258.

[51] G. P. Krielaart, J. Sietsma, and S. van der Zwaag, "Ferrite formation in Fe-C alloys during austenite decomposition under non-equilibrium interface conditions," *Materials Science and Engineering: A*, vol. 237, no. 1, pp. 216–223, 1997, doi: https://doi.org/10.1016/S0921-5093(97)00365-1.

[52] G. Purdy and J. Kirkaldy, "Kinetics of proeutectoid ferrite reaction at an incoherent interface, as determined by a diffusion couple.," *Transactions of the Metallurgical Society of AIME*, 1963.

[53] J. R. Bradley, H. I. Aaronson, K. C. Russell, and W. C. Johnson, "Effects of austenitizing temperature on the kinetics of the proeutectoid ferrite reaction at constant austenite grain size in an Fe-C alloy," *Metallurgical Transactions A*, vol. 8, no. 12, pp. 1955–1961, 1977, doi: 10.1007/bf02646570.

[54] K. R. Kinsman and H. I. Aaronson, "Influence of al, co, and si upon the kinetics of the proeutectoid ferrite reaction," *Metallurgical Transactions B*, vol. 4, pp. 956–967, 1973, doi: https://doi.org/10.1007/BF02645596.

[55] C. Atkinson, H. B. Aaron, K. R. Kinsman, and H. I. Aaronson, “On the growth kinetics of grain boundary ferrite allotriomorphs,” *Metallurgical Transactions volume 4*, pp. 783–792, 1973, doi: 10.1007/BF02643088.

[56] A. Saha, G. Ghosh, and G. B. Olson, “An assessment of interfacial dissipation effects at reconstructive ferrite–austenite interfaces,” *Acta Materialia*, vol. 53, no. 1, pp. 141–149, 2005, doi: 10.1016/j.actamat.2004.09.011.

[57] J. Sietsmaa and S. der Zwaagb, “A concise model for mixed-mode phase transformations in the solid state,” *Acta Materialia*, vol. 52, no. 14, pp. 4143–4152, 2004, doi: https://doi.org/10.1016/j.actamat.2004.05.027.

[58] M. Hillert, “Diffusion and interface control of reactions in alloys.,” *Metallurgical Transactions A*, vol. 6, 1975, doi: https://doi.org/10.1007/BF02673664.

[59] E. Gamsjager, M. Militzer, F. Fazeli, J. Svoboda, and F. D. Fischer, “Interface mobility in case of the austenite-to-ferrite phase transformation.,” *Computational Materials Science*, vol. 37, no. 1–2, pp. 94–100, 2006, doi: https://doi.org/10.1016/j.commatsci.2005.12.011.

[60] C. Bos and J. Sietsma, “A mixed-mode model for partitioning phase transformations.,” *Scripta Materialia*, vol. 57, no. 12, pp. 1085–188, 2007, doi: https://doi.org/10.1016/j.scriptamat.2007.08.030.

[61] J. Agren, “A simplified treatment of the transition from diffusion controlled to diffusion-less growth.,” *Acta Metallurgica*, vol. 37, no. 1, pp. 181–189, 1989, doi: https://doi.org/10.1016/0001-6160(89)90277-0.

[62] H. I. Aaronson and V. F. Zackay, “Decomposition of Austenite by Diffusional Processes: Proceedings of a Symposium Held in Philadelphia ... 1960, Under the Sponsorship of ... American Institute of Mining, Metallurgical and Petroleum Engineers,” 1962, Interscien.

[63] G. R. Purdy, D. H. Weichert, and J. S.Kirkaldy, “Growth of proeutectoid ferrite in ternary iron-carbon-man-ganese austenites,” *Transactions of the American Institute of Mining, Metallurgical and Petroleum Engineers*, vol. 230, no. 5, pp. 1025–1034, 1964.

[64] H. S. Zuroba, C. R. HutchinsonbA, G. R. Purdya, A. Béchéc, and Y. J. M. Bréchetd, “A transition from local equilibrium to paraequilibrium kinetics for ferrite growth in Fe–C–Mn: A possible role of interfacial segregation,” *Acta Materialia*, vol. 56, no. 10, pp. 2203–2211, 2008, doi: https://doi.org/10.1016/j.actamat.2008.01.016.

[65] H. S. Zurob, C. R. Hutchinson, Y. Bréchet, H. Seyedrezai, and G. R. Purdy, “Kinetic transitions during non-partitioned ferrite growth in Fe-C-X alloys,” *Acta Materialia*, vol. 57, no. 9, pp. 2781–2792, 2009, doi: 10.1016/j.actamat.2009.02.029.

[66] H. S. Zurob, D. Panahi, C. R. Hutchinson, Y. Brechet, and G. R. Purdy, “Self-consistent model for planar ferrite growth in Fe-C-x alloys,” *Metallurgical and Materials Transactions A*, vol. 44, no. 8, pp. 3456–3471, 2013, doi: 10.1007/s11661-012-1479-8.

[67] A. Phillion *et al.*, “Studies of the influence of alloying elements on the growth of ferrite from austenite under decarburization conditions: Fe-C-Ni alloys,” *Metallurgical and Materials Transactions A*, vol. 35, pp. 1237–1242, 2004, doi: https://doi.org/10.1007/s11661-004-0297-z.

[68] M. Enomoto, “Comparison of alloy element partition behavior and growth kinetics of proeutectoid ferrite in Fe-C-X alloys with diffusion growth theory,” *Transactions of the Iron and Steel Institute of Japan*, vol. 28, no. 10, pp. 826–835, 1988, doi: 10.2355/isijinternational1966.28.826.

[69] M. Enomoto, “Local conditions at moving α/γ boundaries of proeutectoid ferrite transformation in iron alloys,” *Metallurgical and Materials Transactions A: Physical Metallurgy and Materials Science*, vol. 37, no. 6, pp. 1703–1710, 2006, doi: 10.1007/s11661-006-0113-z.

[70] H. I. Aaronson, W. T. Reynolds, and G. R. Purdy, “Coupled-solute drag effects on ferrite formation in Fe-C-X systems,” *Metallurgical and Materials Transactions A: Physical Metallurgy and Materials Science*, vol. 35 A, no. 4, pp. 1187–1210, 2004, doi: 10.1007/s11661-004-0294-2.

[71] M. Enomoto and H. I. Aaronson, “Partition of Mn during the growth of proeutectoid ferrite allotriomorphs in an Fe-1.6 at. pct C-2.8 at. pct Mn alloy,” *Metallurgical Transactions A*, vol. 18, no. 9, pp. 1547–1557, 1987, doi: 10.1007/BF02646138.

[72] A. K. Shah and R. C. Sharma, “Ferrite transformation in fe-c-mn alloys.,” *International Journal of Materials Research*, vol. 74, no. 6, pp. 394–401, 1983, doi: https://doi.org/10.1515/ijmr-1983-740610.

[73] C. Capdevila, J. Cornide, K. Tanaka, K. Nakanishi, and E. Urones-Garrote, “Kinetic Transition during Ferrite Growth in Fe-C-Mn Medium Carbon Steel,” *Metallurgical and Materials Transactions A*, vol. 42, 2011, doi: https://doi.org/10.1007/s11661-011-0650-y.

[74] H. S. Zurob, C. R. Hutchinson, Y. Brechet, and G. R. Purdy, “A study of the austenite to ferrite transformation in Fe-C-X alloys using decarburization experiments.,” *Solid-Solid Phase Transformations in Inorganic Materials*, vol. 1, pp. 111–116, 2005.

[75] C. R. Hutchinson, H. S. Zurob, and Y. Brechet, “The growth of ferrite in Fe-C-X alloys: The role of thermodynamics, diffusion, and interfacial conditions.,” *Metallurgical and Materials Transactions A*, vol. 37, pp. 1711–1720, 2006, doi: https://doi.org/10.1007/s11661-006-0114-y.

[76] J. R. Bradley and H. I. Aaronson, “Growth kinetics of grain boundary ferrite allotriomorphs in Fe-C-X alloys,” *Metallurgical and Materials Transactions A*, vol. 12, pp. 1729–1741, 1981, doi: https://doi.org/10.1007/BF02643755.

[77] K. Oi, C. Lux, and G. R. Purdy, “A study of the influence of Mn and Ni on the kinetics of the proeutectoid ferrite reaction in steels.,” *Acta Materialia*, vol. 48, no. 9, pp. 2147–2155, 2008, doi: https://doi.org/10.1016/S1359-6454(00)00041-0\.

[78] H. Chen and S. van der Zwaag, “Application of the cyclic phase transformation concept for investigating growth kinetics of solid-state partitioning phase transformations,” *Computational Materials Science*, vol. 49, no. 4, pp. 801–813, 2010, doi: https://doi.org/10.1016/j.commatsci.2010.06.026.

[79] H. Chen and S. Van Der Zwaag, “Indirect evidence for the existence of the Mn partitioning spike during the austenite to ferrite transformation,” *Philosophical Magazine Letters*, vol. 92, no. 2, pp. 86–92, 2012, doi: 10.1080/09500839.2011.634840.

[80] H. Chen, “Cyclic Partial Phase Transformations In Low Alloyed Steels: Modeling and Experiments,” 2013. doi: https://doi.org/10.4233/uuid:66975e4a-4b2d-4933-95c5-f180b6605882.

[81] M. Hillert, “Nature of local equilibrium at the interface in the growth of ferrite from alloyed austenite,” *Scripta Materialia*, vol. 46, no. 6, pp. 447–453, 2002, doi: 10.1016/S1359-6462(01)01257-X.

[82] Z. K. Liu and J. Agren, “On the transition from local equilibrium to paraequilibrium during the growth of ferrite in Fe-Mn-C austenite,” *Acta Metallurgica*, vol. 37, no. 12, pp. 3157–3163, 1989, doi: https://doi.org/10.1016/0001-6160(89)90187-9.

[83] C. R. Hutchinson and Y. Brechet, “Thermodynamics, Microstructures and Plasticity,” *Thermodynamics, Microstructures and Plasticity*, no. January, 2003, doi: 10.1007/978-94-010-0219-6_9.

[84] F. Fazeli and M. Militzer, “Application of solute drag theory to model ferrite formation in multiphase steels,” *Metallurgical and Materials Transactions A: Physical Metallurgy and Materials Science*, vol. 36, no. 6, pp. 1395–1405, 2005, doi: 10.1007/s11661-005-0232-y.

[85] K. Lücke and K. Detert, “A quantitative theory of grain-boundary motion and recrystallization in metals in the presence of impurities,” *Acta Metallurgica*, vol. 5, pp. 628–637, 1957.

[86] J. W. Cahn, “The impurity-drag effect in grain boundary motion,” *Acta Metallurgica*, vol. 10, no. 9, pp. 789–798, 1962, doi: 10.1016/0001-6160(62)90092-5.

[87] K. Lücke and H. P. Stüwe, *Recovery and Recrystallization of Metals*. Interscience, 1963.

[88] A. T. Wicaksono, “A note on the Cahn solute drag model,” vol. 1, no. July 2015, pp. 1–12, 2016, doi: 10.6084/m9.figshare.1491502.v1.

[89] Y. Mishin, “Solute drag and dynamic phase transformations in moving grain boundaries,” *Acta Materialia*, vol. 179, pp. 383–395, 2019, doi: 10.1016/j.actamat.2019.08.046.

[90] M. Hillert and B. Sundman, “A treatment of the solute drag on moving grain boundaries and phase interfaces in binary alloys,” *Acta Metallurgica*, vol. 24, no. 8, pp. 731–743, 1976, doi: 10.1016/0001-6160(76)90108-5.

[91] M. Hillert, J. Odqvist, and J. Ågren, “Comparison between solute drag and dissipation of Gibbs energy by diffusion,” *Scripta Materialia*, vol. 45, no. 2, pp. 221–227, 2001, doi: 10.1016/S1359-6462(01)01022-3.

[92] G. R. Purdy and Y. J. M. Brechet, “A solute drag treatment of the effects of alloying elements on the rate of the proeutectoid ferrite transfromtion in steels,” *Acta Materialia*, vol. 43, no. 10, pp. 3763–3774, 1995.

[93] M. Enomoto, “Influence of solute drag on the growth of proeutectoid ferrite in Fe-C-Mn alloy,” *Acta Materialia*, vol. 47, no. 13, pp. 3533–3540, 1999, doi: 10.1016/S1359-6454(99)00232-3.

[94] M. Enomoto, N. Maruyama, K. M. Wu, and T. Tarui, “Alloying element accumulation at ferrite/austenite boundaries below the time-temperature-transformation diagram bay in an

Fe-C-Mo Alloy," *Materials Science and Engineering A*, vol. 343, no. 1–2, pp. 151–157, 2003, doi: 10.1016/S0921-5093(02)00375-1.

[95] K. M. Wu, M. Kagayama, and M. Enomoto, "Kinetics of ferrite transformation in an Fe-0.28mass%C-3mass%Mo alloy," *Materials Science and Engineering A*, vol. 343, no. 1–2, pp. 143–150, 2003, doi: 10.1016/S0921-5093(02)00374-X.

[96] J. Odqvist, M. Hillert, and J. Agren, "Effect of alloying elements on the γ to α transformation in steel. I," *Acta Materialia*, vol. 50, no. 12, pp. 3213–3227, doi: https://doi.org/10.1016/S1359-6454(02)00143-X.

[97] T. F. Majka, D. K. Matlock, and G. Krauss, "Development of microstructural banding in low-alloy steel with simulated Mn segregation," *Metallurgical and Materials Transactions A: Physical Metallurgy and Materials Science*, vol. 33, no. 6, pp. 1627–1637, 2002, doi: 10.1007/s11661-002-0172-8.

[98] C. C. Tasan, J. P. M. Hoefnagels, and M. G. D. Geers, "Microstructural banding effects clarified through micrographic digital image correlation," *Scripta Materialia*, vol. 62, no. 11, pp. 835–838, 2010, doi: 10.1016/j.scriptamat.2010.02.014.

[99] L. Schemmann, S. Zaefferer, D. Raabe, F. Friedel, and D. Mattissen, "Alloying effects on microstructure formation of dual phase steels," *Acta Materialia*, vol. 95, pp. 386–398, 2015, doi: 10.1016/j.actamat.2015.05.005.

[100] J. Verhoeven, "Banding: Microsegregation-Induced," *Encyclopedia of Iron, Steel, and Their Alloys*, pp. 320–330, 2016, doi: 10.1081/e-eisa-120052346.

[101] K. Geels, *Metallographic and materialographic specimen preparation, light microscopy, image analysis and hardness testing Kay*. 2016.

[102] C. García De Andrés, F. G. Caballero, C. Capdevila, and L. F. Álvarez, "Application of dilatometric analysis to the study of solid-solid phase transformations in steels," *Materials Characterization*, vol. 48, no. 1, pp. 101–111, 2002, doi: 10.1016/S1044-5803(02)00259-0.

[103] J. Opara and A. Wrożyna, "Development and validation of a quantitative dilatometric analysis model of austenite decomposition into ferrite and pearlite," *Prace Instytutu Metalurgii Żelaza*, vol. 67, pp. 24–32, 2015.

[104] T. Ferreira and W. Rasband, "ImageJ: User Guide." 2012. doi: 10.1038/nmeth.2019.

[105] D. J. Larson, T. J. Prosa, R. M. Ulfig, B. P. Geiser, and T. F. Kelly, *Local Electrode Atom Probe Tomography*. Springer Science+Business, 2013. doi: 10.1007/978-1-4614-8721-0.

[106] T. Kelly and M. Miller, "Atom probe tomography," *Review of scientific instruments*, vol. 78, 2007, doi: https://doi.org/10.1063/1.2709758.

[107] D. Seidman, "Three-dimensional atom-probe tomography: Advances and applications," *Annual Review of Materials Research*, vol. 37, pp. 127–158, 2007, doi: 10.1146/annurev.matsci.37.052506.084200.

[108] T. F. Kelly and D. J. Larson, "Local electrode atom probes," *Materials Characterization*, vol. 44, no. 1–2, pp. 59–85, 2000, doi: 10.1016/S1044-5803(99)00055-8.

[109] T. F. Kelly, P. P. Camus, D. J. Larson, L. M. Holzman, and S. S. Bajikar, “On the many advantages of local-electrode atom probes,” *Ultramicroscopy*, vol. 62, no. 1–2, pp. 29–42, 1996, doi: 10.1016/0304-3991(95)00086-0.

[110] “MyScope microscopy training.” https://myscope.training/

[111] M. K. Miller and R. G. Forbes, “Atom probe tomography,” *Materials Characterization*, vol. 60, no. 6, pp. 461–469, 2009, doi: 10.1016/j.matchar.2009.02.007.

[112] W. Lefebvre-Ulrikson, F. Vurpillot, and X. Sauvage, *Atpm Probe Tomography: Put Theory Into Practice*. Elsevier Inc., 2016.

[113] M. K. Miller and M. G. Hetherington, “Local magnification effects in the atom probe,” *Surface Science*, vol. 246, no. 1–3, pp. 442–229, 1991, doi: https://doi.org/10.1016/0039-6028(91)90449-3.

[114] F. Vurpillot, A. Bostel, and D. Blavette, “Trajectory overlaps and local magnification in three-dimensional atom probe,” *Applied Physics Letters*, vol. 76, no. 21, pp. 3127–3129, 2000, doi: 10.1063/1.126545.

[115] B. Gault, M. P. Moody, J. M. Cairney, and S. P. Ringer, *Atom Probe Tomography*. Springer, 2012. doi: 10.1007/978-1-4614-3436-8_6.

[116] D. Larson, B. Gault, B. P. Geiser, F. De Geuser, and F. Vurplilot, “Atom probe tomography spatial reconstruction: Status and directions,” *Current Opinion in Solid State and Materials Science*, vol. 17, no. 5, 2013, doi: https://doi.org/10.1016/j.cossms.2013.09.002.

[117] B. Gault *et al.*, “Spatial resolution in atom probe tomography,” *Microscopy and Microanalysis*, vol. 16, no. 1, pp. 99–110, 2010, doi: 10.1017/S1431927609991267.

[118] T. Kelly, E. Voelkl, and B. Geiser, “Practical Determination of Spatial Resolution in Atom Probe Tomography,” *Microsc Microanal*, vol. 15, no. Suppl 2, pp. 1188–1189, 2009, doi: 10.1017/S143192760909.

[119] P. Maugis and K. Hoummada, “A methodology for the measurement of the interfacial excess of solute at a grain boundary,” *Scripta Materialia*, vol. 120, pp. 90–93, 2016, doi: 10.1016/j.scriptamat.2016.04.005.

[120] P. Echlin, *Handbook of Sample Preparation for Scanning Electron Microscopy and X-Ray Microanalysis*. Springer Science+Business Media, 2009.

[121] L. Reimer, *Scanning Electron Microscopy Physics of Image Formation and Microanalysis*, 2nd ed. Springer, 1985.

[122] W. Zhou and Z. L. Wang, *Scanning microscopy for nanotechnology: Techniques and applications*. Springer Science, 2006. doi: 10.1007/978-0-387-39620-0.

[123] D. Stojakovic, “Electron backscatter diffraction in materials characterization,” *Processing and Application of Ceramics*, vol. 6, no. 1, pp. 1–13, 2012, doi: 10.2298/pac1201001s.

[124] A. J. Schwartz, M. Kumar, B. L. Adams, and D. P. Field, *EBSD in Materials Science*, 2nd ed. Springer Science+Business Media, 2009.

[125] P. W. H. Bragg and W. L. Bragg, “The reflection of X-rays by crystals,” vol. 17, pp. 428–438, 1913, doi: https://doi.org/10.1098/rspa.1913.0040.

[126] “EBSD explained. Oxford Instrument Analytical - thechical briefing.” Oxford Instrument, 2004.

[127] T. Maitland and S. Sitzman, “(EBSD) Technique and Materials Characterization Examples,” in *Scanning microscopy for nanotechnology: Techniques and applications*, Springer Science, 2006, pp. 41–76.

[128] D. Chen, J. C. Kuo, and W. T. Wu, “Effect of microscopic parameters on EBSD spatial resolution,” *Ultramicroscopy*, vol. 111, no. 9–10, pp. 1488–1494, 2011, doi: 10.1016/j.ultramic.2011.06.007.

[129] M. M. Nowell, S. I. Wright, and J. O. Carpenter, “Differentiating ferrite and martensite in steel microstructures using electron backscatter diffraction,” *Materials Science and Technology Conference and Exhibition 2009, MS and T’09*, vol. 2, no. March, pp. 933–943, 2009.

[130] S. I. Wright and M. M. Nowell, “EBSD Image Quality Mapping,” *Microscopy and Microanalysis*, vol. 12, pp. 72–84, 2006, doi: 10.1017/S1431927606060090.

[131] P. Trimby, “EBSD Data Processing best practice,” 2021. https://nano.oxinst.com/library/blog/ebsd-data-processing-best-practice

[132] EDAX, “Welcome to oim analysis 5.3.” TexSEM Laboratories, 2007.

[133] “OIM Analysis Tutorials.”

[134] L. Germain, “Mémoire d’habilitation à diriger des recherches: Apports des reconstructions des microtextures parentes dans l ’ étude,” 2014.

[135] H. S. Ubhi, J. Parsons, N. Othen, S. Campbell, R. Poole, and A. Gholinia, “In-situ EBSD phase transformation and recrystallisation,” in *Journal of Physics: Conference Series*, 2014, vol. 522, no. 1. doi: 10.1088/1742-6596/522/1/012011.

[136] M. Humbert, L. Germain, N. Gey, and E. Boucard, “Evaluation of the orientation relations from misorientation between inherited variants: Application to ausformed martensite,” *Acta Materialia*, vol. 82, pp. 137–144, 2015, doi: 10.1016/j.actamat.2014.09.007.

[137] L. Germain, N. Gey, R. Mercier, P. Blaineau, and M. Humbert, “An advanced approach to reconstructing parent orientation maps in the case of approximate orientation relations: Application to steels,” *Acta Materialia*, vol. 60, no. 11, pp. 4551–4562, 2012, doi: 10.1016/j.actamat.2012.04.034.

[138] L. Germain, S. R. Dey, M. Humbert, and N. Gey, “Determination of parent orientation maps in advanced titanium-based alloys,” *Journal of Microscopy*, vol. 227, no. 3, pp. 284–291, 2007, doi: 10.1111/j.1365-2818.2007.01812.x.

[139] S. R. Dey, L. Germain, M. Humbert, S. Suwas, and E. Bouzy, “Determination of parent β-phase orientation from inherited orthorhombic phase in β → O + B2 phase transformation of Ti-22Al-25Nb alloy,” *Philosophical Magazine Letters*, vol. 85, no. 9, pp. 463–471, 2005, doi: 10.1080/09500830500305186.

[140] L. Germain, D. Kratsch, M. Salib, and N. Gey, “Identification of sub-grains and low angle boundaries beyond the angular resolution of EBSD maps,” *Materials Characterization*, vol. 98, pp. 66–72, 2014, doi: 10.1016/j.matchar.2014.10.007.

[141] T. Furuhara, H. Kawata, S. Morito, G. Miyamoto, and T. Maki, “Variant selection in grain boundary nucleation of upper bainite,” in *Metallurgical and Materials Transactions A: Physical Metallurgy and Materials Science*, May 2008, vol. 39 A, no. 5, pp. 1003–1013. doi: 10.1007/s11661-008-9510-9.

[142] D. J. Larson *et al.*, “Field-ion specimen preparation using focused ion-beam milling,” *Ultramicroscopy*, vol. 79, no. 1–4, pp. 287–293, 1999, doi: 10.1016/S0304-3991(99)00055-8.

[143] D. W. Saxey, J. M. Cairney, D. McGrouther, T. Honma, and S. P. Ringer, “Atom probe specimen fabrication methods using a dual FIB/SEM,” *Ultramicroscopy*, vol. 107, no. 9, pp. 756–760, 2007, doi: 10.1016/j.ultramic.2007.02.024.

[144] M. K. Miller, K. F. Russell, and G. B. Thompson, “Strategies for fabricating atom probe specimens with a dual beam FIB,” *Ultramicroscopy*, vol. 102, no. 4, pp. 287–298, 2005, doi: 10.1016/j.ultramic.2004.10.011.

[145] N. Yao, *Focused ion beam systems: Basics and applications*. Cambridge University Press, 2007.

[146] L. Giannuzzi and F. Stevie, *Introduction to Focused Ion Beams: Instrumentation, Theory, Techniques and Practice*. Springer, 2005. doi: 10.1201/b16235-20.

[147] W. Brezna, H. Wanzenböck, A. Lugstein, E. Bertagnolli, E. Gornik, and J. Smoliner, “Scanning capacitance microscopy investigations of focused ion beam damage in silicon,” *Physica E: Low-Dimensional Systems and Nanostructures*, vol. 19, no. 1–2, pp. 178–182, 2003, doi: 10.1016/S1386-9477(03)00330-8.

[148] S. Rubanov and P. R. Munroe, “FIB-induced damage in silicon,” *Journal of Microscopy*, vol. 214, no. 3, pp. 213–221, 2004, doi: 10.1111/j.0022-2720.2004.01327.x.

[149] J. O. Douglas, P. A. J. Bagot, B. C. Johnson, D. N. Jamieson, and M. P. Moody, “Optimisation of sample preparation and analysis conditions for atom probe tomography characterisation of low concentration surface species,” *Semiconductor Science and Technology*, vol. 31, no. 8, pp. 1–12, 2016, doi: 10.1088/0268-1242/31/8/084004.

[150] M. K. Miller and K. F. Russell, “Atom probe specimen preparation with a dual beam SEM/FIB miller,” *Ultramicroscopy*, vol. 107, no. 9, pp. 761–766, 2007, doi: 10.1016/j.ultramic.2007.02.023.

[151] K. Thompson, D. Lawrence, D. J. Larson, J. D. Olson, T. F. Kelly, and B. Gorman, “In situ site-specific specimen preparation for atom probe tomography,” *Ultramicroscopy*, vol. 107, no. 2–3, pp. 131–139, 2007, doi: 10.1016/j.ultramic.2006.06.008.

[152] J. M. Cairney, D. W. Saxey, D. McGrouther, and S. P. Ringer, “Site-specific specimen preparation for atom probe tomography of grain boundaries,” *Physica B: Condensed Matter*, vol. 394, no. 2, pp. 267–269, 2007, doi: 10.1016/j.physb.2006.12.024.

[153] J. Takahashi, K. Kawakami, Y. Yamaguchi, and M. Sugiyama, “Development of atom probe specimen preparation techniques for specific regions in steel materials,”

Ultramicroscopy, vol. 107, no. 9, pp. 744–749, 2007, doi: 10.1016/j.ultramic.2007.02.008.

[154] F. Pérez-Willard *et al.*, "Focused ion beam preparation of atom probe specimens containing a single crystallographically well-defined grain boundary," *Micron*, vol. 39, no. 1, pp. 45–52, 2008, doi: 10.1016/j.micron.2007.01.001.

[155] M. L. Taheri, J. T. Sebastian, B. W. Reed, D. N. Seidman, and A. D. Rollett, "Site-specific atomic scale analysis of solute segregation to a coincidence site lattice grain boundary," *Ultramicroscopy*, vol. 110, no. 4, pp. 278–284, 2010, doi: 10.1016/j.ultramic.2009.11.006.

[156] P. W. Trimby, "Orientation mapping of nanostructured materials using transmission Kikuchi diffraction in the scanning electron microscope," *Ultramicroscopy*, vol. 120, pp. 16–24, Sep. 2012, doi: 10.1016/j.ultramic.2012.06.004.

[157] M. Miller and R. Forbes, *Atom-Probe Tomography: The Local Electrode Atom Probe*. 2014. doi: 10.1007/978-1-4899-7430-3_5.

[158] "Ivas™ 3.8 User Guide." 2016.

[159] B. Gault, F. De Geuser, L. T. Stephenson, M. P. Moody, B. C. Muddle, and S. P. Ringer, "Estimation of the reconstruction parameters for atom probe tomography," *Microscopy and Microanalysis*, vol. 14, no. 4, pp. 296–305, 2008, doi: 10.1017/S1431927608080690.

[160] P. Bas, A. Bostel, B. Deconihout, and D. Blavette, "A general protocol for the reconstruction of 3D atom probe data," *Applied Surface Science*, vol. 87–88, no. C, pp. 298–304, 1995, doi: 10.1016/0169-4332(94)00561-3.

[161] B. P. Geiser, T. F. Kelly, D. J. Larson, J. Schneir, and J. P. Roberts, "Spatial Distribution Maps for Atom Probe Tomography," *Microscopy*, pp. 437–447, 2007, doi: DOI: 10.1017/S1431927607070948.

[162] B. Geiser, D. J. Larson, T. J. Prosa, and T. F. Kelly, "Using Spatial Distribution Maps to Estimate APT Efficiency," *Microscopy and Microanalysis*, vol. 19, pp. 31–33, 2013, doi: 10.1017/S1431927613006995.

[163] "User Guide Ivas™ 3.6.8." 2014.

[164] D. Blavette, P. Duval, L. Letellier, and M. Guttmann, "Atomic-scale APFIM and TEM investigation of grain boundary microchemistry in astroloy nickel base superalloys," *Acta Materialia*, vol. 44, no. 12, pp. 4995–5005, 1996, doi: 10.1016/S1359-6454(96)00087-0.

[165] F. R. Foulkes, "Thermodynamics (V)," *Physical Chemistry for Engineering and Applied Sciences*. pp. 197–226, 2020. doi: 10.1201/b12732-15.

[166] B. W. Krakauer and D. N. Seidman, "Absolute atomic-scale measurements of the Gibbsian interfacial excess of solute at internal interfaces," *Physical Review B*, vol. 48, no. 9, pp. 6724–6727, 1993, doi: 10.1103/PhysRevB.48.6724.

[167] G. I. da Rosa, "Mechanisms and consequences of boron segregation at austenite grain boundaries in advanced high strength steels," 2018.

[168] V. I. Levitas, “Unambiguous Gibbs dividing surface for nonequilibrium finite-width interface: Static equivalence approach,” *Physical Review B - Condensed Matter and Materials Physics*, vol. 89, no. 9, 2014, doi: 10.1103/PhysRevB.89.094107.

[169] T. Frolov and Y. Mishin, “Thermodynamics of coherent interfaces under mechanical stresses. I. Theory,” *Physical Review B - Condensed Matter and Materials Physics*, vol. 85, no. 22, pp. 12–15, 2012, doi: 10.1103/PhysRevB.85.224106.

[170] C. Wang and H. Morgner, “The dependence of surface tension on surface properties of ionic surfactant solution and the effects of counter-ions therein,” *Physical Chemistry Chemical Physics*, vol. 16, no. 42, pp. 23386–23393, 2014, doi: 10.1039/c4cp03607g.

[171] O. C. Hellman and D. N. Seidman, “Measurement of the Gibbsian interfacial excess of solute at an interface of arbitrary geometry using three-dimensional atom probe microscopy,” *Materials Science and Engineering A*, vol. 327, no. 1, pp. 24–28, 2002, doi: 10.1016/S0921-5093(01)01885-8.

[172] P. Nozières and D. E. Wolf, “Interfacial properties of elastically strained materials - I. Thermodynamics of a planar interface,” *Zeitschrift für Physik B Condensed Matter*, vol. 70, no. 3, pp. 399–407, 1988, doi: 10.1007/BF01317248.

[173] D. E. Coates, “Diffusion-controlled precipitate growth in ternary systems I,” *Metallurgical Transactions*, vol. 3, no. 5, pp. 1203–1212, 1972, doi: 10.1007/bf02642453.

[174] G. Demange *et al.*, “Atomistic study of the fcc→bcc transformation in a binary system: Insights from the Quasi-particle Approach,” *Acta Materialia*, vol. 226, no. 117599, 2022, doi: https://doi.org/10.1016/j.actamat.2021.117599.

[175] O. Kapikranian *et al.*, “Atomic structure of grain boundaries in iron modeled using the atomic density function,” *Physical Review B*, no. April 2014, 2013, doi: 10.1103/PhysRevB.89.014111.

[176] A. Vaugeois, “Modélisation de l’influence de la structure des joints de grains sur les phénomènes de ségrégation,” Normandie Université, 2017.

[177] A. G. Khachaturyan, *Theory of structural transformations in solids*. 2008.

[178] Y. M. Jin, A. G. Khachaturyan, and Y. M. Jin, “Atomic density function theory and modeling of microstructure evolution at the atomic scale Atomic density function theory and modeling of microstructure evolution,” vol. 013519, no. 2006, 2009, doi: 10.1063/1.2213353.

[179] M. Lavrskyi, H. Zapolsky, and A. G. Khachaturyan, “ARTICLE Quasiparticle approach to diffusional atomic scale self-assembly of complex structures : from disorder to complex ... Quasiparticle approach to diffusional atomic scale self-assembly of complex structures : from disorder to complex crystals and do,” no. January, 2016, doi: 10.1038/npjcompumats.2015.13.

[180] A. Stukowski, “Modelling and Simulation in Materials Science and Engineering Visualization and analysis of atomistic simulation data with OVITO – the Open Visualization Tool Visualization and analysis of atomistic simulation data with OVITO – the Open Visualization Tool,” 2010, doi: 10.1088/0965-0393/18/1/015012.

[181] L. Q. Chert and J. Shen, “Applications of semi-implicit Fourier-spectral method to phase field equations,” vol. 108, pp. 147–158, 1998.

[182] A. Goryaeva, “fratons2atoms, https://github.com/agoryaeva/fratons2atoms,” 2021.

[183] D. Hull and D. J. Bacon, *Introduction to Dislocations*, 4th editio. 2011.

[184] P. K. Tripathi, S. K. Maurya, and S. Bhowmick, “Role of disconnections in mobility of the austenite-ferrite inter-phase boundary in Fe,” *Phys. Rev. Materials*, vol. 2, no. 11, pp. 1–8, 2018, doi: https://doi.org/10.1103/PhysRevMaterials.2.113403.

[185] C. Bos, J. Sietsma, and B. J. Thijsse, “Molecular dynamics simulation of interface dynamics during the fcc-bcc transformation of a martensitic nature,” pp. 1–7, 2006, doi: 10.1103/PhysRevB.73.104117.

[186] X. Ou, J. Sietsma, and M. J. Santofimia, “Molecular dynamics simulations of the mechanisms controlling the propagation of bcc / fcc semi-coherent interfaces in iron Molecular dynamics simulations of the mechanisms controlling the propagation of bcc / fcc semi-coherent interfaces in iron,” *Modelling and Simulation in Materials Science and Engineering*, vol. 24, no. 5, 2016, doi: doi:10.1088/0965-0393/24/5/055019.

[187] A. Stukowski and K. Albe, “Extracting dislocations and non-dislocation crystal defects from atomistic simulation data,” *Modelling and Simulation in Materials Science and Engineering*, vol. 18, no. 8, 2010, doi: 10.1088/0965-0393/18/8/085001.

[188] A. Stukowski, V. V Bulatov, and A. Arsenlis, “Automated identification and indexing of dislocations in crystal interfaces Automated identification and indexing of dislocations in crystal interfaces,” 2012, doi: 10.1088/0965-0393/20/8/085007.

[189] A. Borgenstam, A. Engström, L. Höglund, and J. Ågren, “DICTRA, a tool for simulation of diffusional transformations in alloys,” *Journal of Phase Equilibria*, vol. 21, no. 3, pp. 269–280, 2000, doi: 10.1361/105497100770340057.

[190] Thermo-Calc AB, “Diffusion Module (DICTRA) Quick Start Guide - Graphical Mode,” 2021.

[191] G. Miyamoto and T. Furuhara, “Interaction of alloying elements with migrating ferrite/austenite interface,” *ISIJ International*, vol. 60, no. 12, pp. 2942–2953, 2020, doi: 10.2355/isijinternational.ISIJINT-2020-216.

[192] G. H. Zhang, R. Wei, M. Enomoto, and D. W. Suh, “Growth kinetics of proeutectoid ferrite in Fe-0.1C-1.5Mn-1Si quaternary and Fe-0.1C-1.5Mn-1Si-0.2Al quinary alloys,” *Metallurgical and Materials Transactions A: Physical Metallurgy and Materials Science*, vol. 43, no. 3, pp. 833–842, 2012, doi: 10.1007/s11661-011-1000-9.

[193] G. Korablev, “Calculation of activation energy of diffusion and self-diffusion,” *European Chemical Bulletin*, vol. 7, no. 1, pp. 23–29, 2018, doi: 10.17628/ecb.2018.7.23-29.

[194] B. M. Jenkins *et al.*, “Observation of Mn-Ni-Si-rich features in thermally-aged model reactor pressure vessel steels,” *Scripta Materialia*, vol. 191, pp. 126–130, 2021, doi: 10.1016/j.scriptamat.2020.09.029.

[195] N. Perez, *Electrochemistry and Corrosion Science*, 2nd ed. Springer, Cham. doi: https://doi.org/10.1007/978-3-319-24847-9.

[196] H. Jin, I. Elfimov, and M. Militzer, “First-principles simulations of binding energies of alloying elements to the ferrite- austenite interface in iron,” *Journal of Applied Physics*, vol. 123, 2018, doi: 10.1063/1.5020166.

[197] C. L. White, W. A. Coghlan, M. Trans, and C. L. White, ““ The Spectrum of Binding Energies Approach to Grain Boundary Segregation,” vol. 8, no. January 1977, pp. 1403–1411, 2014.

[198] M. Enomoto, C. L. White, and H. I. Aaronson, “Evaluation of the effects of segregation on austenite grain boundary energy in Fe-C-X alloys,” *Metallurgical Transactions A (Physical Metallurgy and Materials Science)*, vol. 19 A, no. 7, pp. 1807–1818, 1988, doi: 10.1007/BF02645149.

[199] M. Guttmann, “Equilibrium segregation in a ternary solution: A model for temper embrittlement,” *Surface Science*, vol. 53, no. 1, pp. 213–227, 1975, doi: 10.1016/0039-6028(75)90125-9.

[200] H. P. Van Landeghem *et al.*, “Solute Segregation During Ferrite Growth: Solute/Interphase and Substitutional/Interstitial Interactions,” *Jom*, vol. 68, no. 5, pp. 1329–1334, 2016, doi: 10.1007/s11837-016-1852-y.

[201] J. Nutter, “Direct TEM Observation of the Movement of the Austenite-Ferrite Interface in Steels,” 2018. [Online]. Available: http://etheses.whiterose.ac.uk/23849/

[202] G. R. Purdy, “The dynamics of transformation interfaces in steels-II. Transformations in FE-C-MO alloys at intermediate temperatures,” *Acta Metallurgica*, vol. 26, no. 3, pp. 487–498, 1978, doi: 10.1016/0001-6160(78)90174-8.

[203] J. Nutter, H. Farahani, W. M. Rainforth, and S. van der Zwaag, “Direct TEM observation of α/γ interface migration during cyclic partial phase transformations at intercritical temperatures in an Fe-0.1C −0.5Mn alloy,” *Acta Materialia*, vol. 178, pp. 68–78, 2019, doi: 10.1016/j.actamat.2019.07.047.

[204] K. Gurnett and T. Adams, “Considerations for GaN-powered base stations,” *III-Vs Review*, vol. 19, no. 7, pp. 20–22, 2006, doi: 10.1016/S0961-1290(06)71818-X.

[205] O. H. Nielsen and R. M. Martin, “Stresses in semiconductors: Ab initio calculations on Si, Ge, and GaAs,” *Physical Review B*, vol. 32, no. 6, pp. 3792–3805, 1985, doi: 10.1103/PhysRevB.32.3792.

[206] R. Stadler, W. Wolf, R. Podloucky, G. Kresse, J. Furthmüller, and J. Hafner, “Ab initio calculations of the cohesive, elastic, and dynamical properties of by pseudopotential and all-electron techniques,” *Physical Review B - Condensed Matter and Materials Physics*, vol. 54, no. 3, pp. 1729–1734, 1996, doi: 10.1103/PhysRevB.54.1729.

[207] M. Jamal, S. Jalali Asadabadi, I. Ahmad, and H. A. Rahnamaye Aliabad, “Elastic constants of cubic crystals,” *Computational Materials Science*, vol. 95, pp. 592–599, 2014, doi: 10.1016/j.commatsci.2014.08.027.

[208] T. Paszkiewicz and S. Wolski, “Elastic properties of cubic crystals: Every’s versus Blackman’s diagram,” *Journal of Physics: Conference Series*, vol. 104, no. 1, 2008, doi: 10.1088/1742-6596/104/1/012038.

[209] A. Dahlström, “Influence of a mechanical load on the ageing of Fe-Cr alloys,” 2019, doi: https://tel.archives-ouvertes.fr/tel-02316065.

[210] E. V. Pereloma, F. Al-Harbi, and A. A. Gazder, “The crystallography of carbide-free bainites in thermo-mechanically processed low Si transformation-induced plasticity steels,” *Journal of Alloys and Compounds*, vol. 615, no. December, pp. 96–110, 2014, doi: 10.1016/j.jallcom.2014.05.123.

Nanoscale investigation of austenite/ferrite transformation interfaces in Fe-Mn-C at different intercritical temperatures

Abstract

The austenite (γ)-to-ferrite (α) phase transformation is involved in the production line of most modern steel, such as the class of advanced high-strength steels (AHSS). Therefore, it plays a critical role in tailoring the final steel microstructure and thus its mechanical properties. Many different models have been developed to predict the kinetics of austenite-to-ferrite phase transformation and tailor the final fraction of formed ferrite. Two thermodynamic based models, namely, Local Equilibrium (with partitioning – LEP and without partitioning of alloying elements – LENP) and ParaEquilibrium, are widely used currently. However, it has long been realised that the interaction between the alloying elements and the migrating transformation interface can dramatically modify the kinetics of ferrite growth through the phenomenon known as Solute Drag (SD). This interaction, which is not considered in the previous models, leads to the solute segregation at the interface, that may retard the motion of the austenite/ferrite transformation interface. Prediction of solute elements redistribution between ferrite and austenite and at the interface are different with the different approaches. Therefore, the aim of this study was to investigate the γ/α transformation interfaces at the nanoscale and quantify the local solute enrichment that can help identify the operative mode of ferrite growth.

In this work, interfacial segregation in a Fe-C-Mn model alloy is experimentally investigated by Atom Probe Tomography (APT), which is a well-suited technique for quantitatively measuring the solute concentration profile across interfaces at the near-atomic scale. Electron Backscatter Diffraction (EBSD), Focused Ion Beam (FIB), Transmission Kikuchi Diffraction (TKD) techniques were used for the site-specific specimen preparation for APT investigation. The EBSD data were used to determine the orientation relationships (ORs) between the formed ferrite and prior austenite, as it is expected that ORs may affect the interface mobility and thus solute segregation at the interface. A large number of γ/α interfaces were successfully analysed, and the Mn composition profiles through interfaces were discussed and compared to the predictions of existing models for austenite-to-ferrite transformation in steel.

Meanwhile, atomistic modeling using the new Quasiparticle approach (Atomic Density Function theory) has been applied to study the γ/α transformation interface migration at the atomic scale in pure iron. Different orientation relationships (OR) between the austenite and ferrite phases have been considered. The effect of the ORs on the structure and mobility of α/γ interfaces is discussed.

Keywords: austenite to ferrite transformation, transformation interfaces, interfacial segregation, atom probe tomography (APT), orientation relationships (ORs), dual-phase (DP) steel, atomistic modelling.

Étude à l'échelle nanométrique des interfaces de transformation austénite/ferrite dans Fe-Mn-C à différentes températures intercritiques

Résumé

La transformation de phase austénite (γ)-ferrite (α) fait partie intégrante du procédé de fabrication de la plupart des aciers modernes, tels que la classe des aciers avancés à haute résistance (AHSS). Par conséquent, elle joue un rôle essentiel dans l'adaptation de la microstructure finale de l'acier et donc de ses propriétés mécaniques. De nombreux modèles différents ont été développés pour prédire la cinétique de la transformation de l'austénite en ferrite et adapter la fraction finale de ferrite formée. Deux modèles basés sur la thermodynamique, à savoir, l'équilibre local (avec partitionnement - LEP et sans partitionnement des éléments d'alliage - LENP) et métastable, sont largement utilisés actuellement. Cependant, on s'est rendu compte depuis longtemps que l'interaction entre les éléments d'alliage et l'interface de transformation mobile peut modifier considérablement la cinétique de croissance de la ferrite à travers le phénomène connu sous le nom de "trainage" (SD). Cette interaction, qui n'est pas considérée dans les modèles précédents, conduit à la ségrégation du soluté à l'interface qui peut retarder le mouvement de l'interface de transformation austénite/ferrite. La prédiction de la redistribution des éléments solutés entre la ferrite et l'austénite et à l'interface est différente selon les différentes approches. Par conséquent, le but de cette étude était d'étudier les interfaces de transformation γ/α à l'échelle nanométrique et de quantifier l'enrichissement local en soluté qui peut aider à identifier le mode de croissance de la ferrite.

Dans ce travail, la ségrégation interfaciale dans Fe-C-Mn modèle est étudiée expérimentalement par Sonde Atomique Tomographique (SAT), qui est une technique bien adaptée pour mesurer quantitativement le profil de concentration de soluté à travers les interfaces à l'échelle quasi-atomique. Les techniques de Diffraction des Electrons RétroDiffusés (EBSD), de Faisceau d'Ions Focalisé (FIB) et de Transmission Kikuchi Diffraction (TKD) ont été utilisées pour la preparation ciblée d'échantillons pour l'étude APT. Les données EBSD ont été utilisées pour déterminer les Relations d'Orientation (ORs) entre la ferrite formée et l'austénite mère, car on s'attend à ce que les ORs puissent affecter la mobilité de l'interface et donc la ségrégation du soluté à l'interface. Un grand nombre d'interfaces γ/α ont été analysées avec succès, et les profils de composition de Mn obtenus à travers les interfaces ont été discutés et comparés à la prédiction des modèles existants pour la transformation austénite-ferrite dans l'acier.

Parallèlement, une modélisation atomistique utilisant la nouvelle méthode des quasi-particules (fonction de densité atomique - ADF) a été appliquée pour étudier la migration de l'interface de transformation γ/α à l'échelle atomique dans le fer pur. Différentes relations d'orientation (ORs) entre les phases d'austénite et de ferrite ont été considérées. L'effet des ORs sur la structure et la mobilité des interfaces α/γ est discuté.

Mots-clés : transformation de l'austénite en ferrite, interfaces de transformation de phase, ségrégation interfaciale, Sonde Atomique Tomographique (SAT), Relations d'Orientation (ORs), acier biphasé (DP), simulation atomistique.